DETERMINING THE IMPACT OF OSTEOCYTE LACUNAR-CANALICULAR TURNOVER ON BONE MATRIX QUALITY

by

Ghazal Vahidi

A thesis submitted in partial fulfillment
of the requirements for the degree

of

Doctor of Philosophy

in

Mechanical Engineering

MONTANA STATE UNIVERSITY
Bozeman, Montana

July 2024

DEDICATION

Dedicated to Amir, Zari, Mahvash, Behzad, and Masoud. I would not be here without you.

ACKNOWLEDGEMENTS

This accomplishment, or anything else for that matter, would not have been possible without the boundless support, love, and encouragement of many wonderful people over the years. First and foremost, I owe endless gratitude to my lovely family—parents, grandparents, cousins, aunts, uncles, in-laws, and everyone in between—and all my friends, who are located all over the world. Without them, I wouldn't be where I am today, writing my doctoral dissertation.

I am deeply grateful to have crossed paths with my advisor, Dr. Chelsea Heveran. Her perpetual support and mentorship have played a critical role in shaping who I am today, personally and professionally. Under her guidance, I have grown significantly as a scientist, mentor, and person. I am so thankful to have been part of the Heveran lab. Each member, whether a graduate or undergraduate student, has been my friend, supporter, cheerleader, colleague, and source of inspiration. I am also immensely thankful to my committee members, Dr. Lewis Cox, Dr. Ron June, Dr. Steve Martin, and Dr. Vanessa Sherk. Each of them played a crucial role throughout my dissertation process. This journey would not have been possible without them. My community at MSU and in the beautiful, magical Bozeman made this experience truly lovely!

Lastly, I would like to thank my husband, Amir, from the bottom of my heart. His love, encouragement, support, and very presence have made both my PhD journey and my life journey a treat. Also, special love-filled gratitude to my lovely pets, Hazel and Loki, for their emotional support and unwavering love and cuteness.

TABLE OF CONTENTS

TABLE OF CONTENTS CONTINUED

TABLE OF CONTENTS CONTINUED

TABLE OF CONTENTS CONTINUED

LIST OF TABLES

Table Page

LIST OF FIGURES

Figure Page

LIST OF FIGURES CONTINUED

Figure Page

LIST OF FIGURES CONTINUED

Figure Page

LIST OF FIGURES CONTINUED

Figure Page

LIST OF FIGURES CONTINUED

Figure Page

LIST OF FIGURES CONTINUED

Figure Page

LIST OF FIGURES CONTINUED

Figure Page

LIST OF FIGURES CONTINUED

Figure Page

LIST OF FIGURES CONTINUED

Figure Page

LIST OF FIGURES CONTINUED

Figure Page

LIST OF FIGURES CONTINUED

Figure Page

LIST OF FIGURES CONTINUED

Figure Page

LIST OF FIGURES CONTINUED

Figure Page

ABSTRACT

Bone fragility in aging is a major unsolved health problem. Existing treatments for bone fragility are effective for about 50% of the population who suffer from loss of bone mass in aging. However, bone fracture resistance is also determined by the quality of bone tissue, including microarchitecture and matrix properties of the bone. Recently-emerging therapeutics targeting bone matrix quality present new avenues for addressing bone fragility. New data suggests that osteocytes, the most abundant and longest-living bone cells, interact with bone matrix in ways that have been likely overlooked. Osteocytes interact with the bone matrix through resorbing and replacing the bone tissue in their expansive lacunar canalicular system, in a process called LCS turnover. Osteocyte LCS turnover might play an important role in maintaining matrix quality and bone fracture resistance throughout life. However, fundamental knowledge gaps persist regarding this process and its impact on bone matrix properties. In this dissertation, we investigated the impacts of aging on abundance, frequency, and dynamics of osteocyte LCS turnover. We also studied the impacts of osteocyte LCS turnover on the matrix properties of its surrounding tissue. Our findings revealed that osteocyte LCS turnover is a prevalent, frequent, and dynamic process but this process significantly declines with aging. The large decline in LCS turnover in aging can have significant implications for bone quality and fracture resistance. We also demonstrated that osteocyte LCS turnover impacts the matrix quality of its local bone tissue, including modulus and energy dissipation, with nanoscale gradations around lacunae and canaliculi. We adapted contact-resonance atomic force microscopy for mapping the viscoelasticity of hydrated bone at the nanoscale. Findings from this study demonstrate that bone viscoelasticity is highly variable at the nanometer-scale and is higher than bulk bone around some canaliculi. Our data highlight a need to revisit how osteocytes perceive strains, since bone properties differ near lacunae and canaliculi compared with bulk bone tissue. Our findings together demonstrate, for the first time, that the quality of a substantial amount of bone surrounding the LCS is influenced by the frequent and abundant osteocyte LCS turnover, and this process declines with aging. These findings motivate investigating the direct influence of the osteocyte on bone matrix properties in aging and disease.

.

INTRODUCTION

1.1 Overview

Despite decades of research related to osteoporosis and related drug development, bone fractures in aging are still a major public health issue[1–5]. It is estimated that more than half of women and one third of men over 50 will experience a bone fracture[1,2]. Direct healthcare costs for fragility fractures are estimated to reach 100 billion dollars by 2040[6]. Bone mass decreases with aging due to dysregulation in the activities of bone-resorbing osteoclasts and bone-forming osteoblasts[7,8]. This loss of bone mass is clearly evident in patients with osteoporosis, as indicated by low bone mineral density (BMD) scores[9–11]. However, BMD does not fully predict fracture risk. The loss of bone mass only accounts for about 50% of fragility fractures, with the remainder occurring in individuals who are not osteoprotic[12,13]. Further, treatments for loss of bone mass, including antiresorptive and anabolic antibody treatments, are not always sufficient to prevent fractures for many individuals[14–18]. The quality of bone tissue also plays a role in determining bone fracture resistance. Bone quality' is an umbrella term that encompasses all bone features, other than bone mass[14,19–24].-This includes features spanning multiple length scales, from macro to nanoscale, such as bone microstructure and geometry, bone hierarchical organization, bone tissue composition and the quality of extracellular matrix[3,5,21,22,24,25]. Bone matrix properties play crucial roles in determining bone strength and toughness[14–18]. Bone matrix quality may offer opportunities for new therapeutic targets for bone fragility, particularly because new data suggests that osteocytes, the most abundant and longest-living bone cells, interact with bone matrix in ways that have been likely overlooked[26–31].

The purpose of this dissertation is to investigate the ability of the osteocyte to impact the material properties of bone matrix through a process called lacunar-canalicular turnover. This introductory chapter serves to frame the critical gaps in how osteocytes interact with bone matrix, the scale and prevalence of these interactions, the impacts on bone matrix properties, and the need for new methodologies to assess these interactions.

1.2 Bone Fracture Resistance Includes Strength and Toughness

Bone is made of 65 wt.% mineral phase, 25 wt.% organic matrix phase, and 10 wt.% water[23,32]. Bone mineral primarily consists of hydroxyapatite, which is among the smallest naturally occurring crystals[33,34]. The organic component of bone is primarily composed of collagen type I, but also include collagen types II, III, V, and others, as well as non-collagenous proteins such as osteocalcin and osteopontin[35–40]. Mineralized collagen fibers, the basic building blocks of bone, form when layers of plate-shaped mineral aggregates, measuring up to a couple of hundred nanometers in length, combine with collagen microfibrils[38,41]. Collagen microfibrils are assembled from collagen triple helices, which are self-assembled collagen chains[38,41]. Mineralized collagen fibrils, interconnected by enzymatic and non-enzymatic crosslinks, further assemble into organized and unorganized geometrical patterns, depending on the type of bone [38,41]. All bones feature an outer shell of cortical bone, either fully or partially filled with cancellous bone. Cortical or compact bone is a dense and solid structure with highly organized lamellae, which consist of organized sheets of fibrils with unidirectional sheets and twisted plywood patterns[42]. Lamellar layers in the cortical bone of large animals further assemble into osteons, forming concentric nested coils around the Haversian canal system[42,43]. Cancellous, trabecular, or spongy bone also comprises lamellae, but instead of unidirectional fibril bundles

with alternating orientations as seen in cortical bone, lamellae in cancellous bone arrange irregularly, in a lattice-like pattern with intersecting trabeculae[41–44].

Healthy bones have significant resistance to bone fractures because they are both tough and strong. Bone is strong because it can withstand significant loads without deforming permanently and failure[45]. Strength is important for withstanding high loads; therefore, it is most directly related to fractures during a single event such as a falling[46–50]. Bone is tough because when submitted to loads, it can absorb a considerable amount of energy from growth and propagation of a pre-existing crack, before breaking through plastic deformation[4,15,21,50–56]. Bone fracture toughness is essential for enduring moderate single loading events, especially when combined with a pre-existing crack[4,15,21,50–56]. Bone also has fatigue toughness, which means it can resist many loading cycles, at magnitudes below the material strength, without failure[45,57]. Fatigue toughness is essential for repetitive stress or impact over time[46–50]. The unique combination of these properties has given bone its extraordinary ability to resist fractures under various loading conditions[3,5,21,22,24,25]. For some skeletal sites like vertebrae, bone strength is the dominant tissue material property relevant to clinical fractures. For other sites like hip, fracture toughness and strength both significantly contribute to resistance against fractures[48]. Bones experience a variety of loading conditions in daily life, including sudden impacts, repetitive stresses, and bending moments[48] and not all fragility fractures are caused by the same loading conditions[48]. Bone with low toughness is more prone to brittle fractures and bone with low strength, the post-yield regime would not be reached, and bone would fracture before yield[58–60].

Aging decreases bone fracture resistance, including both strength and toughness, through several multiscale changes to the musculoskeletal system. This includes alterations not only in

bone mass and microstructure[3,7,61,62] but also in bone tissue material properties such as modulus and viscoelasticity, microdamage accumulation, degree of mineralization, collagen properties and cross-linking density, and bone water[3,5,7,56,61–64]. These factors, all related to bone toughening mechanisms and resistance to fracture across multiple length scales (more details in sections 1.4 and 1.7), contribute to loss of bone toughness with aging[45].

1.3 Bone Fracture Resistance Is Determined by Bone Mass and Bone Quality

Bone strength is determined in part by bone quantity. T-scores or Z-scores derived from dual-energy X-ray absorptiometry (DXA) are standardized ways to monitor bone mineral content and areal bone mineral density[5]. Currently, clinical assessment of fracture risk relies on this measurement as it is proven to successfully predicts more than half of bone clinical fracture cases[1,12,13,65–68]. Bone strength is also determined by bone quality. Bone microarchitecture, one important aspect of bone quality, contributes to bone strength through some measures, including cortical bone width and porosity as well as trabecular bone width, connectivity, and anisotropy[16,23,32,69,70]. Bone composition, another important aspect of bone quality, also contributes to bone strength. Bone mineral, which has a modulus of about of 120 GPa[71,72], plays a major role in contributing to bone stiffness and strength[73]. The degree of enzymatic collagen crosslinking also positively influences bone strength[73].

Bone toughness has many contributing factors. Bone has a complex hierarchical structure with several levels of organic and inorganic components from whole bone level with trabecular and cortical components and major building blocks of bone down to nanoscale collagen microfibrils and mineral aggregates (**Figure 1.1**)[41,44,74–78]. Because bone structure is hierarchical

and highly complex, bone fracture toughness and tissue toughening mechanisms must be considered at multiple dimensional scales. To understand these toughening mechanisms, we first need to understand how cracks advance in the tissue. Cracks initiate and propagate when the elastic energy dissipated by the advancement of a crack equals or exceeds the energy required to create new material surfaces[49,50,57]. Therefore, energy-dissipating or toughening mechanisms make it more challenging to break a material. In bone, energy dissipation and toughening mechanisms exist from nanoscale to macroscale.

Bone has intrinsic and extrinsic toughening mechanisms. Intrinsic toughening mechanisms refer to the inherent properties and structures within the bone tissue that works ahead of a crack tip and includes characteristics related to tissue viscoelasticity and plastic deformation[50,57,79–82]. The intrinsic toughening mechanisms of bone serve to enhance bone fracture toughness by creating plastic zones around crack tips where bone undergoes plastic deformation in the vicinity of a crack tip[50,57,79–82]. These mechanisms enable localized failure through the dissipation of crack energy[50,57,79–82]. These multiscale mechanisms, from the nanoscale to the microscale, typically involve traits of the bone organic matrix, and interactions between bone organic matrix with the mineral phase and water[50,57,79–82]. Some of these mechanisms are microcracking, plastic deformation of collagen molecules, stretching and gliding of collagen fibrils, enzymatic collagen crosslinking, and sacrificial bonding of noncollagenous proteins such as osteopontin, and stabilizing of collagen-mineral interface by water through hydrogen bonding with the organic matrix and electrostatic attractions with the mineral phase[39,83–86]. The extrinsic toughening mechanisms of bone, which are the main source of bone's toughness at larger scales, do not necessarily increase bone energy dissipation and resistance to

crack initiation[50,52,87–92]. Instead, they work behind a crack tip and "shield" the crack tip from the force needed for crack propagation[50,93]. Fibril bridging, crack deflection, crack twisting and formation of microcracks are among these mechanisms[50,52,87–92]. Therefore, the extracellular matrix can dissipate the energy of crack initiation and propagation, across multiple length scales, through various toughening mechanisms and contribute to bone quality and fracture resistance.

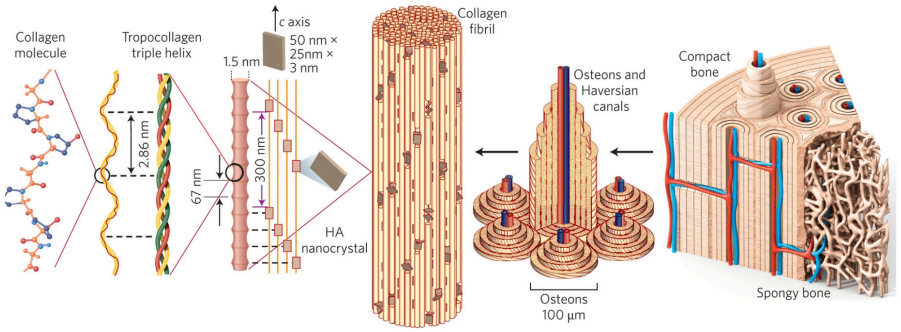

Figure 1.1. Bone hierarchical structure. At the macroscale, bone comprises cortical (compact) and trabecular (spongy) components. Compact bone includes osteons (which are not present in mice), composed of sheets of lamellae and Haversian canals. Lamellae are made of mineralized collagen fibrils, the primary building block of bones, which consist of hydroxyapatite nanocrystals combined with collagen microfibrils in a helical structure at the nanoscale level. Adapted *with permission* from ref. [74]

1.4 The Properties of Bone Matrix Are Dynamic and Depend on Tissue Maturation and Aging

Bone matrix has heterogeneous material properties in part because bone matures over time and not all components of a bone are the same age. The maturation of tissue from time of deposition is different from systemic aging. When bone tissue is deposited by osteoblasts, it initially consists of an unmineralized organic matrix, predominantly composed of collagen fibers and non-collagenous proteins[94,95]. This matrix, referred to as osteoid, provides the framework for bone formation[94,95]. As mineralization progresses, calcium and phosphate ions, sourced from the nearby blood supply and the extracellular fluid surrounding the bone cells, are deposited onto the

collagen matrix. This results in the formation of hydroxyapatite crystals, which transform the initially soft osteoid into hardened bone tissue[94–96]. As hydroxyapatite crystals grow, they become more densely-packed and orderly-organized, while the organic matrix starts to crosslink[96,97].

The mature bone tissue undergoes remodeling, where old or damaged bone is resorbed by osteoclasts and replaced with new bone by osteoblasts[98–100]. This cycle ensures that bone tissue remains healthy, adaptive, and capable of responding to changes in mechanical loading and metabolic demands over time[98–100]. These cells can also perform independently[101]. The bone modeling process involves the uncoordinated removal and deposition of bone and often serves to alter bone size and geometry during development, or to adapt bone shape to significant changes in skeletal loading[102]. Bone turnover is a broader term that describes the removal and replacement of bone, but it conveys that this process is uncoordinated (unlike remodeling) and does not have the functionality of bone modeling[102]. Bone remodeling occurs in larger animals, while tissue turnover occurs in both small animals (including rodents) and large animals [102]

Aging is associated with numerous changes to skeletal physiology that can impact bone matrix properties. These include increased inflammation, increased oxidative stress, alterations in hormonal and mechanical signaling, disruption in production of growth factors and cytokines, and changes to the activities of bone cells[103–107]. Bone cell turnover also changes in aging with deleterious disruptions in the exquisite balance between bone formation of osteoblasts and bone resorption of osteoclasts[7,8,17,108]. Increase in osteoclast bone resorption and decreases in osteoblast bone formation are important hallmarks of aging skeleton (details in section 1.5). Aging decreases collagen enzymatic crosslinks and increases nonenzymatic crosslinks[3,5,7,56,61–64]. Changes to bone mineralization are not consistent across studies; some studies report increased

or decreased mineralization with aging and some report no change[3,109–112]. These changes are directly and indirectly associated with disruptions in bone toughening mechanisms. For example, decreased enzymatic collage crosslinks and increased non-enzymatic crosslinks (e.g., advanced glycation end-products) in aging would decrease collagen fibril strain and plasticity and encourage the fiber separation during cracks, thereby diminishing bone's intrinsic toughening mechanism[15,113]. In another example, aging-related microstructural changes in osteons and tissue cement lines reduce the size of crack bridging and crack deflection, leading to decreased potency of extrinsic toughening mechanisms[15,91,114,115]. The functions of bone cells, their relationship with bone matrix, and changes to these relationships in aging are investigated in the next sections.

1.5 Maintenance of Mineral Homeostasis by Bone Cells

Bone has three primary types of cells: osteocytes, osteoblasts, and osteoclasts. The cellular and molecular mechanisms for osteoblasts and osteoclasts in bone remodeling and maintaining bone quality have been extensively studied[99,100,102,116]. While roles for the osteocyte in coordinating osteoblasts and osteoclasts are well-known, other roles, such as lacunar-canalicular turnover, are less studied but may contribute to both mineral homeostasis and the maintenance of bone matrix quality.

1.5.1 Osteoclasts

Osteoclasts are the primary bone-resorbing cells. These large, multinucleated cells arise from the differentiation of hematopoietic stem cells into the macrophage lineage through the action of macrophage colony-stimulating factors (promote the proliferation and prolong the lifespan of osteoclastic precursor cells) and receptor activator of nuclear factor κB ligand

(RANKL, essential for osteoclast differentiation, fusion, and lifespan)[117,118]. Osteoclasts have a relatively short lifespan, typically ranging from a few days up to 6 weeks[119,120]. The primary role of osteoclasts is the demineralization and degradation of bone matrix. They achieve this by adhering to the bone surface, forming an actin-rich sealing zone, and releasing protons and proteases from their ruffled border at the membrane[117,118]. The acidic environment they create through the release of hydrogen ions facilitates the removal of bone mineral, while their secreted enzymes such as cathepsin K digest the remaining bone matrix[121]. Aging-induced increased bulk bone removal in osteoclasts is driven by pathways such as RANKL/RANK/OPG signaling[108,122] and forms the basis of many bone fragility treatments, such as antiresorptive drugs. The considerable success of antiresorptive drugs like bisphosphonate and denosumab primarily stems from their ability to reduce osteoclast population and functionality[123,124].

1.5.2 Osteoblasts

Osteoblasts serve as the primary bone-forming cells, responsible for producing both the organic and inorganic components of the bone matrix. Osteoblasts are differentiated from mesenchymal stem cells and compete with other cell types for differentiation from mesenchymal stem cells, including adipocytes and chondrocytes depending on several factors such as aging, obesity, and osteopetrosis[125,126]. Osteoblasts produce a substantial volume of macromolecules, including collagenous and non-collagenous proteins during the process of generating unmineralized osteoid[127]. It has been suggested that osteoblasts mineralize the osteoid by depositing calcium phosphate in the form of hydroxyapatite when provided with a nucleation site[127]. The specific mechanisms of matrix mineralization are still being explored, and some recent work suggests that late-stage osteoblasts or even osteocytes may play more important

roles in tissue mineralization than has been previously appreciated[128,129]. Osteoblasts have a limited life spans ranging from days to few months[130]. At the end of their life cycle, osteoblasts can have three different fates: (i) they can undergo apoptosis, (ii) become bone-lining cells located at the bone surface, or (iii) become embedded in the bone matrix, undergo structural changes, and differentiate into osteocytes[131–133].

The formation, differentiation, apoptosis, and function of bone cells are tightly interdependent[117,125,134–136]. Osteoblastic-lineage cells are the primary producers of RankL and macrophage colony-stimulating factors, responsible for inducing osteoclast differentiation and through pathways like OPG/RankL/RANK they also affect osteoclast activity or apoptosis[117,125,134–136]. Conversely, osteoclasts can affect osteoblast formation and differentiation by secreting soluble factors like SEMA4D or influence formation by promoting or inhibiting osteoblastic precursors [117,125,134–136]. Aging decreases the osteoblast population and bone formation activity[7,108] through several factors including impaired mineralization capacity in senescent osteoblasts which also induces osteoclast bone resorption and osteoclastogenesis via pathways like IL-6[137], reduced osteoblast numbers, dysfunctions in signaling pathways such as Wnt signaling, and increased osteoclast-induced sclerostin signaling[7,8,17,108].

1.5.3 Osteocytes

Osteocytes are the most abundant bone cells, constituting 90-95% of all bone cells, with approximately 42 billion osteocytes in the adult human skeleton (> 20 years)[131,138–140]. They have an average half-life of 25 years, making them the longest-lived residents of the bone tissue[131,138,139,141]. Osteocytes are descendants of mesenchymal stem cells through osteoblast differentiation[131]. Some osteoblasts become trapped in the bone matrix during the bone formation

process and undergo dramatic changes in their cell body structure to become osteocytes[131]. Their polygonal structure starts to elongate into a football shape, and they begin to extend dendrites, in a polarized manner, toward the mineralizing fronts (when transitioning from osteoid osteocytes to mineralizing osteocytes)[131]. This is followed by dendrites extending to either the vascular space or bone surface (when transitioning from mineralizing osteocytes to mature osteocytes)[131,142,143]. Mature osteocytes usually maintain their polarity in the directionality of the dendrites and the directionality of their perilacunar mineralization, such that mineral deposition typically occurs on the side of the embedding cell[144]. Osteocytes, along with their dendrites, excavate the bone matrix into holes called lacunae and channels called canaliculi, forming their lacunar-canalicular system (LCS, **Figure 1.2**). Each cell body resides in one lacuna with 20-126 dendrites extending into the canalicular space[131,138,140]. In the adult human skeleton, the surface area of LCS has been estimated to be more than 215 m^2 (on par with a tennis court) with an end-to-end length of 175 km[140]. This complex network allows osteocytes to connect with each other, osteoblasts, osteoclasts, nerve cells, bone vessels, and the bone marrow.

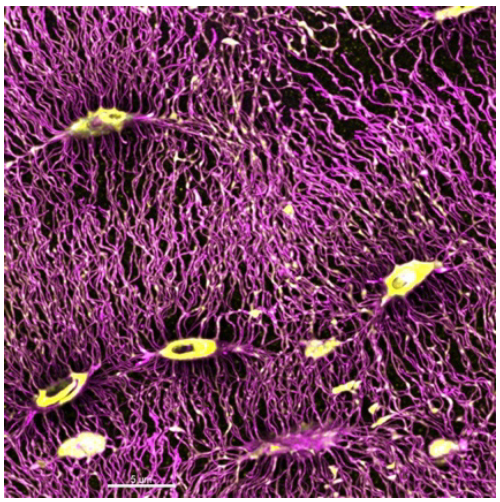

Figure 1.2. Osteocyte lacunar-canalicular system (LCS). Osteocytes reside within a vast and complex network of lacunar holes and canalicular channels. Basic fuchsin staining (magenta, ex vivo staining of embedded bones) illustrates the extensive porosity of the lacunar-canalicular system (LCS) in cortical bone. Calcein-stained tissue (yellow, in vivo fluorochrome injection administered 2 days before euthanasia) shows bone mineralization. We used an inverted confocal laser scanning microscope (CLSM- Leica Stellaris DMI8) to take this figure. This figure was used in [26,29].

Osteocytes orchestrate the activities of osteoblasts and osteoclasts. They promote bone formation in osteoblasts through the mechanical loading-induced activation of the Wnt/β-catenin signaling pathway[145]. This pathway also plays a key role in regulating osteoblastic-lineage cell proliferation, differentiation, and apoptosis[146,147]. Osteocytes maintain bone formation activity in check by secreting sclerostin and dickkopf-1 (DKK-1), which are upregulated in response to proinflammatory cytokines. These molecules inhibit bone formation by suppressing Wnt signaling[145–148]. Osteocytes can also modulate bone resorption activity in osteoclasts as well as the osteoclastogenesis through RankL-OPG signaling[148–150]. The RankL/OPG pathway is upregulated by proinflammatory cytokines and downregulated by mechanical loading[151–153]. Osteocytes express RankL, especially in regions of osteocytic apoptosis, promoting osteoclastic activity. Additionally, osteocytes secrete OPG, which competes with RankL for the RANK

receptor, thereby suppressing osteoclast activity[149,150,154–156]. As previously discusses, these osteocyte mediated pathways, including Wnt/sclerostin and RankL/OPG form the basis for the antiresorptive and anabolic treatments of bone frgaility[157].

Osteocytes are endocrine cells. Despite being buried deep within the bone tissue, fluid flow through the LCS exposes osteocytes to hormones and factors circulating in the blood. Osteocytes secrete signaling factors, including fibroblast growth factor 23 (FGF23), into the circulatory system to modulate the behavior of distant organs such as the parathyroid, kidney, gut microbiome, and heart[144,158–161]. The communication between bone and kidney is essential for maintaining serum phosphate levels, which rely on the circulating levels of FGF23[144,160]. Moreover, the levels of circulating FGF23 and secreted parathyroid hormone (PTH) are directly linked, rendering the parathyroid gland an endocrine target for osteocytes[144,161]. PTH secretion directly elevates circulating FGF23 levels, while FGF23 reciprocally acts on the parathyroid gland to decrease PTH secretion[162–164]. PTH plays a well-known role in calcium homeostasis.

Two primary theories have been proposed for how osteocytes sense mechanical signals and initiate the regulation of bone remodeling activity. (i) Osteocytes can directly sense the tissue strain and mechanical deformation of the perilacunar bone matrix. Studies show that tissue strains are amplified near osteocytes, but the reasons and mechanisms for this strain amplifications are not completely understood[165–167]. (ii) Mechanical loading on the skeleton triggers interstitial fluid flow within the LCS. Shear stresses resulting from these fluid flow changes are sensed by the osteocyte cell body and the dendrites and their processes[168,169.] Stimulation of the osteocytes either way activate osteocyte signaling pathways such as interleukin-6 (IL-6), RankL/OPG, Wnt/β-catenin, sclerostin, and the calcium signaling[170–175].

A newer role for osteocytes is lacunar-canalicular bone turnover (reviewed in detail in section 1.6). In LCS turnover, osteocytes remove and replace bone mineral and possibly matrix adjacent to lacunae and canaliculi[26–28,30,176–187]. This process has the potential to influence bone matrix properties for a sizable quantity of bone in a manner that could be affected by aging.

Aging increases osteocyte cell death and senescence and decreases osteocyte autophagy, which impairs cellular repair mechanisms and promotes cell death pathways like apoptosis[156,188–193]. Apoptotic osteocytes decrease OPG expression and enhance RankL signaling of other osteocytes, boosting osteoclast activity[193]. Additionally, changes to osteocyte cell body, dendrite, and LCS morphology and architecture (details in section 1.6) with aging have deleterious effects on osteocyte mechanosensation and bone responsiveness to skeletal loading[104,175]. Whether aging affects LCS turnover is an unanswered question.

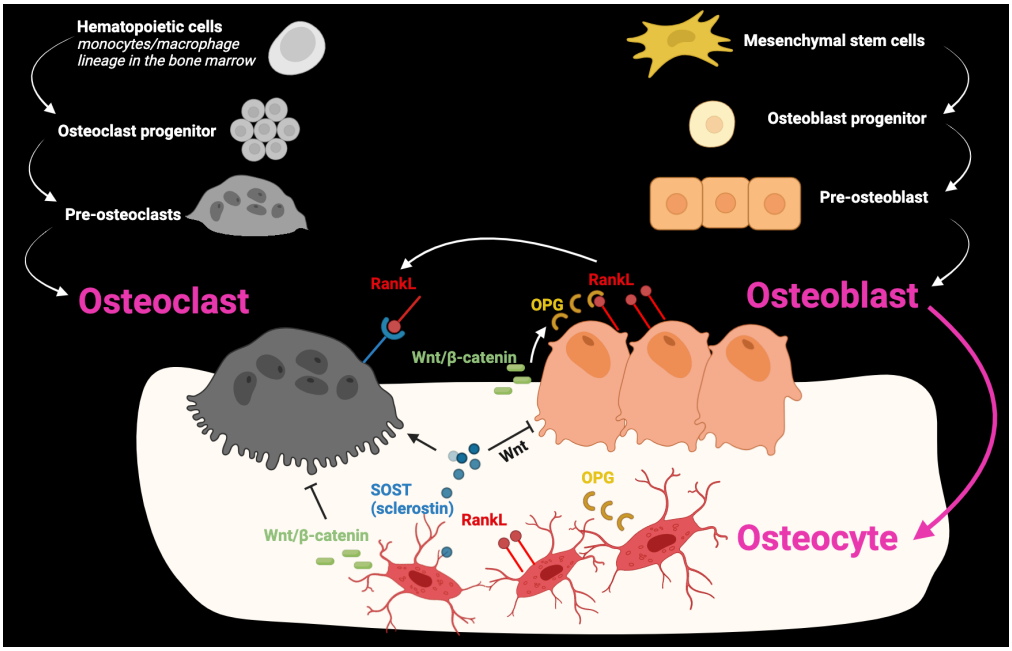

Figure 1.3. Bone cells. Osteoblasts, osteocytes, and osteoclasts secrete molecules that mutually influence each other in paracrine and endocrine manners, ensuring a balance between bone formation and bone resorption is maintained. Osteoblasts and osteocytes promote osteoclastogenesis through pathways such as RankL and inhibit bone resorption through pathways including OPG. Osteocyte-derived SOST promotes osteoclastogenesis and inhibits osteoblast differentiation. Osteoclasts secrete signaling molecules, which interact with osteoblasts and osteocytes, influencing bone formation. Figure created on BioRender.

1.6 Osteocyte Lacunar-Canalicular Bone Turnover

1.6.1 History

Osteocytes can directly modify their surrounding bone tissue by resorbing the bone mineral and matrix and replacing at least the bone mineral. This process is known by various names such as perilacunar remodeling, LCS remodeling (as referred to in chapters 2 and 4), or, as termed in this thesis, LCS turnover[26]. Osteocytic osteolysis, or the enlargement of osteocyte lacunae and canaliculi, was first proposed by Belanger *et al* in the 1960s[194]. They observed lacunar enlargements in chicks on a low calcium diet or administrated PTH. However, the concept of osteocytes being able to remove their perilacunar tissue was dismissed until years

later[26,144]. Another study on rat tibia at that time reported tartrate-resistant acid phosphatase (TRAP) activity, marker of acidification and bone resorption, around osteocytes. However, this finding was also dismissed as a diffusion artifact from osteoclasts[195].

Although osteocytic bone resorption and formation were reported multiple times over the next decades[195–200], advances in imaging technologies, gene analyses, and transgenic mice in more recent decades have convincingly determined that osteocytes are indeed capable of removing and replacing bone mineral[182,184]. In rodent models, osteocyte lacunar sizes were found to increase during lactation and return to their normal size after weaning[182]. It was also found in same rodent models that genes such as TRAP and cathepsin K, which were previously considered specific to osteoclasts, were elevated in osteocytes during lactation and returned to normal levels with weaning[182,184,201]. Similar results were replicated on different strains of mice and rats by other studies during lactation and other conditions of increased calcium demand, such as PTH treatment[26,28,177,182,183,185,197,202–205]. More recently, changes in aging were found to LCS geometry in humans and rodents, including smaller and less connected lacunae and canaliculi[206–208]. These studies leave many questions about the purpose of osteocyte LCS turnover, occurrence outside of large perturbations to calcium homeostasis, the frequency and prevalence of this process, the mediators of LCS turnover, and how this process changes with aging and disease.

1.6.2 What Drives LCS Turnover?

While it is not entirely certain why LCS turnover occurs, the drivers of this process convincingly include the regulation of systemic mineral homeostasis, as evidenced by LCS bone resorption in response to lactation and other sources of calcium pressure. Considering the sheer amount of tissue adjacent to this very large network, LCS turnover is a much faster strategy for

calcium homeostasis than recruitment of osteoclasts[26,131,184]. Levels of circulating PTH and PTHrP increases in conditions such as lactation, egg production, or PTH treatments, which promotes osteocytic osteolysis[26,209,210]. Continued elevated systemic PTH signaling induces LCS resorption of both mineral and matrix components of tissue by inducing acidification through proton pumps and degrading enzymes such as ATPase family, cathepsins, and matrix metalloproteinases[182,187,211]. It is also observed that when the calcium demand ceases, bone mineral is re-deposited, enabling peri-osteocytic matrix homeostasis[182,184,202,203].

Although PTH signaling is largely systematic, research suggests that LCS turnover can be also mediated locally through osteocytic TGF-β signaling. Deletion of osteocyte-specific TGF-β signaling in mice disrupts LCS turnover and decreases LCS bone resorption[180,186,212]. Other works suggest that disruption in osteocyte mechanotransduction via deletion of transcriptional regulators such as Yes-associated protein (YAP) and transcriptional co-activator with PDZ-binding motif (TAZ) also disrupts LCS turnover[179]. Thus, LCS turnover is most likely mediated by both systemic and local factors.

Osteocyte peri-LCS bone deposition has been observed in rodents and humans through the systemic injection of calcium-binding fluorochrome labels[30,179,182,187,197,213]. Although these labels are traditionally used to measure mineral deposition by osteoblasts, high-resolution imaging has enabled us to capture extensive fluorochrome labeling within both osteocyte lacunae and canaliculi (**Figure 1.2**). Extensive fluorochrome labeling has been observed around lacunae in several studies outside of the calcium pressure context[30,179,187], which suggests that osteocyte LCS mineralization may be a more active and widespread phenomenon than has been previously appreciated. In one study, approximately 60% of lacunae in the femoral midshaft cross-section of

wild-type male and female C57BL/6 mice at 28 days exhibited calcein labels administered 2 days prior to euthanasia[179]. Another investigation discovered that in the mid-cortical cross-section of the tibia, about 55% of lacunae displayed calcein labels injected 5 days before euthanasia in 2-month-old male wildtype littermates of MMP13 (matrix metalloproteinase) knockout mice with a mixed C57BL/6 genetic background[187]. The dynamics of LCS turnover are not known, nor are the changes to these dynamics in aging.

1.6.3 Changes to LCS Turnover in Aging

In aging, osteocytes become senescent or apoptotic[190,193] and require greater strains to engage in anabolic signaling[8,175,214,215]. Aging also decreases LCS morphology and architecture[206,208,216–218]. Previous works reported that in aged mice, lacunae are smaller, rounder, less-oriented, and less-abundant compared to skeletally-mature young mice[206,208,219]. Several works reported that aging decreases lacunar number density and increases lacunar sphericity in humans and rodents[89,220–223]. The canalicular network also degenerates with aging; canalicular and dendrite numbers both decrease in aged mice[206]. Altered lacunar morphology and number density alone cannot explain how aging alters osteocyte LCS turnover. For example, smaller lacunae with aging could result from either (i) fewer osteocytes to activate LCS turnover, (ii) decreased LCS bone resorption per osteocyte, (iii) increased LCS bone formation/mineralization per osteocytes, or (iv) a combination of altered cellular participation and activity.

1.6.4 Does LCS Turnover Impact Bone Matrix Properties?

Several prior studies utilizing transgenic mouse models that produce an aging-like phenotype to LCS geometry suggest that suppressed LCS turnover has the potential to reduce the quality of bone matrix[179,186,187]. Mice with an osteocyte-intrinsic defect in TGF-β signaling had

decreased bone fracture resistance[186]. The authors highlighted that LCS turnover defects can cause severe bone fragility even when the bone quantity is normal. In another study on mice with systemic MMP13 deletion, researchers reported suppressed LCS turnover and also bone quality (e.g., increased nonenzymatic crosslinks and decreased collagen orientation) and lower fracture toughness[187]. Interfering with osteocyte-intrinsic YAP/TAZ signaling in mice was also reported to impact LCS turnover and decrease fracture toughness[179]. Given the similarity of these phenotypes and aged LCS, a compelling hypothesis is that LCS turnover has an important role in regulating bone quality but that this process diminishes in aging. However, several critical gaps must be overcome with regards to understanding the amount of bone matrix that osteocytes interact with through LCS turnover and the impacts on bone matrix properties, as well as whether these processes change in aging.

Osteocytes can demineralize bone and does so during skeletal calcium mobilization[26,28,177,182,183,185,197,202–205]. Osteocytes can also re-mineralize bone, as visualized by fluorochrome labels around LCS as well as the decrease in LCS size after removing calcium pressure[182,184,202,203]. However, the spatial extent and dynamics of this process is not yet defined.

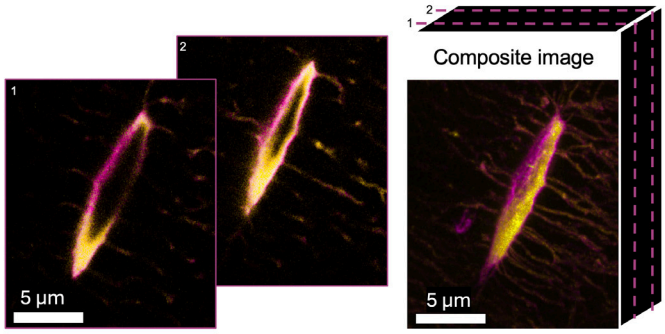

Figure 1.4. Osteocyte lacunae can show double labels when administered at short timepoints before euthanasia. In vivo serial fluorochrome labeling (calcein in yellow, 2 days before euthanasia; alizarin in magenta, 8 days before euthanasia) in a female 5 mo C57BL/6JN mouse reveals double-labeled lacunae.

The ability of LCS turnover to remove and deposit the bone matrix is not as established as for bone mineral, in part due to technical challenges to performing these assessments[26,28]. Some evidence points toward the possibility that osteocytes can impact bone matrix. For instance, one study showed rings of demineralized bone around osteocyte lacunae that stained positive for hematoxylin and toluidine blue[197]. However, these rings could be residual matrix after mineral resorption or new osteoid produced by osteocytes. Older radiolabeling studies on egg-laying hens during a period of calcium repletion showed [3H] proline-labeled collagen around osteocyte lacunae[224,225]. Additionally, Villanueva osteochrome-stained transiliac bone biopsies revealed osteoid-positive lacunae[213]. In experiments with GFPtpz inserted into the mouse pro α2(I) collagen N-terminus under the control of the 3.6-kb type I collagen promoter, strong bright bands of GFP signals were observed around osteocytes[226]. Although direct investigation of osteocytes' ability to produce osteoid is lacking, numerous transcriptomic studies have revealed that the osteocyte transcriptomic signature is enriched for genes involved in both mineral and matrix resorption (e.g., cathepsin K, tartrate-resistant acid phosphatase, vacuolar ATPase family, DMP1, MEPE) as well as tissue deposition (osteocalcin, osteonectin, Col1a1, Col1a2), sometimes surpassing osteoblasts[227–230].

In summary, fundamental critical gaps persist regarding the osteocyte lacunar canalicular turnover. What are the extent and dynamics of LCS turnover? How much bone tissue is affected by LCS turnover? How often LCS turnover happens? Is this process different among osteocytes from different bone types and skeletal sites? Does this process impact material properties of the tissue surrounding LCS, and if so, how? Does aging impact LCS turnover and the interaction of

this process with the bone matrix, and if so, how? Filling these fundamental gaps would provide the platform to investigate osteocyte LCS turnover as a therapeutic target for bone fragility.

1.7 Measuring the Impacts of LCS Turnover on Bone Tissue

LCS turnover can impact bone quality and tissue level material properties of the matrix surrounding the LCS[28]. However, a crucial gap in the literature is that most investigations into the impacts of LCS turnover on bone matrix quality relied on microscale tools such as nanoindentation, Raman spectroscopy, or backscattered SEM (discussed further in Chapter 2). These microscale tools lack the sensitivity and resolution required to assess the gradation of bone material behavior or composition that happens at sub-microscale distances from lacunae. Studies on young adult mice under normal conditions have reported similar tissue modulus or composition between bone located 1–5 μm from lacunae and farther away at 7-15 μm[183,203]. When there is a significant perturbation in mineral homeostasis, such as during lactation, PTH or glucocorticoid treatments, or metabolic diseases, bone located close to osteocyte lacunae, at similar distances as reported before, exhibits lower mineralization or stiffness compared to bone located farther away[231–239]. These results together signify a need to zoom in by at least an order of magnitude (from microscale to 10s – 100s of nanometers) to investigate the effects of LCS turnover on peri-LCS tissue properties. Indeed, ultrahigh-resolution synchrotron-based CT and transmission electron microscopy reveal a gradation in bone composition extending hundreds of nanometers away from LCS walls such that the lowest mineralization is observed immediately adjacent to lacunar and canalicular walls, with mineral density peaking at a distance of 200–400 nm away[240,241]. Synchrotron-based techniques offer the necessary resolution to assess the

composition of peri-LCS tissue, yet they are accessible to only a few researchers and do not measure bone material properties.

Atomic force microscopy (AFM) could be a promising tool to assess the nanoscale material properties of peri-LCS tissue. While AFM has been used to map the heterogeneity of bone modulus and hardness, prior studies did not studies quantify spatial variation in material properties near the LCS. It would be valuable to map spatial variations of material properties like modulus around lacunae for osteocytes that did or did not recently engage in LCS turnover (i.e., label-positive) and assess the impact of age on these spatial distributions. It would also be valuable to map nanometer-resolved spatial distributions of bone viscoelasticity near osteocytes, since these properties are relevant to understanding the impact of these cells on bone matrix and, conversely, the impacts of bone matrix on osteocyte mechanosensation.

Contact resonance AFM (CR-AFM) is a promising approach for making these measurements but requires adaptation to use on bone. CR-AFM provides information about sample material properties, such as viscoelasticity or energy dissipation, through the resonant frequencies and mode shape of an oscillating cantilever beam in contact with a sample[242]. The viscoelasticity of biological specimens, including bone, depends on their hydrated state[243–245]. Therefore, conducting CR-AFM in liquid environment has significant applications. However, there are some challenges associated with applying this methodology to bone or materials similar to bone, which is why there have been no CR-AFM investigations in these types of tissue to date. First, implementing previously established CR-AFM dual-AC resonance tracking for continuous mapping of viscoelasticity[242] proves challenging on stiff or non-uniform structures. Next, conducting CR-AFM in liquid is challenging due to the complexities introduced by fluid

interactions with the cantilever beam, which impacts the contact mechanisms and the subsequent measurements. A few studies have proposed corrections for the hydrodynamic effect[242,246–248], but the specific adjustments to implement the technique on bone or other stiff, complex material systems have yet to be made.

1.8 Dissertation Aims

The overarching hypothesis of this dissertation is that osteocyte LCS turnover is an abundant, frequent and dynamic process that plays an important role in maintaining the matrix quality of peri-LCS tissue, and that aging decreases the prevalence and dynamic LCS turnover process. The long-term goal of these projects is to understand the impacts of changes to LCS turnover in aging on bone fracture resistance and mechanosensitivity.

Chapter 2 provides a detailed literature review of the current understanding of the effects of LCS turnover on bone quality and discusses available tools to study LCS turnover at length scales relevant to these investigations.

Chapter 3 reports "**Study 1- "Aging decreases osteocyte lacunar-canalicular turnover in female C57BL/6JN mice**". The purpose of this study was to determine the percentage of osteocytes engaged in LCS bone mineralization and resorption in the femur of skeletally-mature young adult (5-month) and early-old-age (22-month) female. We also explored the impact of aging on the dynamics of these processes. We conducted serial fluorochrome labeling, confocal microscopy, and immunohistochemistry studies of both cortical and cancellous compartments of the femur. We also tested the hypothesis that the LCS turnover activity depends on natural variations in tissue strain and that this relationship changes in aging by comparing LCS bone mineralization dynamics between femur regions with distinct natural strain variations. In this

study, we presented the first evidence that osteocyte participation in mineralizing their surroundings is highly abundant in both cortical and cancellous bone of young adult female mice. We showed that aging significantly reduces cortical and cancellous osteocyte participation in perilacunar bone mineralization and resorption, in a manner likely dependent on tissue strain.

Chapter 4 discusses Study 2- "**Perilacunar bone tissue exhibits sub-micrometer modulus gradation which depends on the recency of osteocyte bone formation in both young adult and early-old-age female C57Bl/6 mice**". The purpose of this study was to investigate whether sub-microscale gradation of tissue modulus exists in peri-lacunar tissue and if these modulus gradations are impacted by LCS turnover activity. We also explored whether aging impacts perilacunar modulus gradation. We employed atomic force microscopy (AFM) to generate nanoscale-resolution modulus maps for embedded cortical femur osteocyte lacunae from young adult and early-old-age female mice. We used fluorochrome labeling and confocal microscopy to identify the lacunae with and without active LCS turnover activity. In this study, we reported, for the first time, that bone modulus is graded at the sub-micrometer scale around osteocyte lacunae and that this gradation depends on recent osteocyte LCS turnover activity. Lacunae with recent turnover activity are surrounded by a region of lower modulus tissue. We also show that aging alters some features of perilacunar bone modulus gradation. I am the second author of this paper, and my role involved contributing to AFM method development and data collection. I was responsible for developing confocal laser scanning microscopy methods, collecting data, conducting data analyses, and creating visualizations. I contributed to writing the original draft of the paper, reviewing and editing it, as well as responding to reviewers.

Chapter 5 reports Study 3- "**Contact resonance atomic force microscopy on hydrated bone reveals nanometer-scale heterogeneity in energy dissipation that depends on proximity to canaliculi**". The purpose of this study was to employ and adapt a liquid CR-AFM approach for its first usage on bone to evaluate the viscoelastic properties of hydrated bone tissue at the nanometer length-scale. We quantified the tissue's energy dissipation (tan δ) and its heterogeneity, both adjacent to osteocyte canaliculi and in bulk bone tissue away from these structures in hydrated cortical bone for young adult female C57BL/6JN mice. We demonstrated that bone tissue energy dissipation (tan δ) is highly heterogenous in hydrated bone tissue. We also showed that tan δ frequently shows spatial patterning near canaliculi. These data necessitate an updated understanding to the role of bone material property heterogeneity in bone biomechanics as well as the role of local viscoelasticity to osteocyte mechanosensation. Moreover, the approach developed in this study is expected to make CR-AFM measurement more accessible to bone researchers.

Chapter 6 provides concluding remarks on my dissertation studies and proposes future directions for this research. Collectively, these studies signify that LCS turnover has important impacts on bone matrix properties and that aging changes how osteocytes interact with bone matrix. The data generated in this thesis will provide novel insights into osteocyte-matrix interacts that can hopefully be used by others to help design new therapies that target the improvement of bone matrix properties in aging.

CHAPTER TWO

LACUNAR-CANALICULAR BONE REMODELING: IMPACTS ON BONE QUALITY AND TOOLS FOR ASSESSMENT

Contribution of Authors and Co-Authors

Manuscript(s) in Chapter(s) 1

Author: Ghazal Vahidi

Contributions: conceptualization, writing original draft, review and editing

Co-Author: Caleb Rux

Contributions: writing original draft, review and editing

Co-Author: Vanessa Sherk

Contributions: conceptualization, review and editing

Co-Author: Chelsea Heveran

Contributions: conceptualization, writing original draft, review and editing

Manuscript Information

Ghazal Vahidi, Caleb Rux, Vanessa Sherk, Chelsea Heveran

Bone

Status of Manuscript:
☐ Prepared for submission to a peer-reviewed journal
☐ Officially submitted to a peer-reviewed journal
☐ Accepted by a peer-reviewed journal
☒ Published in a peer-reviewed journal

Elsevier
February 2021
Volume/Issue 143
https://doi.org/10.1016/j.bone.2020.115663

Abstract

Osteocytes can resorb as well as replace bone adjacent to the expansive lacunar-canalicular system (LCS). Suppressed LCS remodeling decreases bone fracture toughness, but it is unclear how altered LCS remodeling impacts bone quality. The first goal of this review is to assess how LCS remodeling impacts LCS morphology as well as the composition and mechanical properties of surrounding bone tissue. The second goal is to compare tools available for the assessment of bone quality at length-scales that are physiologically-relevant to LCS remodeling. We find that changes to LCS morphology occur in response to a variety of physiological conditions and diseases and can be classified in two general phenotypes. In the 'aging phenotype', seen in aging and in some disuse models, the LCS is truncated and osteocytes apoptosis is increased. In the 'osteocytic osteolysis' phenotype, which is adaptive in some physiological settings and possibly maladaptive in others, the LCS enlarges and osteocytes generally maintain viability. Bone composition and mechanical properties vary near the osteocyte and change with at least some conditions that alter LCS morphology. However, few studies have evaluated bone composition and mechanical properties close to the LCS and so the impacts of LCS remodeling phenotypes on bone tissue quality are still undetermined. We summarize the current understanding of how LCS remodeling impacts LCS morphology, tissue-scale bone composition and mechanical properties, and whole-bone material properties. Tools are compared for assessing tissue-scale bone properties, as well as the resolution, advantages, and limitations of these techniques.

2.1 Introduction

Osteocytes are terminally-differentiated osteoblasts that reside in holes in the bone matrix termed lacunae. Dendritic processes from the cell wall extend through a network of canaliculi to form gap junctions with other osteocytes.[249–251] The osteocyte performs many functions, including mechanotransduction, coordination of osteoclasts and osteoblasts, and participation in systemic mineral homeostasis.[249–251] In recent years, the lacunar-canalicular system (LCS) is acknowledged to directly participate in bone tissue remodeling. The impact of LCS remodeling on bone tissue composition and mechanical properties is potentially very significant. There are ~42 billion osteocytes in the adult human (>20 years old) skeleton[252], with 20-126 canaliculi each[235,252–255], which together have a surface area of ~215 m^2.[252] The expansive network of bone that can potentially undergo LCS remodeling far exceeds the surface available for remodeling by osteoclasts and osteoblasts.[256]

The first observations that the osteocyte can modify surrounding bone matrix were made more than 50 years ago by Belanger, who reported proteolytic activity in mature osteocytes.[257] The first of many reports of altered LCS remodeling were for osteocytic osteolysis – the enlargement of lacunae and canaliculi.[257–261] In the last decade, interest in LCS remodeling has greatly increased. It is now identified that altered LCS remodeling can also contract, as opposed to expand, lacunar and canalicular morphologies.[262–266] Several mechanisms are now identified for how osteocytes modify their surrounding bone tissue environment. Osteocytes resorb bone by acidification[267], as well as by production of matrix metalloproteinases[259,268–270], cathepsin K[259,271], and tartrate-resistant acid phosphatase.[259,272] Osteocytes can build bone by deposition of

new osteoid.[259,272,273] Bone resorption and deposition occurs along the osteocyte lacuna as well as along dendrites extending into canaliculi.[259,274,275]

LCS remodeling has the potential to impact bone tissue maturity, the effective age of a packet of bone tissue.[276] With time from osteoid deposition, bone tissue undergoes rapid primary mineralization (days) and then slower secondary mineralization (months).[276,277] Mineral characteristics also change with maturity; more mature hydroxyapatite crystals are larger, more perfect, and have increased carbonate substitution.[278,279] Enzymatic and non-enzymatic collagen crosslinks both accumulate in the maturating tissue.[280] More mature tissue is compositionally less heterogeneous[281,282] and has increased microcracks.[283] Conventionally, bone tissue maturity is considered to result from a balance between osteoblastic deposition and osteoclastic resorption.[276] Because the osteocyte can both resorb and replace bone, it is possible that tissue maturity can be 'refreshed' for tissue adjacent to lacunar and canaliculi by more frequent LCS remodeling.

A growing body of knowledge demonstrates that LCS morphologies change in aging, unloading, estrogen deficiency and other conditions that lower bone fracture resistance.[231,262,264–266,284–286] Several questions need to be addressed to improve the understanding of the role of the LCS in tissue-scale bone quality and whole-bone fracture resistance. First – what is the impact of altered LCS remodeling on tissue-scale bone tissue composition and mechanical properties? Second – when are changes to LCS remodeling adaptive versus maladaptive from the perspective of bone quality maintenance? These questions currently complicate interpreting the significance of altered LCS morphologies that occur in many physiological conditions.

The purpose of this Review is to summarize current knowledge about the role of the LCS and its regulation of bone tissue quality. We consider the current state of knowledge about how LCS remodeling affects network morphology, bone tissue composition and mechanical properties, and the impacts of these tissue-scale changes to whole-bone material properties. In addition, we compare the advantages, limitations, and resolution of tools available to study bone quality local to the LCS. Finally, we address current gaps of knowledge to drive future directions.

2.2 The Significance of LCS Remodeling on Bone Quality and Fracture Resistance

2.2.1 Does LCS Remodeling and Perilacunar Bone Quality Impact Bone Fracture Resistance?

Genetic mouse models suggest that reduced LCS remodeling, which is sometimes termed perilacunar remodeling (PLR) or perilacunar-canalicular remodeling (PLCR) diminishes bone quality and fracture toughness.[270,287,288] Mouse models producing a phenotype of decreased LCS remodeling concurrent with decreased notched fracture toughness include MMP13$^{-/-}$ [287] and DMP1-Cre$^{+/-}$; TGFβ$^{fl/fl}$ [270], both in 2-month old male mice. DMP1-Cre$^{+/-}$;MMP13$^{fl/fl}$ does not reduce bone work to failure from three-point bending in 2-month or 4-month male mice[289], although this quantification of bone toughness is known to be more variable that notched fracture toughness.[290] Together, these genetic models implicate the TGFβ pathway in the maintenance of bone fracture resistance. The specific reasons why diminished LCS remodeling affects fracture resistance in these models are not clear. These models result in reduced perilacunar bone resorption or deposition[287,289] and also result in smaller lacunar morphology[270,289], increased nonenzymatic collagen crosslinks[287], and decreased flexural and tissue-scale moduli[270], all of

which have the potential to impact whole-bone fracture resistance. These models are a compelling basis for considering that LCS remodeling is important for bone quality, but there several important gaps in understanding. First, the relationship between LCS bone remodeling and fracture resistance is not clear. For example, it is not reported if conditional knock out mice have a positive correlation between LCS remodeling and fracture resistance, and if this relationship would also be detected in wild type mice. Second, these deletions occur while the skeleton is growing, which may confound the role of the osteocyte in development versus maturity in maintaining bone tissue quality. Ultimately, it is not yet understood if LCS remodeling is important for maintaining bone quality and fracture resistance in health, as well as what would constitute a deleterious alteration to the frequency or extent of this remodeling. As reviewed in subsequent sections, LCS network geometries as well as the composition and mechanical properties of bone tissue local to the LCS may all change in response to altered remodeling (**Table 2.1**). These changes, in turn, may influence whole-bone mechanics, including fracture resistance.

2.2.2 The Impact of LCS Remodeling on LCS Morphology

The role of the osteocyte in remodeling bone tissue is currently most studied from the perspective of LCS morphology, which is readily assessed using a number of imaging techniques. Osteocytes participate in calcium homeostasis, partly through PTHrP stimulation, by resorbing bone surrounding lacunae and canaliculi to liberate calcium.[267] Osteocyte lacunae and canaliculi enlarge for lactating C57Bl/6 and CD1 mice, and then recover after weaning, indicating that osteocytes are capable of producing bone matrix.[259,275,285] However, the effects of lactation on lacunae may depend on the genetic strain of the animals tested. For example, Naval

Medical Research Institute (NMRI) mice[291] do not undergo lacunar morphological changes with lactation. Some of these effects could also relate to litter size, as smaller litter sizes (which occur with some strains) produce less calcium demand for the lactating mother.[292–294] Exogenous parathyroid hormone (PTH) treatment stimulates calcium release and affects lacunar geometries. Lacunae enlarge for Wistar rats treated continuously[261] or C57Bl/6 mice treated intermittently[295] with PTH (1,34). Intermittently elevated PTH due to exercise may only have a mild effect on lacunar morphology in areas that are receiving sufficient baseline mechanical loading, but this requires further investigation.[232] Lacunar morphologies are also responsive to disruptions in phosphate homeostasis. The underlying pathologic conditions in these studies complicates interpretations of the involvement of LCS remodeling. For example, osteocyte lacunae are larger for mice with x-linked hypophosphatemia than for wild type controls.[296] LCS remodeling could be altered, but these results could also be related to global differences in phosphate availability and bone mineralization. Lacunar morphology appears to be altered in chronic kidney disease (CKD), which affects phosphate homeostasis. In humans, iliac crest biopsies from patients with high-turnover CKD do not have different lacunar areas from low-turnover CKD, but do have increased lacunar number density, perimeter, and porosity. Further, lacunar number density and area were positively correlated with serum PTH.[297] However, it is important to note that it is not yet clear whether changing lacunar morphologies in CKD are a product of altered phosphate levels or may instead reflect changes from other features of the disease, including inflammation and oxidative stress.

Lacunar morphologies also change with aging and this appears to be conserved across species. 3D measurements reveal that aged mice (24 mo) have less-abundant osteocyte lacunae

compared with skeletally-mature young mice (6 mo), and are smaller, rounder, and less-oriented (**Figure 2.1** and **Figure 2.2**).[262,298] Lacunar number density declines with aging for male[262,286] and female[286] mice, which recapitulates the same effect in humans.[299–302] Further, an association between increased age and decreased lacunar volume and increased lacunar roundness is seen for mice at several load-bearing skeletal sites[262,284,286] as well as for female humans.[303] These effects are dependent on sex; female 22 month-old mice have smaller osteocyte cell volume but not lacunar volume compared with 5 month-old comparisons, yet males have decreased lacunar volume over the same time period.[286] The canalicular network also degenerates with aging. Canalicular and dendrite numbers each decrease with aging in male and female mice.[286] It is unclear why aging produces changes to LCS morphology, but the increased osteocyte apoptosis, autophagy, and senescence in aging may have roles in these network changes due to the accompanying loss of mechanical sensitivity.[304–306]

Lacunar morphologies appear to be sensitive to unloading. Common models of disuse and the osteocyte include sciatic neurectomy, hindlimb unloading, Botox immobilization, and microgravity.[264–266,307,308] These studies mostly agree that unloading results in smaller and more spherical lacunae and increased osteocyte apoptosis. In a study of 30-week female Sprague Dawley rats, sciatic neurectomy at 3 weeks of age reduced both lacunar volume and number density.[265] Hindlimb unloading of 6 mo old male Sprague Dawley rats for 28 days increased osteocyte apoptosis and decreased lacunar number density.[266] Additionally, 1 month of spaceflight for 23-week old C57Bl/6N male mice also resulted in smaller, more spherical, and less-abundant lacunae, as well as increased fraction of empty lacunae.[264] However, not all unloading studies find this ‘aging’ phenotype. In a study of 14-week old Wistar female rats

administered Botox in a hindlimb, osteocyte lacunar size, shape, and density were not affected in a 28-week period following injection.[307] Spaceflight can also produce an osteocytic osteolysis phenotype. Female C57Bl6/mice subjected to 15 days of flight had larger and more elongated lacunae in ischial cortical bone, with no evidence of osteocyte death.[308]

Exercise does not have a simple relationship with LCS morphology. Aerobic exercise causes an increase in PTH to counteract the loss of ionized calcium, which occurs in the first couple of minutes of exercise and persists until the end of the bout of exercise.[309,310] However, aerobic exercise does not clearly increase lacunar size.[232] Lacunar area was not significantly increased for 16-week old C57Bl/6 mice subjected to 30-min of running for 21 days, although the perilacunar bone was significantly less mineralized[232]. Zebrafish exercised in a swim tunnel for 4 weeks had similar lacunar volume and sphericity in vertebral bone compared with non-exercised controls.[311] Importantly, the effect of exercise paradigms that engender high mechanical strains (e.g., resistance training, jumping) on LCS has not been tested. Resistance training decreases PTH during the exercise and jumping decreases PTH after exercise, which may further affect the osteocyte in comparison with aerobic training.[312,313] Ultimately, the paucity of studies about the effects of loading and unloading on LCS remodeling, as well as inconsistent loading/unloading models, species, skeletal site, sex and age of study animals across investigations contribute to a persistant gap in understanding about the effects of loading on the osteocyte.

Both estrogen deficiency[314] and antiresorptives[315] affect osteocyte viability and behavior, and so several investigations assessed whether OVX or common osteoporosis treatments also affect osteocyte lacunar morphologies. Lane and coworkers found that osteocyte lacunae were

~5% larger at 21 days after OVX for 6 month old Swiss-Webster mice compared with sham controls.[231] Sharma *et al* found increased lacunar-canalicular porosity and canalicular diameter, but no change in lacunar number density for Sprague Dawley rats 6 weeks from OVX versus sham controls.[233] However, OVX is not always found to influence the LCS. Stern and coworkers found that lacunar sizes and number density were not different 8 weeks after OVX, with or without sequential osteoporosis treatment, for 6 month Sprague Dawley rats compared with sham controls.[234]

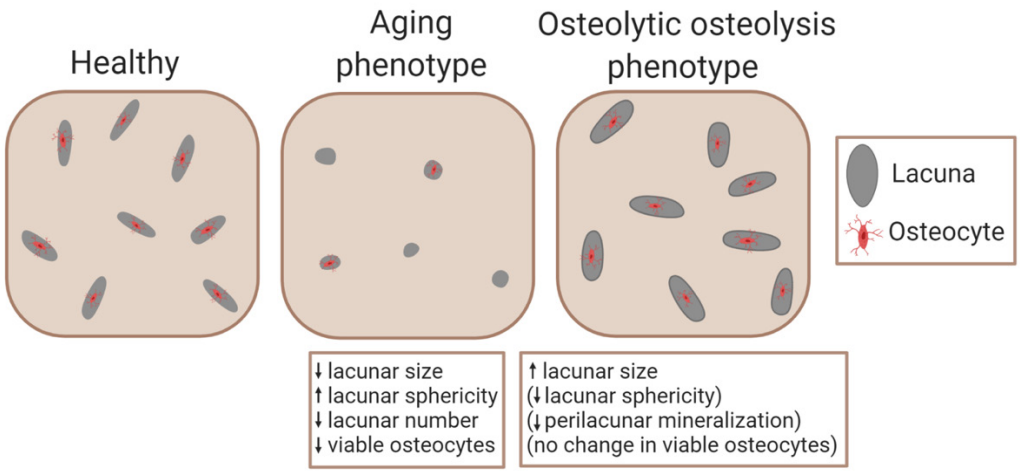

Figure 2.1. Two phenotypes for LCS remodeling. Compared with healthy reference bone, the 'aging' phenotype is associated with smaller, more spherical, and fewer lacunae, with higher osteocyte apoptosis. The 'osteolytic osteolysis' phenotype is more variable. In all cases, lacunae and canaliculi are enlarged. Sometimes lacunae are elongated and surrounded by less-mineralized bone, while osteocyte viability usually does not decrease.

Data across physiological models suggest that the osteocyte could have ‘adaptive’ and ‘maladaptive’ responses to changing physiological conditions (**Figure 2.2**). The ‘aging’ phenotype of smaller and more spherical lacunae, together with increased apoptosis, is likely maladaptive. This phenotype appears in aging[262,263] and unloading[265,266] and sometimes appears in spaceflight[264] and glucocorticoid therapy.[268] It is not clear whether this phenotype emerges

because of increased senescence, apoptosis, inflammation, osteocyte metabolic dysfunction, of some combination of these events. It is further unclear whether the ‘aging’ phenotype is caused by, or instead causes, impaired mechanosensation. A separate phenotype of abundant large and elongated lacunae is not clearly adaptive nor maladaptive. Sometimes, this ‘osteocytic osteolysis’ phenotype may be adaptive, as for lactation[259,275] or PTH treatment.[295] Other times, this phenotype may be maladaptive. For instance, in high-turnover CKD, lacunar size is positively correlated with serum PTH[297], and LCS remodeling increases.[273] Interestingly, this phenotype is generally not associated with apoptosis, indicating a continued active role of the osteocyte whether in health or disease. There may be additional adaptive functions of the ‘osteocytic osteolysis’ phenotype. From FEA results (reviewed in 1.7), increased lacunar size and decreased perilacunar tissue modulus, which often accompanies increased lacunar size, both increase perilacunar tissue strain.[234,316] It is possible that osteocytes may be able to amplify local bone tissue strains, which could sometimes represent an adaptive functionality. Studies that investigate LCS geometries together with perilacunar bone composition are needed for better contextualizing whether LCS remodeling is adaptive or maladaptive in particular physiological conditions. Further, the region of bone investigation should be carefully decided. Lamellar bone has fewer but larger and more elongated lacunae, while woven bone has more lacunae which are also more spherical and randomly oriented.[236] Thus, lacunar morphological differences in diseases that increase woven bone formation, such as diabetes and obesity, may be a reflection of the differences in bone tissue organization as opposed to an indication of adaptive or maladaptive osteocyte response.[317,318]

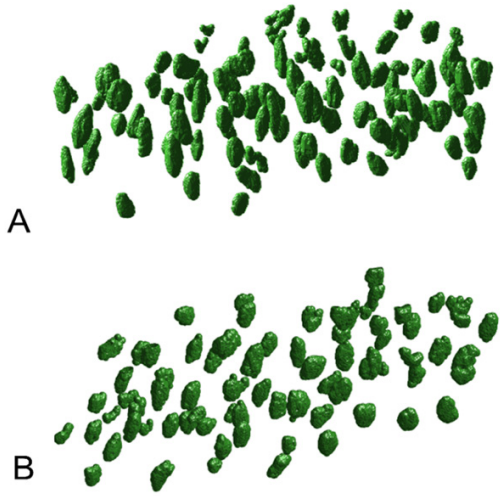

Figure 2.2. 3D osteocyte lacunar geometries change with age. Compared with 6-month male mice (A), lacunae in bones from 24-month male mice (B) are smaller, more spherical, and sparser. (reprinted from[262])

2.2.3 The LCS and Bone Mineralization

The distribution of hydroxyapatite mineral in bone tissue is not homogenous and is impacted by proximity to the LCS. Most bone mineral is located within 1.2-1.4 micrometers of a canalicula.[319,320] Bone mineral quantity appears to be graded within the immediate vicinity of the LCS.[274,319–321] Hesse *et al* studied human jaw bone specimens from adult donors (ages 19-72) that were healthy or had bisphosphonate-induced osteonecrosis with synchrotron x-ray computed tomography.[319] Most mineral was located very close (< 0.5 μm) to canaliculi and lacunae, and then mineral density decreased radially outwards until reaching asymptotic values. Mineral gradients were more profound for healthy patients than for those with osteonecrosis, in which case there was less contrast between the high mineralization alongside the LCS walls and the mineral-saturated osteonecrotic bone matrix. These data suggest that a larger mineral gradient is indicative of recent or continuous remodeling. Another study, by Kerschnitzki and coworkers, assessed healthy ovine cortical bone with both CLSM and synchrotron small-angle x-ray

scattering and determined that hydroxyapatite mineral platelets were thicker alongside the LCS.[320] Minerals were larger and more oriented in regions with denser lacunae and canaliculi. Also in support of higher mineral adjacent to lacunae, Gardinier *et al* found that the first 2.5 μm-thick concentric ring away from the lacunar wall in male control C57Bl/6 mice had higher backscattered scanning electron microscopy (BSEM) grey level and thus mineralization when compared with bone further from the lacuna.[232]

Not all studies agree that mineral density is greatest at the LCS boundary. Nango and coworkers, using synchrotron x-ray CT and also transmission electron microscopy (TEM), found the opposite effect in terms of mineral graduation and distance from canaliculi.[274] These authors studied healthy adult C57Bl/6 mice, as well as mice that were lactating, receiving PTH treatment, or osteopetrotic. In all conditions studied, mineral density was lowest in the hundreds of nanometers alongside the canalicular wall and gradually increased within the first 2 micrometers. Similar mineralization gradients were found around lacunae, including some with higher mineralization local to the lacuna wall. In agreement with these findings, Kaya *et al* reported that bone mineralization assessed by backscattered electron microscopy was decreased near canaliculi for both lactating and control mice.[275] Importantly, the tissue age for lacunae and canaliculi with these different mineralization profiles is not determined. It is possible that high- or low-mineralization adjacent to the LCS is an indicator of tissue maturation (i.e., lower mineralization indicates recent remodeling) but this idea requires investigation.

Comparisons of mineralization between bone adjacent and farther away from the LCS are probably dependent on the choice of technique. For example, while BSEM, synchrotron x-ray CT, and TEM find mineral gradients near the LCS in healthy bone[232,274,275,319,320], Raman

spectroscopy studies often do not find differences in mineralization between perilacunar and non-perilacunar bone except for extreme osteocyte osteolysis phenotypes.[231,232,295,322] Part of this discrepancy might be that most Raman spectroscopy studies have termed the first 5 μm line of bone extending from the lacunar wall the 'perilacunar' region[232,295,322], while high-resolution imaging demonstrates that most of the mineral gradient exists within the first micrometer from the LCS.[274,319,320] Indeed, Gardinier *et al* found no difference in mineral:matrix or carbonate:phosphate between perilacunar and non-perilacunar bone in sedentary controls (not treated with PTH) rats for the same study that found higher mineral in the first 2.5 μm near lacunae using BSEM.[232]

The LCS may also participate in the process of bone tissue mineralization. Finite element modeling of bone primary and secondary mineralization demonstrates that diffusion alone cannot account for the amount of calcium transported from a Haversian canal surface to mineralizing bone tissue.[277] Some experimental data supports the concept of the LCS participating in bone mineralization. In a study of rhodamine-stained femur sections from female adults and children, mineral density measured from quantitative backscattered electron imaging (qBEI) was increased in osteons with greater canalicular network length.[323] However, whether the LCS has passive or active roles in bone mineralization is yet to be determined.

2.2.4 The Impact of Altered LCS Remodeling on Bone Composition

Altered LCS remodeling may affect either bone mineral content, mineral maturity, or both. Not surprisingly, conditions associated with calcium homeostasis and the 'osteocytic osteolysis' lacunar phenotype can produce lower mineralization near the LCS.[231,274,275] When glucocorticoid treatment produces this phenotype, profound hypomineralization halos are

detected in 25 μm-radius regions surrounding lacunae.[231] PTH(1,34) treatment of young adult male C57Bl/6J mice increases lacunar area and decreases bone mineralization in the first 5 μm of perilacunar bone compared with bone farther away.[295]Exercise does not significantly increase lacunar size, but does decrease mineral:matrix from Raman spectroscopy in the first 5 μm of perilacunar bone compared with sedentary mice.[232] Interestingly, while the expansion of lacunae and canaliculi during lactation inherently imply mineral resorption, changes to peri-LCS bone tissue mineralization in lactation are not greater than for non-lactating controls.[274,275] Thus, osteocytic osteolysis is not necessarily associated with detectable differences in bone mineralization near the LCS.

In some cases, altered mineral maturity is observed for the 'osteocytic osteolysis' phenotype. Differences were not detected in Raman spectroscopy mineral:matrix or BSEM mineralization for lactating, 1-week post weaning, and control C57Bl/6 mice, but a decrease in carbonate:phosphate was detected for lactating mice when compared with controls.[275] These measurements were not collected for bone immediately adjacent to the LCS but were instead collected away from periosteal and endocortical forming surfaces, suggested that this change in bone composition were nonetheless the result of altered LCS remodeling. After 21 days of exercise for male C57Bl/6 mice, perilacunar bone (first 5 μm from lacunar wall) had lower mineral:matrix and higher carbonate:phosphate than sedentary controls.[232] PTH(1,34) treatment, meanwhile, decreased carbonate:phosphate in male C57Bl/6 mice.[295] Changes in mineral maturity may have a different meaning for LCS remodeling than changes in mineralization. Decreased carbonate:phosphate indicates lower average mineral maturity, and thus this may indicate that bone replacement is relatively frequent.[279,324] Alternatively, lower

carbonate:phosphate may indicate recent bone resorption, as hydroxyapatite with higher carbonate substitution may dissolve first.[275,324]

To our knowledge, bone tissue composition has not been studied around lacunae or canaliculi in aging or in disease models that produce the 'aging' phenotype of LCS remodeling. However, infilling of osteocyte lacunae with dense mineral is noted to occur in studies of aged human bone.[299] The lack of compositional data corresponding to this phenotype of altered LCS remodeling represents a major gap in knowledge that may yield insights into maintenance of skeletal fracture resistance through the lifespan.

2.2.5 The Impact of LCS Remodeling on Bone Tissue Mechanical Properties

Bone mechanical properties vary surrounding the LCS (**Figure 2.3**). Zhang and colleagues[325] used nanoindentation and atomic force microscopy (AFM) to map moduli for lacunae and canaliculi for 4-month old female Wistar rats. Moduli were lower and more variable for 1-5 μm thick non-concentric regions adjacent to lacunae. The modulus of peri-canalicular bone was also lower adjacent to canaliculi, although the modulus increased with distance down the canaliculi, away from the lacunar wall. For some studies, modulus appears to vary more than bone tissue composition with distance from the LCS. Stern and coworkers[234] studied sham or OVX rats treated with various sequences of osteoporosis drugs or vehicle. Six-linear profiles extending 20 μm (1 μm spacing) were placed for each studied lacuna. For sham rats, the modulus of bone in the first 5 μm away from the lacunar wall was ~13% lower than the modulus of bone 16-20 μm from the lacuna. The decrease in modulus for perilacunar from non-perilacunar bone was less with OVX (~6%) and varied for OVX-treatment groups (3-11%). In a later study, Taylor *et al* studied the same bone samples, but different individual lacunae, and

collected 20-μm linear profiles (1 μm spacing) using Raman spectroscopy.[322] For data pooled across all groups, there were small (≤ |2|%) but significant increases in mineral:matrix and collagen maturity and decreases in crystallinity and carbonate:phosphate for perilacunar compared with non-perilacunar bone. There may be several reasons for the greater changes in modulus, as opposed to tissue composition, for perilacunar versus non-perilacunar bone. Nanoindentation modulus of bone is affected by mineral content and mineral/matrix maturity but also the nanoporosity and organization of the bone tissue composite.[326,327]

The 'osteocytic osteolysis' phenotype is sometimes associated with a larger region of lower bone modulus near the LCS. Lane and coworkers found that glucocorticoid treatment lowered nanoindentation modulus by ~40% in the hypomineralization 'halos'.[231] Kaya *et al* found that modulus from microindentation was 10-13% lower, depending on cortical location, for lactating versus control mice.[275] The authors attributed the variation in modulus to increased microporosity in lactation as opposed to changes in mineralization. Importantly, microindentation creates much larger indents than nanoindentation, and thus averages bone material properties over a larger volume. Differences in perilacunar bone mechanical properties for the 'aging' phenotype are not yet determined.

The mechanical properties of bone tissue near the LCS may impact whole-bone material properties. Stern *et al*[234] found that ultimate stress, work to failure, yield stress, and elastic modulus of the whole bone were modestly but significantly negatively correlated to the elastic modulus of perilacunar bone, but not non-perilacunar bone matrix, for OVX rats receiving sequential osteoporosis treatments. Importantly, it is not known if these treatments affected LCS remodeling activity or osteocyte viability. The heterogeneity of bone near osteocytes could also

impact whole-bone fracture resistance. Tai and colleagues, using nanoscale bone mechanical property maps collected from AFM as inputs to FE models, proposed that bone's nanoscale heterogeneity allows for energy dissipation and could inhibit crack propagation.[328] In support of these ideas, the AFM study from Zhang and coworkers[325] found that the mechanical heterogeneity and also average dissipated energy were both higher in perilacunar and pericanalicular bone compared with bone farther away. However, the influence of LCS remodeling frequency and peri-LCS material properties on whole-bone fracture resistance is not yet determined.

2.2.6 Influence of Altered LCS Remodeling on Strain Experienced by the Osteocyte

Changes to lacunar morphologies may influence the applied mechanical strain to the osteocyte environment. McCreadie *et al* performed a finite element (FE) analysis on two different-shaped lacunae with 12.0 mm×6.8 mm×5.8 mm and 17.4 mm×4.8 mm×3.8 mm dimensions for an applied triaxial strain resembling a physiological load in trabeculae.[329] The lacuna with greater aspect ratio experienced higher maximum principal strains along the lacunae major axis. These strains (up to about 10,000 μstain along the perilacunar bone major axis, but less than 2000 μstain for the osteocyte) would be classified as 'overload' from in vivo movement studies, demonstrating that the osteocyte may experience very different loading than the overall bone tissue environment.[330] In a different study, an FE model of an ellipsoid osteocyte lacuna interconnected with cylindrical channels representing groups of canaliculi was developed to examine how the dimensions of lacunar axes impact surrounding tissue strains.[331] A compressive load representative of walking was applied to a simulated whole femur. When the major lacunar axis increased from 10 μm to 20 μm, a 3.50% increase of the maximum

compressive strain (~10,000 μstrain) was found at sites where these canaliculi meet the lacuna. In this study, the anisotropy ratio and dimensions of canaliculi remained constant between models. Prendergast and coworkers reported that lacunae perpendicular to a tensile load experienced greater strain than those parallel to the load.[332] Taken together, these studies imply that lacunar size and shape may affect mechanical sensitivity because of higher received strains at the osteocyte. Further, applying loads from a novel direction could induce greater bone adaptation because of the higher strains engendered.

The contrast between perilacunar and non-perilacunar bone moduli may also influence strains experienced by the osteocyte, separately from the effects of changing lacunar size. Stern *et al* measured perilacunar and non-perilacunar bone moduli for OVX mice treated with various sequences of osteoporosis treatments or sham controls, and then utilized FEA to assess the impact of perilacunar modulus on lacunar strain.[234] The highest strains were found for sham mice, which also had the highest contrast between perilacunar and bone matrix moduli. In another study, Bonivtch (Stern) and coworkers[316] used an FE model with variations in canalicular diameter, perilacunar modulus, and size of the perilacunar zone. They found that a lower perilacunar tissue modulus and increased canalicular diameter both increased strain at the canalicular-lacunar insertion. For a decrease in perilacunar modulus of 15% and 40% (taken as examples from the study's modulus-strain curves), the tissue strain increased by ~5% and ~15%, respectively. These relationships were independent of the size of the perilacunar zone and minimally influenced by the canalicular diameter. Changes in perilacunar tissue strains may affect how osteocytes sense their external environment and regulate the activities of osteoblasts and osteoclasts.[249,251,333] Taken together, these FE models suggest that lacunar size, shape, and

orientation have modest influence on the strain experienced by osteocytes and that perilacunar modulus may have a greater impact. Changes to osteocyte strain would be expected to affect osteocyte mechanosensitivity and the coordination of osteoblasts and osteoclasts.[334]

Table 2.1. LCS properties with different physiological and disease conditions

Physiological condition	**Experimental model and skeletal sites**	**Changes to osteocyte viability**	**Changes to LCS morphology**	**Peri-LCS tissue composition & mineralization**	**Peri-LCS mechanical properties**
Mineral homeostasis					
Lactation	C57Bl/6 mice *14-20 week females*[275]*, midshaft femur.* *3-5 month females*[285]*, fibula.*		*Lactation vs control or 1 week post weaning* ↑ lacunar area[275] *Lactation vs virgin control* ↑ lacunar volume[285]	*Lactation vs control or 1 week post weaning* ↓ carbonate:phosphate ratio[275] No changes in mineral:matrix ratio[275]	*Lactation vs control* ↓ elastic modulus for bone tissue with greater canalicular density[275]
	CD1 mice[9] *12 weeks before pregancy and weaning, multiple skeletal sites.*		*Lactation vs control or 1 week post weaning* ↑ lacunar area for cortical and trabecular tibiae, cortical lumbar vertebrae, but not calvaria		
	NMRI mice[291] *10-19 week females, cortical tibia.*		*Lactation vs control or 28 days post weaning* No changes in lacunar area		
PTH	Wistar rats[261] *8 months of age (sex not stated)*		*PTH(1,34)-treated continuously vs vehicle:* ↑ lacunar area		

	4 week PTH treatment. Cortical tibia.				
	C57Bl/6J mice[295] *16 week males* *3 week treatment, cortical tibia*		*Intermittent PTH(1,34) treatment vs saline vehicle:* ↑ lacunar area	*Perilacunar vs. non-lacunar region PTH(1,34)-treated groups:* ↓ mineral:matrix ratio	
X-linked hypophosphatemia	C57BL/6J mice[296] *75 day females and males, cortical tibia*		*Hyp vs WT:* ↑ lacunar volume, surface area, lacunar number density ↓ canalicular number density and branching		
Chronic kidney disease (CKD)	Human iliac crest[297] *Men and women, mean age 56*		*High turnover vs low turnover CKD:* No changes in lacunar area. ↑ Lacunar number density, lacunar perimeter, lacunar porosity.		
Bisphosphonate and glucocorticoid treatments					
Bisphosphonate-related osteonecrosis (BRONJ)	Human jawbone[319] *BRONJ or healthy controls; females and male adults.*			*BRONJ vs controls:* ↓ mineral gradient from LCS wall to adjacent bone tissue.	

Glucocorticoid treatment (GC)	Swiss-Webster mice[231] *6 month males* *21 days of prednisolone treatment or placebo.* *Lumbar vertebra.*	*GC treatment vs placebo:* ↑ osteocyte apoptosis	*GC treatment vs placebo:* ↑ lacunar area	*GC treatment, perilacunar vs non-perilacunar bone:* ↓ mineral:matrix ratio	*GC treatment, perilacunar vs non-perilacunar bone:* ↓ elastic modulus
Sex hormones and osteoporosis					
Ovariectomy (OVX)	Swiss-Webster mice[231] *6 month females, 21 days post OVX or Sham surgeries. Lumbar vertebra.*	*OVX vs Sham:* No difference in osteocyte apoptosis	*OVX vs Sham:* ↑ lacunar area	*OVX vs Sham treatment, perilacunar vs non-perilacunar bone* No changes in mineral:matrix ratio	*OVX vs Sham treatment, perilacunar vs non-perilacunar bone* No changes in elastic modulus
	Sprague-Dawley rats[233] *20 week females* *6 weeks post-OVX or Sham surgeries.* *Proximal tibia.*		*OVX vs Sham:* ↑lacunar-canalicular porosity and canalicular volume at metaphysis. No changes in lacunar volume or lacunar number density.		
	Sprague-Dawley rats *6 month females* *8 week post-OVX* *270 days of different sequences of*		*OVX & OVX-treatment groups vs Sham:*	*Perilacunar vs non-lacunar regions for pooled samples across groups:*	*Perilacunar vs. non-lacunar regions for*

	osteoporosis treatments[234,322]*Cortical tibia.*		No difference in lacunar size or lacunar number density[234]	↓ carbonate:phosphate ratio ↑ mineral:matrix ratio ↑ collagen maturity ↓ crystallinity[322]	*pooled samples:* ↓ elastic modulus[234] *OVX & OVX-treatment groups vs sham:* ↓ elastic modulus contrast for perilacunar vs non-perilacunar region[234]
Unloading					
Sciatic neurectomy	Sprague Dawley rats[265] *30 week females; sciatic neurectomy at 3 weeks. Cortical tibia.*		*Sciatic neurectomy vs control:* ↓ lacunar volume ↓ lacunar number density		
Hindlimb unloading	Sprague Dawley rats[266] *28 week males* *HLU via tail suspension for 28 days. Distal femur.*	*HLU vs control:* ↑ osteocyte apoptosis ↓ occupied lacunae	*HLU vs control:* ↓ lacunar number density		
Spaceflight	C57Bl/6N mice[264] *23 week males* *1 month of flight, cortical femur.*	*Flight vs control:* ↑ fraction of empty lacunae	*Flight vs control:* ↓ lacunar volume:total volume (medial zone only) ↓ lacunar volume (posterior zone only) ↑ sphericity of lacunae (posterior zone only)		

	C57Bl/6 mice[308] *16 week females* *15 days of flight, ischia*	*Flight vs control:* No changes in empty lacunae	*Flight vs control:* ↑ lacunar area and perimeter ↓ sphericity of lacunae ↑ canalicular diameter No changes in lacunar number density		
Botox	Wistar rats[307] *14 week females, 28 week period post-injection, cortical femur.*		*Botox vs contralateral or external control:* No changes in lacunar size or number density over 28 weeks post-injection		
Exercise					
Aerobic exercise	C57Bl/6 mice[232] *16 week males* *30 min of running for 21 days, cortical tibia.*		No changes in lacunar area	*Perilacunar vs. non-lacunar region in exercise group:* ↑ carbonate:phosphate ratio ↓ mineral:matrix ratio	
	Zebrafish[311] *4.5 month old* *4 weeks of exercise in a swim tunnel. Vertebrae.*		No changes in lacunar volume and sphericity		
Aging					
Mouse models	C57Bl/6 mice[286] *5, 22-23 month females and males. Cortical femur.*	*With increase in age:* ↓ osteocyte cell volume ↓ fraction of empty lacunae in females	*With increase in age:* ↓ lacunar volume in distal but not midshaft femur, *in males* ↓ lacunar number density ↓ canalicular and dendrite number		
	C57Bl/6 mice[262,298]		*With increase in age:* ↓ lacunar area and volume		

	6, 18, 24 month males. Cortical tibia.		↓ lacunar number density ↑ sphericity of lacunae		
	C57BL/6JRccHsd mice[284] *5, 23 month females. Fibula.*		*With increase in age:* ↓ lacunar volume ↑ sphericity of lacunae		
Human models	Human cortical femur[299] *10-90 year old females and males.*		*With increase in age:* ↓ lacunar number density	*With increase in age:* ↑ number of highly mineralized lacunae	
	Human cortical femur[300] *16-73 years. Females and males. Cortical femur.*		*With increase in age:* ↓ lacunar number density		
	Human iliac crest bone[301] *Females and males, mean age 57 years*	*For >55 years years vs <55 years* ↓ Osteocyte number density No changes in fraction of empty lacunae	*For >55 years vs <55 years* ↓ lacunar number density No change in lacunar area		
	Human iliac crest bone[302] *19-97 year old females and males*		*With increase in age:* No changes in lacunar volume ↓ lacunar number density		
	Human femur cortical bone[303] *20-86 year females*		*With increase in age:* ↓ lacunar volume ↓ sphericity of lacunae		

2.3 Choosing Tools to Study LCS Bone Quality

The focus of this section is on techniques with microscale or sub-microscale resolution appropriate for resolve changes to bone tissue local to the LCS (**Table 2.2**). Tools that require synchrotron radiation, which delivers high-resolution imaging of bone structure and mineralization [274,307,319,335] but is limited to very few researchers, are reviewed briefly here and thoroughly elsewhere.[336–339]

2.3.1 Chemistry and Composition

In Raman spectroscopy, molecules within the specimen are excited by the incident monochromatic laser light. While the majority of photons elastically scatter from the sample and return to the detector with no change in energy, a small fraction of the light (~1 in 10^7 photons) inelastically scatters off of the sample and either gains or loses energy.[340] The wavelength differences between the scattered and incident light correspond with specific molecular vibrations, leading to characteristic frequency shifts in the Raman spectrum.[341] Raman spectroscopy is appropriate for the surface analysis of bulk samples and thus does not require preparing transparent sections.

Raman spectroscopy produces a bone 'signature' that can be studied for characteristics of bone mineral, collagen, and noncollagenous proteins. The bone mineral phase is primarily monitored through phosphate vibrations, including symmetric stretching of the phosphate to oxygen (P-O) bonds (ν_1 PO_4), doubly degenerate O-P-O bending (ν_2 PO_4), asymmetric P-O stretching (ν_3 PO_4), and triply degenerate O-P-O bending (ν_1 PO_4). Meanwhile, carbonate is present within the hydroxyapatite lattice as substitutions, including A type (carbonate substitution

in hydroxide site) and B type (carbonate substitution in phosphate sites). [324,341–343] The carbonate measured at ~1070 cm^{-1} by Raman spectroscopy is B-type.[324] Collagen is monitored through amide I, amide II and amide III bands, as well as proline, hydroxyproline, and phenylalanine. The CH_2 band is associated with collagen side chains but also noncollagenous proteins. [341–343]

Raman measurements are usually provided in peak ratios, due to the sensitivity of the technique to surface roughness and height. Mineral to matrix ratio is assessed from ratios of the phosphate and collagen bands. While the ν_1PO_4 and amide I bands have the greatest signal intensity, these bands have a major polarization mismatch and thus their relative intensities depend on sample orientation.[344] Several other ratios, including ν_1PO_4:proline and ν_2 PO_4:amide III have minimal polarization sensitivity and are often better choices.[344,345] The degree of carbonate substitution is usually measured as carbonate to ν_1PO_4 ratio.[341] Crystallinity, shown to correlate with the mineral c-axis length from XRD, is measured as the inverse of the full-width at half maximum intensity of the ν_1PO_4 band.[346] Each of these ratios can be measured from intensities or areas, for hydrated and dehydrated specimens. It is typical to subtract the contributions of embedding media (e.g., PMMA) from Raman spectra, and various protocols exist to subtract background fluorescence.[341–343]

Raman spectroscopy achieves microscale lateral and depth resolution. The depth resolution is a function of sample refractive index, incident wavelength, and microscope numerical aperture. A relationship between depth resolution and these parameters was estimated by Juang et al[347] as in Equation 1:

$$\Delta z = \pm \frac{4.4\lambda n}{2\pi(NA)^2} \qquad \text{Equation 1}$$

Where Δz is the depth of focus that measures the tolerance of placement of the image plane in relation to the lens, NA is the numerical aperture of the objective lens, n is the refractive index of the immersion medium, and λ is the wavelength of the light. For a NA of 0.75, a wavelength of 785 nm, and an estimated refractive index of bone tissue set to 1.56, the estimated depth for bone would be around 1.5 μm.[348,349] The lateral resolution for Raman microscopy is given by Equation 2:[344]

$$\Delta x = \frac{0.61\lambda(laser)}{NA} \qquad \text{Equation 2}$$

where Δx is the radius of lateral resolution. For a NA of 0.75 and a wavelength of 785 nm, the estimated lateral resolution for bone would be ~0.6 μm. Both lateral and depth estimates represent 'best case resolutions' which are, in reality, greater because of sample roughness.

Raman spectroscopy has appropriate resolution to detect tissue maturation in the days to weeks after osteoid deposition in cortical rat bone.[278] Thus, it is compelling to consider how Raman spectroscopy can also yield information about the tissue maturity local to the LCS. However, several challenges limit this approach. First, tissue remodeling may be limited to the first micrometer from a lacuna, which competes with the resolution limit of this technique.[341,342] Next, while mineral:matrix ratio would be expected to change with tissue maturation, simultaneous changes to both the mineral and collagen phases local to the LCS can reduce the 'signal' of this biological effect (i.e., ratio stays close to constant despite changing numerator and denominator).

In Fourier transform infrared spectroscopy measurement of bone, transmitted light excites the bond vibrations of bone tissue. The characteristic wavelength of these excited vibrations corresponds to the IR absorption peaks. It is required to study thin (2–5 μm)

transparent sections. Common outcomes include mineral to matrix ratio, carbonate to phosphate ratio, crystallinity (mineral size and perfection), and collagen crosslinking maturity. However, the lateral resolution of FTIR is 6-10 μm, which competes with the spatial dimensions of lacunae themselves.[343,350–352] For this reason, FTIR may be appropriate for surveying compositional properties of bone matrix as influenced by changes in LCS networks but is less appropriate for ascertaining gradients in bone composition local to individual features of these networks.

In scanning electron microscopy, incident electrons interact with the bone sample surface to acquire either morphological or compositional images. Several types of imaging are available, probing different interactions between the incident electrons and the sample surface and delivering height and/or compositional data at a range of spatial resolutions spanning many orders of magnitude.

Secondary electrons (SE) are generated when the incident electron beam interacts with and ejects weakly bound valence or conduction-band electrons in the sample due to inelastic scattering.[353] SE electrons have low kinetic energy, which is reduced further through energy loss while traveling through the material. Thus, secondary electrons that reach the detector are generated from the top few nanometers from the surface of the bone tissue. SE imaging yields topographic contrast to reveal morphologic features that can be used for measuring two-dimensional, nanoscale geometric information about the LCS, but not about bone mineral or matrix density. The finely focused beam produces excellent depth of field which provides for 3D representation of the imaged object. Secondary mode SEM can be complemented with acid etching to reveal canalicular attachments to osteocytes.[234,235,259]

Backscattered scanning electron microscopy (BSEM) provides compositional contrast, where mean atomic number elements are more efficient at generating backscattered electrons and thus appear brighter.[353] The backscatter coefficient, η, is the proportion of the incident electrons that return to the sample detector. The backscatter coefficient increases nonlinearly with increasing atomic number, Z, as described by Arnal *et al*[354,355] (Equation 3):

$$\eta = 2^{\frac{-9}{\sqrt{Z}}} \qquad \text{Equation 3}$$

When measurement conditions are the same, a linear relationship is expected between grey level and backscattered coefficient[356], thus measured grey level from BSEM can be related to the effective Z for the bone tissue composite.

BSEM, when used qualitatively, provides definition between bone matrix and void spaces. Quantitative BSEM, usually referred to as either quantitative backscattered electron imaging (qBEI) or quantitative backscattered scanning electron microscopy (qBSE), delivers bone compositional data and is performed with the use of calibration materials. Reference standards of carbon and aluminum bracket the typical Z range of bone (9-13)[357] and are typically used to calibrate the sample grey levels.[282,323,358] Other reference standards, such as custom-made lithium borosilicate glasses, are less frequently used but can closely bracket the expected elemental density range of bone.[356,359]

qBEI and qBSE employ somewhat different approaches for measuring bone composition. In qBEI, the grey level of the sample as well as calibration standards are measured. Through setting the carbon and aluminum standards at specific grey levels (i.e., 25 and 225, respectively, for 8-bit images) the grey level of calibrated sample images can be related to weight percent calcium, where each grey level step represents an increase of 0.17% calcium.[323,358] A histogram

of calcium weight percentages is generated from non-black pixels (which after calibration represent plastic or voids). The weighted average of this histogram is Ca_{Mean}. Ca_{Peak} is measured at the peak position of the histogram, the most frequently occurring value. Ca_{Width} is the full width at half maximum height of the histogram and represents heterogeneity of mineral content.[276,282,323,345,358,360,361] This method assumes that variation in grey level intensity is solely due to variation in calcium content and not other elements. The calcium weight percent measured from qBEI was found to have a strong correlation with v_2PO_4:amide III from Raman spectroscopy in human osteons.[345] Good correspondence is also seen with calcium weight percent measured from SEM-EDS.[358] Meanwhile, in qBSE, the calibrated grey levels are related to a mineral volume fraction.[327,356,359,362,363] This mineral volume fraction is based on treating bone like a two-phase composite with organic and mineral phases of with given densities.[356]

Several considerations are important when using qBEI/qBSE for measurement of LCS bone tissue mineralization and quality. These techniques are able to monitor weight percentage of calcium, and thus provide an indication of tissue mineralization, but cannot measure collagen quantity or quality. qBEI/qBSE are also sensitive to a number of features that can affect the proportion of backscattered electrons arriving at the detector, including sample roughness, probe current and gain, and working distance, and thus care is required to assure low variance within and between imaging sessions. BSEM generally involves accelerating voltages of at least 10 kV (15-30 kV are common). As accelerating voltage decreases, charging effects increase as electrons concentrate near the sample surface. At very low accelerating voltages (< 2 kV), the relationship between atomic number and backscattered coefficient breaks down and the influence of the coatings and surface contamination on the backscattered coefficient can be problematic.[364,365]

BSEM generally requires that nonconductive samples, such as bone, have a conductive coating (usually carbon). The resolution of BSEM depends on accelerating voltage. From Monte Carlo simulations, the most common interaction depth and radius of collectable BSEs for bone are ~0.5 and 1 μm at 15 kV and ~1 and 1.5 μm at 20 kV.[366] Thus, BSEM techniques, while having several advantages, do not have the required resolution for all questions involving bone composition local to the LCS.

Electron dispersive spectroscopy is a technique that can generate spot (~1 micron) elemental analyses or 2D elemental maps of sample surfaces by detecting characteristic secondary X-rays produced in the particle-beam interaction. When an incident electron interacts with an atom, a core electron is ejected and an outer electron fills the vacancy, releasing an x-ray with a wavelength that is proportional to the energy difference between the orbitals for that element. These x-rays occur at specific energy levels for each element; as a large number of atoms interact with the beam within the excitation volume, a spectrum of characteristic peaks is generated that that can serve to identify the elemental composition of the material.[353,367] The elemental resolution depends on the detector. Beryllium windows, which are now antiquated, cannot detect elements below sodium. Ultrathin polymer windows can detect lighter elements (including C, N, and O). However, detection efficiency is still low, as it is more difficult to ionize atoms for light elements. Modern silicon drift detectors, which do not require a window, offer improved detection of light elements.[368] SEM-EDS can deliver qualitative elemental maps or semi-quantitative measurement for spot analyses. Reliable semi-quantitative measurement requires studying flat samples with low surface roughness (i.e., well-polished), and are improved through studying elemental reference standards with the same beam conditions.[367]

SEM-EDS has sometimes been used in bone research to study Ca/P ratios, where higher ratios may be associated with more mature bone.[235,369] SEM-EDS could be employed for elemental mapping of the LCS, but several considerations are important. First, while hydroxyapatite mineral would be readily mapped through monitoring calcium or phosphorus peaks, the ability to monitor the organic phase of bone depends on the instrument's detector and window. For systems capable of reliably monitoring light elements, nitrogen may be a better choice to monitor collagen than carbon. This is because carbon is present in hydroxyapatite, embedding materials, and surface contaminants. Second, because bone is insulating, a conductive coating is required. Third, SEM-EDS detectors are usually mounted at an angle. In the authors' experience, it is possible to observe 'shadowing' where the surface of a lacuna closer to the detector appears richer in the element of interest than the far surface. Rotating the sample and scanning the same area again can confirm whether or not this effect is happening. The lateral and depth resolution of SEM-EDS depends on accelerating voltage and material analyzed. From a Monte Carlo simulation performed by the authors of this Review using NIST DTSA II at 15 kV, x-ray emissions for calcium are generated within a volume with radius and depth dimension of ~2.5 μm each. For nitrogen, this volume has lateral radius of about ~2 μm and a depth of ~1 μm.[370] Thus, while SEM-EDS may be able to monitor density of both mineral and collagen matrix, it still may not be sensitive to bone compositional changes, especially for mineral, immediately adjacent to the LCS.

Auger electron spectroscopy (AES) is a technique commonly used in analytical surface characterization, but not yet commonly applied to mineralized tissues. When incident electrons interact with atoms, a core electron is ejected, and an outer electron fills the vacancy. The excess

energy of this transition can be emitted as an x-ray (see SEM-EDS) or can be transferred to an outer electron, which is then emitted from the atom (i.e., Auger emission). While the sum electron yield of these two processes is unity, they do not have the same probability. Auger emission dominates for light elements, while the emission of x-rays increases with atomic number. While atomic ionization can happen beyond a micrometer of depth, Auger electrons have relatively low energy and thus their mean free paths are small. Thus, AES is limited to the first few nanometers of depth from the surface.[371]

AES is able to characterize elements characteristic of either bone mineral or matrix. The kinetic energy of the Auger emission is characteristic of the emitting atom. Because AES is a three-electron process, it is not able to identify H or He, but can identify all heavier elements. The AES detector is generally mounted coaxial to the electron beam, eliminating the shadowing effects that can interfere with SEM-EDS of the LCS (note: such detector geometries are available but uncommon for EDS detectors). As with other SEM techniques, AES can be used to inventory elements present on a material surface in survey mode, it is possible for rastering scans to produce compositional maps of surfaces on a sub-micron scale, and ion beam sputtering procedures can be used to obtain compositional depth profiles into a material. Because Auger peaks are relatively small compared to background energy, it is common to analyze the first derivative of the spectra in order to identify elemental peaks, and published sensitivity factors can be used to determine sample surface composition.[371,372]

Several considerations need to be maintained for AES analysis of bone. First, because ultrahigh vacuum (10^{-9} torr) is required, PMMA or other off-gassing resins should be avoided, even if the resins are acceptable in conventional SEM techniques. Next, the sample should be

thoroughly dehydrated. Third, insulating materials are challenging when using AES. Conductive coatings are not permissible because of the low interaction depth of the technique (i.e., the signal would only represent the coating). A number of strategies exist for studying insulating samples. These include tilting the sample, lowering the beam energy or current, neutralizing the surface with noble gas ions, or mounting thin sections on a conductive sample holder.[371] Another strategy is to coat the sample surface with a metal coating and either mask an area of interest or sputter off the coating with argon, or another inert gas, for a specific a region of interest. This same technique can be used to mill the surface for depth-profiling, but care should be taken to not preferentially etch atoms or introduce sample roughness.[371–373]

AES is only sparingly reported for bone[369,374,375]. A few studies employed AES to study calcium:phosphate ratio in bone pieces[374] or ground bone pellets[369,374], or mineralization and oxide formation of bone implant surfaces.[372,375] AES was able to distinguish osteoporotic bone from healthy bone as SEM-EDS at several skeletal sites for adult New Zealand White rabbits.[369] AES has also delivered elemental composition, including mineral and collagen components, for dental tissues.[373,376] To the best of our knowledge, AES has not been reported for studies of bone tissue surrounding the LCS. Although care needs to be taken to prepare appropriately smooth and dehydrated surfaces, AES does not require thin sections and, when performed properly, is not destructive. Thus, it is possible to pair AES and other techniques, such as atomic force microscopy, to generate complementary nanoscale maps of bone material properties near the LCS.

Transmission electron microscopy (TEM) allows nanoscale resolution of bone morphology and mineralization. However, the technique requires bone tissue fixation, followed

by the preparation of ultrathin sections.[377] TEM is useful for the study of mineralization of bone matrix around lacunae and canaliculi.[274] Bright field imaging yields images of mineral as well as collagen, while dark field imaging delivers images that are dark except for where apatite scatters electrons from the 002 plane.[378] Thus, TEM can deliver crystal morphology and arrangement of crystals on collagen fibers.[377–380] TEM can also be used to identify crystal phase and thickness through diffraction-based techniques.[380,381] It is also possible to decalcify ultrathin sections to allow comparisons of mineralized and demineralized surfaces, which is useful for studying collagen characteristics.[377] However, TEM has a number of limitations. In addition to being particularly labor intensive to prepare, ultrathin sections are not suitable for nanomechanical assessment on the same regions due to both substrate and fixation effects.

The use of high-resolution microcomputed tomography (μCT) to monitor bone, including LCS network architecture, is the subject of several recent reviews[337,382,383] and is therefore discussed only briefly here. μCT allows for non-destructive three-dimensional analysis of internal bone tissue structure and mineralization.[382] Standard μCT does not achieve adequate resolution to visualize the LCS. Higher resolution μCT is now available as laboratory systems. These systems (e.g. Zeiss Xradia, Scanco 50, Bruker SkyScan 2214) can achieve submicroscale voxel resolution and have been used to image lacunae[288,384,385] and sometimes canaliculi.[386] Synchrotron-based CT systems (SRμCT) achieve higher resolution (50 nm to 150 nm[319,387,388]), which allows visualization of canaliculi[389] as well as measurement of microcracks.[390–392] When SRμCT is used in conjunction with XRD, mineral orientation can be estimated.[393] When used with SAXS, mineral shape, orientation, and quantity are accessible.[320,394–396] Ptychographic x-ray μCT is another technique relevant to LCS measurements.[397–399] Multiple high-resolution

interference patterns are produced by scanning the specimen at several offset locations. These interference patterns are overlapped and then processed to reconstruct the 3D refractive index distribution of the specimen. This allows for quantitative volumetric mapping of both real (phase change) and imaginary (absorption) components of the reflective index. Using this approach, ptychographic x-ray tomography can achieve resolution (16-44 nm[400,401]) and contrast great enough to estimate nanoscale bone density variations of ~0.2%.[402]

2.3.2 Mechanical Properties of Bone Tissue

Nanoindentation is a technique for microscale assessment of mechanical properties. This instrumented indentation technique utilizes a diamond tip that presses into the sample surface as displacement is recorded.[403] Tip actuators are either electrostatic or electromagnetic and allow either driving either a load-control or displacement-control indentation. Most nanoindentation tips are machined from diamond. Pyramidal (i.e., Berkovich) and conicospherical geometries are most common. While a sharp, unworn Berkovich tip has an apical radius of ~125 nm, most indentations in bone are placed to depths of 300 nm – 1 micrometer and thus engage contact radii of 1-2 micrometers. Indentation plastic zones are assumed to extend to 1.5 times the contact radius for bone, and thus consecutive indents are usually spaced a minimum of 3 times the contact radius.[404,405] The lower limit of lateral and depth resolution is also influenced by the indenter noise floor and the sample surface roughness.[406]

In nanoindentation, typical measurements include modulus and hardness. Assuming elastic-plastic contact (a reasonable assumption for PMMA-embedded bone), the unloading curve is assumed to represent primarily elastic behavior. Thus, the stiffness is measured from a tangent line taken near the beginning of unloading. Stiffness is converted to modulus through

measuring the tip contact area. Unlike traditional hardness testing, where residual tip areas are measured optically, nanoindentation tip areas are too small to efficiently measure directly. Instead, the tip is calibrated with respect to contact depth on reference standards (e.g., fused quartz), and contact depth is measured as a function of maximum depth.[403,407] Nanoindentation hardness is measured from the peak load divided by the contact area. Because elasticity is not neglected, nanoindentation hardness differs from conventional hardness testing for materials that are not perfectly plastic.[408] Measurement of time-dependent material properties through either performing creep or stress-relaxation tests or using dynamic nanoindentation are also well-developed for bone.[326,403,409,410] Most nanoindentation systems are capable of time-efficient two-dimensional mapping. Correlative work has also been used, where site-matched nanoindentation and either Raman spectroscopy or qBSE/qBEI allow correlation of composition and mechanical properties.[278,281,298,359,404]

Atomic force microscopy (AFM) is a technique that utilizes a tip with specified geometry attached to the end of a cantilever of known stiffness to provide nanoscale-resolution maps of material morphology and modulus. Features as small as canaliculi can be accurately mapped.[325] A stiff tip (e.g., silicon nitride) is attached to a cantilever, which can interact with the sample in various contact (i.e., dragging) or tapping type modes in raster scans of the material. The deflection of the cantilever during contact with the sample is monitored through the reflection of the laser off of the cantilever and onto a photodiode. AFM can be used to calculate sample modulus. Indentations can be applied to the material to generate force-distance curve. The force is calculated assuming that the cantilever behaves as a Hookean spring (Force = k*deflection), where k is the cantilever spring constant. From each curve, the modulus is calculated from the

Hertzian contact model or variations upon it (e.g., adjusting for adhesion with models such as the Derjaguin-Muller-Toporov).[411] The position of the tip when it engages with the sample surface is also calculated and stored. This allows for sample topography to be determined simultaneously with modulus. Material properties can also be calculated through contact resonance AFM, where the tip is oscillated through a range of frequencies in contact with the sample. The contact and free (i.e., not touching the sample) resonant frequencies are used to calculate sample material properties, including modulus.[405]

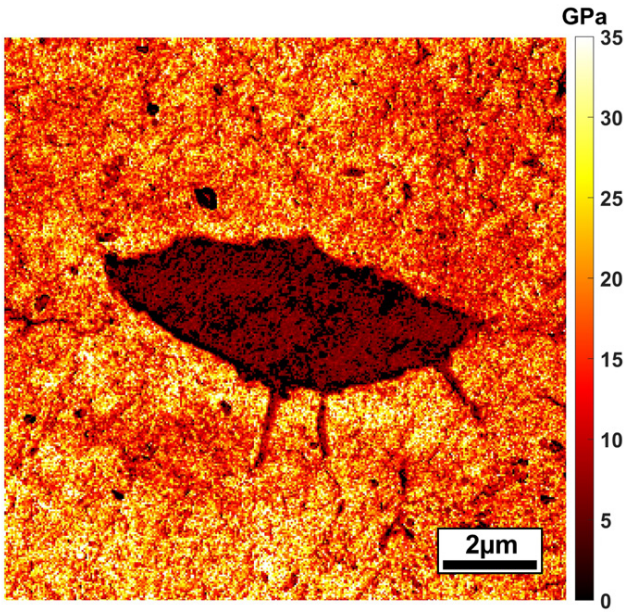

Figure 2.3. Bone tissue modulus varies at the submicroscale surrounding an osteocyte lacuna. This modulus map was generated for PMMA-embedded and polished murine bone using atomic force microscopy.

Several considerations should be maintained for reliable AFM stiffness mapping. Relatively high stiffness tips need to be used to obtain reliable data on stiff materials, such as bone.[405] These tips are typically more expensive and more difficult to tune due to their relatively high fundamental frequency. They also tend to wear quickly, which necessitates frequently

calibrating the tip to ensure accurate measurement data. Despite these challenges, AFM is a promising way to study bone topology and material properties on the nanometer length scale and can be employed to study a variety of questions surrounding the osteocyte (**Figure 2.3**).

Table 2.2. Tools for assessing peri-LCS bone quality

Technique	**Resolution**	**Advantages**	**Limitations**	**References** *use of technique for LCS analysis # General reference papers
Vibrational spectroscopy				
Raman spectroscopy	Lateral: 0.6 -1 µm Depth: 1.5 µm	• Sensitive to bone mineral density as well as mineral and matrix maturity. • Hydrated, dehydrated, and embedded samples can all be studied. • Not limited to transparent samples.	• Changing mineral:matrix ratio may result from either altered mineral, matrix, or bone. • Large maps are time intensive.	231,232,275,295, 322*, 341–343#
Fourier-transform infrared spectroscopy (FTIR)	Lateral: 6-10 µm. Depth: 2-5 µm (thickness of transparent thin sections).	• Sensitive to bone mineral density as well as mineral and matrix maturity. • High signal:noise ratio.	• Transparent sections required. • Resolution is low compared with LCS dimensions. • Significant interference from water; embedded samples required.	343,351,412#
Electron microscopy				
Secondary mode SEM	Lateral and depth: As low as ~10 nm for field-emission SEM	• Possible to image lacunar and canalicular geometries. Acid-etching aids the visualization of canaliculi. • Low accelerating voltages can be used.	• High vacuum generally required for high magnifications. • Metal surface coating typically required for bone.	235,259,413,414*, 353#

Backscattered SEM (BSEM) and quantitative backscattered electron imaging (qBEI)	Lateral: ~0.4 µm at 15kV Depth: ~ 0.9 µm at 15 kV	• Displays compositional contrast. • Rapid mapping possible. • High contrast between bone tissue and LCS features. • Can deliver %Ca or mineral volume fraction when reference standards are used appropriately.	• Not sensitive to bone matrix. • Samples need carbon coating. • Low accelerating voltages not possible for quantitative work; limits resolution.	BSEM: [259,267,271,273,275,291,414]* qBEI: [232,235,236,415]*
SEM-electron dispersive spectroscopy (SEM-EDX)	Lateral: 0.5-2.5 µm Depth: 0.5-1 µm	• Detects mineral content (Ca and P maps). • Samples can also be imaged with other SE or BSE.	• Older detectors cannot detect matrix elements. • Shadowing effect from detector angle.	[232,369]* [368,416]#
Transmission electron microscopy (TEM)	Lateral: < 1 nm Depth: 50-100 nm	• Can measure lacunar and canalicular ultrastructure • Can measure mineral size, shape, and phase. • Demineralized samples can be assessed for collagen orientation.	• Sample fixation necessary. • Ultrathin samples required.	[274,414,417]* [377–380]#
High resolution 3D imaging				
High-resolution computed tomography (µCT) (commercially-available lab systems)	Pixel: 0.6-2 µm	• Non-destructive 3D imaging. • Can measure lacunae and sometimes canaliculi.	• Beam hardening artifacts. • Insufficient spatial resolution for some structural questions.	[288,418–420]* [383]#
Synchrotron-radiation (SR-µCT)	Pixel: 50 nm- 150 nm	In addition to µCT advantages: • Resolution allows detection of canaliculi and microcracks. • No beam hardening artifact.	• Limited access. • Complex additional instruments. • High radiation rate.	[274,307,319,335,389,421–432]*

		• When combined with SAXS/XRD can measure crystal orientation, size, and distribution.		337,382,383#
Ptychographic x-ray μCT	Pixel: 16-44 nm	• Higher resolution than SR-μCT. • The resolution does not depend on the lens (only wavelength limited).	• Similar limitations as SR-μCT.	402,433–435∗ 337,399,402,435–437#
Tissue-scale indentation				
Atomic force microscopy (AFM)	Lateral: ~20 nm Depth: ~20 nm	• Hydrated, dehydrated, and embedded samples can all be imaged. • Sufficient resolution to determine modulus for nanoscale LCS structural features. • LCS geometries can also be measured.	• Difficult to image high modulus materials. • Requires fine surface polish. • Depth of topographic features accuracy dependent on adjacent surface features and sample roughness. • Time intensive. • Tips are fragile and wear quickly. • Requires frequent tip calibration.	325,438∗ 404,405,411#
Nanoindentation	Lateral: > 1 μm Depth: > 100s of nm – 1 μm	• Capable of mapping relatively large regions (100+ μm). • Diamond tips less prone to wear. • Designed for stiff substrates.	• Resolution is not well matched for gradation around canaliculi. • Requires fine surface polish. • Time intensive • Requires tip area calibration.	231,233,234,325∗ 326,403#

2.4 Key Questions and Future Directions

Substantial evidence supports that osteocytes can resorb and replace tissue local to the lacunar-canalicular system (LCS) but we do not yet fully understand the reasons for, or repercussions of, LCS remodeling (Error! Reference source not found.). It is not contentious that the LCS participates in calcium homeostasis, but participation in phosphate homeostasis is less

certain. Evidence also points towards the LCS having a role in bone tissue mineralization during health, and this begets additional questions about the role of the LCS at different stages of bone tissue maturation.

There is not a simple relationship between LCS remodeling and bone health, as there are at least two separate phenotype that occur throughout physiological and disease models. The 'aging' phenotype, in which osteocytes are less viable and LCS network architecture is contracted, and the 'osteocytic osteolysis' phenotype, in which LCS networks are enlarged. While the 'aging' phenotype appears to be maladaptive (i.e., more clearly associated with osteocyte dysfunction), 'osteocytic osteolysis' is probably adaptive on some occasions and maladaptive on others. In lactation, for example, liberation of mineral is adaptive, but in glucocorticoid therapy, larger lacunae and hypomineralization are not obviously helpful to the organism.

The essential question is whether and how LCS remodeling affects bone fracture resistance. A major current limitation is the lack of understanding of how tissue toughening mechanisms are affected by LCS remodeling. It is not sufficiently understood whether tissue composition and mechanical properties vary between remodeling and non-remodeling lacunae and canaliculi in health and in disease, as well as which of these changes are significant for bone mechanics. Work is needed across the lifespan and across disease models to understand the impacts of LCS remodeling on whole bone fracture resistance.

Moving forward, it is essential to employ the right tools to investigate the impacts of LCS remodeling on bone quality. One challenge is that many bone characterization techniques involve microscale-or-greater resolution, while bone composition often varies at the nano-submicroscale

near lacunae and canaliculi. It is important to not fall victim to 'false negatives' because of low resolution measurements. As an analogue, for several years, it was unclear if osteocyte lacunar morphologies change in aging. Multiple groups now show that lacunae indeed become smaller and more spherical with aging, but witnessing these changes required 3D visualization (as opposed to 2D). We expect that high-resolution mapping of bone composition and mechanical properties near osteocytes will yield insights that are not apparent with lower-resolution techniques. These careful efforts are needed for unraveling the possible roles of the osteocyte in bone quality maintenance and for identifying whether this most-abundant bone cell could be a compelling new target for preventing bone fracture.

Table 2.3. Key questions about LCS remodeling and future directions for research.

Key questions	Future directions
Does LCS participate in bone mineralization?	• How does the LCS affect primary and secondary mineralization? • Do mineral gradients near the LCS reflect tissue maturation? • How is mineralization around the LCS affected by aging and disease?
How does altered LCS remodeling affect bone quality and tissue through whole-bone length-scales?	• Does the frequency of LCS remodeling change in health and with aging and disease? • Does tissue composition and mechanical properties vary between remodeling and non-remodeling lacunae and canaliculi? • Does LCS remodeling affect mineral and collagen turnover around individual osteocytes? • How are tissue toughening mechanisms are impacted by LCS remodeling?
How should tissue composition and mechanical properties be assessed near the LCS?	• Do insufficiently high-resolution techniques result in 'false negatives' about material property gradation near the LCS? • How many lacunae / canaliculi per sample should be assessed to generalize LCS remodeling phenotype?

2.5. Acknowledgement

This work was supported by the Department of Mechanical & Industrial Engineering and College of Engineering at Montana State University. We are grateful for helpful discussions with Nathaniel Rieders and Dr. David Mogk at the Montana State University Imaging and Chemical Analysis Laboratory. Research reported in this publication was supported by the National Institute of General Medical Sciences of the National Institutes of Health under Award Number P20GM103474. The content is solely the responsibility of the authors and does not necessarily represent the official views of the National Institutes of Health.

CHAPTER THREE

AGING DECREASES OSTEOCYTE PERI-LACUNAR-CANALICULAR SYSTEM TURNOVER IN FEMALE C57BL/6JN MICE

Contribution of Authors and Co-Authors

Manuscript(s) in Chapter(s) 1

Author: Ghazal Vahidi

Contributions: investigation; methodology; data curation; formal analysis; visualization; writing – original draft; writing – review and editing

Co-Author: Connor Boone

Contributions: investigation; methodology; writing – review and editing

Co-Author: Fawn Hoffman

Contributions: formal analysis; Investigation; methodology; writing – review and editing

Co-Author: Chelsea Heveran

Contributions: conceptualization; methodology; formal analysis; resources; project administration; supervision; writing - original draft; writing - review and editing

Manuscript Information

Ghazal Vahidi, Connor Boone, Fawn Hoffman, Chelsea Heveran

Bone

Status of Manuscript:
☐ Prepared for submission to a peer-reviewed journal
☐ Officially submitted to a peer-reviewed journal
☐ Accepted by a peer-reviewed journal
☒ Published in a peer-reviewed journal

Elsevier
September 2024
Volume/Issue 186
https://doi.org/10.1016/j.bone.2024.117163

Abstract

Osteocytes engage in bone resorption and mineralization surrounding their expansive lacunar-canalicular system (LCS) through peri-LCS turnover. However, fundamental questions persist about where, when, and how often osteocytes engage in peri-LCS turnover and how these processes change with aging. Furthermore, whether peri-LCS turnover depends on tissue strain remains unexplored. To address these questions, we utilized confocal scanning microscopy, immunohistochemistry, and scanning electron microscopy to characterize osteocyte peri-LCS turnover in the cortical (mid-diaphysis) and cancellous (metaphysis) femurs from young adult (5 mo) and early-old-age (22 mo) female C57BL/6JN mice. LCS bone mineralization was measured by the presence of perilacunar fluorochrome labels. LCS bone resorption was measured by immunohistochemical marker of bone resorption. The dynamics of peri-LCS turnover were estimated from serial fluorochrome labeling, where each mouse was administered two labels between 2 and 16 days before euthanasia. Osteocyte participation in mineralizing their surroundings is highly abundant in both cortical and cancellous bone of young adult mice but significantly decreases with aging. LCS bone resorption also decreases with aging. Aging has a greater impact on peri-LCS turnover dynamics in cancellous bone than in cortical bone. Lacunae with recent peri-LCS turnover are larger in both age groups. Our data support the hypothesis that peri-LCS turnover is associated with cortical and intracortical positions for 22 mo mice but not for 5 mo mice. The impact of aging on decreasing peri-LCS turnover may have significant implications for bone quality and mechanosensation.

3.1 Introduction

The loss of bone fracture resistance in aging is a major public health problem[2]. Osteocytes, the most abundant and longest-lived bone cells[131,138], are well known to regulate both bone mass and bone matrix quality through the coordination of osteoblasts and osteoclasts[24,131,138]. The osteocyte is the topic of interest for new approaches to manage bone fragility in aging, since over time many of these cells become senescent or apoptotic[190,193] and require greater strains to engage anabolic signaling[8,175,214,215]. Osteocytes live in a porous network within lacunae connected by canaliculi and can remove and replace (i.e., turn over) bone surrounding this network[24,26,28,131,138] (**Figure 3.1A**). There is abundant evidence that aging decreases lacunar and canalicular sizes and connectivity in both rodents and humans[26,28,206,208,218,439]. These geometric changes imply that bone resorption and mineralization by osteocytes alongside the lacunar-canalicular system (LCS) also shift in aging, with possible impacts to bone quality and mechanosensation[24,26,27,131,138,175]. However, many fundamental knowledge gaps persist about how osteocytes interact with their surrounding bone tissue and how these processes change in aging.

The impacts of osteocyte peri-LCS turnover (alternatively termed peri-lacunar, peri-lacunar-canalicular, or lacunar-canalicular remodeling) on the aging skeleton are uncertain, in part because the percentage of osteocytes that engage in bone resorption or mineralization alongside the LCS is unknown[26,28,131,138]. As witnessed in studies of rodent lactation or PTH treatment, osteocytes can expand lacunae and canaliculi through production of acids as well as enzymes such as cathepsins and matrix metalloproteinases (MMPs)[26,28,182–184,197,203,211,213,440]. These pores can then recover to their original size, implying bone re-mineralization[182,184]. When

mice are injected with fluorochrome labels after weaning, abundant fluorochrome labels are observed[182]. However, labeled osteocyte lacunae are also seen in several studies where rodents were not under applied calcium pressure[30,179,187], which suggests that osteocyte LCS mineralization may be a more active and widespread phenomenon than has been previously appreciated. For example, we previously demonstrated that ~60% of randomly-selected lacunae from the femoral midshaft cross-section were labeled with calcein administered 2 days before euthanasia in 5-month and 22-month female C57BL/6 mice[30]. In another study, ~60% of the lacunae in the femoral midshaft cross-section of wild-type male and female C57BL/6 mice at 28-day had calcein labels administered 2 days before euthanasia[179]. Another group found that in the mid cortical cross-section of tibia, ~55% of lacunae showed calcein labels injected 5 days before euthanasia in 2-month male wildtype littermates of MMP13 knockout mice with a mixed C57BL/6 genetic background[187]. These studies differ in age, label dosage, time of injection, region of evaluation, and mouse genetic background. Furthermore, while cortical and cancellous bone differ in their metabolic activities[99,441,442], it is unknown whether osteocyte peri-LCS turnover activity varies between these compartments. To investigate the potential impact of peri-LCS turnover on bone quality and mechanosensation in aging, it is essential to determine the percentage of osteocytes participating in mineralization and resorption in both young adult and aged mice.

The dynamics of peri-LCS turnover are also essential to defining the potential impact of the osteocyte on its surrounding bone. These dynamics have been challenging to study, since LCS bone mineralization and resorption require different bone preparation and analyses. The percentage of osteocytes participating in LCS bone mineralization can be monitored by

fluorochrome labeling[26,28,30,179,184,187,197,213] (**Figure 3.1**). The percentage of osteocytes resorbing bone is instead measured through immunohistochemical markers of matrix metalloproteinases and other targets[179,187,218] **(Figure 3.2D)**. However, there has been a need for an approach to estimate the dynamics of bone turnover from the same bone sections. Serial fluorochrome label injections at short intervals before euthanasia can help address this gap in knowledge (**Figure 3.1B**). It is not possible to assess whether an individual mouse had labeled bone that was later removed. However, the average percentage of lacunae showing labels administered at specific time points (e.g., 2 through 16 days) can allow estimation of how long labels persist following deposition. Furthermore, when serial labels are delivered to the same mice, double labels can provide an indication of how long LCS mineralization can occur (**Figure 3.1B**). Double labels have thus far only been quantified in lactation studies as evidence of bone infilling following the removal of calcium pressure with weaning[182]. To interpret these peri-LCS turnover dynamics, it is also necessary to assess whether common fluorochrome labels (i.e., calcein and alizarin) show similar retention around osteocyte lacunae.

Another question is whether osteocyte peri-LCS turnover is mechanosensitive and if the dependence of this process on tissue strain changes with aging. Osteocytes are mechanosensitive cells and their signaling activity depends on tissue strain[131,138,214,443,444]. Moreover, osteocytes are less mechanosensitive in aging and require greater strains to engage anabolic signaling[8,175,214,215,218]. peri-LCS turnover has the potential to influence osteocyte mechanosensation through altering the shape of the porous LCS network as well as the flow characteristics within it[167,445–447]. Furthermore, as shown in our recent work using atomic force microscopy, recent LCS mineralization increases the compliance of bone within several hundred

nanometers of LCS walls[30], which would likely contribute towards strain amplification[447]. However, whether peri-LCS turnover influences - or is influenced by - strains experienced by the osteocyte is not yet understood. Since long bones experience tissue strains that vary in direction and magnitude[448,449], determining how peri-LCS turnover varies throughout femoral cross-sections can help answer first questions about whether this process is associated with tissue strain in young adult and aged mice.

The purpose of this study is to test the hypothesis that aging decreases the percentage of osteocytes engaged in LCS bone mineralization and resorption and alters the dynamics of these processes. This hypothesis was tested by serial fluorochrome labeling and immunohistochemistry studies of cortical and cancellous bones of the femur in 5-month and 22-month female C57BL/6JN mice. We further hypothesized that the peri-LCS turnover activity depends on variation in tissue strain and that this relationship changes in aging, which we tested by comparing LCS bone mineralization dynamics between femur regions of interest and with distance from the endocortical to periosteal surfaces. Moreover, we hypothesized that peri-LCS turnover activity and impacts of aging would vary for osteocytes located in the lamellar versus non-lamellar compartments of cortical bone, considering previous findings indicating that osteocyte lacunar geometry is influenced by bone structural organization[450,451].

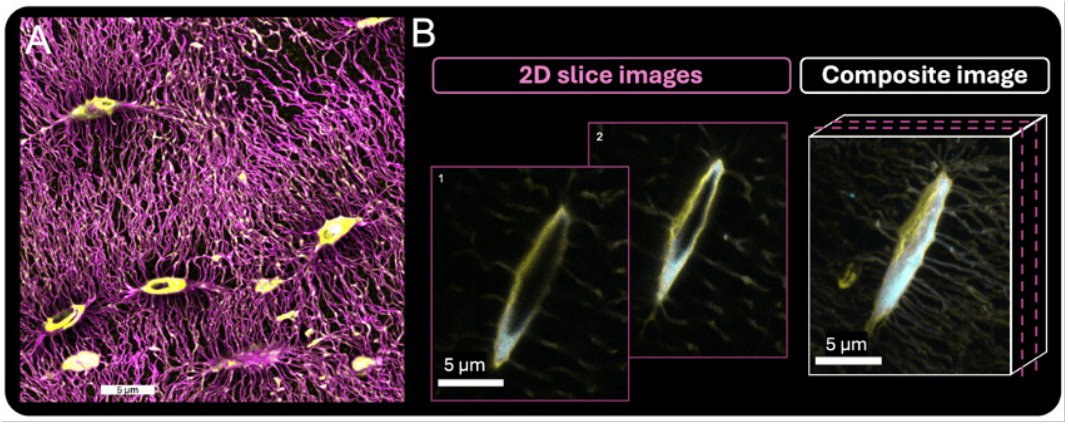

Figure 3.1. Osteocyte lacunar-canalicular system (LCS). A) Osteocytes live in an expansive and intricate network of lacunar holes and canalicular channels. Basic fuchsin staining (magenta, ex vivo staining of embedded bones) shows the extensive LCS porosity of cortical bone. Calcein-stained tissue (yellow, in vivo fluorochrome injection 2 days before euthanasia) indicates bone mineralization. B) Osteocyte lacunae can show double labels when administered at short timepoints before euthanasia. In vivo serial fluorochrome labeling (calcein in yellow, 2 days before euthanasia; alizarin in blue, 8 days before euthanasia) in a female 5 mo C57BL/6JN mouse reveals double-labeled lacunae. Figure 1 generated by G. Vahidi and reprinted with permission from Current Osteoporosis Reports.

3.2 Materials and Methods

3.2.1 Animal Model

All animal procedures were approved by Montana State University's Institutional Animal Care and Use Committee. 5 months old young adult (5 mo, n = 20) and 22 months old early-old-age (22 mo, n=16) female C57BL/6JN mice from the National Institutes of Aging colony were utilized in this study. Mice had a minimum of two weeks to acclimatize to the MSU animal facility before the beginning of the label studies. Mice had *ad libitum* access to water and standard chow. Each mouse was administrated two intraperitoneal injections of fluorochrome labels, calcein (20 mg/kg, i.p.) and alizarin (30 mg/kg, i.p.) at two specific dates that varied for each group of mice. The goal was to collect data for injection dates that include 16d, 8d, 4d, or 2d before the euthanasia, while each group of mice received only two injections with specific

timing and sequence of the injections (**Figure 3.2A**). For example, a group of mice received 2d calcein and 4d alizarin whereas another group received 2d alizarin and 16d calcein. To ensure that label identity was not confounded with the specific time points, some mice received the calcein injection first and the alizarin injection second. Other mice received label injections in the opposite order. No significant effects of label type (i.e., alizarin or calcein) were observed on the percentage of labeled lacunae (**Figure A1**). Therefore, we aggregated the label identity data, pooling alizarin and calcein data for each label date with n = 4-16 sample per age/label date group. Labeling group sample sizes were as followed: in 5 mo group, mice received labels at 2d (n=16), 4d (n=6), 8d (n=10), or 16d (n=8) before euthanasia; in 22 mo group: mice received labels at 2d (n=10), 4d (n=4), 8d (n=9), or 16d (n=9) before euthanasia. All mice received two labels. Mice were euthanized at 5 or 22 months of age via isoflurane inhalation followed by cervical dislocation.

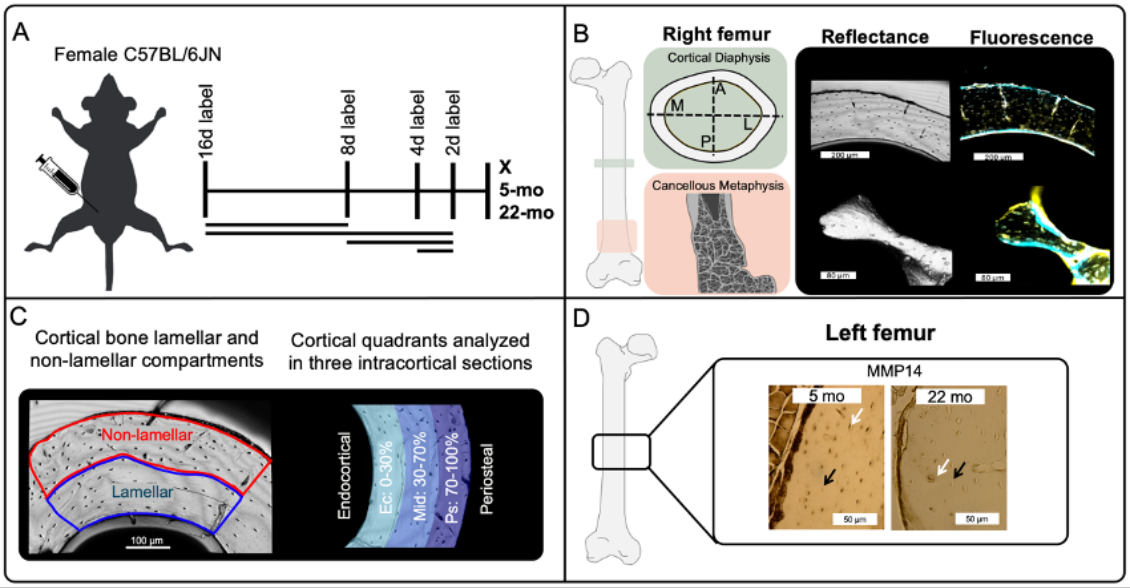

Figure 3.2. Schematic of study experimental procedures. A) Each group of mice received intraperitoneal injections of fluorochrome labels at two specific dates (16d, 8d, 4d, or 2d) before euthanasia at either 5 months or 22 months of age. B) The femur diaphysis (A/P/M/L regions) and distal metaphysis were imaged with a confocal microscope in fluorescence and reflectance modes to evaluate labeled and unlabeled lacunae on the bone surface. Representative images show 2d calcein labels (yellow) and 8d alizarin labels in (blue) for 5 mo mice. C) Cortical bone was visually divided into lamellar and non-lamellar compartments for further analyses. Cortical bone was also divided into three intracortical sections for analysis based on variation in tissue strain. D) MMP14+ lacunae were counted to quantify perilacunar bone resorption for cortical bone. White arrows show MMP14+ lacunae and black arrows show unlabeled lacunae.

3.2.2 Sample Preparation

Right femurs were harvested, cut transversely in half at the femoral midshaft, and then the proximal and distal fragments were embedded in non-infiltrating epoxy (Epoxicure 2, Buehler) without any ethanol dehydration steps, air-drying, or fixation. The proximal side of the mid-shaft cross-section was used for cortical bone studies. The embedded distal halves were cut through the sagittal plane to expose femoral metaphysis for cancellous bone studies, using a low-speed diamond saw (Isomet, Buehler). All samples were polished to achieve a mirror-like finish, using wet silicon carbide papers (600 and 1000 grits, Buehler) followed by Rayon fine cloths and alumina pastes (9, 5, 3, 1, 0.5, 0.3, and 0.05 µm, Ted Pella, Inc.).

Left femurs were harvested and immediately fixed with 10% neutral-buffered formalin, decalcified with EDTA disodium salt dihydrate, dehydrated in a graded ethanol series, embedded in paraffin, transversely cut at femoral midshaft, and each half was serially sliced into 5-micron-thick horizontal cortical diaphysis sections for immunohistochemistry analyses.

3.2.3 Analysis of Bone-mineralizing Osteocytes via Fluorochrome Labeling

An inverted confocal laser scanning microscope (CLSM- Leica Stellaris DMI8, Wetzlar, Germany) was used to identify labeled and unlabeled osteocyte lacunae using a 20× lens (dry, 0.75 NA, 0.78 μm lateral resolution) at 600 Hz speed with a 1024 × 1024 resolution, and pinhole set at 1 Airy unit. Calcein labels were visualized using an excitation wavelength of 488 nm and emission wavelength of 500–540 nm. Alizarin labels were visualized using an excitation wavelength of 561 nm and emission wavelength of 600–645 nm. The reflectance mode was used to image the bone surface, allowing measurement of the total number of lacunae. Then, fluorescence images were taken from the same site to measure the number of fluorochrome-labeled lacunae. The percentage of fluorochrome-labeled lacunae on the bone surface was calculated as the ratio of labeled lacunae to all lacunae on the bone surface (**Figure 3.2B**). All images were collected in z-stacks (~30 μm thickness, 0.6 μm between slices) to confirm whether the surface-visible lacunae were labeled or not in 3D space. For each channel (alizarin and calcein) in every image, we calculated the mean and standard deviation of the grayscale intensity using ImageJ[452]. Then, we determined a minimum intensity value by adding 1.5 times the standard deviation to the mean grayscale intensity. Using Imaris 9.3, we set the minimum threshold of fluorescent intensity for each channel in each image to this calculated value.

The percentage of bone-mineralizing osteocytes (i.e., labeled lacunae) was measured for cortical bone within anterior (A), posterior (P), medial (M) and lateral (L) regions of interest (ROIs) at the femoral midshaft (**Figure 3.2B**). For each ROI, this percentage was also separately reported for lamellar and non-lamellar compartments of cortical bone, which were visually identified from reflectance images (**Figure 3.2C**), to assess the impact of different bone types on bone-mineralizing osteocytes.

We also investigated the effect of natural strain variations that exist in cortical femur diaphysis[453] on osteocyte bone mineralization activity. First, we compared the percentage for bone-mineralizing osteocytes between anterior (close to femur loading axis) and medial (close to femur neutral axis) ROIs (**Figure 3.6A**). These quadrants were chosen because the anterior femur experiences tensile strains while the medial quadrant experiences consistently lower strains. By contrast, the posterior and lateral quadrants experience more complicated stresses [453]. Because tensile strains increase from the endocortical to periosteal surfaces of the anterior quadrant [453], we also compared the percent of bone mineralizing lacunae with respect to intracortical position with relation to the endocortical surface: 0-30%, 30-70%, and 70-100% of the cortical thickness (**Figure 3.2C**). We referred to the sections as Ec (endocortical, 0-30%), Mid (middle, 30-70%), and Ps (periosteal, 70-100%). These same regions were also assessed for the medial quadrant, which has much less intracortical stress variation[453]. For analyses of cancellous bone, multiple trabecular regions (**Figure 3.2B**)) were selected from the metaphysis of each mouse, exposed by sagittal sectioning of the femur's distal half. The percentage of labeled lacunae was calculated for each trabecular region (**Figure 3.2B**)), and then the mean and standard deviation of all trabecular regions in each mouse were reported. Custom Matlab codes

were employed for these analyses (MATLAB codes available on GitHub repository: https://github.com/Ghazal-vhd/LCST_LabelCount_Femur.git). These codes counted the number of lacunae on the bone surface from reflective images and the number of labeled lacunae from fluorescence images within regions of interest defined by the user, calculating the percentage of labeled lacunae for both cortical and cancellous regions.

During data collection, the laser for the Leica Stellaris DMI8 was updated from a diode laser to a white light laser while the detectors remained unchanged. Emission and excitation ranges were kept similar, but adjustments were made to the new laser's settings such as gain and power to ensure a uniform image production. All images, both pre- and post-update, were normalized to their respective mean and variable intensity, as previously described. Our analysis revealed no discernible impact of the laser change (included as a blocking factor in all the statistical models) on any outcomes.

The high-resolution images in **Figure 3.1** were from cortical femurs of a 5 months old female C57BL/6JN mouse. This mouse received alizarin injection 8 days and calcein injection 2 days before euthanasia. Both femurs were dehydrated with degraded ethanol series and embedded in polymethyl methacrylate. The right femur was stained with basic fuchsin during the dehydration process[454,455] and used for **Figure 3.1A**. Images were taken with a 63×-oil immersion objective using the same Leica Stellaris DMI8 confocal microscope.

3.2.4 Analysis of Osteocyte Matrix Metalloproteinase Expression by Immunohistochemistry

Paraffin-embedded left distal femurs were used for immunohistochemistry (IHC) following previously published protocols[456]. Slides were dewaxed and rehydrated (ethanol and distilled water series). Subsequently, the slides were incubated in Innovex Uni-Trieve retrieval

solution (329ANK, Innovex Animal IHC kit) for 30 min in a 65 °C water bath. Slides were blocked with the Innovex kit's Fc-block and Background Buster, each for 45 minutes in the room temperature. Next, samples were incubated with the primary antibodies (1:100 anti-MMP14; ab38971 both diluted in PBS) for one hour at room temperature and subsequently with secondary antibodies (Linking Ab, 329ANK) and peroxidase (HRP) enzyme for 10 minutes each at room temperature. Following this, the slides were treated with DAB working solution at room temperature for 5 minutes, washed with PBS, and mounted with Innovex Advantage permanent mounting media. Negative controls were conducted by replacing the primary antibody with rabbit IgG at the same concentration. Images were captured using a Nikon E-50i microscope (Nikon, Melville, NY, SA) with dry 4× (full cortical cross-section) and dry 20× (each cortical ROI) objectives (**Figure 3.2D**). For MMP14 comparisons, we had n=18 and n=20 mice for 5 mo and 22 mo groups, respectively. The mean percentage of MMP14+ osteocyte lacunae for each cortical ROI (A, P, M and L) was quantified using ImageJ. This percentage was not characterized in cancellous bone due to sample availability.

3.2.5 Analysis of Lacunar Geometry via Scanning Electron Microscopy

A subset of samples (n=6 per age) was coated with a thin layer of carbon for lacunar geometrical analyses via backscattered scanning electron imaging (Zeiss Supra 55VP field emission SEM, 15 kV, 60 μm aperture size, 400× magnification, and 9.1 mm working distance). Samples were mounted in a custom holder that ensures flat surfaces at the same height[457]. Images were collected for the anterior ROI. A custom Matlab code was used to calculate lacunar geometry for the lamellar compartment of cortical bone[206]. An area filter removed objects smaller than ~5 μm^2 and larger than ~200 μm^2. Them, pores smaller than ~70 μm^2 were

considered lacunae. The following parameters were calculated: lacunar porosity (%), lacunar number density (#/ mm^2), lacunar area (μm^2, the area of an ellipse fitted to the segmented 2D osteocyte lacunae), lacunar major and minor axes (μm), and lacunar circularity (i.e., ratio of minor to major axis of the fitted ellipse, where a value of 1 indicates a perfect circle). We also assessed differences in lacunar geometry between labeled and unlabeled lacunae for a small subset of samples that were labeled 8 days and 2 days before euthanasia in both 5 mo (n=4) and 22 mo (n=3) groups. We overlapped the SEM images with CLSM maps of labeled and unlabeled lacunae to test whether lacunar area differs between bone-mineralizing and non-bone-mineralizing osteocytes.

3.2.6 Statistical Analyses

Mixed model ANOVA, with mouse as the random effect, tested whether percentage of bone-mineralizing osteocytes depended on the fixed effects of age, tissue strain (i.e., A/P/M/L ROIs), label date, or interactions of these variables for cortical bone. Additional mixed model ANOVAs were utilized for lamellar and non-lamellar cortical compartments. For the comparisons of intracortical distances (0-30%, 30-70%, and 70-100%), the two age groups were separated and for each age, mixed model ANOVA with mouse as a random effect was used to test if the percentage of bone-mineralizing osteocytes (for 2d and 16d labels, separately) depended on the fixed effects of ROI, intracortical distance, or their interactions. For cancellous bone, two-way ANOVA was employed to test if age, label date, and the interaction of these factors affect percentage of bone-mineralizing osteocytes. Since the confocal laser was changed mid-study, this was included as a blocking factor in these models. Because the laser change was not a significant effect for any measure, this blocking factor was removed, and models were

rerun. Mixed model ANOVA with mouse as a random effect was used to test if the percentage of MMP14+ lacunae depends on age, ROI, or their interactions. We tested the effect of age on the measurements of lacunar geometry from SEM using a two-sample t-test. For the lacunar area differences between labeled and not labeled lacunae, we employed mixed model ANOVA with mouse as the random effect and age and label status (yes or no) as fixed effects. For all models, model residuals were checked for satisfaction of assumptions of normality and homoscedasticity. Dependent variables were log-transformed if necessary to satisfy these assumptions. Significance was set a priori to $p < 0.05$. Significant interactions between factors were followed up with Tukey post hoc tests. All analyses were performed with Minitab (20).

3.3 Results

3.3.1 Aging Decreases the Number of Osteocytes Participating in Peri-LCS Turnover

Osteocyte participation in mineralizing their immediate surrounding was highly abundant in the cortical and cancellous femur of young adult C57BL/6JN mice. However, with aging, there was a large decrease in the percentage of recently bone-mineralizing osteocytes (i.e., 2d labeled lacunae) in both cortical and cancellous regions. In the cortical bone of 5 mo mice, 80% of lacunae showed 2d labels, while in 22 mo mice, 50% of lacunae had 2d labels. Thus, from 5 mo to 22 mo, there was a 38% reduction in the percentage of 2d labeled lacunae in cortical bone ($p < 0.001$, **Figure 3.3A & C**). In cancellous bone of 5 mo mice, 85% of the lacunae had 2d labels, while in 22 mo mice, 58% of lacunae showed 2d labels. Therefore, aging reduced the percentage of 2d labeled lacunae by 32% ($p < 0.001$, **Figure 3.3B & D**).

The percentage of double-labeled lacunae (i.e., positive for both 2d and 16d labels) was also abundant in 5 mo femurs, with more than 45% of the lacunae in cortical bone and 60% of lacunae in cancellous bone having double-labels. The percentage of double-labeled lacunae decreased with aging. In 22 mo mice, 26% of lacunae in cortical bone and 10% of lacunae in cancellous bone showed double-labels. Thus, from 5 mo to 22 mo, there were 45% ($p = 0.05$, **Figure A2**) and 85% ($p < 0.001$, **Figure A2**) fewer double-labeled lacunae in cortical and cancellous tissues, respectively.

The percentage of MMP14+ lacunae (i.e., positive for a marker of bone resorption) was also highly abundant in femoral cortical bone of 5 mo mice. For these young adult mice, more than 75% of cortical lacunae were positive for MMP14 (**Figure 3.3E & F**). With increased age, there was a significant decrease in the percentage of MMP14+ lacunae (22 mo vs 5 mo: -10%, $p < 0.001$). The percentage of MMP14+ lacunae was not characterized in cancellous bone due sample availability and future investigations would benefit from this analysis.

Our data showed greater variability in the percentage of bone mineralizing osteocytes in both cortical and cancellous bones of 22 mo mice compared to 5 mo mice (SD comparisons of 22 mo vs 5 mo groups; Cortical: +60%, $p < 0.05$; Cancellous: +230%, $p < 0.001$; p values are from Bartlett and Levene tests of equality of variances between the two groups). This is consistent with observations of higher variability in bone matrix quality and LCS characteristics with aging[3,206,458–461].

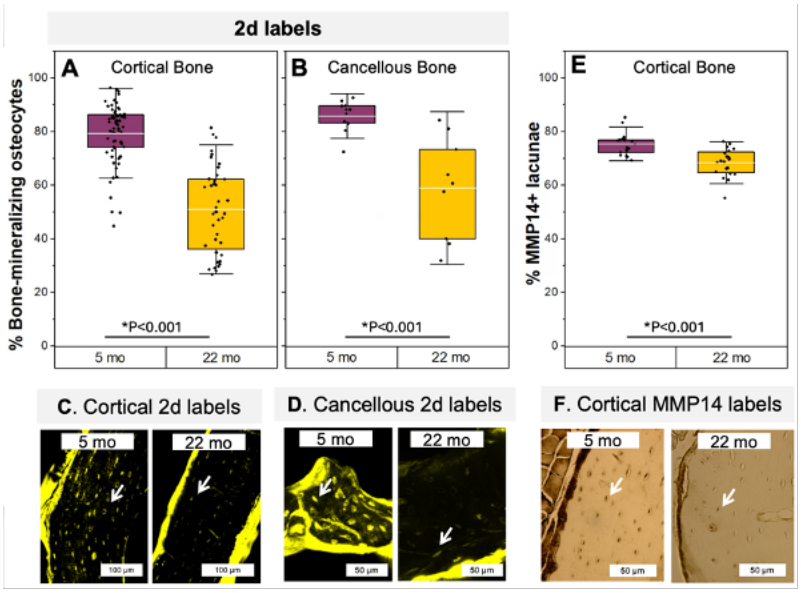

Figure 3.3. The effect of aging on cortical and cancellous osteocyte bone mineralization and resorption. Bone-mineralizing osteocytes were less abundant with aging in both A) cortical and B) cancellous bone. Only 2d labels are shown here. C & D) Representative fluorescence images of calcein labels for 5 mo and 22 mo mice shown. For 2d label comparisons, we had n=16 and n=10 mice for 5 mo and 22 mo groups, respectively. E & F) Aging also decreased the percentage of MMP14+ lacunae in cortical bone. White arrows show 2d labeled (yellow) or MMP14+ lacunae. All data are reported as percentages (labeled lacunae/all lacunae). For MMP14 comparisons, we had n=18 and n=20 mice for 5 mo and 22 mo groups, respectively. Boxplots represent mean value (cross), interquartile range (box), minimum/maximum (whiskers), and symbols representing all data points. All p-values correspond with results of the omnibus ANOVA test. * indicates a significant effect of age.

3.3.2 Aging Alters Peri-LCS Turnover Dynamics More for Cancellous Than for Cortical Bone

The percentage of labeled lacunae decreased for injection dates further from euthanasia. For cancellous bone from 5 mo mice, the percentage of 16d labeled lacunae was 29% ($p < 0.001$) lower compared to 2d labeled lacunae ((**Figure 3.4E & G**). By contrast, at 22 mo, the percentage of 16d labeled lacunae was 81% ($p < 0.001$) lower compared to 2d labeled lacunae (**Figure 3.4F & H**), suggesting that the rate of label disappearance is higher with increased age in cancellous bone. In cancellous bone of both 5 mo and 22 mo groups, the percentage of 8d labels decreased

compared to 2d labels (5 mo: -15%, $p < 0.001$, 22 mo: -39%, $p < 0.001$), while the percentage of 4d labels was not different from 2d labels ($p > 0.05$).

In cortical bone of 5 mo mice, there were 44% ($p < 0.001$) fewer lacunae labeled at 16d compared to 2d ((**Figure 3.4A & C**). For 22 mo mice, there were 61% ($p < 0.001$) fewer 16d labeled lacunae compared to 2d labeled lacunae ((**Figure 3.4B & D**), implying that in cortical bone, peri-LCS turnover undergoes a more modest change with aging compared to cancellous bone. There were 47% ($p < 0.001$) fewer lacunae with 8d labels compared to 2d labels in cortical bone of 22 mo mice, however, 8d label percentage was not different from 2d label percentage in 5 mo mice ($p > 0.05$). The percentage of 4d labels was not different from 2d labels ($p > 0.05$ for either age).

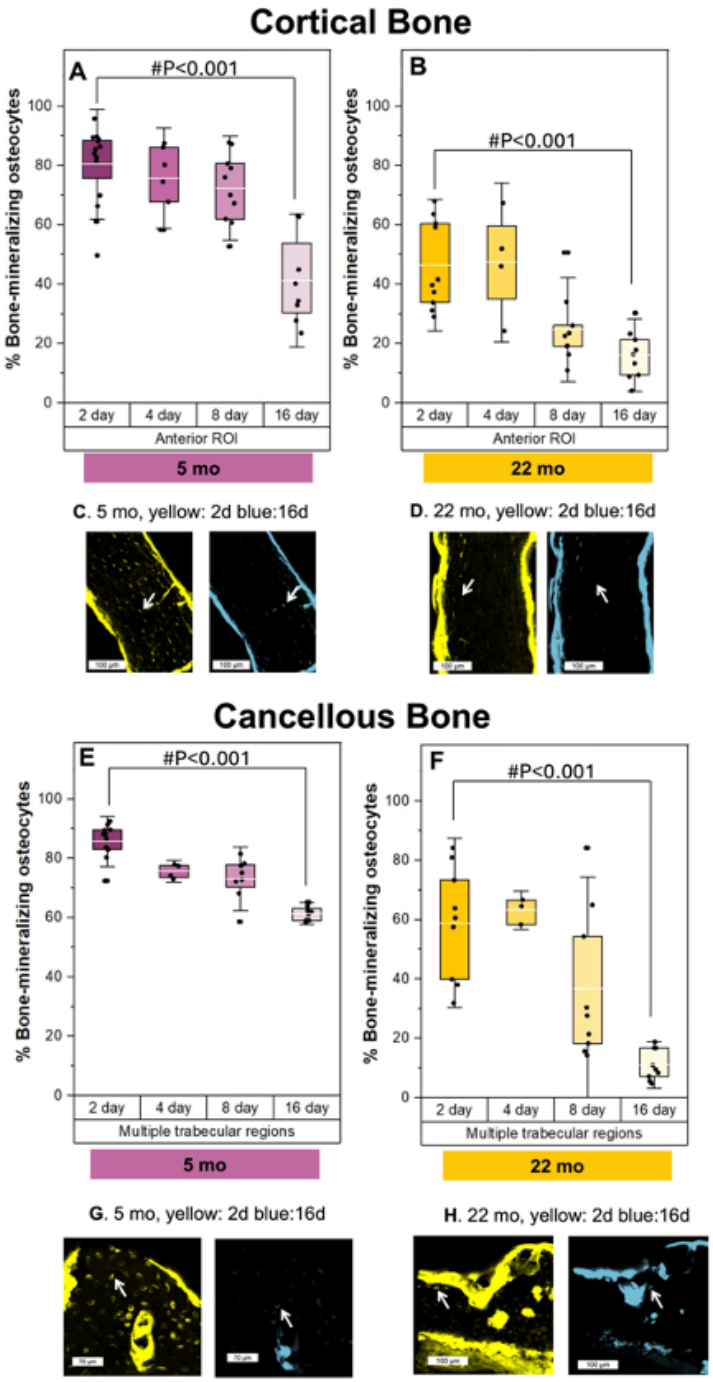

Figure 3.4. The effect of aging on the dynamics of osteocyte bone turnover. A-D) In cortical bone, compared to 2d labels, labels administrated 16d before euthanasia were 44% and 61% less abundant in 5 mo and 22 mo mice, respectively. E-H) In cancellous bone, compared to 2d labels, 16d labels were 29% and 81% less abundant in 5 mo and 22 mo mice, respectively, suggesting aging alters peri-LCS turnover dynamics more for cancellous than for cortical bone. Data for other ROIs of cortical bone are shown in supplementary information. All data are reported as

percentages (labeled lacunae/all lacunae). Representative fluorescence images of 2d labels (calcein label is shown in yellow) and 16d labels (alizarin label is shown in blue) for 5 mo and 22 mo samples shown in both cortical and cancellous tissues. White arrows show 2d labeled lacunae. For the 5 mo group, sample sizes were: 2d (n=16), 4d (n=6), 8d (n=10), and 16d (n=8). For 22 mo group, sample sizes were: 2d (n=10), 4d (n=4), 8d (n=9), and 16d (n=9). Boxplots represent mean value (cross), interquartile range (box), minimum/maximum (whiskers), and symbols representing all data points. All p-values correspond with results of the omnibus ANOVA test. # indicates a significant effect of injection date.

3.3.3 The Impact of Aging on Peri-LCS Turnover Is Similar Between Lamellar and Non-Lamellar Compartments of Cortical Bone

Since osteocyte lacunar geometry depends on the bone structural organization (e.g., lamellar vs non-lamellar bone)[450,451], we further divided the cortical bone into lamellar and non-lamellar compartments. We observed a similar age-induced decline in the percentage of bone-mineralizing osteocytes in both lamellar (for M ROI, 22 mo vs 5 mo: -49%, $p < 0.001$) and non-lamellar (for M ROI, 22 mo vs 5 mo: -46%, $p < 0.001$) bones (**Figure 3.5**, **Figure A3** shows data for all ROIs). Similarly, in both age groups, 16d labels were significantly less abundant compared to 2d labels in both lamellar (for M ROI, 5 mo 16d vs 2d: -40%, 22 mo 16d vs 2d: -62%, all $p < 0.001$) and non-lamellar compartments (for M ROI, 5 mo 16d vs 2d: -45%, 22 mo 16d vs 2d: -60%, all $p < 0.001$) of cortical bone (**Figure 3.5**).

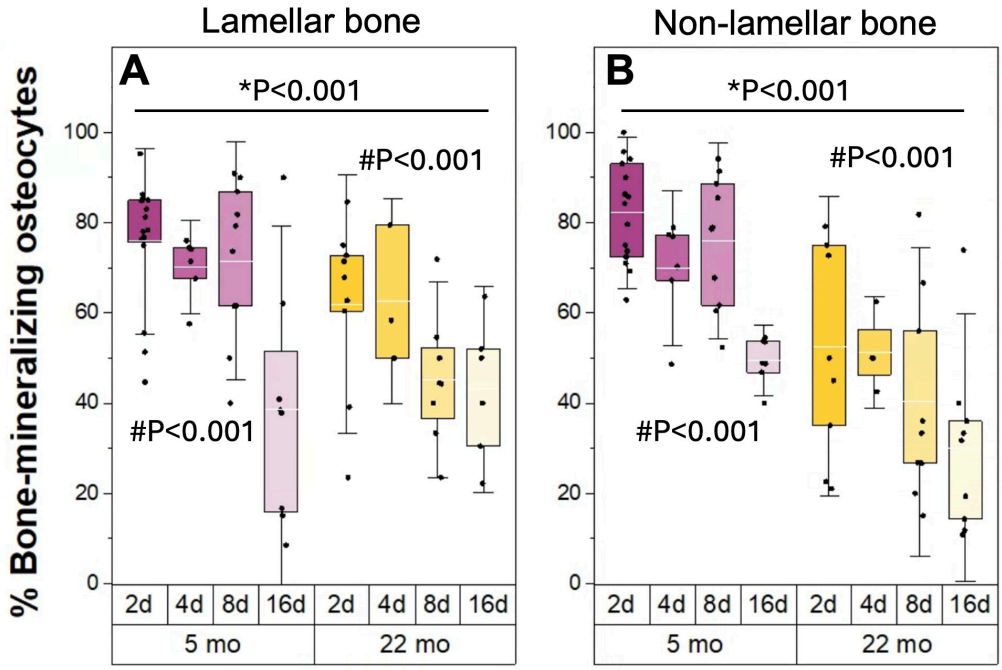

Figure 3.5. The effect of aging is similar in reducing *peri*-LCS bone mineralization for both lamellar and non-lamellar bone. For both A) lamellar and B) non-lamellar compartments of cortical bone, aging reduced the percentage of bone-mineralizing osteocytes. For both types of tissues, 16d labeled lacunae were significantly less abundant compared to 2d labeled lacunae regardless of the age group. Data are shown for the medial ROI, where we consistently observed comparable amounts of both lamellar and non-lamellar bone across all mice. In contrast, the size of lamellar and non-lamellar bone regions varied significantly in the other ROIs, and some mice did not have non-lamellar bone in the anterior ROI. Results for all ROIs are presented in Figure A3. All data are reported as percentages (labeled lacunae/all lacunae). Boxplots represent mean value (cross), interquartile range (box), minimum/maximum (whiskers), and symbols representing all data points. All p-values correspond with results of the omnibus ANOVA test. * indicates a significant effect of age. # indicates a significant effect of injection date.

3.3.4 The Relationship Between Peri-LCS Turnover and Cortical Quadrant and Intracortical Location of Osteocytes Depends on Age

In mouse femur cross-section, the strain environment is distinct between anterior (A), posterior (P), medial (M), and lateral (L) ROIs based on their position with respect to the femur loading axis and natural axis ((**Figure 3.6A**)[453]. Because the osteocyte is a mechanosensitive cell[448,449], we compared LCS bone mineralization and resorption for these ROIs. In 5 mo mice, we did not find a relationship between LCS turnover dynamics and the position of the osteocytes

in distinct strain environments of the femur cortex ($p = 0.815$, (**Figure 3.6B**). However, in 22 mo mice, we found an association between the peri-LCS turnover dynamics and the position of the osteocytes in different ROIs of cortical femur (age and ROI interaction $p < 0.001$). Osteocytes in the medial ROI of aged femurs (close to femur neutral axis) had higher participation in mineralizing their surrounding compared to those in the other three ROIs (e.g., M vs A: +44% $p<0.001$, (**Figure 3.6B**). There were no differences in the percentage of labels among anterior, posterior, and lateral ROIs. Notably, the decay of 16-day labels exhibited a slower pace in the medial ROI in comparison to the others. ROI did not impact the percentage of MMP14+ lacunae in 5 mo or 22 mo mice ($p = 0.7$).

Ascenzi *et al*. demonstrated that for the anterior ROI of the mouse femur, intracortical tissue tensile strains increases with distance from the centroid[453]. However, in the medial ROI, which is close to the femur neutral axis, strains are lower and are relatively unaffected by distance from the centroid. The intracortical strain distribution is more complex for posterior and lateral ROIs[453]. Therefore, we divided anterior and medial ROIs with simpler and more distinct strain distribution patterns into three sections with respect to the position between the endocortical and periosteal surfaces. Distance sections included Ec: 0-30%, Mid: 30-70%, and Ps: 70-100% (**Figure 3.6A**). There were no significant interactions between ROI and distance for either 5 mo or 22 mo mice. In 5 mo mice, both 2d labeled and 16d labeled lacunae percentages were influenced by the intracortical position but not by ROI. At this age, posthoc testing reveals that the lacunae closest to the periosteal surface (Ps: last 70-100% of cortical thickness) had a smaller percentage of 2d labels compared to the other two distances (Ec = Mid > Ps, $p = 0.017$, **Figure 3.6C**). There were fewer 16d-labeled lacunae within the middle distance (Mid: 30-70%

of cortical thickness) compared to other distances (Ec = Ps > Mid, p = 0.038, **Figure 3.6D**). Differences in the percentage of labeled lacunae with intracortical position were more pronounced for 22 mo mice. At this age, lacunae within the middle intracortical distance had lower percentage of 2d labels compared to other the other distances (Ec = Mid > Ps, p = 0.001, **Figure 3.6E**). Periosteal distance section in 22 mo mice showed the highest percentage of 16d labels compared to the other distances (Ec = Mid < Ps, p < 0.001, **Figure 3.6F**).

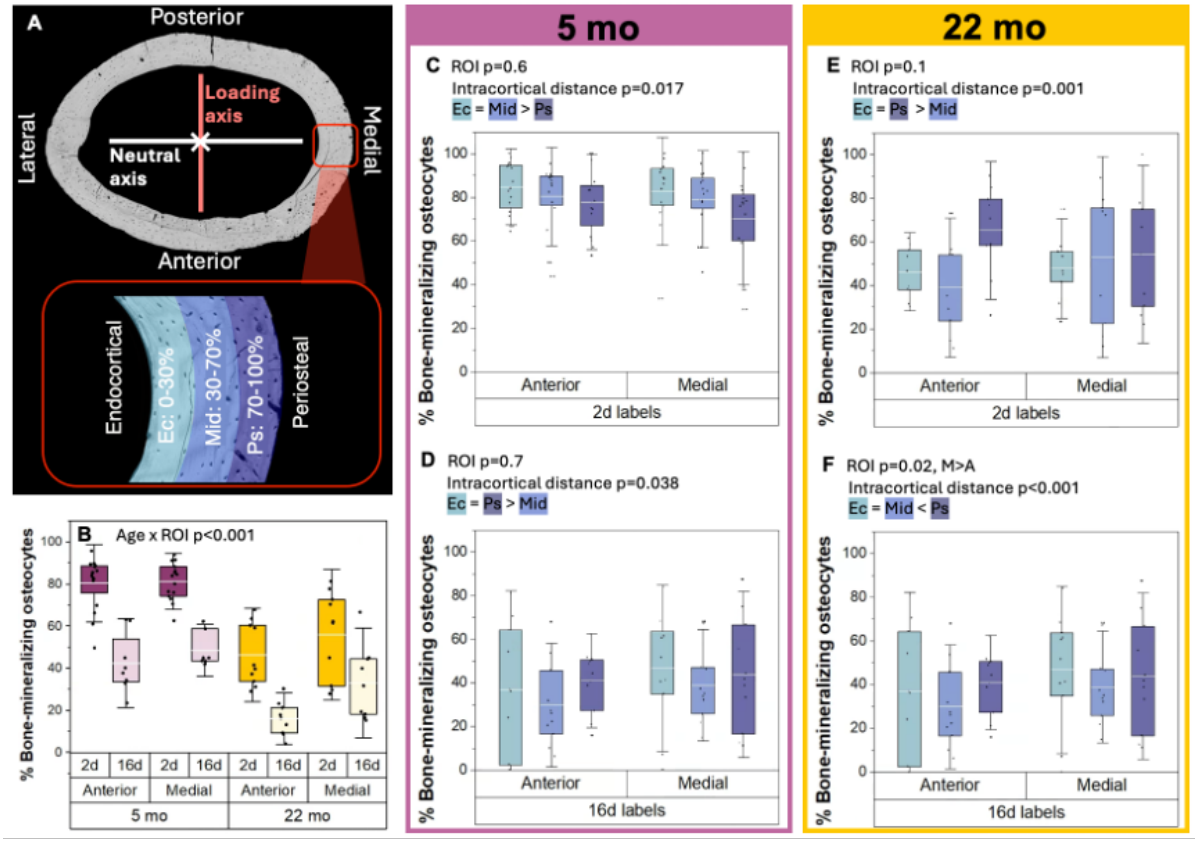

Figure 3.6. Associations between tissue strain and osteocyte participation in LCS bone mineralization. A) Schematic of anterior, posterior, medial, and lateral ROIs and their position with respect to the femur loading axis and natural axis. Anterior and medial ROIs were divided into three distance sections from the endocortical surface (0-30%, 30-70%, and 70-100% of cortical thickness) for further investigation of whether osteocyte bone mineralization is associated with differences in tissue strain. B) In 5 mo mice, anterior vs medial ROI did not impact the percentage of bone-mineralizing osteocytes. However, for 22 mo mice, lacunae in the medial ROI had the highest percentage of labeling compared to all ROIs. There were no significant interactions between ROI and distance for either 5 mo or 22 mo mice. C) In 5 mo mice, the percentage of 2d labeled lacunae was lowest in the region closest to periosteal surface, for both anterior and medial ROIs. D) For 5 mo mice, the percentage of 16d labeled lacunae was lowest in the middle intracortical region, for both anterior and medial ROIs. E) In 22 mo mice, the percentage labeling differences between intracortical sections were larger. Middle intracortical section in 22 mo mice had fewer 2d labeled lacunae compared to other sections in both anterior and medial ROIs. F) In 22 mo mice, the percentage of 16d labeled lacunae was highest in the region closest to periosteal surface and16d labels consistently showed higher percentages in the medial ROI compared anterior ROI. Data are reported as percentages (labeled lacunae/all lacunae). Boxplots represent mean value (cross), interquartile range (box), minimum/maximum (whiskers), and symbols representing all data points. All p-values correspond with results of the omnibus ANOVA test.

3.3.5 Osteocytes with active Peri-LCS turnover have larger lacunae

We conducted a quantitative analysis of backscattered SEM images at the anterior ROI of femoral cross-sections to assess whether lacunar geometry changes with aging and the recency of labeling. Since lacunar geometry differs between lamellar and non-lamellar bones, and the relative size of these regions changes in aging, we restricted our analyses to lamellar bone. We chose the anterior ROI because, compared to other ROIs, it was consistently composed mostly of lamellar bone. Compared with 5 mo mice, 22 mo mice had decreased cortical lacunar porosity (-27%, p=0.037) but not lacunar number density (p=0.35) (**Figure A4**). Older mice also had smaller lacunae, as seen by smaller lacunar area (-22%, p=0.02), major axis (-12%, p=0.045), minor axis (-15%, p=0.05) (**Figure 3.7A-B, Figure A4**). No changes were seen in lacunar circularity with age. It is noted that previous work found that 2D SEM analysis is insufficient to detect expected increased sphericity in lacunae with aging[206].

We also asked whether lacunar size differs between labeled and unlabeled lacunae by overlaying SEM and CLSM maps of the anterior region at the cortical midshaft femur for only a subset of SEM samples that had 2d and 8d labels. The distribution of labeled lacunar sizes is approximately normal for both 5 mo and 22 mo mice (**Figure 3.7B & E**). By contrast, the sizes of unlabeled lacunae show closer to a uniform distribution for both ages. Our data suggest that recent peri-LCS turnover increases lacunar area (**Figure 3.7B & E)**. Labeled lacunae had larger mean (+11% in 5 mo and +14% in 22 mo, both p = 0.05) and median lacunar areas compared with unlabeled lacunae (**Figure 3.7A & D & G**).

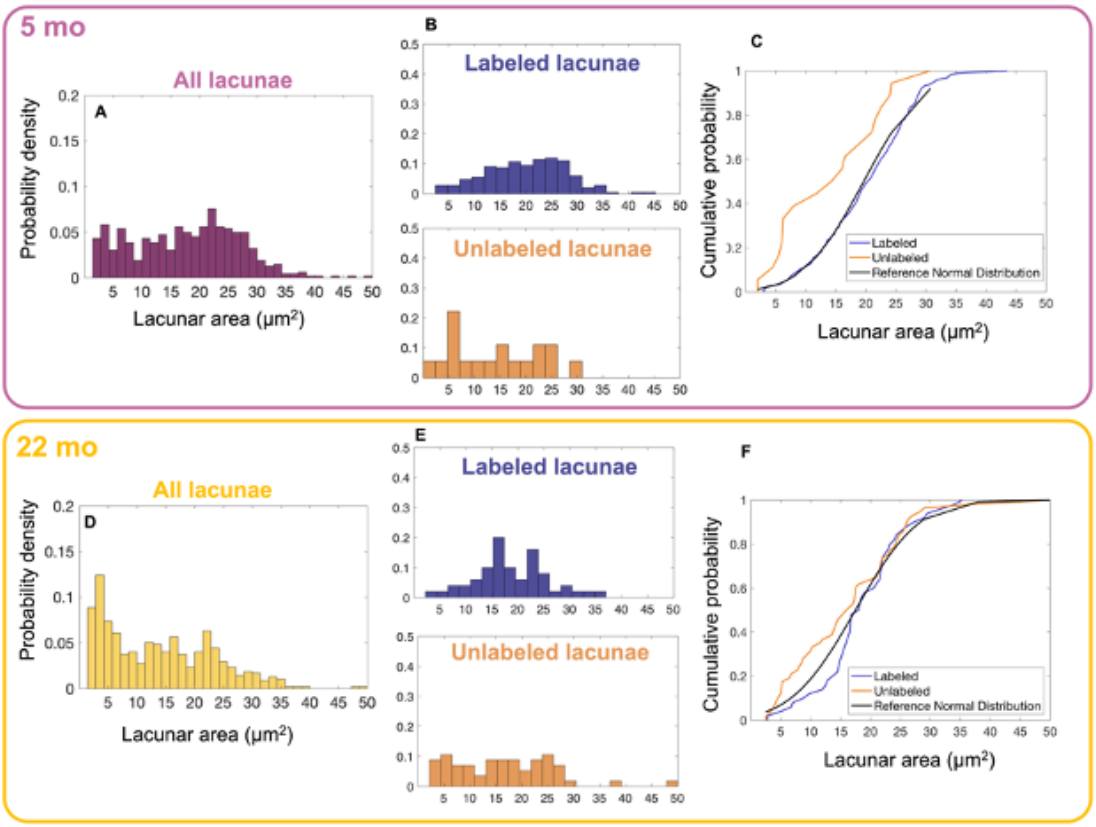

G

		Mean lacunar area (μm²)	Median lacunar area (μm²)
5 mo	Labeled	19.97 ± 0.48	20.38 (Q1=14.25, Q3=25.63)
	Unlabeled	17.99 ± 1.76	18.75 (Q1=12.38, Q3=23.63)
22 mo	Labeled	19.00 ± 0.96	18.50 (Q1=14.00, Q3=22.75)
	Unlabeled	16.39 ± 1.13	16.63 (Q1=9.06, Q3=20.19)

Figure 3.7. Osteocytes with active mineralization have larger lacunae. Overlayed SEM and CLSM maps show that A-G) labeled lacunae had larger areas compared to unlabeled lacunae in both age groups. A-C) The distribution of lacunar sizes in 5 mo mice (n=4) was approximately normal for labeled lacunae (i.e., 2d labeled and/or 8d labeled). However, the distribution of lacunar sizes for unlabeled lacunae (i.e., no 2d or 8d labels) deviated from normality. D-F) In 22 mo mice (n=3), labeled lacunae had a distribution of lacunar sizes that was closer to normal whereas unlabeled lacunae did not have a normal distribution. The distributions in E-F are depicted as probability density function as well as cumulative density function plots. Data in table are represented as mean with standard error and median with first and third quartiles.

3.4 Discussion

Osteocyte lacunar-canalicular system (LCS) turnover has been of high research interest as a possible contributor to age-related changes in bone fracture resistance[26–28,30,131,138]. Extensive evidence indicates that age reduces osteocyte viability and mechanosensitivity[8,27,175,214,215,218] and truncates lacunar and canalicular dimensions and connectivity[26,28,206,208,218,439]. These changes imply that there is a decrease in peri-LCS turnover in aging, which could have impacts to osteocyte mechanosensitivity and bone matrix quality[26,27,179,187,208,218]. At present, however, more questions than answers exist about where and how often osteocytes remove and replace their surrounding bone. Our study aimed to test the hypothesis that fewer osteocytes participate in LCS bone mineralization and resorption in aging C57BL/6JN female mice (5 mo vs 22 mo). In this work, we find that aging reduces cortical and cancellous osteocyte participation in both perilacunar bone mineralization and resorption, in a manner that likely depends on tissue strain.

The osteocyte is known to remove and replace bone surrounding the LCS in response to perturbations in calcium homeostasis (e.g., lactation, PTH)[26,28,182–184,197,203,211,213,440], However, the participation of osteocytes in peri-LCS turnover outside of calcium pressure is uncertain[26]. We utilized serial fluorochrome labeling to estimate where, when, and how often osteocytes turn over their surrounding bone. Each mouse in this study was administered two fluorochrome labels at different times before euthanasia. We find that osteocyte bone turnover is highly prevalent in young adult mice, in both cortical and cancellous bone. Over 80% of osteocytes show fluorochrome labeled lacunae administrated 2 days before euthanasia. These numbers decrease to around 45% at 16 days before euthanasia, suggesting rapid bone turnover (**Figure 3.4**). Since label disappearance is an indirect indicator of bone resorption, we stained decalcified sections

from the contralateral femurs for MMP14. Previous studies suggest that under conditions of elevated PTH signaling, osteocytes can acidify and demineralize bone matrix using matrix-degrading enzymes such as cathepsins and matrix metalloproteinases, in a process known as osteocytic osteolysis[182,187,211]. We show that in 5 mo mice, a comparable percentage of osteocytes are positive for bone resorption (i.e., MMP14-positive) as for bone mineralization (i.e., fluorochrome-labeled) (**Figure 3.3**). Together, these data suggest that osteocytes in the young adult murine skeleton engage in a pattern of frequent, near-daily bone mineralization along the LCS, coupled with frequent bone resorption events.

Aging has established deleterious impacts on the osteocyte. With increased age, osteocyte apoptosis and senescence both increase while autophagy decreases[190,462]. Aging reduces the size of lacunae and canaliculi, as well as the connectivity of this network[26,28,206,208,218,439]. These changes imply, but do not determine, that peri-LCS turnover also changes with age. Here, we report that aging also reduce LCS bone mineralization and, to a lesser extent, resorption activities. Compared with 5 mo mice, 22 mo mice have a 58% decrease in the percentage of 2d labeled lacunae and a 10% decrease in the percentage of MMP14+ lacunae in cortical bone ((**Figure 3.3**). The rate of decrease in label percentage from 2d to 16d in cortical bone is similar across ages. These data suggest that while the number of osteocytes participating in peri-LCS turnover decreases with aging, active osteocytes of different-aged cortical bone may have a characteristic time span of bone deposition before resorption events. The characteristics of peri-LCS turnover did not differ between lamellar and non-lamellar bone at either 5 or 22 mo ages. This is an important finding, since bone organization changes with aging and previous studies have shown that aging affects LCS geometry and density differently in these bone types[450,463–465].

These data add to our understanding of aging bone biology by providing the first evidence that peri-LCS turnover activity declines with aging.

Osteocytes reside within cortical and cancellous bone but may have distinct roles within each of these compartments and different aging-induced impacts in their behaviors. There was a smaller age-related decline in the percentage of osteocytes engaged in LCS bone mineralization in cancellous versus cortical bone (-31% vs -58%, **Figure 3.3**). While the dynamics of bone turnover did not change significantly with age in cortical bone (i.e., comparable rate of decrease in labeled lacunae from 2d to 16d between ages), age greatly increased the frequency of bone turnover in cancellous bone (**Figure 3.4**). These data suggest that more osteocytes remain active in cancellous bone and may increase their rate of bone turnover compared with cortical bone. Cancellous bone is known to be more metabolically active than cortical bone[99,441,442]. It is possible that cancellous osteocytes have increased burden of participating in calcium homeostasis in the aging skeleton, but this hypothesis remains speculative at this time.

Our data suggest that the smaller lacunae reported in numerous imaging studies of the aging skeleton[26,28,206,208,218,439] are associated with decreased osteocyte bone turnover. From coupling scanning electron microscopy measurements of lacunae with fluorochrome labeling, we find that osteocytes that are engaged in recent bone mineralization, regardless of the age group, reside within larger lacunae compared to osteocytes without labels (**Figure 3.7**). This result suggests that bone resorption events remove a considerable quantity of bone. It is yet to be fully determined which specific additional factors osteocytes employ to promote, or inhibit, local bone mineralization and/or formation. For example, it is well established that osteoblasts participate in local bone mineralization through shuttling hydroxyapatite precursors in vesicles to be released

near forming surfaces[466]. Whether osteocytes engage in these active mineralization or mineral inhabitation processes should be investigated.

The influence of aging on osteocyte peri-LCS turnover may be associated with tissue strain. As an initial test of this relationship, we assessed changes in peri-LCS turnover with the spatial position of osteocytes within the cortical femur. We tested the association of peri-LCS turnover activities between the different quadrants of the mouse femoral cross-section, which vary in strain magnitudes and directions, as well as the variation in intercortical tissue strain with distance from the femoral centroid [453] (**Figure 3.6**). In young adult mice, we did not find sufficient evidence to support the hypothesis that peri-LCS turnover depends on the position of osteocytes within the femur cortex. However, in early old age mice, we found evidence that osteocyte LCS bone mineralization depends on the position of osteocytes within the cortical femur. Compared with osteocytes in anterior and posterior regions of cortical bone (i.e., higher tensile and compressive strains under loading, respectively [448,449]), more osteocytes in the medial region of aged bones (i.e., closer to neutral axis) were engaged in LCS bone mineralization (i.e., highest percentage of 2d labels) and the peri-LCS turnover rate was decreased (i.e., smallest change in the presence of 16d labels compared to 2d labels). Additionally, for aged mice, there was a stronger relationship between the position of lacunae within the cortical thickness and peri-LCS mineralization, where 2d labels were more abundant in both endocortical and periosteal surfaces compared to the middle section and 16d labels were the most abundant closest to the periosteal surface. These data suggest that there may be an association between intracortical strain and LCS bone turnover activities that is evident in aging. However, there are important limitations to this analysis, as the observed spatial interactions with peri-LCS turnover could be

contributed to by factors other than tissue strain, such as specific nutrient gradients, tissue maturity variations, access to biochemical signals, and differences in shear stress induced by interstitial fluid flow between different cortical ROIs and intracortical distances[453,467–470]. Future research needs to determine if and how peri-LCS turnover is associated with changes in skeletal strain, whether there is a minimum strain required to engage osteocyte peri-LCS turnover, and if this strain threshold changes with aging.

With aging, osteocytes become less mechanosensitive[8,27,175,214,215,218]. A persistent question is why aging has this effect on these long-lived cells. It has been recognized for many years that substantial strain amplification must occur for osteocytes to respond with anabolic signals to normal skeletal loads[165,172,443]. The changes in lacunar and canalicular shape with age may reduce tissue strain and fluid flow shear stress to contribute to these age-related changes in strain experienced by the cell, as shown by several finite element modeling studies [445,471]. Our data add to this understanding by showing that changes in osteocyte lacunar size with age are approximately bimodal in distribution (i.e., only some aged osteocytes have much reduced lacunar size). Further, we show that labeled osteocyte lacunae are larger than non-labeled lacunae at both ages. Lacunar enlargement with recent peri-LCS turnover activity has been previously shown under high calcium demands such as lactation or PTH treatment[182,184,194,211]. Our observations suggest that contributions to osteocyte mechanosensation derived from geometric factors (i.e., shape of lacunae and canaliculi and the impact of these shape changes on fluid flow) is likely influenced by the activity of these cells in turning over their local bone. Additionally, our prior work demonstrated that labeled osteocyte lacunae are surrounded by more compliant (i.e., lower modulus) bone[30]. Thus, changes to peri-LCS turnover in aging have

multiple potential avenues for altering strain experienced by osteocytes. Our result that aging decreases the percentage of osteocytes engaged in LCS bone mineralization and resorption, but not the apparent rate of label disappearance (i.e., an estimate of resorption), may align with data from studies on the impact of aging on calcium signaling. In the cortical bone of 22 mo female C57BL/6JN mice, there are fewer osteocytes (~ -60%) with active calcium signaling compared to younger mice, yet the remaining osteocytes respond to mechanical load with Ca^{2+} peaks of comparable intensities to those observed in young mice[214]. It is not yet understood whether populations of aged osteocytes with different LCS bone turnover characteristics vary in their mechanosensitivity. Together, these data suggest that major gaps still exist in our understanding about the strain experienced by the osteocyte and how these strains change in aging.

Our data also add to the emerging understanding of the osteocyte as a cell with the potential to directly modify bone matrix properties. Studies on transgenic mice with suppressed TGF-β or YAP/TAZ signaling, or systemic MMP13 deletion, demonstrate that mice with a decreased ability to engage peri-LCS turnover have more fragile cortical bone[27,179,187,212]. A recent study explored the role of osteocytes in the loss of bone matrix quality in aging by distinguishing matrix characteristics that decline in aging in a manner that is either TGFβ-dependent or -independent. The study demonstrated an essential role for osteocyte TGFβ signaling in regulating not only LCS integrity but also collagen material behavior. By contrast, mineral characteristics were regulated independently of TGFβ signaling[27]. We add to this understanding by showing that osteocyte interaction with bone matrix significantly decreases in age. In addition, our earlier work showed that peri-LCS turnover increases perilacunar bone compliance in both young adult (5 mo) and early-old-aged (22 mo) mice[30]. Together, these data

build an argument towards the importance of the osteocyte in maintaining bone matrix quality and the decline of these matrix-regulatory processes in aging.

Aging impacts LCS geometry in both humans and rodents, such as decreased lacunar and canalicular size and connectivity[206,207,222,223,472]. If aging also reduces LCS turnover in humans in a similar way that is seen for mice in this study, the quality of a large amount of bone tissue could be impacted. An adult human skeleton contains approximately 42 billion osteocytes each with a lacunar surface area of roughly 336 μm^2, compromising a 215 m^2 total surface area[140,473]. From AFM[30] and synchrotron microscopy data[223,240,474], the region of bone tissue impacted by LCS turnover might be estimated to extend to about 1 micrometer from lacunar walls. Assuming a similar reduction from 80% to 50% of osteocytes engaged in LCS turnover in aging for humans, the amount of bone tissue impacted by this bone turnover would decrease from 4.7 m^2 to 2.4 m^2. Importantly, these estimates are only based on peri-lacunar bone turnover and not peri-canalicular bone turnover and are therefore most likely underestimates. Determining peri-LCS turnover dynamics and the impacts of aging in humans is an important future research direction.

There were several important limitations to this study. First, age-related changes in metabolic processes and LCS network architecture may impact fluorochrome dye uptake between cells in young and old bones, and this limitation should be addressed in future studies. However, our work provides key recommendations for measuring the dynamics of LCS bone mineralization. We find that 2d and 4d labels do not yield statistically significant results across different skeletal sites and ages. In contrast, 8d labels show differences from 2d labels in aged cortical bones and both ages for cancellous bone, while 16d labels are consistently lower compared to 2d labels across all groups. We also found that the order of labeling (calcein first,

then alizarin, or vice versa) does not affect the results. In this study, we did not investigate the impact of aging on LCS bone resorption, as indicated by MMP14+ lacunae, through other resorption biomarkers such as TRAP, cathepsin K, or MMP13, but this would be valuable in future investigations. Additionally, our study focused solely on female mice, whereas the literature highlights important sex differences in osteocyte physiology[27,475]. Moreover, extending the age range of the study would be beneficial to exploring whether peri-LCS turnover changes during the developmental and advanced ages. In this study, it was not possible to investigate the age of individual osteocytes in older bones and discern whether the active osteocytes were young or old.

In summary, this study presents the first evidence that osteocyte participation in mineralizing their surroundings is highly abundant in both cortical and cancellous bone of young adult female C57BL/6JN mice. In aging, there are fewer osteocytes with active peri-LCS turnover (both bone mineralization and resorption), yet turnover dynamics remain mostly similar in cortical bone of 5 mo and 22 mo mice, suggesting that active osteocytes engage in a characteristic peri-LCS turnover response. Our results also demonstrate that the impacts of aging on peri-LCS turnover are not uniform throughout the femoral cortex and might differ with tissue strain. The large decline in peri-LCS turnover in aging can have significant implications for bone quality, since osteocytes with active turnover have larger lacunae in both age groups as well as more compliant perilacunar tissue[30]. These results together signify a potential role for osteocyte bone turnover in the loss of bone fracture resistance and changes in mechanosensation in aging.

3.5 Acknowledgments

This research was made possible by the Department of Mechanical & Industrial Engineering and the College of Engineering at the Montana State University. This work represents the views of the authors and not necessarily those of the sponsors. Research reported here is supported by NSF 2120239 and NIH R03AG068680. Imaging method development and data collection were made possible by the help of Dr. Heidi Smith from the Center for Biofilm Engineering imaging facility at Montana State University, supported by funding from the National Science Foundation MRI Program (2018562), the M. J. Murdock Charitable Trust (202016116), the US Department of Defense (77369LSRIP & W911NF1910288), and by the Montana Nanotechnology Facility (an NNCI member supported by NSF Grant ECCS-2025391). We thank Dr. Albert Parker for his assistance in statistical analyses. Steven Watson is thanked for his help with image processing and dissection. Kenna Brown and Connor Devine are thanked for their assistance with tissue harvest. Grace Roaming, Chloe Woodwall, and Shane Stauffer are thanked for their help with sample preparation. We thank Fatema Aljamal, Leah Davidson, Torie Prall, Megan Brenna, Kelly Silk, and Allison Stevens for their help with initial steps of method development for this project. Alexey Dynkin is appreciated for manuscript proofreading. We thank Montana State University's Animal Resource Center staff and especially Tamara Marcotte for the help in providing excellent mouse care.

CHAPTER FOUR

PERILACUNAR BONE TISSUE EXHIBITS SUB-MICROMETER MODULUS GRADATION WHICH DEPENDS ON THE RECENCY OF OSTEOCYTE BONE FORMATION IN BOTH YOUNG ADULT AND EARLY-OLD-AGE FEMALE C57BL/6 MICE

Contribution of Authors and Co-Authors

Manuscript(s) in Chapter(s) 1

Author: Caleb Rux

Contributions: investigation; methodology; data curation; formal analysis; visualization; writing – original draft; writing – review and editing

Co-Author: Ghazal Vahidi

Contributions: investigation; methodology; data curation; formal analysis; visualization; writing – original draft; writing – review and editing

Co-Author: Amir Darabi

Contributions: investigation; methodology; data curation; writing – original draft; writing – review and editing

Co-Author: Lewis Cox

Contributions: conceptualization and design, writing original draft, review and editing

Co-Author: Chelsea Heveran

Contributions: conceptualization and design, writing original draft, review and editing

Manuscript Information

Caleb Rux, Ghazal Vahidi, Amir Darabi, Lewis Cox, Chelsea Heveran

Status of Manuscript:
☐ Prepared for submission to a peer-reviewed journal
☐ Officially submitted to a peer-reviewed journal
☐ Accepted by a peer-reviewed journal
☒ Published in a peer-reviewed journal

Elsevier
April 2022
Volume/Issue 157
https://doi.org/10.1016/j.bone.2022.116327

Abstract

Osteocytes resorb and replace bone local to the lacunar-canalicular system (LCS). However, whether osteocyte remodeling impacts bone quality adjacent to the LCS is not understood. Further, while aging is well-established to decrease osteocyte viability and truncate LCS geometry, it is unclear if aging also decreases perilacunar bone quality. To address these questions, we employed atomic force microscopy (AFM) to generate nanoscale-resolution modulus maps for cortical femur osteocyte lacunae from young (5 mo) and early-old-age (22 mo) female C57Bl/6 mice. AFM-mapped lacunae were also imaged with confocal laser scanning microscopy to determine which osteocytes recently deposited bone as determined by the presence of fluorochrome labels administered 2d and 8d before euthanasia. Modulus gradation with distance from the lacunar wall was compared for labeled (i.e., bone forming) and non-labeled lacunae in both young and aged mice. All mapped lacunae showed sub-microscale modulus gradation, with peak modulus values 200-400 nm from the lacunar wall. Perilacunar modulus gradations depended on the recency of osteocyte bone formation (i.e., the presence of labels). For both ages, 2d-labeled perilacunar bone had lower peak and bulk modulus compared to non-labeled perilacunar bone. Lacunar length reduced with age, but lacunar shape and size were not strong predictors of modulus gradation. Our findings demonstrate for the first time that osteocyte perilacunar remodeling impacts bone tissue modulus, one contributor to bone quality. Given the immense scale of the LCS, differences in perilacunar modulus resulting from osteocyte remodeling activity may affect the quality of a substantial amount of bone tissue.

4.1 Introduction

Osteocytes, the most common cells in bone, live in a dense interconnected network of micrometer-scale voids in mineralized bone tissue (lacunae) connected by sub-micrometer-radius channels (canaliculi) [238,251,252,274,426,476,477]. The lacunar-canalicular system (LCS) has an estimated 215 m^2 surface area in the human skeleton [252] and its trillions of connections allow for osteocytes to communicate within the skeletal network as well as to the kidneys, parathyroid, vasculature, and muscle [251,478,479]. Osteocytes can modulate the size of the LCS through either resorbing bone [257,260,261,480,481] or replacing new osteoid [237,263,264,266,272–274,480,482] in a process termed LCS remodeling. This process contributes to systemic calcium homeostasis, as demonstrated by expanding lacunae and canaliculi in lactation and recovery after weaning [237,480,483]. It is not yet understood if LCS remodeling also contributes to the maintenance of bone quality. This question is of importance because LCS geometries truncate in aging [298,302,334,482,484–489], which suggests that aging alters LCS remodeling activity.

Prior work suggests that LCS remodeling has the potential to reduce bone quality. In DMP1 – conditional TGFβ receptor deletion [490] and global knockout of MMP13 [287], both phenotypes demonstrate reduced LCS remodeling activity together with reduced notched fracture toughness. However, it is not clear why bone with less LCS remodeling has lower bone fracture resistance. It is possible that morphological changes to the LCS affect the tendencies of cracks to initiate and propagate. On the other hand, LCS remodeling could directly benefit bone quality. Improvements in bone quality with LCS remodeling could result from a decrease in tissue maturity (e.g., decreased mineralization and modulus) in the vicinity of lacunae and canaliculi, since overly mature tissue is less able to engage intrinsic toughening mechanisms such as

fibrillar sliding [239,491]. However, it has not been evaluated whether bone material properties near the LCS are influenced by the remodeling activity of the osteocyte.

It is possible to evaluate bone modulus gradations near bone-forming and non-bone-forming osteocytes by using fluorochrome labeling and high-resolution material property mapping. Fluorochrome labels are small enough to travel through the LCS and are observed to label lacunae [492–499]. While they may also label canaliculi, most confocal techniques lack the appropriate resolution to discern these smaller features. Bone quality adjacent to lacunae has usually been evaluated with conventional microscale-resolution bone quality characterization tools (i.e., Raman spectroscopy, nanoindentation, quantitative backscattered scanning electron microscopy), but these techniques fail to identify material property variation near lacunae outside of extreme phenotypes [231–239]. The lack of detection of material property variation near lacunae is likely a reflection of the limited resolution of these tools, since line profiles collected through synchrotron-based techniques with nanoscale resolution demonstrates mass gradation near lacunae and canaliculi on the scale of hundreds of nanometers away from LCS walls [274,319]. To date, perilacunar bone modulus has been mapped with AFM [238] but the spatial gradation of modulus has not been quantified. Furthermore, the gradation in perilacunar bone modulus has not been compared for bone-forming and non-bone-forming osteocytes and has not been compared for young and aged bone.

Atomic force microscopy (AFM) is well-suited for mapping bone modulus near bone-forming and non-bone-forming osteocytes. AFM can quantitatively assess modulus on the order of 10s of nanometers using fast force mapping techniques. AFM has been used to demonstrate that modulus is heterogeneous near lacunae and canaliculi in 4-month female Wistar rats,

although this study did not identify whether characteristic modulus gradients exist with respect to distance from the LCS, nor whether these gradients depend on osteocyte bone formation or aging [238]. Several challenges exist in analyzing 2D perilacunar modulus maps, including reliably defining and smoothing the lacunar edge for a variety of lacunar shapes and sizes, sequentially expanding the lacunar edge by a given step size to create analysis regions (e.g., pixels with set range of distances from the lacunar wall), and determining appropriate step sizes for resolving modulus gradation with distance from the lacunar wall. Thus, we first sought to generate an analytic approach to analyzing 2D perilacunar modulus maps for the purpose of characterizing modulus gradation and comparing these gradations between bone-forming and non-bone-forming osteocytes at two ages.

The purposes of this study were to (1) develop an approach to analyze AFM-generated modulus maps of perilacunar bone for 2D spatial gradation, (2) determine whether labeled lacunae have different perilacunar modulus gradation than non-labeled lacunae, and (3) estimate whether aging impacts perilacunar modulus gradation. To investigate our research question, we utilized skeletally-mature young adult (5 mo) and early-old-age (22 mo) female C57Bl/6 mice, since this mouse model and age range produce marked changes in LCS morphology [263]. We hypothesized that lacunae would demonstrate modulus gradation in agreement with mass gradation reported with high-resolution techniques, that labeled lacunae would have lower moduli than non-labeled lacunae, and that aging would decrease the size of the region of lower-modulus bone near lacunae.

4.2 Materials and Methods

4.2.1 Animal Models

This investigation was conducted in two studies. The first study, in which methods were developed for AFM perilacunar bone modulus analysis, a 7-month-old female C57Bl/6 mouse was obtained from a live animal colony (group housed, 3 mice per cage, standard rodent chow and water provided *ad libitum*) at Montana State University. This mouse was euthanized via CO_2 inhalation. The second study, which evaluated the effects of age and label on perilacunar modulus gradation, included 5-month (n = 5) and 22-month-old (n = 5) female C57Bl/6 mice from Charles River Laboratory. These mice were administered calcein (20 mg/kg) and alizarin (30 mg/kg) labels *via* intraperitoneal injection 8d and 2d before euthanasia, respectively. An additional n = 3 mice per age were studied with label order reversed (e.g., alizarin administered at 8d, calcein administered at 2d). Mice were group housed (2-5 per cage), fed low fat diet (Research Diets D12450H; 10% kcal from fat) *ad libitum* for 8 weeks prior to euthanasia as controls for another study, provided water *ad libitum*, and euthanized via isoflurane inhalation. All animal procedures were approved by the Montana State University Institutional Animal Care and Use Committee.

4.2.2 Sample Preparation

Left femurs were harvested and fresh frozen at -20° C immediately after euthanasia. Femurs were gently thawed and tested to failure in three-point bending (results reported in a separate study). The distal halves of the femurs were histologically dehydrated in a graded ethanol series and embedded in poly(methyl) methacrylate (PMMA). Embedded distal femurs were sectioned at the midshaft using a low-speed diamond saw (Isomet, Buehler, Lake Bluff, IL),

to obtain a transverse section with a 5 mm thickness. Then, cortical surfaces were polished with 600 and 1200 grits of wet silicon carbide papers (Buehler, Lake Bluff, IL), followed by fine polishing with Rayon fine clothes and different grades of alumina pastes (9, 5, 3, 1, 0.5, 0.3, and 0.05 μm) to achieve a mirror-like finish. Between polishing steps, sections were sonicated in tap water to remove any remaining particles. Embedded femur sections were mounted on a metal disk using epoxy (MasterBond EP29, Hackensack, NJ). A glass slide of the same 5 mm height was mounted next to the embedded femur section to be used for tip radius calibration.

An additional femur from a C57Bl/6 female 5-month old mouse was harvested for a preliminary comparison of the effects of bone tissue hydration on perilacunar bone modulus. This mouse also received fluorochrome bone labels at 8d and 2d before euthanasia. The femur was not subjected to mechanical testing. The femur was air dried after tissue harvest, embedded in non-infiltrating epoxy (Buehler Epoxicure 2) and sectioned and polished consistent with the methods described for the PMMA-embedded specimens. The femur was never exposed to ethanol. The sample was rehydrated via immersion in tap water 10 minutes before AFM testing. The sample surface was wicked dry with a KimWipe before AFM testing.

4.2.3 AFM Mapping

Atomic force microscopy (AFM) analyses were performed with an Asylum Research Cypher S force microscopy system with an etched silicon tip (RTESPA-525, 200 N/m spring constant, Bruker AFM Probes, Camarillo, CA). AFM was operated in two different modes: AC tapping mode (for topography scans) and fast force mapping (for modulus maps). Using AC tapping mode, the cantilever was driven at a constant amplitude at its resonance frequency and scanned across the surface to measure topography of the bone samples and to locate lacunae.

Fast force mapping generated an array of local force-distance curves, obtained at high speed with nanometer spatial resolution and was used to characterize modulus profiles around lacunae. Tip parameters were calibrated and resulting force curves were fit to a Hertzian contact model to calculate the contact modulus of the material (**Figure B5**) [500]. First, calibration of a cantilever spring constant was obtained *via* thermal tune. Next, a force-distance curve was performed on a silicon wafer (Silicon inc., Boise, ID) to calculate optical lever sensitivity. Once these values were obtained, tip radius was calibrated by first acquiring a fast force map (320 x 320-pixel map) of a glass surface with known modulus (72 GPa, Fisherbrand, Pittsburgh, PA) then identifying the tip radius value needed to generate agreement of the Hertz model with the glass calibration surface.

For each bone, lacunae were randomly selected from the anterior side of the midshaft cortical cross-section. Selected lacunae were at least >20 μm away from bone endocortical and periosteal surfaces. A topographical lacunar map was first generated using AC mode, then fast force mapping generated a 512 x 512-pixel (12 x 12 μm map size at scan rate of 300 Hz) of lacuna with a ~ 20 nm resolution. A threshold of 500 nN was found to provide sufficient signal to noise ratio in the force curves and good agreement with the Hertzian contact models. While force curves represent an intermittent contact, rather than continuous contact technique, measurements of modulus must still account for potential tip wear. Tip radius was calibrated both before and after every fast force map of bone tissue was obtained, and the mean value of tip radius input into the Hertz model for modulus calculations. Tip radii were kept between 10 nm (pristine) and 20 nm at the start of the scan, as these values are consistent with typical tip wear in literature and are smaller than the resolution of acquired modulus maps [501,502]. The average change in tip radius

was 1.06 nm per full scan, corresponding to approximately 5% drift in modulus for all samples. For reliability, we considered larger values of tip radius (i.e., > 20 nm) to violate the desired resolution and to have the potential for tip fracture or contamination and thus associated data were not considered. In our MATLAB-based segmenting and thresholding procedure, we excluded measurements <5 GPa since these values would be indistinguishable from PMMA, and a very small number of measurements >90 GPa as these values are most likely a result of indenting alumina beads embedded in the sample during polishing.

Six additional lacunae were mapped for a semi-hydrated femur to estimate the effects of hydration on perilacunar modulus gradation. These lacunae were also located in the anterior quadrant, at least 30 μm away from periosteal or endocortical surfaces. AFM maps were obtained and analyzed as described for PMMA-embedded sections, with the exception that moduli values <5 GPa were not excluded, since there was not a plastic phase within the mapped area. AFM indentation extension curves did not show evidence of snap-on and thus the Hertz model was used for modulus calculations (**Figure B5**).

4.2.4 Importing Data and Identifying the Lacunar Edge

Initially, square maps (equal number of x and y pixels) are imported to MATLAB as .csv files (**Figure 4.1a**). The lacunar edge is defined for each map and points within the lacuna are masked out. Because dendrites extend from the lacunar wall, erosion is necessary to define a close-fitting lacunar edge. Erosion is performed based on a diamond-shaped element with size specified by the user (i.e., larger elements yield more aggressive erosion). The results of this step are shown in **Figure B1**. This step creates an array of points that describes the lacunar boundary. This process is repeated to create an over-eroded boundary. This over-eroded boundary will be

utilized later in the code to create sequential boundaries. An over-eroded boundary is required due to an inherent dilation when using a smoothing function later in the code.

4.2.5 Map and Edge Rotation

Next, maps are rotated about the lacunar centroid so that the ellipsoidal long axis of the lacuna is vertical. This step reduces distortion of sequential boundaries during dilation steps later in the code.

4.2.6 Creation of Sequential Boundaries

The lacunar edge boundary created from the over-erosion step will be used to create sequential boundaries (e.g., separated by a specified distance) surrounding the lacuna. User inputs include the number of desired dilations (e.g., number of sequential regions of interest with increasing distance from the lacunar wall), the distance between each boundary, and the map dimensions. The results of this step are 'unsmoothed' boundaries, as shown in **Figure 4.1b**.

4.2.7 Smoothing of Sequential Boundaries

The sequential boundaries are then smoothed via a convolution matrix [503]. This achieves a boundary that closely matches lacunar geometry but removes more harsh edges and features that need not be considered. However, this step inherently dilates the lacunar edge somewhat, hence over-erosion is necessary in pre-processing. The results of the smoothing are shown in **Figure 4.1c**.

4.2.8 Binning and Analyzing Points Between Concentric Boundaries

Next, points within each two sequential boundaries are binned (**Figure 4.1d**). The x-y position of each pixel is matched with a corresponding modulus. Lastly, a histogram is created

for each region using a range of 1 GPa for histogram bin sizes (for example, if the range of the points within a certain region is 5.7 to 34.2 GPa there would be a bin for 5-6, 6-7, etc. up to 34-35) (**Figure 4.1e**). Several statistical measurements are made for each concentric region, including mean, median, standard deviation, range, and full width at half maximum.

4.2.9 Analysis of Modulus Versus Distance from the Lacunar Wall

Using measures calculated from histograms, modulus versus distance profiles were generated (**Figure 4.1f**). From these profiles, measures included the peak modulus (greatest mean modulus of all concentric regions versus distance from the lacunar wall), the bulk modulus (the mean modulus of the last concentric ring, 1.8-2 μm), the difference between the peak and bulk measures, the edge-to-peak and peak-to-bulk slopes (GPa/μm), and perilacunar area before peak modulus. Additionally, slopes were also calculated after normalizing to the peak modulus of a given map. Peak to bulk difference and slopes were also calculated for standard deviations.

4.2.10 Confocal Laser Scanning Microscopy Imaging

Samples were imaged using an upright confocal microscope (Leica SP3,) with the following parameters: 40x water immersion lens, laser wavelength excitation of 488 nm (emission length 502-540) for calcein labels and 561 and 633 nm (emission length 580-645) for alizarin labels, pinhole set at 1 Airy unit, 1024 × 1024 resolution with a 600 Hz speed, and laser intensity set at 50% of the full power. The gain and offset were chosen such that in the images acquired the lacunae and their perilacunar remodeling were visible with minimum amount of noise. Z-stacks of images were acquired from the surface through the maximum depth where signal was observable, approximately 30 μm. The spacing between each slice was 0.8 μm. A

composite image was formed by overlaying all slices (Imaris 9.3). Determination of whether a lacuna was labeled or not was made by evaluating composite images and then, in the case of potential non-labeled lacunae, checking each slice to confirm. All lacunae included in the study analysis (i.e., mapped with AFM and determined to be labeled or not labeled) were observable on the surface.

4.2.11 Data Analysis

Mixed-model ANOVA evaluated the impact of the fixed effects of label (labeled vs no label) and age (5 vs 22 mo) and the random effect of individual mouse on measures pertaining to modulus variation near lacunae (e.g., peak modulus, bulk modulus, etc). Residuals for all models were checked for normality and equal variance. The dependent variable was natural log transformed, if necessary, to satisfy these assumptions. Significance was defined *a priori* as $p < 0.05$. In the case of a significant interaction between age and label, post-hoc tests were adjusted for family-wise error with the Bonferroni procedure (i.e., 2 comparisons: label vs non-labeled at each age; critical α adjusted to $p < 0.025$). All analyses were performed using Minitab v.19.

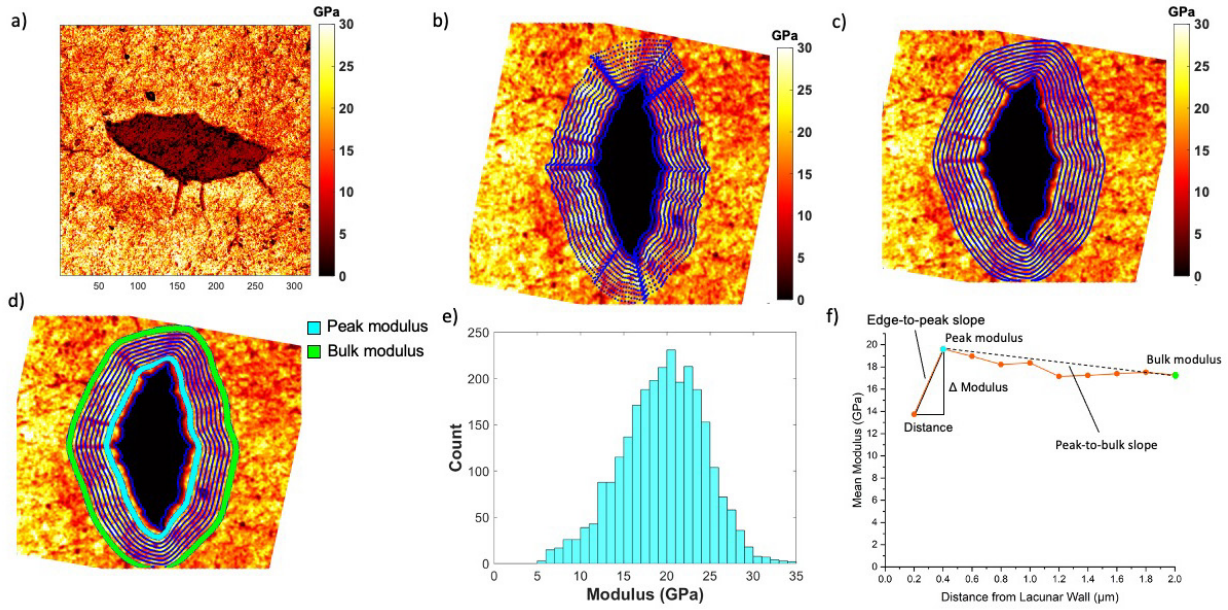

Figure 4.1. a) An AFM modulus map for osteocyte perilacunar bone tissue. b) Raw modulus maps are processed through masking, rotation, and dilation steps. Sequential concentric rings are assigned for analysis. In this image, concentric rings are distanced by 0.2 μm. c) A convolution operation smooths boundaries to identify the lacunar wall. d-e) All pixels for an individual concentric ring, such as shown in cyan, are used to construct a histogram (bin size 1 GPa) of moduli. f) The modulus versus distance gradation profile corresponding to mean modulus values found within sequential concentric ring regions (cyan indicating the region that contains the peak mean modulus, green indicating the region that contains the bulk mean modulus value).

4.3 Results

We first developed AFM mapping and analysis techniques in order to determine whether perilacunar modulus demonstrates gradation with respect to distance from the lacunar wall and at what resolution this gradation is apparent. We then used these mapping and analysis parameters to investigate the influence of osteocyte bone formation activity on perilacunar modulus in skeletally-mature (5 mo) and early-old-age (22 mo) female C57Bl/6 mice.

4.3.1 Perilacunar Bone Tissue Has Sub-Micrometer-Scale Modulus Gradation

Atomic force microscopy fast force mapping demonstrates that bone modulus has sub-micrometer-scale gradation adjacent to osteocyte lacunae in cortical bone of the murine femur (**Figure 4.1a**). To assess the effect of distance from the lacunar wall on modulus, we initially obtained eight maps from one 7-month female C57Bl/6 mouse. For each map, we binned pixels within regions of three different step sizes, 0.2, 0.5, and 1μm, extending outward to 2 μm from the lacunar wall. The smallest step size, 0.2 μm, was selected because this distance is greater than the smallest lacunar spatial features but does not reduce the number of pixels per ring to such a low level as to impede interpretation of histograms. Further, gradations in mass density from synchrotron line profiles occur at a similar length scale [319]. We also studied 0.5 μm and 1 μm step sizes (i.e., averaging over all pixel modulus values within concentric rings of this width), since these resolutions are close to those of other common bone quality measurement techniques (e.g., Raman spectroscopy, backscattered scanning electron microscopy, nanoindentation). At each distance, a mean and a standard deviation were calculated from a histogram of all pixels within the region (**Figure 4.1**).

Analysis of all maps at each of the three step sizes demonstrates that step size influences the ability to discern modulus gradation (**Figure 4.2a**). At a step size of 0.2 μm, the modulus rose to a peak at 0.2-0.4 μm from the lacunar wall and then declined towards a bulk bone (i.e., 2 μm from the lacunar wall). These gradations were apparent in both raw data and data normalized to a peak value per lacunar map. The larger step sizes of 0.5 μm and 1 μm failed to capture the rise to a peak and decline to bulk seen in mean modulus values when using a finer 0.2 μm step size (**Figure 4.2a**). Standard deviation was also evaluated at each step size. Using a 0.2 μm step size,

standard deviation was found to be greatest close to the lacunar wall and declined within 0.4-0.6 µm to stable values (**Figure 4.2b**). However, standard deviation was less sensitive to step size. All three step sizes detected a decrease in standard deviation with distance from the lacunar wall, although the resolution of this effect improves with finer step size. Modulus versus distance profiles for all eight lacunae mapped in this first study are shown in **Figure 4.3** and **Figure 4.4**.

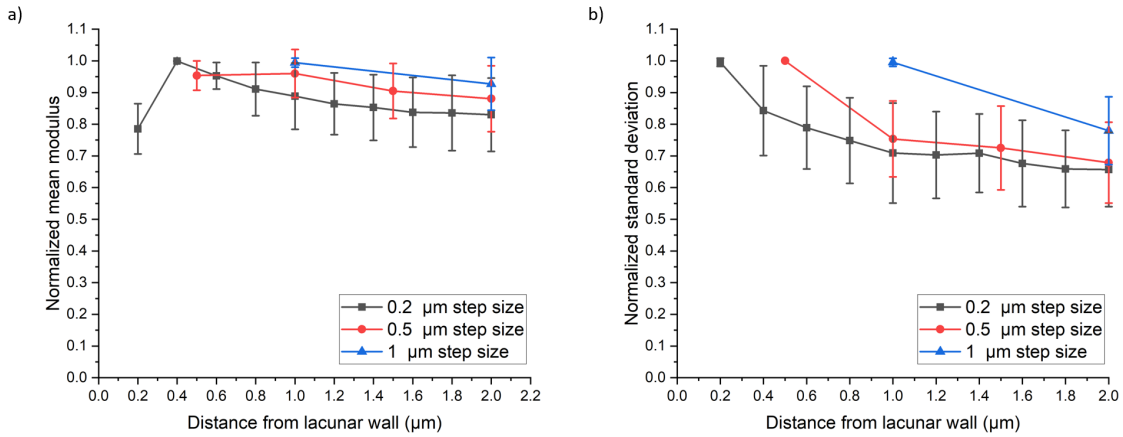

Figure 4.2. a) Normalized mean moduli versus distance from the lacunar wall is plotted with data from 0.2, 0.5, and 1 µm step sizes extending to 2 µm from the lacunar edge. The distance from the lacunar wall indicates the outer distance of a bin (e.g., 0.4 µm means 0.2 – 0.4 µm). Error bars represent one standard deviation. b) Normalized standard deviations versus distance from the lacunar wall is plotted with data from 0.2, 0.5, and 1 µm step sizes extending to 2 µm from the lacunar edge. Error bars represent one standard deviation. Plots created from eight AFM maps obtained from lacunae from one 7-month female C57Bl/6 mouse.

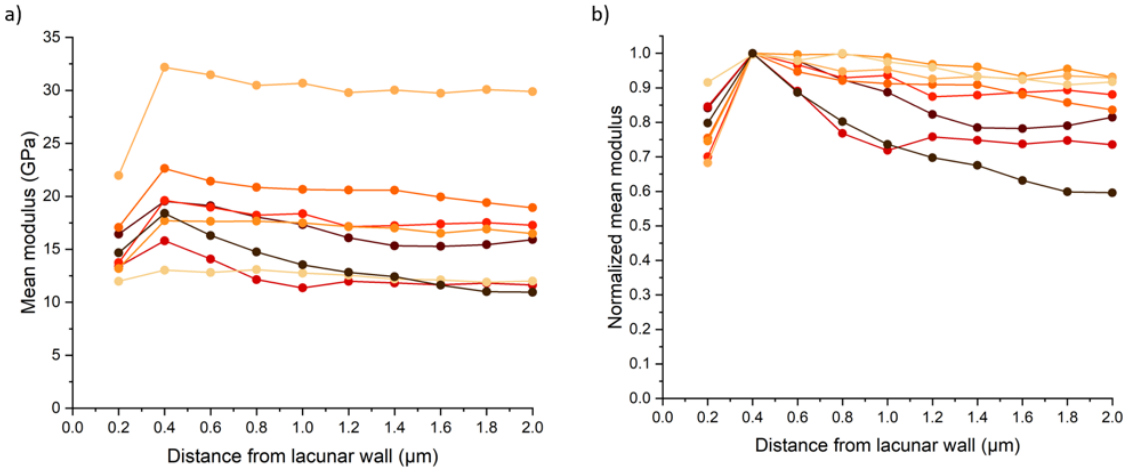

Figure 4.3. a) Mean modulus for each concentric ring plotted against distance from the lacunar wall. The distance from the lacunar wall indicates the outer distance of a bin (e.g., 0.4 μm indicates the 0.2 – 0.4 μm bin). Connected dots each represent individual osteocyte lacuna map. b) Normalized mean modulus for each concentric ring plotted against distance from the lacunar wall. Mean modulus values were normalized against the peak mean modulus value for a given map. Plots created from eight AFM maps obtained from lacunae from one 7-month female C57Bl/6 mouse.

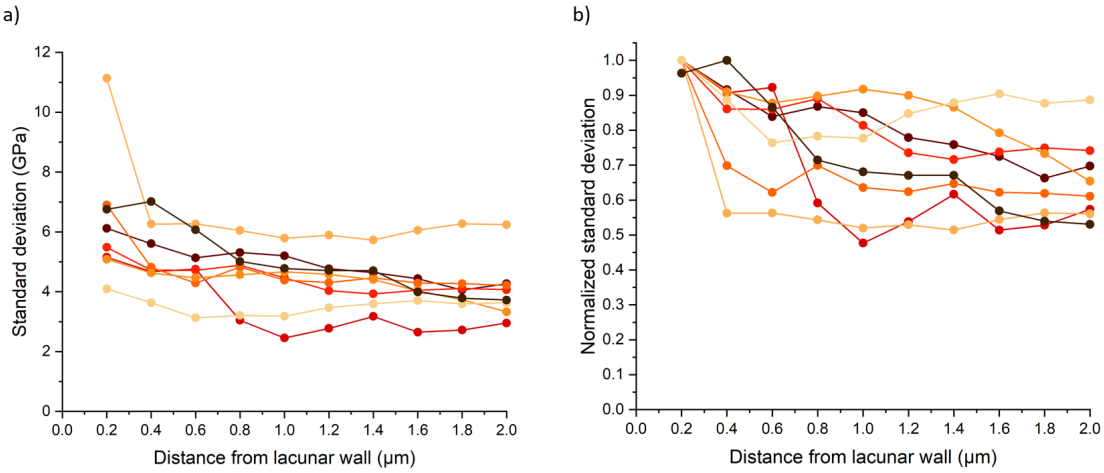

Figure 4.4. a) Mean standard deviation for each concentric ring plotted against distance from the lacunar wall. The distance from the lacunar wall indicates the outer distance of a bin (e.g., 0.4 μm means 0.2 – 0.4 μm). Connected dots each represent individual osteocyte lacuna map. b) Normalized standard deviations for each concentric ring plotted against distance from the lacunar wall. Standard deviation values were normalized against the peak standard deviation value for a given map. Plots created from eight AFM maps obtained from lacunae from one 7-month female C57Bl/6 mouse.

4.3.2 Bone-forming Osteocytes Have Distinct Perilacunar Modulus Gradation Compared with Non-Bone-Forming Osteocytes

We first utilized confocal laser scanning microscopy (CLSM) to investigate whether labels administered 2 days and 8 days before euthanasia would be observed for 5 mo- and 22 mo-old mice. Calcein and alizarin labels were both abundantly observed for both ages of mice when administered 2 days before euthanasia (**Figure B2**). By contrast, labels from calcein or alizarin administered at 8 days before euthanasia were infrequently observed, precluding comparison of perilacunar properties from different labeling dates. While future work would benefit from a closer labeling interval, our findings nonetheless suggest that osteocytes frequently deposit new osteoid and that this bone tissue undergoes frequent turnover.

We then evaluated whether osteocyte remodeling affects perilacunar bone tissue modulus gradation (Figure 4.5 and Figure 4.6). Of the lacunae randomly selected for AFM mapping, 60% were labeled with alizarin (administered 2 days before euthanasia) for both 5 mo and 22 mo mice (5 lacunae / mouse, 5 mice / age, N = 50 lacunae). None of the mapped lacunae were labeled with calcein (administered 8 days before euthanasia). Mixed model ANOVA showed that labeled lacunae had lower peak modulus (-11.72%, $p < 0.05$) and bulk modulus (-10.06%, $p < 0.05$, **Table 4.1**). There were no interactions between label and age for these measures. Of note, several labeled lacunae had much greater distance to the peak mean modulus. However, on average, the distance to peak mean did not differ between labeled and non-labeled lacunae. Labeled lacunae also had decreased peak standard deviation (-11.06%, $p < 0.05$) and bulk standard deviation (-12.61%, $p < 0.05$).

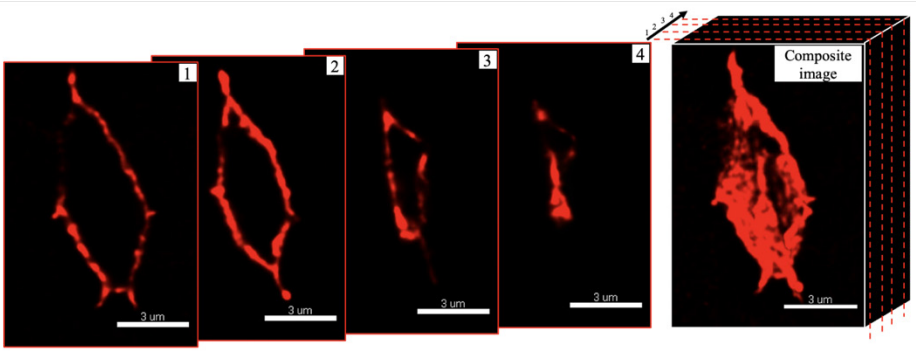

Figure 4.5. Representative labeled lacuna from confocal microscopy. The composite image was generated from overlaying all slices for the Z-stack. Image 1 demonstrates labeling near the lacuna surface, while slices 2-4 show the progression of labeling with depth.

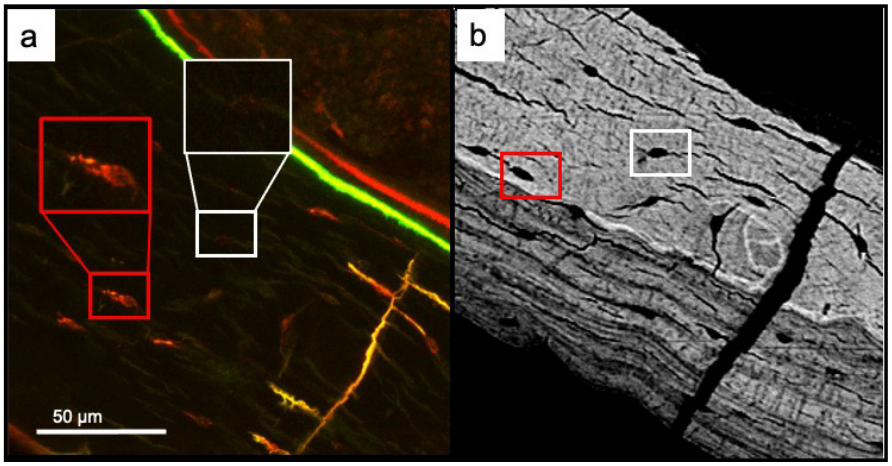

Figure 4.6. Remodeling osteocytes (red box: alizarin labeled lacuna) versus non-remodeling osteocytes (white box: non-labeled lacuna) imaged with a) confocal laser microscopy (63x-water immersion objective) and b) scanning electron microscopy (carbon coated surface, BSE mode, 15 kV, 400x). The CLSM image is a composite of a Z-stack of images, demonstrating that non-labeled lacunae were not labeled on another slice away from the surface.

The presence of fluorochrome labels did not significantly affect other measures of modulus gradation, including slope of the lacunar edge to peak modulus and the slope from the peak modulus to bulk modulus (**Table 4.1**). Measures of lacuna size, including area, minor and major axis length, and sphericity (minor / major axes) were not different between labeled and non-labeled lacunae. Additionally, there were no significant interactions with labels and aging for these measures.

4.3.3 Age Affects Some Aspects of Lacunar Size and Perilacunar Modulus Gradation

The lacunar major axis was smaller for 22 mo compared with 5 mo mice (-11.93%, $p < 0.05$), although area and minor axes where not changed (we note that major and minor axis lengths were determined through obtaining an elliptical fit for each lacunae, while area was determined through the number of pixels thresholded out by the MATLAB image processing code). The mean slope peak-to-bulk was significantly impacted by age; 22 mo mice showed a more gradual decrease in mean modulus from peak mean to bulk bone mean (-30.05%, $p < 0.05$, **Table 4.1**). There was a significant interaction between age and label for the bulk standard deviation normalized to the peak ($p < 0.05$). This measure evaluates the difference in heterogeneity of bulk bone compared to near the lacunar edge (typically where the maximum standard deviation occurs). This interaction is driven by increased normalized standard deviation for labeled compared with non-labeled lacunae for young mice. However, the p-value (+13.35%, $p = 0.040$) is not small enough to be considered a significant difference given our Bonferroni correction for family-wise error. Importantly, several measures (e.g., lacunar sphericity, $p = 0.081$; modulus slope from edge:peak, $p = 0.070$) had the potential to be underpowered for the effect of age given our small sample size of $n = 5$ mice / age.

4.3.4 Lacunar Size and Shape Do Not Strongly Correlate with Perilacunar Modulus Gradation

Lacunar size and shape change in aging and are commonly studied with a variety of imaging techniques (e.g., CLSM, high-resolution computed tomography). Therefore, it would be useful to understand whether lacunar morphology can be used as an indication of perilacunar bone quality. We evaluated the strength of relationships between lacunar size and measures of

modulus gradation (**Table B1**). The strongest Pearson correlation was lacuna major axis length vs. mean normalized edge:peak modulus, with r = -0.427. These results demonstrate that lacunar geometry is overall not a strong indicator of measures related to perilacunar modulus gradation.

4.3.5 Bone Tissue Hydration Impacts Some Aspects of Perilacunar Modulus Gradation

Because dehydration and embedding stiffen bone tissue [243–245], we sought to estimate the impacts of PMMA-embedding on perilacunar modulus gradation. Six lacunae were mapped at the anterior quadrant of a transverse section of polished, semi-hydrated cortical femur from a 5 month old C57Bl/6 female mouse. Semi-hydrated bone had lower moduli than for PMMA-embedded bone, as expected [362]. An initial rise in modulus from the lacunar wall for the first several hundred nanometers was observed. Modulus versus distance curves normalized to peak values per lacuna demonstrate that the slope of this gradation was similar for PMMA-embedded and semi-hydrated specimens (**Figures B3** and **B4**). The peak modulus for semi-hydrated bone is less distinct than for PMMA-embedded bone and occurs at a greater distance from the lacunar wall (**Figure B4**).

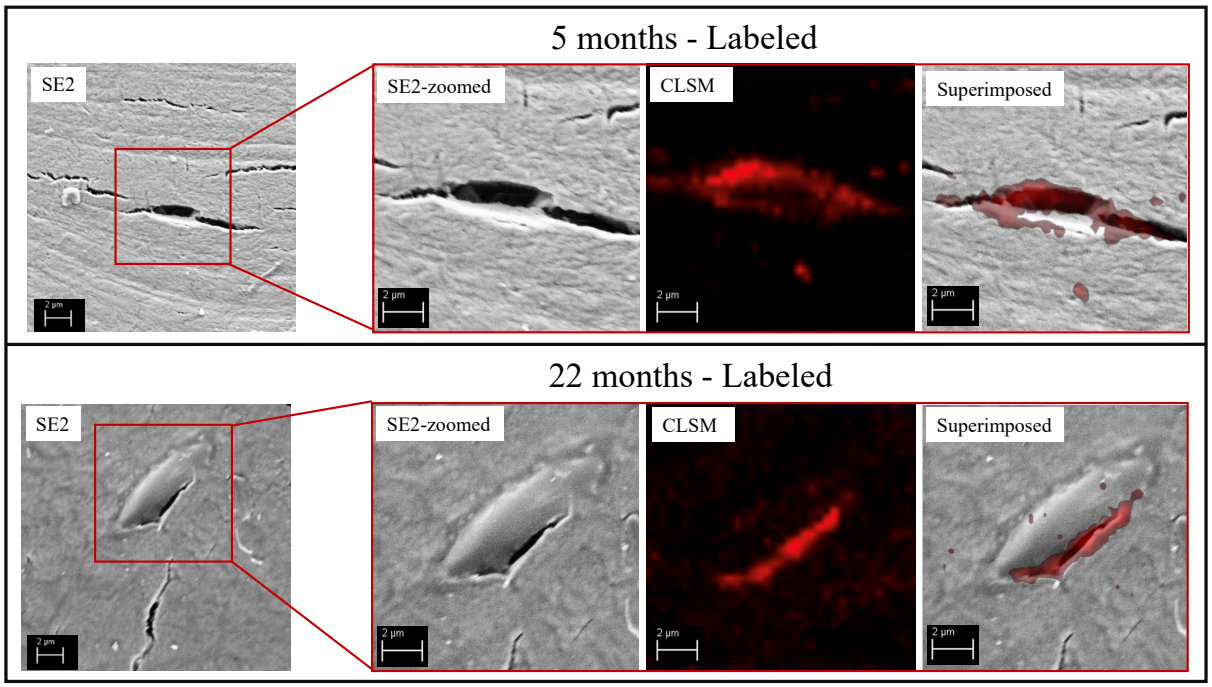

Figure 4.7. Superimposition of CLSM images with secondary mode images from FESEM. The FESEM images were collected at 8-10kx, 4 kV, 9.1 mm working distance).

Table 4.1. Measurements of lacunar morphological and modulus properties for 5 mo and 22 mo mice for bone-forming and non-bone-forming lacunae: Data are presented as marginal mean (adjusted for age and label) ± standard error from mixed-model ANOVA. Bolded text indicates a statistically significant measure ($p < 0.05$). Non-significant p-values are noted for $p \leq 0.10$.

Measure	**5 months**		**22 months**	
	Non-labeled n = 5 mice 5 lacunae / mouse	**Labeled** n = 5 mice 5 lacunae / mouse	**Non-labeled** n = 5 mice 5 lacunae / mouse	**Labeled** n = 5 mice 5 lacunae / mouse
Lacuna cross-sectional area (μm^2) Age: NS Label: NS Age x Label: NS	15.18 ± 1.38	16.05 ± 1.20	14.27 ± 1.40	13.10 ± 1.21
Lacuna major axis length (µm) **Age: p = 0.032** Label: NS Age x Label: NS	10.31 ± 0.53	10.62 ± 0.43	9.13 ± 0.53	9.30 ± 0.43
Lacuna minor axis length (µm) Age: NS Label: NS Age x Label: NS	3.72 ± 0.24	3.95 ± 0.19	4.07 ± 0.24	3.55 ± 0.19
Lacuna sphericity Age: p = 0.081 Label: NS Age x Label: p = 0.092	0.361 ± 0.028	0.385 ± 0.023	0.452 ± 0.028	0.386 ± 0.023
Peak mean modulus (GPa) Age: NS **Label: p = 0.014** Age x Label: NS	38.20 ± 3.38	32.78 ± 3.23	31.39 ± 3.40	28.66 ± 3.24
Area before peak mean modulus (data inversely transformed, μm^{-2}) Age: NS Label: NS Age x Label: NS	0.115 ± 0.013	0.094 ± 0.011	0.105 ± 0.013	0.100 ± 0.011
Bulk mean modulus (GPa) Age: NS **Label: p = 0.031** Age x Label: NS	34.04 ± 3.19	30.21 ± 3.07	28.80 ± 3.21	26.30 ± 3.08
Area before peak standard deviation of modulus (data inversely transformed, μm^{-2}) Age: NS Label: NS Age x Label: NS	0.230 ± 0.023	0.214 ± 0.019	0.248 ± 0.023	0.0228 ± 0.019
Δ Modulus (peak-bulk) (GPa) Age: NS Label: p = 0.10	4.06 ± 0.63	2.65 ± 0.54	2.68 ± 0.64	2.30 ± 0.55

Age x Label: NS				
Normalized modulus bulk:peak Age: NS Label: p = 0.08 Age x Label: NS	0.88 ± 0.02	0.92 ± 0.01	0.91 ± 0.02	0.92 ± 0.01
Modulus slope, peak to bulk (GPa/µm) **Age: p = 0.036** Label : NS Age x Label: NS	-2.54 ± 0.36	-2.22 ± 0.30	-1.82 ± 0.36	-1.52 ± 0.30
Normalized modulus edge:peak Age: NS Label: NS Age x Label: NS	0.68 ± 0.03	0.72 ± 0.03	0.75 ±0.03	0.73 ± 0.03
Modulus slope, edge to peak (GPa/µm) Age: 0.070 Label: NS Age x Label: NS	50.55 ± 6.97	34.01 ± 6.00	25.94 ± 7.06	28.16 ± 6.05
Peak standard deviation of modulus (GPa) Age: NS **Label: p = 0.032** Age x Label: NS	14.68 ± 1.46	12.27 ± 1.40	11.40 ± 1.47	10.93 ± 1.41
Bulk standard deviation of modulus (GPa) Age: NS **Label: p = 0.010** Age x Label: NS	10.42 ± 1.06	9.00 ± 1.02	8.49 ± 1.06	7.53 ± 1.02
Δ Standard deviation of modulus (peak-bulk) (GPa) Age: NS Label: NS Age x Label: p = 0.070	4.26 ± 0.90	3.27 ± 0.85	2.90 ± 0.91	3.41 ± 0.86
Normalized standard deviation of modulus, bulk:peak Age: NS Label: NS **Age x Label: p = 0.014**	0.67 ± 0.05	0.76 ± 0.04	0.77 ± 0.05	0.70 ± 0.04
Standard deviation of modulus slope, peak to bulk (GPa/µm) Age: NS Label: NS Age x Label: NS	-2.39 ± 0.49	-1.82 ± 0.46	-1.61 ± 0.49	-2.02 ± 0.46

4.4 Discussion

The osteocyte lacunar-canalicular system (LCS) is an important contributor to systemic mineral homeostasis. Osteocytes can remove and replace bone mineral around the expansive LCS surface. However, significant questions remain about the impact of LCS remodeling on the quality of bone tissue surrounding this network. Aging truncates LCS morphologies [263,284,298,482,504] and increases the prevalence of osteocyte apoptosis and senescence [299–302]. Therefore, we were motivated to investigate whether osteocyte perilacunar bone modulus gradation, one aspect of bone quality, differs between bone-forming and non-bone-forming osteocytes, and to estimate the impact of aging on these characteristics. We utilized confocal laser scanning microscopy and atomic force microscopy to evaluate gradations in perilacunar bone modulus around bone-forming and non-bone forming cortical femur osteocytes for skeletally mature young adult (5 mo) and early-old-age (22 mo) C57Bl/6 females.

Because synchrotron radiation studies show graded bone mineralization within hundreds of nanometers near lacunar and canalicular surfaces [274,319,426,430–432], our first task was to determine the resolution at which we could resolve gradation in perilacunar moduli. We used AFM to map modulus for 12 μm x 12 μm areas surrounding lacunae (512 x 512 points, ~ 20 nm resolution, ~5 nm indentation depth) and developed an analysis procedure to assess mean modulus at distance increments from the lacunar wall. Using the same maps from an initial set of osteocyte scans from an adult female C57Bl/6 mouse, we investigated modulus gradation from the lacunar wall at 0.2 - 1 μm step sizes outwards to 2 μm from lacunae (**Figure 4.3**). Our data indicate that at 0.2 μm resolution, an increase in modulus to a peak value is apparent, usually within 0.2 – 0.4 μm from the lacunar wall. At either 0.5 or 1 μm step size, these peak values are

not resolved. However, decrease in bone tissue variability with distance from the lacunar wall was resolved at all three step sizes (**Figure 4.2b**). Importantly, our results indicate that many common microscale-resolution bone quality assessment techniques (e.g., instrumented nanoindentation, Raman spectroscopy, quantitative backscattered SEM) may not have adequate resolution to observe gradation in perilacunar bone quality. This is consistent with prior work, where bone material is often observed to not vary at the microscale surrounding lacunae, outside of circumstances with large perturbations to mineral homeostasis [231,233,238,275,295,322,415].

A persistent challenge in osteocyte research is in relating the behavior of individual osteocytes with the impacts to the surrounding bone tissue material. This connection remains elusive, in part because the fixation and decalcification steps necessary to assess parameters of osteocyte behavior (e.g., apoptosis, senescence) generally precludes the determination of bone material properties. In the present work, we introduce a strategy to evaluate the modulus of bone surrounding fluorochrome-labeled or unlabeled osteocyte lacunae. In several prior murine studies, genetic disruptions to LCS bone remodeling decrease the abundance of fluorochrome-labeled cortical lacunae [287,505]. Since these studies decreased osteocyte remodeling and also utilized similar label dosage and timing as our study, we posit that that labeled lacunae are likely an indicator of osteocyte bone formation. We also note that the percentage of labeled osteocytes estimated in our study is similar to the percentage of calcein-labeled lacunae (labels administered 2d before euthanasia) measured at the cortical femur for 28d C57Bl/6 mice in previous work by Kegelman and coauthors [505]. Interestingly, labeled lacunae were also abundant in 22-month-old mice in our study, suggesting that LCS remodeling is still quite active at the cortical femur in

early-old-age female mice. It is not yet known if perilacunar labeling frequency decreases with more advanced aging.

Our findings demonstrate that lacunae labeled with alizarin administered 2 days before euthanasia have distinct modulus gradations compared with non-labeled lacunae. Specifically, the peak and bulk moduli are lower for labeled lacunae. The RMSE surface roughness was very similar between maps generated for labeled (24.9 ± 5.9 nm) and non-labeled lacunae (23.7 ± 5.2 nm), demonstrating that the differences in perilacunar modulus with labeling are unlikely to be attributed to difference in topography between these groups. Labels extended hundreds of nanometers to ~ 1 μm in width beyond the lacunar wall (**Figure 4.7, Figure B6**). It is possible that the labeling itself alters the mineral properties of the bone [506], although it is not determined whether and how this would be expected to influence the bone modulus. Perilacunar modulus gradations were only moderately correlated with lacunar geometry. Thus, morphological techniques alone are not sufficient for assessing changes to perilacunar bone modulus.

The gradations in PMMA-embedded bone are excellent agreement with synchrotron studies that studied gradation in mineral near the LCS in dehydrated human [319] and dehydrated ovine bone [320]. Hesse and co-authors studied lacunae and canaliculi from human mandible and found that mass density increased from the LCS walls to a peak at about 0.2 μm. These peak values were followed by a decrease in mass density with further distance from the LCS walls [319]. In another study, Nango and colleagues assessed lacunae and canaliculi for wild-type and osteoporotic mice using a combination of synchrotron x-ray microscopy and transmission electron microscopy (TEM). The lowest mineralization was adjacent to the lacunar wall and increased with distance to either a peak or an asymptotic value [274]. The close correspondence

between our AFM modulus profiles from PMMA-embedded bone and variation in mass or mineral density at a similar length-scale suggests that our observed modulus gradation reflects variation in bone mineral.

Bone dehydration and embedding increase bone modulus [243–245]. Thus, we sought to estimate the impact of bone dehydration on bone modulus gradation. We completed a preliminary assessment of bone modulus gradation in semi-hydrated bone for six lacunae from the femur of one 5 month old C57Bl/6 female that had not been mechanically tested. The sample was considered semi-hydrated because the hydrated bone surface was wicked dry to avoid hydrodynamic interactions between the cantilever and a fluid layer. As expected, semi-hydrated bone tissue has lower modulus than PMMA-embedded bone. When normalized to the peak value per lacunae, it is apparent that the initial steep gradation in the first 400 nm from the lacunar wall is similar for semi-hydrated and PMMA-embedded samples (**Figure B4**). The PMMA-embedded samples show a clear peak modulus value after the initial rise in modulus and then a distinct taper to a bulk modulus value (**Figure B4**). By contrast, semi-hydrated bone does not produce a peak value after the initial rise in modulus. The differences in modulus profiles may relate to the decreased sensitivity of dehydrated bone modulus to properties of the organic matrix, such as collagen fibril orientation [244]. Mineral gradations near the lacunar edge in semi-hydrated bone appear to correspond to a dominant effect of change in mineralization on modulus, since these gradations are in good agreement with PMMA-embedded bone. However, in the more mineralized bone away farther from the lacunar wall, this variation in modulus is more likely to reflect variation in the properties and structure of the hydrated organic matrix. Thus, we posit that the relatively larger contribution of the organic matrix to the modulus in semi-hydrated bone

may influence the location and value of the peak modulus. The purpose of the semi-hydrated versus PMMA-embedded bone comparison was to estimate the effects of hydration on bone modulus gradation. A more extensive investigation would be required to interpret differences in the effects of labeling and aging on hydrated bone.

Perilacunar bone modulus gradation may be influenced by a combination of active and passive mineralization and demineralization processes. Some degree of passive mineral exchange may occur, since modulus is still graded, albeit differently, for unlabeled lacunae. Mineral exchange could be influenced by direct calcium exchange between bone local to the LCS and interstitial fluid [319]. As suggested by Hesse and co-authors, mass density gradients followed by a peak may indicate a diffusion limit for calcium ions from LCS into the extracellular matrix (ECM). The authors used the size of this zone of lower mass density to estimate the availability of rapidly-exchangeable calcium [319]. However, our finding that labeled lacunae have distinct modulus gradations suggests that mineralization and demineralization processes may have an active contribution from the living osteocyte. Furthermore, osteocytes from human mandible specimens with bisphosphonate-induced necrosis, which are more likely to be apoptotic, also had distinct perilacunar and pericanalicular mass gradation compared with healthy comparisons [319]. Thus, it is possible that contributions from active and passive mineralization and demineralization processes change in diseases and physiological processes where osteocyte viability declines, but addressing these questions requires further investigation.

Aging affected some characteristics of perilacunar modulus gradation and lacunar size in this study, but we were likely underpowered to detect the effect on age on several other measures given our small sample size (n = 5 mice / age). Age significantly decreased the modulus slope

from peak to bulk. On the other hand, the modulus slope from edge to peak was lower for aged mice but the comparison was not significant ($p = 0.081$). Likewise, there was a significant difference in lacunar major axis length with aging, but we did not observe significant differences for other measures of lacunar size and shape that may be expected to change in aging. In particular, lacunar sphericity is expected to increase with aging, but the comparison between young adult and early-old-age mice was not significant in this study ($p = 0.070$). Overall, the specific impacts of perilacunar remodeling on lacunar shape and perilacunar modulus gradation would benefit from investigating more mice across an extended age range.

There are several potential reasons why perilacunar bone modulus gradation may have consequences to the osteocyte. The average perilacunar bone area before the peak modulus for labeled lacunae was 16 μm^2 for PMMA-embedded bone. Because osteocyte lacunae are abundantly labeled, we can estimate that a sizable surface of bone along the expansive LCS has lower modulus associated with osteocyte bone formation. Therefore, changes to osteocyte remodeling with advanced aging or disease may be a mechanism by which bone mineral and matrix are modified. However, while it is possible that the changes seen in perilacunar tissue modulus may affect whole-bone mechanical properties, further studies would be necessary to directly link bone quality across these length-scales. Perilacunar modulus gradation may have a physical consequence to the osteocyte. For instance, a softer zone around the lacuna would be expected to increase the strain experienced by the osteocyte [234,316,507]. Prior computational estimates of osteocyte strain amplification based on differences between perilacunar and bulk bone properties assigned 10 μm of perilacunar tissue with different moduli based on a parametric analysis [316,507]. Another study used instrumented nanoindentation to estimate perilacunar

properties for the first 5 μm from lacunar walls to use as finite element model inputs [234]. The findings from our present work as well as the methods we share for analyzing 2D AFM modulus maps could be utilized to improve estimates about the effect of perilacunar modulus gradation on osteocyte strain amplification in the contexts of bone-forming and non-bone forming osteocytes.

Our study has several limitations. First, bone samples were dehydrated in ethanol and embedded in PMMA. We compared our perilacunar modulus gradation from PMMA-embedded bone with bones that were not embedded and were instead hydrated with tap water. Semi-hydrated bone samples still showed perilacunar modulus gradation, but these gradations had several differences from the PMMA-embedded samples. Next, we did not identify the cause of the bone modulus gradation. It would be valuable to ascertain bone compositional differences at similar length-scales to those probed with AFM, although this is technically quite challenging. Another limitation is that pericanalicular bone tissue was not mapped in this study. In synchrotron studies, bone mass gradation around canaliculi is similar to around lacunae [319], suggesting that AFM may also resolve modulus gradation around these structures. The approach presented herein could be readily modified to map modulus around canaliculi or dendrites. We did not evaluate whether aging decreases the number or proportion of labeled lacunae. However, of all the randomly selected lacunae in this study, a similar proportion were labeled for young adult and early-old-age mice. Finally, this study assessed a small number (n = 5 / group) of young adult and early-old-age C57Bl/6 female mice. While we observed modulus gradation for every perilacunar bone map acquired for both ages, the causes of changes of modulus profiles with age would benefit from additional mice of both sexes across an extended age range.

We report, for the first time, that bone modulus is graded at the sub-micrometer scale around osteocyte lacunae. Perilacunar modulus gradation is distinct for fluorochrome-labeled lacunae for both skeletally-mature young adult and early-old age mice, where the labeled lacunae are surrounded by a region of lower modulus bone. However, perilacunar modulus gradation is not strongly related to the 2D dimensions of the lacuna. Given the immense scale of the LCS and the abundance of osteocyte bone formation, our findings support the possibility that lacunar-canalicular remodeling can impact bone tissue properties, such as modulus.

4.5 Acknowledgements

This work was supported by NIH R03 AG068680, NSF CMMI-2120239, and NIH P20 GM103474. This work was performed in part at the Montana Nanotechnology Facility, a member of the National Nanotechnology Coordinated Infrastructure (NNCI), which is supported by the National Science Foundation (Grant# ECCS-2025391). We thank Dr. Heidi Smith at the MSU Center for Biofilm Engineering for assistance with CLSM imaging.

CHAPTER FIVE

CONTACT RESONANCE ATOMIC FORCE MICROSCOPY ON HYDRATED BONE REVEALS NANOMETER-SCALE HETEROGENEITY IN ENERGY DISSIPATION THAT DEPENDS ON PROXIMITY TO CANALICULI

Contribution of Authors and Co-Authors

Manuscript(s) in Chapter(s) 1

Author: Ghazal Vahidi

Contributions: conceptualization; investigation; methodology; data curation; formal analysis; visualization; writing – original draft; writing – review and editing

Co-Author: Mark Jankauski

Contributions: investigation; methodology; writing – original draft; writing – review and editing

Co-Author: Jason P. Killgore

Contributions: methodology; writing – review and editing

Co-Author: Chelsea Heveran

Contributions: conceptualization; methodology; resources; project administration; supervision; writing - original draft; writing - review and editing

Co-Author: Lewis Cox

Contributions: conceptualization; methodology; resources; project administration; supervision; writing - original draft; writing - review and editing

Manuscript Information

Ghazal Vahidi, Mark Jankauski, Jason P. Killgore, Chelsea Heveran, and Lewis Cox

To be submitted to ACS Nano

Status of Manuscript:
☒ Prepared for submission to a peer-reviewed journal
☐ Officially submitted to a peer-reviewed journal
☐ Accepted by a peer-reviewed journal
☐ Published in a peer-reviewed journal

ACS Publications

Abstract

Hydrated bone tissue is shown to be viscoelastic at milli to micrometer-length scales, which can have important contributions to bone fracture resistance. However, the magnitude and range of bone viscoelasticity (tan δ, a measure of energy dissipation) at the nanometer length-scale is undetermined. This is a critical gap since this length-scale is influenced by the activities of bone cells, including osteocytes, which are subjected to modifications in aging and diseases. Our previous work using atomic force microscopy (AFM) demonstrated spatial variance in modulus at the nanometer-scale near osteocyte lacunae, but the bone energy dissipation and its spatial variations have never been measured in bone, whether near or far from the osteocyte lacunar canalicular system (LCS). This is mostly due to instrumentation challenges of this length scale in hydrated tissues. Here, we adapt a liquid contact resonance AFM (CR-AFM) technique and revise it for the measurement of nanometer-length scale variation in energy dissipation of hydrated bone tissue. We use this approach to demonstrate that bone tissue energy dissipation has a very high spatial variation in hydrated cortical bone for young adult female C57BL/6JN mice, although, our nanometer-scale tan δ results are comparable on average to micrometer-scale tan δ measurements taken at the micrometer-scale for similar bone tissues. We also observe gradation patterns of tan δ near several osteocyte canaliculi. This study is significant because 1) it introduces a robust, repeatable, and accessible method for bone researchers to collect these types of data in bone and 2) these data highlight a need to revisit the understanding of the impact of bone material property heterogeneity on bone biomechanics, as well as the role of local viscoelasticity in osteocyte mechanosensation.

5.1 Introduction

Bone is a hydrated tissue that exhibits a time-dependent, viscoelastic response to loading that depends on the length-scale of the material assessment[64,508–510]. The viscoelasticity of bone tissue is attributed to the composition of bone, which is approximately 65% hydroxyapatite mineral, 25% organic scaffold including collagen and non-collagenous proteins, and 10% water[23,32,511]. For machined, millimeter-scale hydrated specimens of cortical bone for humans and bovines, bone exhibits tan δ values (i.e., the ratio of the loss modulus to the storage modulus, a measure of energy dissipation) ranging from 0.04 to 0.08[510,512,513] and 0.03 to 0.125[514,515], respectively, as determined by dynamic mechanical analyses (DMA). These millimeter-scale measurements indicate low to moderate viscoelasticity. At the micrometer-scale, the variance in bone viscoelasticity is larger and the span includes larger values. Using nano-DMA (i.e., DMA analyses using an instrumented nanoindenter capable of microscale measurements), tan δ for hydrated cortical mouse ranged from 0.01 to 0.5, depending on the location in the cortical bone and the strain of mice[509]. For human hydrated cortical bone, tan δ ranged from 0.03 to 0.25, depending on the frequency[64,516]. The viscoelasticity of bone tissue is important to bone biomechanics for several reasons. First, bone viscoelasticity is an intrinsic toughening mechanism that can contribute to bone fracture toughness by enabling bone to deform plastically and increasing the energy dissipation of crack initiation and propagation[49,50,517–520]. Viscoelasticity and energy dissipation in bone tissue are achieved through multiple mechanisms, including plastic deformation and unwinding of individual collagen molecules[50,521], continuous breaking of collagen crosslinks and sliding of collagen molecules with each other and mineral particles in mineralized collagen fibrils[521,522], prevention of fiber separation by sacrificial non-

collagenous bonds that "glue" mineralized collagen fibrils together[523], and stabilizing of collagen-mineral interface by water through hydrogen bonding with the organic matrix and electrostatic attractions with the mineral phase[524,525]. Second, bone viscoelasticity may be variable at the nanometer-length scale, in part because of the activities of embedded bone cells[526,527]. However, the spatial variance in viscoelasticity at these resolutions is undetermined, in part because of the technical difficulties of obtaining these measurements.

Osteocytes are long-lived cells that are embedded within cortical bone tissue in holes called lacunae that are connected by canaliculi[131]. In addition to their known roles in coordinating the activities of other bone cells (i.e., osteoclasts and osteoblasts), osteocytes have been shown by our group and others to remove and replace at least some components of bone tissue in a process called lacunar-canalicular system turnover (LCS turnover, also called peri-lacunar remodeling or peri-lacunar-canalicular remodeling)[26,28–30,177,187]. This process is highly prevalent and has the potential to impact a significant quantity of bone tissue[26–30,177,179,187]. Further, we have shown that osteocytes likely affect the material properties of their surrounding bone tissue[30]. Specifically, lacunae that show a fluorochrome label, indicating recent mineralization, are surrounded by more compliant bone tissue. It is not yet understood if the osteocyte can also impact local bone viscoelasticity. Since LCS turnover involves at least the demineralization and re-mineralization of bone matrix, and possibly the turnover of organic matrix, impacts to viscoelasticity would be suspected[26,29,30,517–520]. Determining the viscoelasticity of bone near osteocytes is important for understanding both the impacts of this cell on bone matrix and, conversely, the impacts of the properties of bone matrix on osteocyte mechanosensation.

Mapping bone viscoelasticity at the nanometer-length scale for hydrated specimens is a technical challenge. These types of data can be obtained at the microscale using instrumented nanoindentation and nano-DMA, with contact areas in the range of ~1-5 micrometers[509]. This technique lacks the resolution to measure viscoelasticity at a scale relevant to interactions of osteocytes with their surrounding bone matrix[28]. AFM can achieve the desired resolution for these types of studies but has so far has only been used to map quasistatic properties in bone[30,526]. Specifically, most researchers use AFM for small force vs. displacement tests, where modulus is calculated using Hertzian contact mechanics or the Oliver-Pharr method[528,529]. Further, AFM studies are usually conducted for dehydrated bone specimens, which stiffens bone tissue, reduces heterogeneity, and reduces viscoelasticity[243–245]. The nanometer-length scale spatial variation of the viscoelasticity of bone tissue, whether near or far from the osteocyte LCS, is not yet determined, in part due to the technical challenge of obtaining these measurements.

Contact resonance AFM (CR-AFM) is a promising technique that provides nanometer-scale viscoelasticity property measurements[242,246–248,530–535]. CR-AFM utilizes the resonant frequencies and mode shape of an oscillating cantilever beam in contact with a sample to provide information about the sample material properties, such as tan δ[242]. The elastic and damping properties of the material are calculated from the shifts in cantilever resonance properties when it is in contact with the sample, compared to the cantilever properties when it is freely oscillating in air[532,536]. CR-AFM has been employed in air on dry, standard engineering samples such as polystyrene to effectively measure their viscoelastic properties[530]. There are a few instances where CR-AFM has been applied to biological materials, including the dehydrated, PMMA-embedded osteochondral interface[533]. However, the viscoelasticity of biological specimens,

including bone, is much more accurately measured in a hydrated state[243–245]. There are two primary reasons why this methodology has not been applied to bone, or materials similar to bone, to date. The first is that conducting CR-AFM in liquid is challenging due to the complexities introduced by fluid interactions with the cantilever beam (i.e., hydrodynamic effect), which influences the contact mechanisms and the subsequent measurements. While a few studies have proposed corrections for the hydrodynamic effect[242,246–248] , the necessary adjustments to deploy the technique on bone or other stiff, complex material systems have not been made. Second, previous usages of CR-AFM employed dual-AC resonance tracking (DART) to enable continuous maps of viscoelasticity[242]. This technique is difficult to employ on stiff or not completely uniform structures. Here, we present an approach that uses CR-AFM data collection by points, as opposed to over continuous maps with very high speed of data collection, to surmount these limitations. The approach developed here is expected to make the CR-AFM measurement more accessible to bone researchers.

In this study, we employ CR-AFM in liquid to evaluate the viscoelastic properties of hydrated bone tissue at the nanometer length-scale. We quantify bone tissue energy dissipation ($\tan \delta$) and its spatial variance (i.e., heterogeneity), both adjacent to osteocyte canaliculi and in bulk bone tissue away from these structures. We hypothesized that energy dissipation in hydrated bone tissue exhibits greater heterogeneity when measured at the nanometer-length scale compared with measurements collected at larger length scales. We also hypothesized that the tissue surrounding osteocyte canaliculi displays different energy dissipation properties compared to bulk tissue located further from the LCS.

Table 5.1. Summary of terms and parameters for contact-resonance AFM.

Parameter	**Meaning**	**Value**
CR-AFM	Contact resonance atomic force microscopy	NA
Fr	Frequency of resonance peak in contact	NA
QF	Width of resonance peak at half-maximum amplitude of the peak	NA
Fr_{CR}	Raw FR measured in contact with bone	Measured
QF_{CR}	Raw QF measured in contact with bone	Measured
$Fr_{correct}$	Corrected FR after removing the hydrodynamic effect from raw FR	Measured
$QF_{correct}$	Corrected QF after removing the hydrodynamic effect from raw QF	Measured
Fr_{free}	FR measured for free-oscillating cantilever in air	Measured
Fr_{near}	FR measured near the bone sample in water for hydrodynamic corrections	Measured
QF_{near}	QF measured near the bone sample in water for hydrodynamic corrections	Measured
QF_{fluid}	Calculated hydrodynamic damping of the in-contact system	Measured
n	Mode number of a resonance peak	3
K^*	Contact stiffness	Measured
σ	Contact damping	Measured
α	Normalized contact stiffness	Measured
β	Normalized contact damping	Measured
K_c	Cantilever spring stiffness	Measured
η_{air}	Damping correction factor tuned to the cantilever's free response in air	9000
E'	Storage modulus	NA
E"	Loss modulus	NA
tan δ	Loss tangent or factor, E"/E'	Measured
xL	Corresponding solution to the characteristic equation for free flexural vibration: $1 + \cos(xL)\cosh(xL) = 0$, with xL = [1.8751, 4.6941, 7.8548] for flexural mode n = [1, 2, 3]	7.8548
L	Cantilever length	240 μm
L_1	Position of the probe along the cantilever length	240 μm
A	Cantilever cross-sectional area	92 μm^2
b	Cantilever width	40 μm
th	Cantilever thickness	2.3 μm
I	Second area moment ($b*th^3/12$)	40.5 μm^4
E	Cantilever modulus	200 GPa
ρ	Material density	2330 kg/m^3
ρ_{fluid}	Density of water	997 kg/m^3
μ_{fluid}	Shear viscosity of the water	1 mPa.s
Γ	hydrodynamic function	NA
Γ_{real}	Real component of Γ	Measured
$\Gamma_{imaginary}$	Imaginary component of Γ	Measured
Re	Unsteady Reynolds number	Measured

5.2 Materials and Methods

5.2.1 Contact Resonance Atomic Force Microscopy (CR-AFM)

The setup for CR-AFM involving a vibrating probe and cantilever in contact with a viscoelastic sample is illustrated in Figure 5.1A. In CR-AFM, a small elastic cantilever beam is clamped at one end and free at the other, where a sharp silicon probe facilitates sample actuation. Photothermal excitation of cantilever oscillations from 0 Hz to 2 MHz (in water here) captures the response of four resonant modes (Figure 5.1A-B)[242,248,531,536–539]. The cantilever is excited in the free state (e.g., in air) as well as when in contact with a sample. The boundary condition experienced by the cantilever's probe tip when contacting a substrate determines the frequency and quality factor of a resonance peak, and the boundary condition is determined by the viscoelastic properties of the substrate. The relationship of cantilever resonance and substrate viscoelasticity is the basis for contact resonance theory[242,248,531,536–539]. For example, a relatively stiff and elastic substrate would result in resonance peaks occurring at higher frequency of the resonance peak in contact (Fr_{CR}), accompanied by narrower mode shapes. For a viscoelastic material, the damping in the resonance peak is used to assess the viscous characteristics of the material, which is attributed to both Fr_{CR} as well as the width of resonance peak at half-maximum amplitude of the peak, known as quality factor (QF_{CR}) of the resonance peak (Figure 5.1C)[242,537,539]. Sample viscoelastic properties are measured from shifts in the frequency and quality factor while the probe is in contact with the surface as compared with free oscillations in air (Figure 5.1C). There, it is important to measure Fr and QF values both during contact with the sample and during free cantilever vibrations at the corresponding flexural mode in air (ideally in

vacuum, although negligible differences have been reported between air and vacuum measurements[247,534,540]).

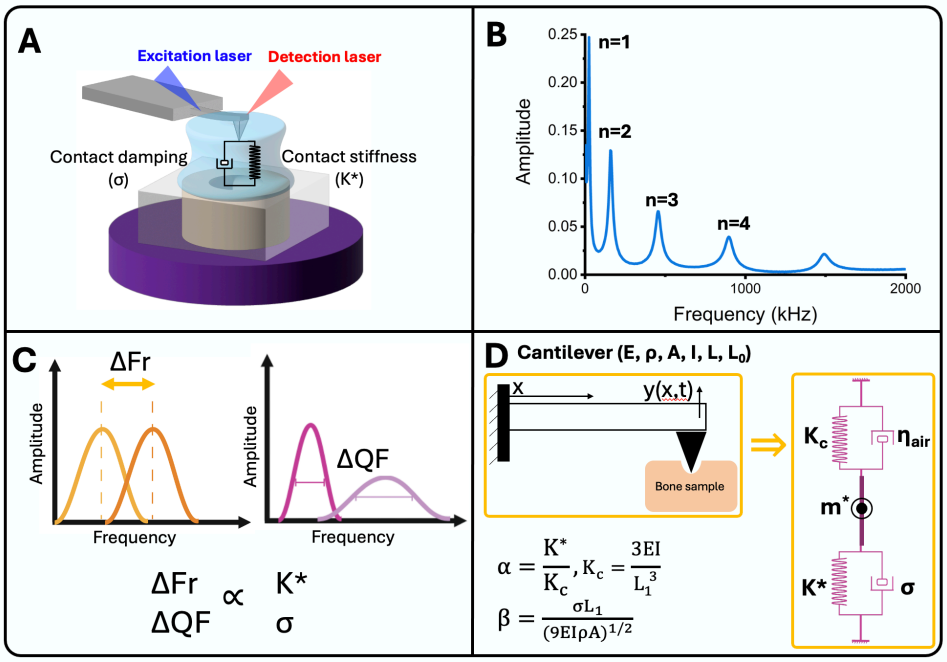

Figure 5.1. Schematic of liquid CR-AFM setup and CR theory. A) The theoretical setup for liquid CR-AFM. A probe and cantilever oscillate while in contact with a viscoelastic sample that is submerged in water. The cantilever is excited with the excitation laser while in contact with the sample. B) The resonance response of the cantilever is be collected for different resonance modes (n). C) In CR-AFM, for the nth resonance mode, the contact resonance properties of the cantilever, contact frequency (Fr_{CR}) and quality factor (QF_{CR}), are collected. The sample's viscoelastic response is measured based on the shifts in the frequency and quality factor in contact compared to in free air measurements. D) The cantilever beam is modeled as a harmonic oscillator with an effective mass of m* with a massless spring with stiffness Kc and a massless dashpot with a damping constant of η_{air}. Contact stiffness (k*) and contact damping (σ) between the cantilever and the material are modeled as a point-mass beam based on the properties of the cantilever beam using Kelvin–Voigt contact theory.

5.2.2 Energy Dissipation (tan δ) Calculation

Contact mechanics models are used to determine the viscoelastic properties of the sample such as storage modulus (E'), loss modulus (E"), and the loss tangent or loss factor, tan δ (E"/E'). To accurately determine the values of E' and E", it is imperative to determine the probe

contact area. This can be accomplished in AFM measurements by analyzing a comparable calibration sample with established viscoelastic properties. The complex heterogeneity of hydrated bone makes selection of an appropriate calibration sample difficult. However, as developed by Hurley *et al*[537], tan δ can be determined directly from the cantilever beam dynamics model, bypassing the intermediate calculations of E' and E" and eliminating the need for a calibration sample for probe geometry. This is accomplished using Equation 1:

$$\tan\delta = (\mathrm{xL})^2 \frac{\beta}{\alpha}\left(\frac{\mathrm{L_1}}{\mathrm{L}}\right)^2 \frac{\mathrm{Fr}_{Correct}}{\mathrm{Fr}_{\mathrm{free}}} \quad (1)$$

Here, xL is the corresponding solution to the characteristic equation for cantilever free flexural vibration as developed by Hurley et al: 1 + cos(xL) cosh(xL) = 0, with xL = [1.8751, 4.6941, 7.8548] for flexural mode n = [1, 2, 3][537]. L_1/L is the relative position of the probe along the cantilever length, which here is set to 1 (AC240TSA-R3, Oxford Instruments, material properties and geometry detailed in Table 5.1). $\mathrm{Fr}_{Correct}$ is the contact frequency after hydrodynamic correction (details in *2.1.4*). $\mathrm{Fr}_{\mathrm{free}}$ is the cantilever free oscillation for the corresponding resonance mode. α and β are the normalized contact stiffness and damping values that are obtained from the contact stiffness (k^*) and damping (σ). k^* and σ are obtained by modeling the cantilever as a point-mass beam as described next.

5.2.3 Cantilever Point-Mass Beam Modeling to Determine Contact Stiffness and Contact Damping

The properties of probe-sample contact are analyzed using a Euler-Bernoulli beam model as reported in detail by Rabe et al[541]. To account for the elastic and damping characteristics of probe-sample contact, a Kelvin-Voigt element models the boundary condition at the point of contact as a linear elastic spring of stiffness k* in parallel with a linear dashpot having a damping

coefficient σ (Figure 5.1D). The beam is a three-dimensional structure with a rectangular cross-sectional area A (width b, thickness th), second area moment I ($b*th^3/12$), and length L. Assuming homogenous properties, the equation of motion for flexural vibrations is:

$$\mathrm{EI}\frac{\delta^4 y}{\delta x^4} + \eta_{air}\rho\mathrm{A}\frac{\delta y}{\delta t} + \rho\mathrm{A}\frac{\delta^2 y}{\delta t^2} = 0 \quad (2)$$

where x represents the axial coordinate along the cantilever, y(x, t) denotes the transverse deflection, ρ denotes material density, E denotes modulus and η_{air} is a damping correction factor tuned to the cantilever's free response in air. All values are listed in Table 5.1. The probe position (L_1) is assumed to be at the end of the beam (x = L, $L_1/L=1$), consistent with the cantilever used in this study. The boundary conditions at the free and fixed end are:

$$\mathrm{EI}\frac{\delta^4 y}{\delta x^4} + \eta_{air}\rho\mathrm{A}\frac{\delta y}{\delta t} + \rho\mathrm{A}\frac{\delta^2 y}{\delta t^2} = 0 \quad (3)$$

$$\frac{\partial}{\partial x}\left(\mathrm{EI}\ \frac{\partial^2 y(L,t)}{\partial x^2}\right) = k^*\mathrm{y(L,t)} + \sigma\ \frac{\partial y(L,t)}{\partial t} \quad (4)$$

$$\mathrm{EI}\ \frac{\partial^2 y(L,t)}{\partial x^2} = 0 \quad (5)$$

$$y(0,t) = 0 \quad (6)$$

We discretize equation (2) into a finite model implemented in Matlab *(Appendix)*. Specifically, we use this model to estimate contact stiffness k^* and contact damping σ from experimental measurements of the cantilever beam's 3rd resonant frequency and quality factor. We chose the 3rd mode for two reasons, 1) matching the dynamic stiffness of the cantilever to the bone sample improves signal to noise ratios and 2) the 3rd mode exhibited superior stability in repeated point measurements. The finite element model consists of 20 uniform length elements, which was sufficient to demonstrate convergence of the third natural frequency. The model was then converted to a state-space framework, where the damping ratios (inversely proportional to

the quality factor) and resonant frequencies are determined via the state matrix poles[542]. We swept over a range of contact stiffness and damping values (grid of 20 each) to identify the corresponding resonant frequencies and quality factors. A viable range of contact stiffness/damping values to model was identified using the non-dimensional stiffness ratio and damping defined by Rabe et al [541]. We subsequently established an interpolation map that facilitating output of contact stiffness and damping given a specific resonant frequency and quality factor input.

Next, we calculated α and β from contact stiffness and damping values for each point:

$$\alpha = \frac{K^*}{K_c} \tag{7}$$

$$\beta = \frac{\sigma L_1}{(9EI\rho A)^{1/2}} \tag{8}$$

where $K_c = \frac{3EI}{L_1^3}$ is the cantilever's spring constant.

5.2.4 Liquid CR-AFM

Several studies have illustrated the effectiveness of CR-AFM measurements in air with standard polymeric samples[242,531,537,539,543]. In fewer instances, biological samples such as engineered plant cells[535,544] and the dehydrated osteochondral interface[533] have been investigated. Conducting CR-AFM in liquid offer significant advantages for samples that derive material properties from interactions with water. Bone, which contains about 10% water by weight, is an example of such a material[63]. The viscoelasticity of bone has impacts on the material properties (e.g., toughness) of the skeleton and potentially on its biological functions (e.g., cell mechanosensation)[510,515,526,545,546]. However, bone viscoelasticity cannot be adequately estimated from dehydrated specimens. It is challenging to collect CR-AFM for hydrated biological

specimens like bone for several reasons. First, there are practical concerns to manage, such as maintaining sample hydration during testing. Second, the traditional piezoelectric excitation used to drive the AFM cantilever can produce unintended resonance responses in the liquid, particularly when the cantilever is in contact with the sample[538,547]. To address this challenge, several studies have suggested direct cantilever excitation by photothermal method[246,248,534,538,547–549]. This is accomplished by positioning a second laser (e.g., BlueDrive photothermal excitation laser) onto the cantilever to oscillate its temperature, inducing bending and driving cantilever motion[246,248,534,538,547–549]. Third, the fluid hydrodynamic interactions between cantilever and sample require an appropriate strategy. In a fluid environment, the behavior of the cantilever during CR-AFM not only depends on the sample material properties but also on the added mass and damping effect of the fluid (Figure 5.2). To address this challenge, a hydrodynamic effect correction method has been introduced and applied in liquid CR-AFM measurements[247,534,538].

Since the cantilever is submerged during the liquid CR measurements, test outcomes should be corrected for the hydrodynamic interactions between the cantilever and fluid environment (Figure 5.2A). The hydrodynamic function, which is frequency-dependent, is typically computed for a cantilever in free oscillation [247,534,538]. However, calculating the hydrodynamic function in contact for CR measurements poses computational challenges and necessitates prior knowledge of the system's geometrical and material properties. These obstacles are overcome by experimentally measuring and reconstructing the hydrodynamic function (Γ) in close proximity (100-200 nm) to the sample surface[247,534] (Figure 5.2B). This approach captures the approximate hydrodynamic behavior of the system during CR measurements. We measured

both the Γ_{real} component (representing mass loading) and the $\Gamma_{imaginary}$ component (representing environmental damping) of the hydrodynamic function, using frequency (Fr_{near}) and quality factor (QF_{near}) at different resonance modes near the bone surface in water (Figure 5.2B). The measurements were conducted using equations 9-11[247,534].

$$\Gamma_{real} = \frac{(\frac{Fr_{free}}{Fr_{near}})^2 - 1}{\chi} \quad (9)$$

$$\Gamma_{imaginary} = \frac{\left(\frac{Fr_{free}}{Fr_{near}}\right)^2}{QF_{near}\,\chi} \quad (10)$$

$$\chi = \frac{\pi}{4}\frac{\rho_{fluid} b^2}{\rho A} \quad (11)$$

where ρ_{fluid} and ρ represent the density of the fluid (here, water) and the cantilever material (silicon, as detailed in Table 5.1), respectively. b is the width and A is the cross-section area of the cantilever as described before. Unsteady Reynolds numbers for each of these frequencies were also calculated.

$$Re = \frac{\rho_{fluid}}{4\mu_{fluid}} b^2 Fr_{near} \quad (12)$$

where μ_{fluid} is the shear viscosity of the fluid.

Next, we calculated the Γ_{real} and $\Gamma_{imaginary}$ for our data from the frequency values of in-contact measurements. Since hydrodynamic functions are frequency-dependent and frequencies shift upon contact, we cannot directly use Γ_{real} and $\Gamma_{imaginary}$ values calculated from the near-surface measurements. Following established procedures, we instead estimated the hydrodynamic function for in-contact measurements by interpolating the measured Γ_{real} and $\Gamma_{imaginary}$ values near the surface and then reading the corresponding Γ_{real} and $\Gamma_{imaginary}$ values for

in-contact frequencies[247,534,535]. The resulting hydrodynamic functions were then plotted as a function of the Reynold's number for each of the near-surface points (Figure 5.2C). To fit these near-surface hydrodynamic functions to a polynomial expansion, we assumed the asymptotic expansion for a long slender beam considering the functional form of the hydrodynamic function[247,534]. We determined the order of the initial terms and incorporated fitting coefficients (a, b, and c) to appropriately fit the data near the surface:

$$\Gamma_{\text{real}} = a_1 + b_1 Re^{-1/2} \tag{13}$$

$$\Gamma_{\text{imaginary}} = a_2 + b_1 Re^{-1/2} + C_2 Re^{-1} \tag{14}$$

Following data collection, for each point of measurement, we calculated the corresponding unsteady Reynold's number ($\text{Re}_{\text{W}_{\text{CR}}}$) from each point's contact frequency and obtained the corresponding Γ_{real} ($\Gamma_{\text{Real}}(\text{Re}_{\text{Fr}_{\text{CR}}})$) and $\Gamma_{\text{imaginary}}$ ($\Gamma_{\text{imaginary}}(\text{Re}_{\text{Fr}_{\text{CR}}})$) values from our fitted curves (Figure 5.2C). Next, we determined the corrected cantilever resonant properties, $\text{Fr}_{\text{correct}}$ and $\text{QF}_{\text{correct}}$, for each point using the following equations [247,534]:

$$\text{Fr}_{\text{correct}} = \text{Fr}_{\text{CR}}[1 + \chi\, \Gamma_{\text{Real}}(\text{Re}_{\text{Fr}_{\text{CR}}}) \tag{15}$$

$$\text{QF}_{\text{correct}} = \frac{1}{\frac{1}{\text{QF}_{\text{CR}}} - \frac{1}{\text{QF}_{\text{fluid}}}} \tag{16}$$

$$\text{QF}_{\text{fluid}} = \frac{\chi^{-1} + \Gamma_{\text{real}}(\text{Re}_{\text{CR}})}{\Gamma_{\text{imaginary}}(\text{Re}_{\text{CR}})} \tag{17}$$

Applying hydrodynamic corrections and controlling for the spurious hydrodynamic effects establishes the in-air-equivalent frequency and quality factor values for contact measurements made in water, thereby isolating sample material properties from damping in water. A more detailed description of the application of the hydrodynamic function can be found elsewhere [247,534].

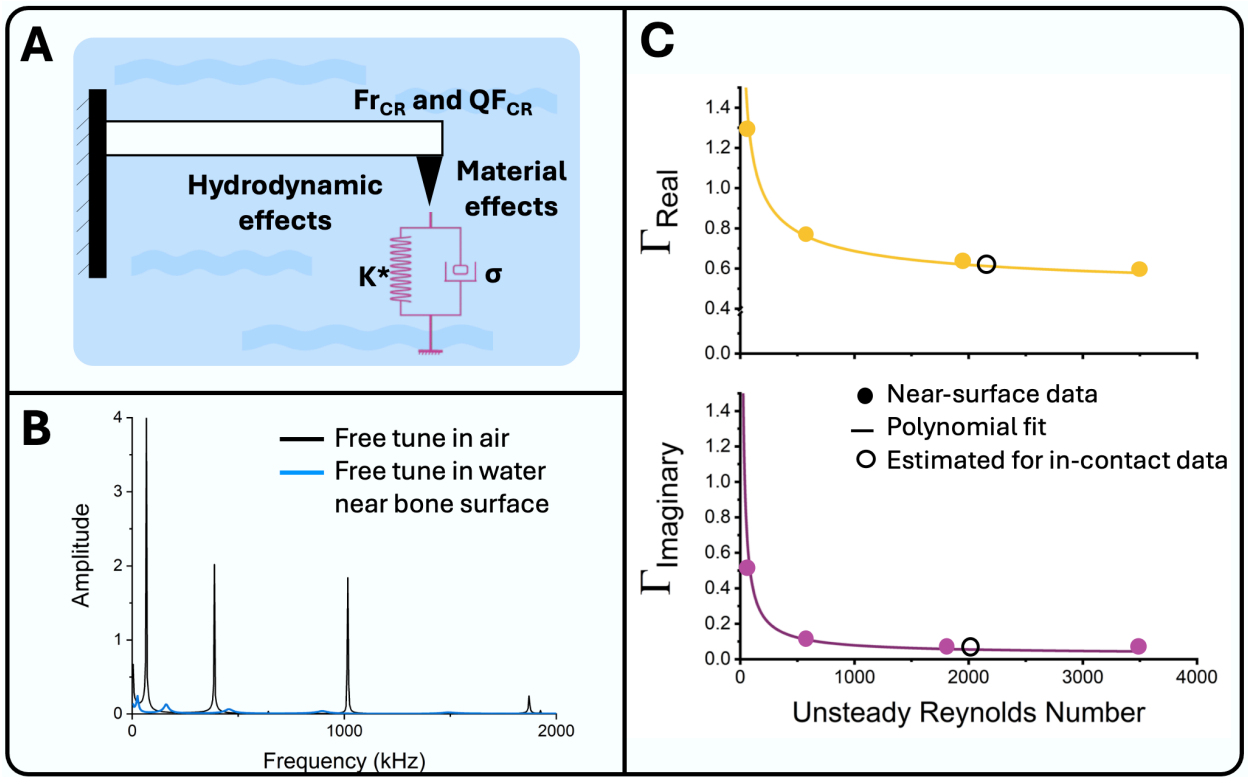

Figure 5.2. Hydrodynamic effect corrections. A) For CR-AFM measurements conducted in water, the measured Fr_{CR} and QF_{CR} values should be corrected to remove the hydrodynamic effect between water and the cantilever. B) The free cantilever resonance response is measured in air and in water, enabling reconstruction of the hydrodynamic function. C) A representative hydrodynamic function, both real and imaginary components, from one cantilever is shown here plotted against the unsteady Reynolds number, which varies as a function of frequency. Solid circles are the measured hydrodynamic function at the first four free resonance frequencies in water by the cantilever near (100-200 nm) the bone surface. These measurements points were fitted using equations 13 and 14, as represented by lines. The unsteady Reynolds numbers were then calculated using the frequency values obtained from CR-AFM measurements in contact with the bone surface. Using these plots, the hydrodynamic function components were estimated (one representative point is shown here as an empty circle). Using equations 15-17, the frequency and quality factor values for all data points were corrected.

5.2.5 Animal Models

All animal procedures were approved by Montana State University's Institutional Animal Care and Use Committee. Young adult 5-month-old (5 mo, n = 3) female C57BL/6JN mice from Jackson Laboratory were utilized in this study. Mice had *ad libitum* access to water and standard chow and were euthanized via isoflurane inhalation followed by cervical dislocation.

5.2.6 Sample Preparation

Right femurs were harvested, cut transversely in half at the femoral midshaft using a low-speed diamond saw (Isomet, Buehler), and then the proximal fragments, without undergoing any ethanol dehydration steps, were embedded in non-infiltrating epoxy (Epoxicure 2, Buehler), allowing for sample rehydration prior to testing. The mid-shaft cross-sections were polished to achieve a mirror-like finish, using wet silicon carbide papers (600 and 1000 grits, Buehler) followed by Rayon fine cloths and alumina pastes (9, 5, 3, 1, 0.5, 0.3, and 0.05 μm, Ted Pella, Inc.). Cross-sections were wrapped in water-soaked gauze and stored at -20 ºC and then rehydrated with tap water for 24 hours prior to analyses in effort to restore bone tissue hydration, which is important for collecting physiologically relevant measures of bone viscoelasticity.

5.2.7 CR-AFM Instrumentation

All analyses were performed with an Asylum Research Cypher S force microscopy system (Asylum Research, Oxford Instruments) with an etched silicon cantilever with gold coating (AC240TSA-R3, Oxford Instruments, material properties and geometry detailed in Table 5.1) and dimensions of 240 × 40 × 2.3 μm. The AFM probe was a sharpened tetrahedral made of silicon, with 14 μm length and tip radius of 7 nm. A BlueDrive photothermal excitation laser (Asylum Research, Oxford Instruments) was used to drive the cantilever at desired frequencies (0-2 MHz sweep in contact). A standard diode laser (Asylum Research, Oxford Instruments) was used to detect cantilever deflection. The BlueDrive laser was positioned at the tip of the cantilever to optimize amplitude values, while the detection laser was situated at the cantilever's end directly above the probe (Figure 5.1A).

5.2.8 CR-AFM Pre-testing Calibration Steps

Prior to each testing session, cantilever deflection sensitivity and cantilever spring constant were calculated using the thermal tuning via Sader method[550]. For each new probe, each of the following calibration steps were conducted. We collected the free (non-contact) frequencies of each cantilever in air and room-temperature tap water using a 4.5 mW BlueDrive drive amplitude with a frequency sweep width of 2 MHz (Figure 5.2B). In air, the cantilever was oscillated freely close to the bone sample surface and frequencies for the first four resonance modes were collected. To achieve near-surface measurements in water, we first perform a force-distance curve. The force trigger was adjusted to 10-12 nN to achieve a retraction distance of 100-200 nm, enabling the subsequent capture of surface-dependent hydrodynamic effects. The frequency and quality factor values for the initial four resonance modes of free oscillation in water, near surface, were recorded. Since the distance between the cantilever and the surface in the near surface measurement was less than 2% of the probe's height, we assume that the distance between the cantilever and the surface is equivalent for both contact and near-surface measurements, establishing known hydrodynamic interactions during data collection. The free frequency and quality factor values were used to estimate the hydrodynamic function and construct the calibration curves (Figure 5.2C) that were used to remove the hydrodynamic effect from contact measurements (detailed in 5.2.3.4).

5.2.9 Measurement of tan δ for Peri-canalicular and Bulk Bone Tissue at Sub-micrometer Scale

All data were collected in the anterior quadrant of the femoral midshaft cross-section. 10 by 10 μm topography maps were randomly collected in the anterior quadrant and used to identify the regions of interest (ROIs) for canaliculi. Peri-canalicular regions were defined as the bone

immediately adjacent to the wall of one canaliculus cross-section (Figure 5.3). A grid of points covering a 500 by 300 nm region adjacent to canalicular wall was established. As shown in Figure 5.3, a row of three points parallel to the canalicular wall (spaced 100 nm apart) was repeated 10 times in the direction perpendicular to the canalicular wall, to cover a distance of 500 nm away from the wall with 50 nm increments. Each peri-canalicular map was further divided into two separate maps for data analyses; points located less than 100 nm away from the canalicular wall (Can-near) versus points located between 100 to 500 nm away from the canalicular walls (Can-far). The 100 nm cutoff was chosen based on the observed gradient patterns in tan δ around some canaliculi in our data. Therefore, we employed this cutoff to assess whether viscoelastic properties would exhibit a similar trend around canaliculi. Bulk regions were defined as areas where no canaliculus (or lacuna) was identified within a 2 by 2 μm vicinity. A grid of points measuring 3 by 10, spaced 100 nm apart, was employed to map the tan δ in bulk regions (Figure 5.3). All regions of interests were selected in the lamellar compartment of cortical bone, with a minimum distance of 20 μm from the bone's endocortical and periosteal surfaces. Maps were at least 1 μm away from an osteocyte lacuna. Data was collected for n=3 mice, each n=3 bulk maps and n=5 peri-canalicular maps.

Following the establishment of spot maps, CR-AFM was conducted in contact mode (BlueDrive CR mode, AFM software, Asylum Research, Oxford Instruments) for each point. To maintain a consistent meniscus of water between the sample surface and probe, a custom aperture was utilized. Drive amplitude was set to 4.5 mW, while the setpoint was adjusted to 0, and the free deflection set to -0.2, ensuring a consistent stress level at the probe-surface contact. Amplitude versus frequency tune data for each measurement point were acquired at the

cantilever's third resonance frequency (n = 3) during contact, with a frequency sweep width of 400 kHz. Uncorrected frequencies (Fr_{test}, the peak frequency) and uncorrected quality factors (QF_{test}, the width of the peak at half-maximum amplitude) were obtained (Figure 5.1). MacroBuilder programming (AFM software, Asylum Research, Oxford Instruments) automated the tuning process and collection of amplitude-frequency curves at each point of a map.

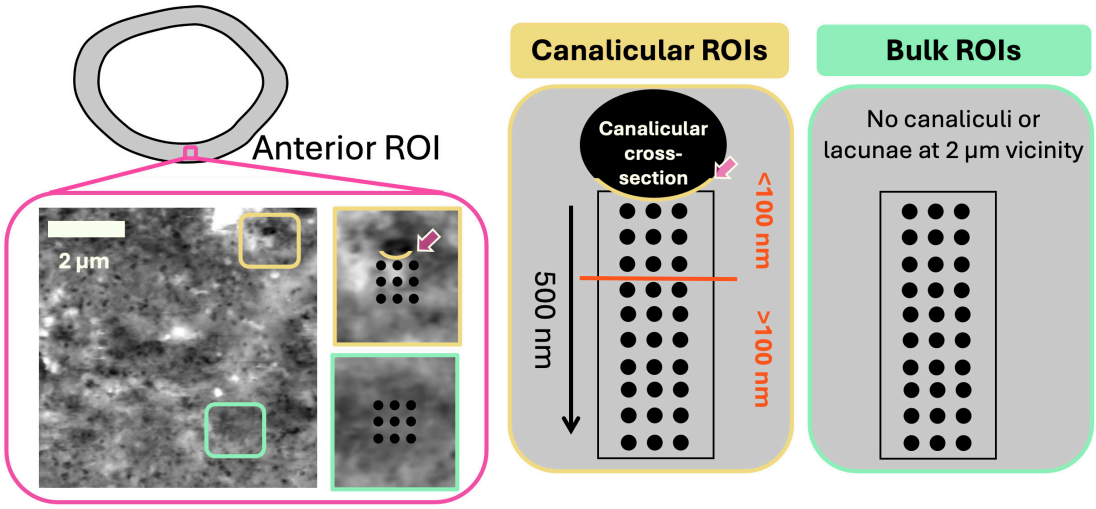

Figure 5.3. Schematic for AFM mapping. All maps were located in the anterior region of the cortical midshaft femur within lamellar bone. Topography maps were used to identify the regions of interest. Canalicular maps (500 by 300 nm, spaced 50 nm apart) were located adjacent to canalicular wall. Canalicular wall shown with a yellow border and a pink arrow. Each canalicular map was divided into two separate maps for data analyses; points located less than 100 nm away from the canalicular (Can-near wall versus the points located between 100 to 500 nm away from the canalicular walls (Can-far) Bulk regions were defined as areas where no canaliculus (or lacuna) was identified within a 2 by 2 µm vicinity. A grid of points measuring 3 by 10, spaced 100 nm apart, was employed to map the tan δ in bulk regions. All regions were chosen with a minimum distance of 20 µm from the bone's endocortical and periosteal surfaces, in the lamellar compartment of the cortical bone, and at least 1 µm away from a lacuna.

5.2.10 CR-AFM Data Processing

Hydrodynamic correction was performed for the frequency and quality factor data as outlined in section 5.2.3.4, using a custom MATLAB code. The Reynolds number ($Re_{Fr_{CR}}$) was calculated for each point (equation 9). Then, equations 13 and 14, corresponding to the

calibration curves in Figure 5.2C, were applied to extract both the real ($\Gamma_{Real}(Re_{Fr_{CR}})$) and imaginary components ($\Gamma_{Imag}(Re_{Fr_{CR}})$) of the hydrodynamic function for each point. Finally, the corrected, in-air-equivalent values of the frequency ($Fr_{correct}$) and quality factor ($QF_{correct}$) were obtained using equations 15-17. The tan δ values of each point was calculated based on $Fr_{correct}$ and $QF_{correct}$ using equation 1.

5.2.11 Statistical Analyses

The mean and standard deviation (heterogeneity) of tan δ were calculated for each map and compared between different ROIs: maps located less than 100 nm away from the canalicular wall (Can-near), maps located 100-500 nm away from the canalicular wall (Can-far), and maps at bulk ROIs located at least 2 μm away from osteocyte canaliculi and lacunae. Mixed model ANOVA, with mouse as the random effect, tested if tan δ (input mean tan δ for of map) or the heterogeneity of tan δ-depended on the fixed effect of map location (Can-near vs. Can-far vs. Bulk). For all models, model residuals were checked for satisfaction of assumptions of normality and homoscedasticity. Significance was set a priori to $p < 0.05$. The relationship between tan δ and distance from the canalicular wall was also investigated over a distance of 500 nm away from the canalicular wall. Data for each map were represented as scatter plots (Figure 5.6) of tan δ versus the distance from the lacunar wall, and then fitted with linear, quadratic, and cubic polynomials. Adjusted R^2 values were compared between the fits, and the best fit was chosen with care taken to be conservative and avoid overfitting. All analyses were performed with Minitab (20).

5.3. Results

5.3.1 Tissue Energy Dissipation (tan δ) Shows Nanoscale Heterogeneity in Hydrated Bones

We used a liquid CR-AFM technique, for the first time on hydrated bone tissue, to measure the energy dissipation and heterogeneity of energy dissipation (i.e., tan δ) for maps with nanometer-length scale resolution (tip radius of 7 nm, contact depth of about 11 nm, indents placed 50 nm apart). A total of 15 canalicular maps and 9 bulk maps were collected, across three different mice. We demonstrated that energy dissipation in hydrated bone tissue is heterogeneous at the sub-micrometer scale (Figure 5.4). We observed a wide range of tan δ values regardless of their proximity to canaliculi, spanning from a minimum of 0.02 to a maximum of 0.8. The nanometer-length scale tan δ of hydrated tissue for bulk bone, located at least 2 μm away from osteocyte canaliculi, was 0.289 ± 0.118. The tan δ was 0.320 ± 0.157 for maps located less than 100 nm away from the canalicular wall (Can-near), and 0.317 ± 0.146 for maps located 100-500 nm away from the canalicular wall (Can-far).

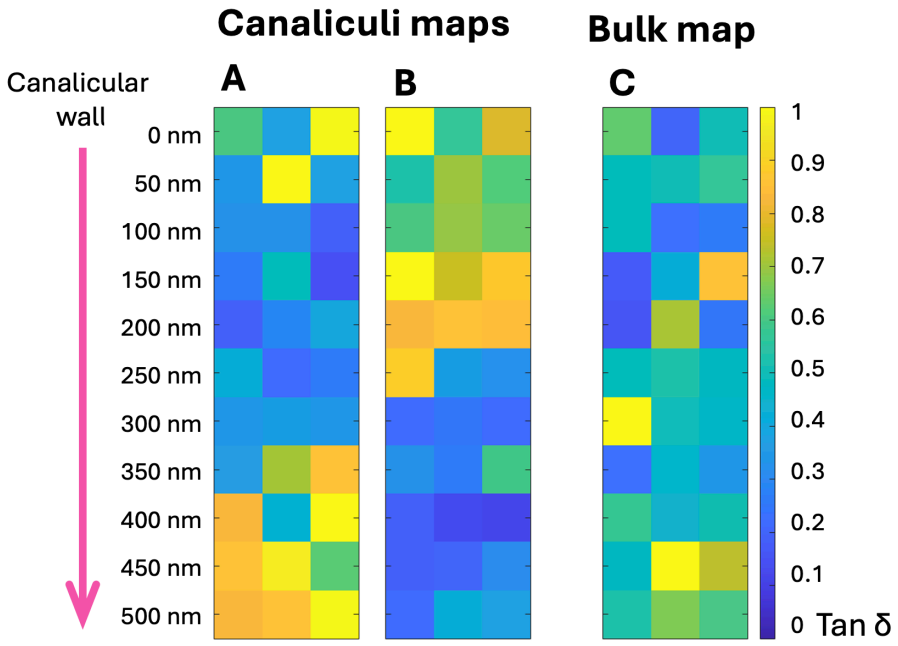

Figure 5.4. Representative canaliculi and bulk maps demonstrating the heterogeneity of energy dissipation at the nanometer length-scale. A and B show two canalicular maps with distinct patterns of tan δ gradations from the canalicular wall. Map A shows a pattern where tan δ is relatively high near the canalicular wall (within the first 50 nm), then decreases to a low value around 150 nm distance, before rising again into the extracellular matrix. Map B demonstrates a pattern where tan δ is high adjacent to the canalicular wall (0 to 100 nm away) and then decreases as the distance into the extracellular matrix increases. Both Maps A and B are representative patterns seen for the mapped canaliculi. Map C shows the heterogeneity of tan δ at nanometer-length scale in bone bulk tissue (i.e., not near canaliculi). For all maps, each heatmap pixel represent a point location in the map. In the canalicular maps, points are located from adjacent the canalicular wall to 500 nm into the bone tissue. In the bulk map, points are from 500 (50 nm apart) by 300 (100 nm apart) nm maps located at least 2 μm away from lacunar and canalicular features. Heatmap color scale shows the values of tan δ.

5.3.2 Tissue Energy Dissipation Was Not Significantly Different Among Canalicular and Bulk Regions of Interest

Mean tan δ values ($p=0.7$) and the heterogeneity of tan δ ($p=0.3$) were not significantly different between the three categorical distances groupings of (1) canalicular near: less than 100 nm away from the canalicular wall, (2) canalicular far: 100-500 nm away from the canalicular wall, or (3) bulk: tissue regions > 2 μm from canaliculi (and lacunae) (**Error! Reference source not found.**).

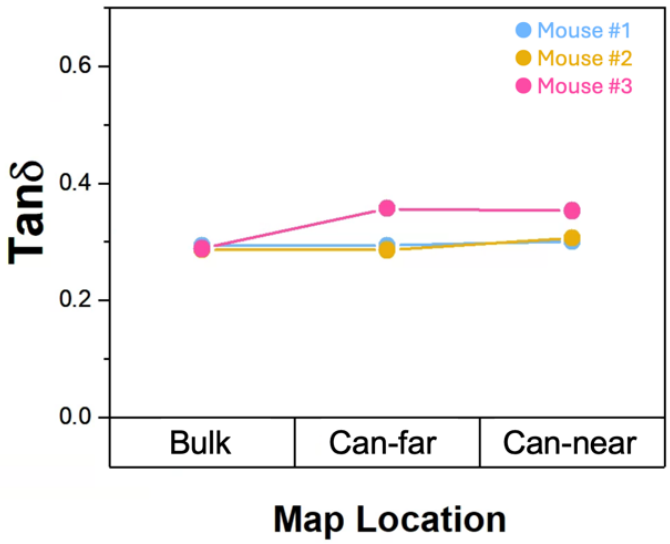

Figure 5.5 Energy dissipation comparisons for different map locations across the mice. There are not statistically significant differences in mean tan δ or heterogeneity of tan δ between canalicular-near (0-100 nm), canalicular-far (100-500 nm) and bulk (> 2 μm) regions of interest. Each solid point on the plot represents the mean tan δ calculated by averaging all the points from all the maps collected at bulk or canalicular regions for that specific mouse.

5.3.3 Tissue Energy Dissipation Showed a Gradation Pattern Around Some Canaliculi

A total of 15 canalicular maps and 9 bulk maps were collected, across three different mice. For 50% of the canalicular maps, tan δ exhibited a discernible spatial relationship between distance from the canalicular wall and tan δ. In all cases, these spatial relationships were best fit with either a quadratic or cubic fit. The adjusted R^2 values ranged from 25% to 65% for these maps. Among the canalicular maps with discernable spatial relationships between distance and tan δ, 70% demonstrated a pattern where tan δ values were initially high immediately adjacent to the canalicular wall (0 to 100 nm away), followed by a decrease as the distance into the extracellular matrix increased (Figure 5.6A). The remaining 30% of maps showed a pattern where tan δ values were high near the canalicular wall (within the first 50 nm), then decreased to a low value around 150 nm distance, before rising again into the extracellular matrix (Figure

5.6B). For other half of canalicular maps, linear, quadratic, or cubic polynomials were unable to adequately fit the data, indicating either no discernible pattern or high variability in the gradation of tan δ around these canaliculi (Figure 5.6C).

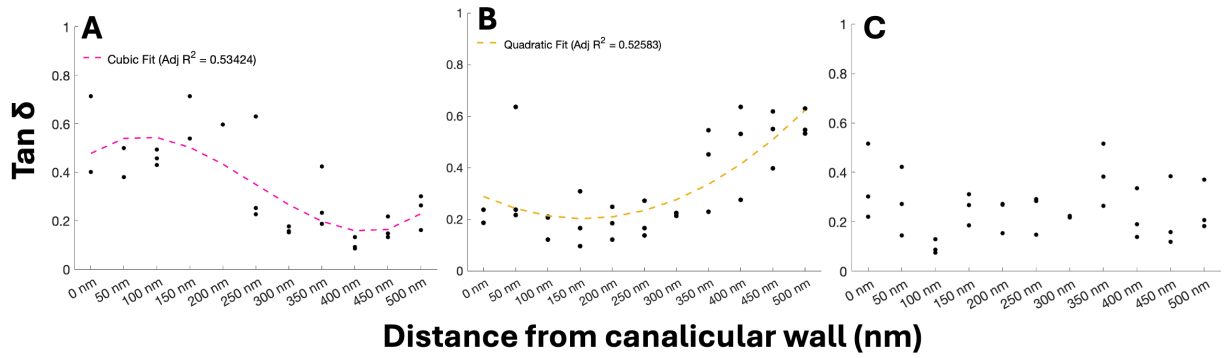

Figure 5.6. Energy dissipation gradation from canalicular walls. A-B) There is a distinct gradation pattern in tan δ values for half of the canalicular maps. From these maps, A) about 70% of them show a specific phenotype for tan δ gradations where tan δ reaches a peak adjacent to the canalicular wall (0 to 100 nm away), which is followed by a decrease as the distance into the extracellular matrix increases. Figure A is representing this first phenotype and data are fitted with a cubic polynomial (R^2 = 53%). B) About 30% of the maps with distinct gradation patterns for tan δ show a gradation where tan δ is relatively high near the canalicular wall (within the first 50 nm), but reaches a minimum value around 150 nm distance, before rising again and maxing out in the extracellular matrix away from canalicular wall. Figure B is representing this second phenotype and data are fitted with a quadratic polynomial (R^2 = 53%). C) The other half of tan δ maps did not show any gradation patterns for energy dissipation around canalicular wall.

5.4 Discussion

Bone is understood to be a viscoelastic tissue, but the range and magnitude of the viscoelasticity depends on the scale of the measurement. Prior work has evaluated bone viscoelasticity for hydrated tissues at the millimeter- and micrometer-length scales[64,509,510,512–516]. The nanometer length-scale is also important, since this length-scale is influenced by the activities of bone cells, including osteocytes[26,29,30,177,187]. Our prior work demonstrated that bone does show spatial variance in modulus at the nanometer-scale near osteocyte lacunae[30]. Bone

viscoelasticity has never been measured in hydrated cortical bone, and its spatial variance at the nanometer-scale, whether near or far from the LCS, is an unresolved question. The purpose of this study was to adapt a contact resonance atomic force microscopy (CR-AFM) technique for the measurement of nanometer-length scale variation in energy dissipation (tan δ). We present a robust, repeatable, and accessible method for collecting these types of measurements in bone. We also use this technique to determine that bone has highly heterogenous nanometer-scale viscoelasticity, which shows spatial patterning near many canaliculi.

Liquid CR-AFM revealed nanometer-scale measurements of bone viscoelasticity, with mean values comparable to micrometer-scale measurements of similar tissues[509]. Pathak et al measured tan δ in hydrated femurs (anterior-medial) of 16-weeks-old C57BL/6 mice, using dynamic nanoindentation with testing frequencies of 10–200 Hz. The authors reported a mean tan δ of ~ 0.2-0.4 for cortical bone, depending on the distance from the endocortical surface[509]. Our study's mean tan δ values closely align with these findings, as we reported an average tan δ of 0.307. Other studies on dehydrated mouse bones have reported much lower tan δ values, ranging from 0.02 to 0.07[551]. This highlights the significant influence of hydrated bone organic matrix and free water on bone viscoelastic properties. While bone mineral imparts stiffness to the material, the hydrated organic matrix and free water contribute to bone energy dissipation[509,552–554]. Common bone tissue dehydration techniques (e.g., ethanol dehydration) cause structural changes to bone matrix and both stiffen the tissue and reduce its viscoelasticity[243–245]. Therefore, studying bone tissue in a hydrated state is essential for characterizing material properties in a condition more similar to in-vivo performance.

While the overall range of our tan δ data is similar to the study by Pathak and co-authors, our heterogeneity is much greater, likely because of the increased resolution of our measurements. The microscale heterogeneity of tan δ observed in their study was ~0.1 to 0.5 for C57BL/6 mice[509]. We observe our range of tan δ values of ~0.02 to 0.8, whether in regions adjacent to canaliculi (up to 500 nm away from the canalicular wall) or in bulk bone tissue distant from canaliculi and lacunae. The impact of bone tissue material property heterogeneity on fracture behavior has been limited to spatial variation in modulus[526]. Now that viscoelasticity mapping is available at the nanometer-scale, these data could be employed to update the understanding of how the spatial variation in time-dependent measures affect bone mechanics, such as crack initiation and propagation, as well as how aging and bone diseases affect these viscoelasticity spatial distributions.

Since osteocytes can modify at least some properties of bone tissue (i.e., modulus)[30], we used CR-AFM to assess whether bone viscoelasticity differs with proximity to canaliculi. We chose to map canaliculi instead of lacunae since most interfaces between osteocytes and bone matrix are along canalicular walls[26,140,241]. First, we binned data within 0-100 nm, 100-500 nm, and >2 μm distances from canaliculi. Neither mean nor heterogeneity of tan δ differed between these three simple distance categories (**Error! Reference source not found.**). However, we observed discernible patterns in tan δ values with distance from the canalicular walls in a large percentage of the assessed canaliculi. About half of the mapped canaliculi showed either a moderate or strong quadratic or cubic fit of tan δ values versus distance from the canalicular wall. About 70% of these ‘patterned’ maps showed a trend where tan δ values are initially high immediately adjacent to the canalicular wall (0 to 100 nm away), followed by a decrease as the

distance into the extracellular matrix increases (Figure 5.6A). The remaining 30% of patterned maps showed a pattern where tan δ values are relatively high near the canalicular wall (within the first 50 nm), then decrease to a low value around 150 nm distance before rising again into the extracellular matrix (Figure 5.6B). These data demonstrate that the spatial distribution of viscoelasticity near osteocytes and their processes is considerably more variable that the spatial distribution of elasticity (i.e., reduced modulus) near lacunae measured from our earlier work[30]. We mapped moduli near osteocyte lacunae in dehydrated cortical bone and found a region of lower modulus bone adjacent to almost all lacunae[30]. However, there are important differences between these data sets, such as bone hydration, and mapping canaliculi vs lacunae. However, it is possible that modulus gradation primarily reflects variation in mineralization[64,555] while viscoelasticity gradation reflects a more complicated scenario of variation in mineralization as well as the cross-linking and hydration of the matrix. In this current paper, we did not investigate whether the variability in tan δ arises from significant differences in storage modulus (the elastic properties of bone, more associated with the bone inorganic matrix) or loss modulus (the damping or viscose property of bone, more associated with the bone organic matrix and bound water). These data would be valuable in future work.

Assessing the spatial variance in viscoelasticity is also important for understanding how osteocytes perceive strain. Osteocytes feel tissue strains both directly and through interstitial fluid flow within their LCS[168,169]. Osteocyte cell bodies and their processes can directly sense the tissue strain and mechanical deformation of the perilacunar and pericanalicular bone matrix[165–167]. It is well-established that some amount of strain amplification must occur for usual loads on the skeleton to translate to anabolic activity by the osteocyte[165–167]. Current modeling efforts to

estimate strain experienced by osteocytes have found that compliance in bone tissue local to osteocytes contributes to greater strain amplification than can be achieved by changes in lacunar and canalicular geometry [165,167,546,556]. If the LCS, or parts of the LCS, are surrounded by a 'sleeve' of viscoelastic tissue, this would have several important impacts for our understanding of osteocyte strain sensing. In a scenario where peri-LCS tissue is more compliant but is not more viscoelastic, strain is amplified and these changes in strain are instantaneous. In a situation where a similar-sized region of bone near the LCS is moderately viscoelastic, strain is still amplified, but less so, because of attenuation of the strain with time. The strain history would also become more complex as experienced by individual cells. It would be beneficial to revisit osteocyte mechanosensing through the lens of peri-LCS viscoelasticity distributions.

This study has important limitations. While bone was maintained in a hydrated state whenever possible during sample preparation and testing, some loss of bound water is inevitable with sample sectioning and polishing. Our tan δ maps were collected using liquid CR-AFM point measurements rather than continuous CR-AFM contact mapping, which would have improved map resolution. However, there are multiple challenges associated with this technique when used on samples with roughness and complicated topographical structures such as bones, including achieving a good contact during fast continuous mapping. Due to other technical limitations, it was not possible to directly measure E' and E''. Additionally, it would be valuable to determine which osteocyte canaliculi were recently mineralizing bone. These assessments are easier for lacunae, which readily show labels. Canaliculi are smaller and their size competes with the ability to discern labels using confocal microscopy.

We adapted CR-AFM for usage on bone and demonstrate that bone tissue energy dissipation (tan δ) is highly heterogenous in hydrated cortical bone for young adult female C57BL/6JN mice. On average, our nanometer-scale tan δ results are comparable to micrometer-scale tan δ measurements taken at the micrometer-scale for similar bone tissues (i.e., cortical mouse bone of the same strain and similar ages). However, our study reveals that (1) cortical bone tan δ is highly heterogenous and (2) that tan δ frequently shows spatial patterning near canaliculi. These data necessitate an updated understanding to the role of bone material property heterogeneity in bone biomechanics as well as the role of local viscoelasticity to osteocyte mechanosensation.

5.5 Acknowledgments

This research was made possible by the Department of Mechanical & Industrial Engineering and the College of Engineering at Montana State University. This work represents the views of the authors and not necessarily those of the sponsors. Research reported here is supported by NSF 2120239 and NIH R03AG068680. Kenna Brown, Connor Devine, and Steven Watson are thanked for their assistance with tissue harvest. This work was performed in part at the Montana Nanotechnology Facility, a member of the National Nanotechnology Coordinated Infrastructure (NNCI), which is supported by the National Science Foundation (Grant# ECCS-2025391). We thank Montana State University's Animal Resource Center staff and especially Tamara Marcotte for the help in providing excellent mouse care.

CHAPTER SIX

CONCLUSION AND FUTURE DIRECTIONS

Concluding Remarks

The purpose of this dissertation was to investigate the direct interactions of osteocytes with bone matrix via lacunar-canalicular system (LCS) turnover. Osteocytes have known, indirect roles in maintaining bone matrix quality and fracture resistance throughout life through regulating the activities of osteoblasts and osteoclasts. Osteocytes can also directly interact with bone matrix through removing and replacing bone tissue surrounding the LCS, but many gaps in knowledge existed about the prevalence of this process, the impacts on bone matrix quality, and the changes to this process with aging. These data are especially important when considering that we are at a pivotal point in the orthopedic field where treatments to target bone matrix properties are starting to be developed to manage bone fragility in aging. The goal for this dissertation was to advance knowledge about whether osteocyte direct interactions with the bone matrix through LCS turnover could represent an overlooked therapeutic target for bone fragility.

The long-term goal of this research direction is to determine whether changes to LCS turnover with aging impact bone fracture resistance (Figure 6.1), since this knowledge would direct whether LCS turnover is a potential treatment target in aging. However, many fundamental knowledge gaps need to be surmounted to answer this question. This dissertation research sought to investigate some of the most fundamental of these questions. The overarching hypothesis of this dissertation was that osteocyte LCS turnover is an abundant, frequent, and dynamic process

that plays an important role in maintaining the matrix properties (i.e., modulus and energy dissipation) of peri-LCS tissue, and that aging decreases the LCS turnover process.

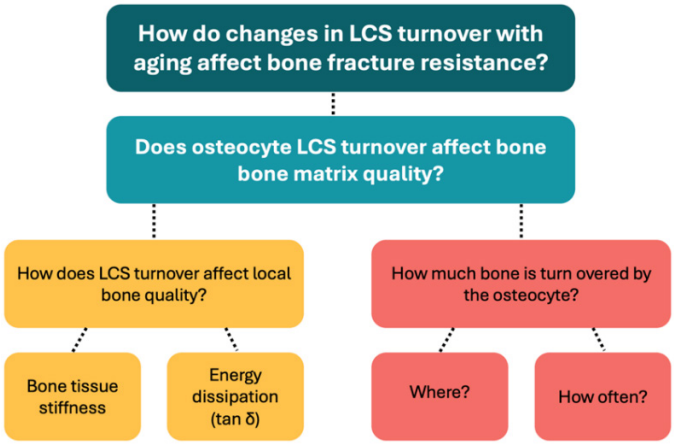

Figure 6.1. Schematic of dissertation research questions.

In **Chapter 3** "Aging decreases osteocyte lacunar-canalicular turnover in female C57BL/6JN mice", we presented novel evidence that osteocyte participation in mineralizing and resorbing the tissue in their LCS is highly abundant in both cortical and cancellous bone of young adult (5 month) female C57BL/6JN mice. We showed, for the first time, that aging significantly decreases the number of osteocytes engaged in LCS turnover. We shared the first evaluation of the impact of age on LCS turnover dynamics. Cortical and cancellous bone showed a different impact of age on LCS turnover, such that aged cancellous bone showed notably decreased label retention compared with cortical bone. Additionally, we demonstrated that under normal conditions osteocytes actively involved in mineralizing their surroundings have larger lacunae in both young and old bones. These data help explain a common observation in bone biology (i.e., smaller lacunae in aging), which has lacked a clear explanation until now. We reported that aging alters the relationship between osteocyte LCS turnover and natural variations in cortical tissue strain. Specifically, in aged but not young adult mice, the abundance and

dynamics of LCS bone mineralization showed an association with variation in cortical tissue strain. The large decline in LCS turnover in aging can have significant implications for bone quality and mechanosensation.

In **Chapter 4** "Perilacunar bone tissue exhibits sub-micrometer modulus gradation which depends on the recency of osteocyte bone formation in young adult and early-old-age C57BL/6 mice", we demonstrated that bone tissue modulus displays sub-micrometer gradation near osteocyte lacunae. Atomic force microscopy with nanoscale resolution revealed that modulus increases gradually from a minimum near the lacunar wall to a peak within 200-400 nm, then decays to reach bulk bone values. This is significant because we showed that microscale resolution, consistent with most prior efforts that do not show material property gradation around lacunae, fails to capture these gradations. Using AFM and fluorochrome labeling, we identified that perilacunar bone modulus gradation depends on recent LCS turnover activity. Labeled lacunae with recent LCS turnover mineralization are surrounded by a sleeve of lower modulus bone and have distinct modulus gradation compared to unlabeled lacunae. When comparing young adult bones to early old age bones, we discovered that perilacunar bone material properties are not influenced by age. Our findings demonstrate, for the first time, that the quality of a substantial amount of bone surrounding the LCS is directly influenced by osteocyte LCS turnover. These findings motivate investigating the direct influence of the osteocyte on bone quality in aging and disease.

In **Chapter 5** "Contact resonance atomic force microscopy on hydrated bone reveals nanometer-scale heterogeneity in energy dissipation that depends on proximity to canaliculi", we adapted CR-AFM technique for usage on bone and demonstrate that bone tissue energy

dissipation (tan δ) is highly heterogenous in hydrated cortical bone for young adult female C57BL/6JN mice. On average, our nanometer-scale tan δ results are comparable to micrometer-scale tan δ measurements taken at the micrometer-scale for similar bone tissues (i.e., cortical mouse bone of the same strain and similar ages). However, our study reveals that (1) cortical bone tan δ is highly heterogenous and (2) that tan δ frequently shows spatial patterning near canaliculi. This study is significant because it introduces a robust, repeatable, and accessible method for bone researchers to collect these types of data in bone and these data highlight a need to revisit the understanding of the impact of bone material property heterogeneity on bone biomechanics, as well as the role of local viscoelasticity in osteocyte mechanosensation.

Overall Takeaways

Data provided in this dissertation demonstrate that osteocyte LCS turnover is a prevalent, frequent, and dynamic process that influences the material properties of tissue surrounding the expansive LCS, but this process significantly declines with aging. Our findings together suggest that LCS turnover could play an important role in maintaining bone tissue matrix quality and mechanosensation and that LCS turnover could be a contributor to the loss of bone fracture resistance in aging. However, there is still a long way to understand the specific role of osteocyte LCS turnover in bone fracture resistance and the potential therapeutics targeting this process for bone fragility. Further research is necessary to comprehend the specific impacts of LCS turnover on several important aspects of bone mechanics and physiology, including (1) bone mechanosensation, which is essential for maintaining various characteristics of bone matrix quality and is influenced by aging and diseases, and (2) tissue toughening mechanism that bone employs across multiple length scales to resist fractures.

Future Directions

Each addressed research question spawns multiple new ones. Here, I will discuss key directions that could build upon this dissertation to bring us closer to designing new therapies targeting osteocyte LCS turnover to prevent bone fragility. These proposed future directions merely scratch the surface of the necessary investigations to unveil how osteocytes impact bone fracture resistance. Many other avenues of research can be explored as future directions, which might encompass understanding how much bone tissue is impacted by LCS turnover in a three-dimensional context, exploring the ramifications of various diseases and physiological conditions on LCS turnover, and evaluating the influence of bone fragility therapies on LCS turnover.

LCS Turnover and Mechanosensation

Osteocytes can perceive skeletal loading through fluid flow-induced shear stress, bone-loading-induced hydrostatic pressure, and loading-induced tissue strains[166,172,443,557]. Mechanical forces on bone can cause fluid to flow in the LCS, applying shear stress on osteocytes and their processes. This drag in turn would deform their membrane and trigger biological responses[172,558]. Osteocytes can also directly sense the local bone matrix strains through the integrins and focal adhesion complexes on their cell body and processes, which mechanically link the cytoskeleton to the extracellular matrix[559–561]. However, levels of tissue strain (typically <0.2%) due to bulk skeletal loadings are not sufficient to stimulate osteocyte signaling[562–564]. Modeling studies propose that small tissue deformations, when applied to the nanoscale actin filament bundles of the cell processes, can be amplified up to 2-3 orders of magnitude[166,172,443,557], which are likely to be biologically relevant to the intracellular biochemical responses of these cells[562–564]

Modifications to LCS turnover can have two-fold impacts on the strain sensed by osteocytes. First, mechanical and material properties of the per-LCS tissue (including elastic modulus and viscoelasticity or energy dissipation) can significantly impact the strains that are sensed by osteocyte as the deformation of the tissue would depend on its material properties[165–167,565]. Second, the varying shapes and sizes of osteocytes and their LCS can directly influence the local mechanical environment they experience and lead to modified mechanoresponses[165,566].

The current understanding is that strain amplification could occur because of changes to the material of peri-LCS tissue, which as we showed osteocyte LCS turnover contributes to these properties. Finite element models demonstrate that a decrease of approximately 40% in the tissue modulus surrounding the LCS leads to an increase of around 15% in tissue strain. Conversely, a 40% increase in perilacunar tissue modulus results in an approximate 10% decrease in maximum strain[165]. However, none of these models have considered the viscoelastic changes of the peri-LCS tissue to better understand the impact of LCS turnover on the strains sensed by osteocytes. We have provided these data for the first time in this dissertation. At minimum, our data suggest that strain amplification near osteocytes should be revisited to account for viscoelasticity. Future work would benefit from revisiting the link between peri-LCS material properties and osteocyte mechanosensation with the updated data provided in this dissertation.

Another aspect of strain amplification is the changes in LCS shape and dimensions which can induce distinct strain patterns along osteocyte lacunae and canaliculi and in their peri-LCS matrix[445,471,567,568]. Strain amplification factors ranging from 4.1 to 1.7 near cell bodies into the extracellular matrix[566] and amplifications of up to 70% near canaliculi-lacuna junctions[569,570] have been observed. Smaller and rounder lacunae in aging have been shown to decrease tissue

strains by around 5% in the vicinity of lacunae and their osteocytes[566]. Lacunar and canalicular enlargement with large perturbations to calcium homeostasis or smaller lacunae and canaliculi with aging implies changes to LCS turnover. Researchers have also demonstrated that the degeneration of LCS volume and connectivity in aging, particularly through the loss of canaliculi, leads to reduced osteocyte mechanosensation through imapired fluid dynamics[218]. However, these important data regarding osteocyte mechanosensation mechanisms need to be updated with our observed changes in the material environment surrounding the LCS for a more thorough understanding of the interactions between LCS turnover and mechanosensation.

It is possible that osteocytes, in response to various processes or conditions such as aging, disuse, and treatments, utilize their LCS turnover to modify their mechanosensation. Alternatively, LCS turnover might incidentally modify mechanosensation. It remains uncertain if LCS turnover serves as a secondary mechanism to mechanosensation, if mechanosensation is secondary to LCS turnover, or if both mechanisms work in tandem. Future studies can employ a more direct approach using in vivo mechanical loading studies together with osteocyte fluorochrome labeling and potentially calcium signaling assays to test this association.

LCS Turnover Tissue Toughening Mechanisms

It is still unknown whether and how LCS turnover specifically impacts bone fracture resistance. It remains undetermined which toughening mechanisms in bone tissue, if any, are influenced by this dynamic and frequent process. Although we did not investigate these critical gaps in this dissertation, the methodology and techniques developed here could benefit future investigations into these questions. The application of our introduced AFM methodology, particularly the technique to measure the viscoelasticity of hydrated tissue at the nanoscale, can

open doors to numerous exciting investigations. Measuring energy dissipation can be combined with other tools, including tools for assessment of tissue mineral and matrix properties (e.g., high-resolution Raman scattering confocal microscopy) as well as indentation-based methods for toughness assessment on a small scale, to systematically investigate if and how LCS turnover affects tissue toughening mechanisms at the nanometer scale. These studies could better elucidate the potential contributions of LCS turnover to bone tissue quality and its resistance to fracture, especially when researched in the contexts of aging, diseases, altered skeletal loading conditions, genetic modifications, and other conditions affecting the energy dissipation properties of perilacunar and pericanalicular tissue.

Osteocytes and Bone Fragility Therapeutics

Future work could significantly benefit from investigating the impact of bone fragility therapeutics on osteocyte LCS turnover. Current therapeutics for bone fragility, commonly designed to sustain and increase DXA-derived bone mineral density[124,571,572], include antiresorptive agents, anabolic agents, or a combination/sequential therapy of both. Further research is needed to understand the potential effects of these therapies on bone matrix quality, another determinant of bone fractur resistance, particularly through possible modifications to osteocyte and their LCS turnover activity. Bisphosphonate antiresorptive agents like alendronate, zoledronic acid, and denosumab (antibody to RankL) reduce the development, activation, survival, and bone resorption activity of osteoclasts[124,572–575]. Anabolic therapies, including teriparatide and romosozumab (sclerostin antibody), involve promoting bone formation through the activation of the canonical Wnt/beta-catenin pathway by downregulation of sclerostin expression in osteocytes[576–581]. It is possible that these drugs, through the suppression of the

RankL-OPG or sclerostin pathways and bone turnover, impacts osteocyte viability and LCS turnover dynamics. Therefore, a valuable future direction could involve investigating the impacts of these interventions on osteocyte LCS turnover and the subsequent effects on bone matrix quality and mechanosensation in accessible rodent models. This is particularly important considering that it is undetermined whether osteocyte-mediated bone resorption and mineralization is also influenced by these therapies by similar mechanisms.

Recently, bone matrix-modifying therapies are being explored, such as GL-0001, an analogue for glucose-dependent insulinotropic polypeptide/glucagon-like peptide-2 (GIP/GLP-2)[582]. GIP and GLP-2 have been the start of the idea of selectively targeting bone tissue material properties, such as enhancing collagen postprocessing and maturity, to improve bone strength, rather than directly addressing low bone mass[583,584]. GL-0001 works together with the cyclic adenosine monophosphate-lysyl oxidase pathway to improve the maturity of collagen and has been shown to enhances both the biomechanical parameters of cortical bone and the material properties of bone extracellular matrix[585]. However, it is unclear how this drug impacts osteocyte LCS turnover. This represents an important critical gap, especially when considering the significant interactions of osteocytes with tissue matrix quality.

Despite recent advancements in targeting bone matrix quality as a therapeutic approach for aging-related fragility, critical questions remain regarding the mechanisms of matrix decline in aging and factors regulating bone matrix quality. Osteocyte interactions with bone matrix, including their mineralization and resorption within lacunar-canalicular spaces, emerge as primary candidates for regulating bone matrix quality. The field of bone research is currently experiencing a pivotal era in the development of therapies targeting the bone matrix, and there is

a significant possibility that osteocytes could play a crucial role in the next generation of bone matrix-modifying interventions.

CUMULATIVE REFERENCES CITED

1. Siris, E. S. *et al. Bone Mineral Density Thresholds for Pharmacological Intervention to Prevent Fractures*.

2. Ensrud, K. E. Epidemiology of fracture risk with advancing age. *Journals of Gerontology - Series A Biological Sciences and Medical Sciences* **68**, 1236–1242 (2013). 10.1093/gerona/glt092

3. Burr, D. B. Changes in bone matrix properties with aging. *Bone* **120**, 85–93 (2019). 10.1016/j.bone.2018.10.010

4. Hernandez, C. J. & Keaveny, T. M. A biomechanical perspective on bone quality. *Bone* **39**, 1173–1181 (2006).

5. Nyman, J. S. & Makowski, A. J. The contribution of the extracellular matrix to the fracture resistance of bone. *Curr Osteoporos Rep* **10**, 169–177 (2012). 10.1007/s11914-012-0101-8

6. Singer, A. *et al.* Treatment rates and healthcare costs of patients with fragility fracture by site of care: a real-world data analysis. *Arch Osteoporos* **18**, (2023). 10.1007/s11657-023-01229-7

7. Almeida, M. Aging mechanisms in bone. *Bonekey Rep* **1**, (2012).

8. Razi, H. *et al.* Aging leads to a dysregulation in mechanically driven bone formation and resorption. *Journal of Bone and Mineral Research* **30**, 1864–1873 (2015).

9. Tu, K. N. *et al. Osteoporosis: A Review of Treatment Options*. **43**, (2018).

10. Cauley, J. A. Osteoporosis: fracture epidemiology update 2016. *Curr Opin Rheumatol* **29**, 150–156 (2017).

11. Services, U. S. D. of H. and H. Bone health and osteoporosis: a report of the Surgeon General. *Rockville, MD: US Department of Health and Human Services, Office of the Surgeon General* **87**, (2004).

12. Bliuc, D., Alarkawi, D., Nguyen, T. V., Eisman, J. A. & Center, J. R. Risk of subsequent fractures and mortality in elderly women and men with fragility fractures with and without osteoporotic bone density: The dubbo osteoporosis epidemiology study. *Journal of Bone and Mineral Research* **30**, 637–646 (2015). 10.1002/jbmr.2393

13. Schuit, S. C. E. *et al.* Fracture incidence and association with bone mineral density in elderly men and women: the Rotterdam Study. *Bone* **34**, 195–202 (2004).

14. Seeman, E. Bone quality: The material and structural basis of bone strength. *J Bone Miner Metab* **26**, 1–8 (2008). 10.1007/s00774-007-0793-5

15. Zimmermann, E. A. & Ritchie, R. O. Bone as a Structural Material. *Adv Healthc Mater* **4**, 1287–1304 (2015). 10.1002/adhm.201500070

16. Zimmermann, E. A. *et al.* Age-related changes in the plasticity and toughness of human cortical bone at multiple length scales. *Proceedings of the National Academy of Sciences* **108**, 14416–14421 (2011).

17. Boskey, A. L. & Coleman, R. Critical reviews in oral biology & medicine: Aging and bone. *J Dent Res* **89**, 1333–1348 (2010). 10.1177/0022034510377791

18. Nalla, R. K., Kruzic, J. J., Kinney, J. H. & Ritchie, R. O. Effect of aging on the toughness of human cortical bone: Evaluation by R-curves. *Bone* **35**, 1240–1246 (2004). 10.1016/j.bone.2004.07.016

19. Fyhrie, D. Summary--Measuring" bone quality". *J Musculoskelet Neuronal Interact* **5**, 318–320 (2005).

20. Turner, C. H. Biomechanics of Bone: Determinants of Skeletal Fragility and Bone Quality. *Osteoporosis International* 97–104 (2002).

21. Donnelly, E. Methods for assessing bone quality: A review. *Clin Orthop Relat Res* **469**, 2128–2138 (2011). PMC3126959

22. Bouxsein, M. L. Bone quality: where do we go from here? *Osteoporos Int* **14 Suppl 5**, 118–127 (2003). 10.1007/s00198-003-1489-x

23. Fonseca, H., Moreira-Gonçalves, D., Coriolano, H. J. A. & Duarte, J. A. Bone quality: The determinants of bone strength and fragility. *Sports Medicine* **44**, 37–53 (2014). 10.1007/s40279-013-0100-7

24. Alliston, T. Biological regulation of bone quality. *Curr Osteoporos Rep* **12**, 366–375 (2014). 10.1007/s11914-014-0213-4

25. Unal, M., Creecy, A. & Nyman, J. S. The role of matrix composition in the mechanical behavior of bone. *Curr Osteoporos Rep* **16**, 205–215 (2018).

26. Heveran, C. M. & Boerckel, J. D. Osteocyte Remodeling of the Lacunar-Canalicular System: What's in a Name? *Current Osteoporosis Reports* **21**, 11–20 (2023). 10.1007/s11914-022-00766-3

27. Schurman, C. A. *et al.* Aging impairs the osteocytic regulation of collagen integrity and bone quality. *Bone Res* **12**, 13 (2024). 10.1038/s41413-023-00303-7

28. Vahidi, G., Rux, C., Sherk, V. D. & Heveran, C. M. Lacunar-canalicular bone remodeling: impacts on bone quality and tools for assessment. *Bone* 115663 (2020). doi:10.1016/j.bone.2020.115663 10.1016/j.bone.2020.115663

29. Vahidi, G., Boone, C., Hoffman, F. & Heveran, C. Aging decreases osteocyte lacunar-canalicular turnover in female C57BL/6 mice. *bioRxiv* 2023.12.15.571934 (2023). doi:10.1101/2023.12.15.571934 10.1101/2023.12.15.571934

30. Rux, C. J., Vahidi, G., Darabi, A., Cox, L. M. & Heveran, C. M. Perilacunar bone tissue exhibits sub-micrometer modulus gradation which depends on the recency of osteocyte bone formation in both young adult and early-old-age female C57Bl/6 mice. *Bone* **157**, (2022). 10.1016/j.bone.2022.116327

31. Robling, A. G. & Bonewald, L. F. The Osteocyte: New Insights. (2020).

32. Luca Dalle Carbonare MD & S. Giannini. Bone microarchitecture as an important determinant of bone strength. *Journal of Endocrinological Investigation* **27**, 99–105 (2004).

33. Beevers, C. A. & McIntyre, D. B. The atomic structure of fluor-apatite and its relation to that of tooth and bone material. (With Plates XVI-XVIII.). *Mineralogical Magazine and Journal of the Mineralogical Society* **27**, 254–257 (1946). DOI: 10.1180/minmag.1946.027.194.05

34. KAY, M. I., YOUNG, R. A. & POSNER, A. S. Crystal Structure of Hydroxyapatite. *Nature* **204**, 1050–1052 (1964). 10.1038/2041050a0

35. Sandberg, M. M. Matrix in cartilage and bone development: current views on the function and regulation of major organic components. *Ann Med* **23**, 207–217 (1991).

36. Garnero, P. The role of collagen organization on the properties of bone. *Calcif Tissue Int* **97**, 229–240 (2015).

37. Depalle, B. *et al.* Osteopontin regulates type I collagen fibril formation in bone tissue. *Acta Biomater* **120**, 194–202 (2021).

38. Stock, S. R. The mineral–collagen interface in bone. *Calcif Tissue Int* **97**, 262–280 (2015).

39. Ingram, R. T., Clarke, B. L., Fisher, L. W. & Fitzpatrick, L. A. Distribution of noncollagenous proteins in the matrix of adult human bone: evidence of anatomic and functional heterogeneity. *Journal of Bone and Mineral Research* **8**, 1019–1029 (2020).

40. Nair, A. K., Gautieri, A., Chang, S.-W. & Buehler, M. J. Molecular mechanics of mineralized collagen fibrils in bone. *Nat Commun* **4**, 1724 (2013).

41. Rodriguez-Palomo, A., Østergaard, M. & Birkedal, H. Bone Hierarchical Structure: Heterogeneity and Uniformity. *Advanced Functional Materials* (2023). doi:10.1002/adfm.202307026 10.1002/adfm.202307026

42. Reznikov, N., Shahar, R. & Weiner, S. Bone hierarchical structure in three dimensions. *Acta Biomater* **10**, 3815–3826 (2014). https://doi.org/10.1016/j.actbio.2014.05.024

43. Buss, D. J., Kröger, R., McKee, M. D. & Reznikov, N. Hierarchical organization of bone in three dimensions: A twist of twists. *J Struct Biol X* **6**, 100057 (2022). https://doi.org/10.1016/j.yjsbx.2021.100057

44. Rho, J.-Y., Kuhn-Spearing, L. & Zioupos, P. Mechanical properties and the hierarchical structure of bone. *Med Eng Phys* **20**, 92–102 (1998). https://doi.org/10.1016/S1350-4533(98)00007-1

45. Hernandez, C. J. & van der Meulen, M. C. H. Understanding Bone Strength Is Not Enough. *Journal of Bone and Mineral Research* **32**, 1157–1162 (2017). 10.1002/jbmr.3078

46. Hart, N. H. *et al.* Biological basis of bone strength: anatomy, physiology and measurement. *J Musculoskelet Neuronal Interact* **20**, 347 (2020).

47. Ritchie, R. O., Kinney, J. H., Kruzic, J. J. & Nalla, R. K. A fracture mechanics and mechanistic approach to the failure of cortical bone. *Fatigue Fract Eng Mater Struct* **28**, 345–371 (2005).

48. Willie, B. M., Zimmermann, E. A., Vitienes, I., Main, R. P. & Komarova, S. V. Bone adaptation: Safety factors and load predictability in shaping skeletal form. *Bone* **131**, 115114 (2020).

49. Ritchie, R. O. The conflicts between strength and toughness. *Nat Mater* **10**, 817–822 (2011). 10.1038/nmat3115

50. Ritchie, R. O. How does human bone resist fracture? in *Annals of the New York Academy of Sciences* **1192**, 72–80 (Blackwell Publishing Inc., 2010). 10.1111/j.1749-6632.2009.05232.x

51. Zimmermann, E. A., Barth, H. D. & Ritchie, R. O. The multiscale origins of fracture resistance in human bone and its biological degradation. *JOM* **64**, 486–493 (2012). 10.1007/s11837-012-0298-0

52. Nalla, R. K., Kruzic, J. J. & Ritchie, R. O. On the origin of the toughness of mineralized tissue: Microcracking or crack bridging? *Bone* **34**, 790–798 (2004). 10.1016/j.bone.2004.02.001

53. Launey, M. E., Buehler, M. J. & Ritchie, R. O. On the Mechanistic Origins of Toughness in Bone. *Annu Rev Mater Res* **40**, 25–53 (2010). 10.1146/annurev-matsci-070909-104427

54. Koester, K. J., Ager Iii, J. W. & Ritchie, R. O. The true toughness of human cortical bone measured with realistically short cracks. *Nat Mater* **7**, 672–677 (2008).

55. Zimmermann, E. A., Gludovatz, B., Schaible, E., Busse, B. & Ritchie, R. O. Fracture resistance of human cortical bone across multiple length-scales at physiological strain rates. *Biomaterials* **35**, 5472–5481 (2014). 10.1016/j.biomaterials.2014.03.066

56. Nyman, J. S., Granke, M., Singleton, R. C. & Pharr, G. M. Tissue-level mechanical properties of bone contributing to fracture risk. *Curr Osteoporos Rep* **14**, 138–150 (2016).

57. Ritchie, R. O. Mechanisms of fatigue-crack propagation in ductile and brittle solids. *Int J Fract* **100**, 55–83 (1999).

58. Burr, D. B. *et al.* Does microdamage accumulation affect the mechanical properties of bone? *J Biomech* **31**, 337–345 (1998). 10.1016/S0021-9290(98)00016-5

59. Peterlik, H., Roschger, P., Klaushofer, K. & Fratzl, P. From brittle to ductile fracture of bone. *Nat Mater* **5**, 52–55 (2006).

60. Burr, D. B. *et al.* Bone microdamage and skeletal fragility in osteoporotic and stress fractures. *Journal of Bone and Mineral Research* **12**, 6–15 (1997).

61. Kiebzak, G. M. Age-related bone changes. *Exp Gerontol* **26**, 171–187 (1991).

62. Boskey, A. L. & Imbert, L. Bone quality changes associated with aging and disease: a review. *Ann N Y Acad Sci* **1410**, 93–106 (2017). 10.1111/nyas.13572

63. Granke, M., Does, M. D. & Nyman, J. S. The Role of Water Compartments in the Material Properties of Cortical Bone. *Calcified Tissue International* **97**, 292–307 (2015). 10.1007/s00223-015-9977-5

64. Singleton, R. C., Pharr, G. M. & Nyman, J. S. Increased tissue-level storage modulus and hardness with age in male cortical bone and its association with decreased fracture toughness. *Bone* **148**, (2021). 10.1016/j.bone.2021.115949

65. Roschger, P., Paschalis, E. P., Fratzl, P. & Klaushofer, K. Bone mineralization density distribution in health and disease. *Bone* **42**, 456–466 (2008). 10.1016/j.bone.2007.10.021

66. Boyde, A., Travers, R., Glorieux, F. H. & Jones, S. J. The mineralization density of iliac crest bone from children with osteogenesis imperfecta. *Calcif Tissue Int* **64**, 185–190 (1999). 10.1007/s002239900600

67. Reid, S. A. & Boyde, A. Changes in the mineral density distribution in human bone with age: image analysis using backscattered electrons in the SEM. *Journal of Bone and Mineral Research* **2**, 13–22 (1987).

68. Perilli, E. *et al.* Failure strength of human vertebrae: Prediction using bone mineral density measured by DXA and bone volume by micro-CT. *Bone* **50**, 1416–1425 (2012). 10.1016/j.bone.2012.03.002

69. Ferguson, V. L., Ayers, R. A., Bateman, T. A. & Simske, S. J. Bone development and age-related bone loss in male C57BL/6J mice. *Bone* **33**, 387–398 (2003). 10.1016/S8756-3282(03)00199-6

70. Wang, X., Shen, X., Li, X. & Mauli Agrawal, C. Age-related changes in the collagen network and toughness of bone. *Bone* **31**, 1–7 (2002).

71. Suchanek, W. & Yoshimura, M. Processing and properties of hydroxyapatite-based biomaterials for use as hard tissue replacement implants. *J Mater Res* **13**, 94–117 (1998).

72. He, L.-H., Standard, O. C., Huang, T. T. Y., Latella, B. A. & Swain, M. V. Mechanical behaviour of porous hydroxyapatite. *Acta Biomater* **4**, 577–586 (2008).

73. Saito, M. & Marumo, K. Collagen cross-links as a determinant of bone quality: A possible explanation for bone fragility in aging, osteoporosis, and diabetes mellitus. *Osteoporosis International* **21**, 195–214 (2010). 10.1007/s00198-009-1066-z

74. Wegst, U. G. K., Bai, H., Saiz, E., Tomsia, A. P. & Ritchie, R. O. Bioinspired structural materials. *Nat Mater* **14**, 23–36 (2015). 10.1038/nmat4089

75. Reznikov, N., Steele, J. A. M., Fratzl, P. & Stevens, M. M. A materials science vision of extracellular matrix mineralization. *Nat Rev Mater* **1**, 1–14 (2016).

76. Weiner, S. & Wagner, H. D. The material bone: structure-mechanical function relations. *Annual review of materials science* **28**, 271–298 (1998).

77. Fratzl, P., Kolednik, O., Fischer, F. D. & Dean, M. N. The mechanics of tessellations–bioinspired strategies for fracture resistance. *Chem Soc Rev* **45**, 252–267 (2016).

78. Reznikov, N., Bilton, M., Lari, L., Stevens, M. M. & Kröger, R. Fractal-like hierarchical organization of bone begins at the nanoscale. *Science (1979)* **360**, (2018). 10.1126/science.aao2189

79. Buehler, M. J. Molecular nanomechanics of nascent bone: fibrillar toughening by mineralization. *Nanotechnology* **18**, 295102 (2007).

80. Smith, B. L. *et al.* Molecular mechanistic origin of the toughness of natural adhesives, fibres and composites. *Nature* **399**, 761–763 (1999).

81. Gupta, H. S. *et al.* Fibrillar level fracture in bone beyond the yield point. *Int J Fract* **139**, 425–436 (2006).

82. Taylor, D., Hazenberg, J. G. & Lee, T. C. Living with cracks: damage and repair in human bone. *Nat Mater* **6**, 263–268 (2007).

83. Paschalis, E. P. *et al.* Bone fragility and collagen cross-links. *Journal of Bone and Mineral Research* **19**, 2000–2004 (2004).

84. McNerny, E. M. B., Gong, B., Morris, M. D. & Kohn, D. H. Bone fracture toughness and strength correlate with collagen cross-link maturity in a dose-controlled lathyrism mouse model. *Journal of Bone and Mineral Research* **30**, 446–455 (2015). 10.1002/jbmr.2356

85. Paschalis, E. P. *et al.* Spectroscopic characterization of collagen cross-links in bone. *Journal of bone and mineral research* **16**, 1821–1828 (2001).

86. Unal, M. & Akkus, O. Raman spectral classification of mineral- and collagen-bound water's associations to elastic and post-yield mechanical properties of cortical bone. *Bone* **81**, 315–326 (2015). 10.1016/j.bone.2015.07.024

87. Voide, R. *et al.* Time-lapsed assessment of microcrack initiation and propagation in murine cortical bone at submicrometer resolution. *Bone* **45**, 164–173 (2009). 10.1016/j.bone.2009.04.248

88. Qiu, S., Rao, D. S., Fyhrie, D. P., Palnitkar, S. & Parfitt, A. M. The morphological association between microcracks and osteocyte lacunae in human cortical bone. *Bone* **37**, 10–15 (2005).

89. Vashishth, D., Verborgt, O., Divine, G., Schaffler, M. B. & Fyhrie, D. P. Decline in osteocyte lacunar density in human cortical bone is associated with accumulation of microcracks with age. *Bone* **26**, 375–380 (2000). 10.1016/S8756-3282(00)00236-2

90. Koester, K. J., Ager, J. W. & Ritchie, R. O. The effect of aging on crack-growth resistance and toughening mechanisms in human dentin. *Biomaterials* **29**, 1318–1328 (2008). 10.1016/j.biomaterials.2007.12.008

91. Zimmermann, E. A. *et al.* Age-related changes in the plasticity and toughness of human cortical bone at multiple length scales. *Proceedings of the National Academy of Sciences* **108**, 14416–14421 (2011).

92. Vashishth, D., Tanner, K. E. & Bonfield, W. Experimental validation of a microcracking-based toughening mechanism for cortical bone. *J Biomech* **36**, 121–124 (2003).

93. Nalla, R. K., Kinney, J. H. & Ritchie, R. O. Mechanistic fracture criteria for the failure of human cortical bone. *Nat Mater* **2**, 164–168 (2003).

94. Safadi, F. F. *et al.* Bone structure, development and bone biology. *Bone pathology* 1–50 (2009).

95. Ozawa, H., Hoshi, K. & Amizuka, N. Current concepts of bone biomineralization. *J Oral Biosci* **50**, 1–14 (2008).

96. Bianco, P. Structure and mineralization of bone. in *Calcification in biological systems* 243–268 (CRC Press, 2020).

97. Boskey, A. L. Mineralization of Bones and Teeth. *Elements* **3**, 385–391 (2007).

98. Pivonka, P. *et al.* Model structure and control of bone remodeling: a theoretical study. *Bone* **43**, 249–263 (2008).

99. Hadjidakis, D. J. & Androulakis, I. I. Bone remodeling. *Ann N Y Acad Sci* **1092**, 385–396 (2006).

100. Allen, M. R. & Burr, D. B. Bone modeling and remodeling. in *Basic and applied bone biology* 75–90 (Elsevier, 2014).

101. Sims, N. A. & Martin, T. J. Coupling the activities of bone formation and resorption: a multitude of signals within the basic multicellular unit. *Bonekey Rep* **3**, (2014). 10.1038/bonekey.2013.215

102. Robling, A. G., Castillo, A. B. & Turner, C. H. Biomechanical and molecular regulation of bone remodeling. *Annual Review of Biomedical Engineering* **8**, 455–498 (2006). 10.1146/annurev.bioeng.8.061505.095721

103. Manolagas, S. C. From estrogen-centric to aging and oxidative stress: a revised perspective of the pathogenesis of osteoporosis. *Endocr Rev* **31**, 266–300 (2010).

104. Carina, V. *et al.* Bone's response to mechanical loading in aging and osteoporosis: molecular mechanisms. *Calcif Tissue Int* **107**, 301–318 (2020).

105. Bektas, A., Schurman, S. H., Sen, R. & Ferrucci, L. Aging, inflammation and the environment. *Exp Gerontol* **105**, 10–18 (2018).

106. Wu, M., Fannin, J., Rice, K. M., Wang, B. & Blough, E. R. Effect of aging on cellular mechanotransduction. *Ageing Res Rev* **10**, 1–15 (2011).

107. Pataky, M. W., Young, W. F. & Nair, K. S. Hormonal and metabolic changes of aging and the influence of lifestyle modifications. in *Mayo Clinic Proceedings* **96**, 788–814 (Elsevier, 2021).

108. Zhang, L. *et al.* Regulatory cellular and molecular networks in the bone microenvironment during aging. *Life Medicine* lnae019 (2024).

109. Currey, J. D., Brear, K. & Zioupos, P. The effects of ageing and changes in mineral content in degrading the toughness of human femora. *J Biomech* **29**, 257–260 (1996).

110. McCalden, R. W., McGeough, J. A. & Barker, M. B. Age-related changes in the tensile properties of cortical bone. The relative importance of changes in porosity, mineralization, and microstructure. *JBJS* **75**, 1193–1205 (1993).

111. Yeni, Y. N., Brown, C. U. & Norman, T. L. Influence of bone composition and apparent density on fracture toughness of the human femur and tibia. *Bone* **22**, 79–84 (1998).

112. Boyce, T. M. & Bloebaum, R. D. Cortical aging differences and fracture implications for the human femoral neck. *Bone* **14**, 769–778 (1993).

113. Vashishth, D. *et al.* Influence of nonenzymatic glycation on biomechanical properties of cortical bone. *Bone* **28**, 195–201 (2001).

114. Koester, K. J., Barth, H. D. & Ritchie, R. O. Effect of aging on the transverse toughness of human cortical bone: Evaluation by R-curves. *J Mech Behav Biomed Mater* **4**, 1504–1513 (2011). https://doi.org/10.1016/j.jmbbm.2011.05.020

115. Nalla, R. K. *et al.* Role of microstructure in the aging-related deterioration of the toughness of human cortical bone. *Materials Science and Engineering: C* **26**, 1251–1260 (2006). https://doi.org/10.1016/j.msec.2005.08.021

116. Raggatt, L. J. & Partridge, N. C. Cellular and molecular mechanisms of bone remodeling. *Journal of Biological Chemistry* **285**, 25103–25108 (2010). 10.1074/jbc.R109.041087

117. Teitelbaum SL. Bone resorption by osteoclasts. *Science (1979)* **289**, 1504–1508 (2000).

118. McDonald, M. M., Kim, A. S., Mulholland, B. S. & Rauner, M. New Insights Into Osteoclast Biology. *JBMR Plus* **5**, (2021). 10.1002/jbm4.10539

119. Marks Jr, S. C. & Seifert, M. F. The lifespan of osteoclasts: experimental studies using the giant granule cytoplasmic marker characteristic of beige mice. *Bone* **6**, 451–455 (1985).

120. Loutit, J. F. & Townsend, K. M. Longevity of osteoclasts in radiation chimaeras of osteopetrotic beige and normal mice. *Br J Exp Pathol* **63**, 221 (1982).

121. Ahn, H., Kim, J. M., Lee, K., Kim, H. & Jeong, D. Extracellular acidosis accelerates bone resorption by enhancing osteoclast survival, adhesion, and migration. *Biochem Biophys Res Commun* **418**, 144–148 (2012).

122. Dougall, W. C. Molecular pathways: osteoclast-dependent and osteoclast-independent roles of the RANKL/RANK/OPG pathway in tumorigenesis and metastasis. *Clinical Cancer Research* **18**, 326–335 (2012).

123. Cummings, S. R. *et al.* Denosumab for Prevention of Fractures in Postmenopausal Women with Osteoporosis. *New England Journal of Medicine* **361**, 756–765 (2009). 10.1056/nejmoa0809493

124. Rogers, M. J., Crockett, J. C., Coxon, F. P. & Mönkkönen, J. Biochemical and molecular mechanisms of action of bisphosphonates. *Bone* **49**, 34–41 (2011). 10.1016/j.bone.2010.11.008

125. Mizoguchi, T. & Ono, N. The diverse origin of bone-forming osteoblasts. *Journal of Bone and Mineral Research* **36**, 1432–1447 (2021). 10.1002/jbmr.4410

126. Garg, P. *et al.* Prospective Review of Mesenchymal Stem Cells Differentiation into Osteoblasts. *Orthopaedic Surgery* **9**, 13–19 (2017). 10.1111/os.12304

127. Long, F. Building strong bones: Molecular regulation of the osteoblast lineage. *Nature Reviews Molecular Cell Biology* **13**, 27–38 (2012). 10.1038/nrm3254

128. Wang, K. *et al.* Osteocytes but not osteoblasts directly build mineralized bone structures. *Int J Biol Sci* **17**, 2430–2448 (2021). 10.7150/ijbs.61012

129. Hasegawa, T. *et al.* Matrix Vesicle-Mediated Mineralization and Osteocytic Regulation of Bone Mineralization. *International Journal of Molecular Sciences* **23**, (2022). 10.3390/ijms23179941

130. Parfitt, A. M. Osteonal and hemi-osteonal remodeling: The spatial and temporal framework for signal traffic in adult human bone. *J Cell Biochem* **55**, 273–286 (1994).

131. Bonewald, L. F. The amazing osteocyte. *Journal of bone and mineral research* **26**, 229–238 (2011).

132. S.C. Miller and W. S. S. Jee. The Bone Lining Cell: A Distinct Phenotype? *Calcified Tissue International* **41**, 1–5 (1987).

133. Jilka, R. L., Weinstein, R. S., Parfitt, A. M. & Manolagas, S. C. Quantifying osteoblast and osteocyte apoptosis: Challenges and rewards. *Journal of Bone and Mineral Research* **22**, 1492–1501 (2007). 10.1359/jbmr.070518

134. Kim, J. M., Lin, C., Stavre, Z., Greenblatt, M. B. & Shim, J. H. Osteoblast-Osteoclast Communication and Bone Homeostasis. *Cells* **9**, (2020). 10.3390/cells9092073

135. Shun-ichi Harada & Gideon A. Rodan. Control of osteoblast function and regulation of bone mass. *Nature* **423**, 349–355 (1991).

136. Jacome-Galarza, C. E. *et al.* Developmental origin, functional maintenance and genetic rescue of osteoclasts. *Nature* **568**, 541–545 (2019).

137. Luo, X. *et al.* Stromal-initiated changes in the bone promote metastatic niche development. *Cell Rep* **14**, 82–92 (2016).

138. Schaffler, M. B., Cheung, W. Y., Majeska, R. & Kennedy, O. Osteocytes: Master orchestrators of bone. *Calcif Tissue Int* **94**, 5–24 (2014). PMC3947191

139. Prideaux, M., Findlay, D. M. & Atkins, G. J. Osteocytes: The master cells in bone remodelling. *Curr Opin Pharmacol* **28**, 24–30 (2016). 10.1016/j.coph.2016.02.003

140. Buenzli, P. R. & Sims, N. A. Quantifying the osteocyte network in the human skeleton. *Bone* **75**, 144–150 (2015). 10.1016/j.bone.2015.02.016

141. Franz-Odendaal, T. A., Hall, B. K. & Witten, P. E. Buried alive: how osteoblasts become osteocytes. *Dev Dyn* **235**, 176–190 (2006).

142. Holmbeck, K. *et al.* The metalloproteinase MT1-MMP is required for normal development and maintenance of osteocyte processes in bone. *J Cell Sci* **118**, 147–156 (2005).

143. Barragan-Adjemian, C. *et al.* Mechanism by which MLO-A5 late osteoblasts/early osteocytes mineralize in culture: similarities with mineralization of lamellar bone. *Calcif Tissue Int* **79**, 340–353 (2006).

144. Dallas, S. L., Prideaux, M. & Bonewald, L. F. The osteocyte: An endocrine cell . . . and more. *Endocrine Reviews* **34**, 658–690 (2013). 10.1210/er.2012-1026

145. Baron, R. & Kneissel, M. WNT signaling in bone homeostasis and disease: from human mutations to treatments. *Nature Medicine* **19**, 179–192 (2013). 10.1038/nm.3074

146. Bullock, W. A., Pavalko, F. M. & Robling, A. G. Osteocytes and mechanical loading: The Wnt connection. *Orthod Craniofac Res* **22**, 175–179 (2019). 10.1111/ocr.12282

147. Tu, X. *et al.* Osteocytes mediate the anabolic actions of canonical Wnt/β-catenin signaling in bone. *Proc Natl Acad Sci U S A* **112**, E478–E486 (2015). 10.1073/pnas.1409857112

148. Pathak, J. L. *et al.* Systemic Inflammation Affects Human Osteocyte-Specific Protein and Cytokine Expression. *Calcif Tissue Int* **98**, 596–608 (2016). 10.1007/s00223-016-0116-8

149. Xiong, J. & O'Brien, C. A. Osteocyte RANKL: New insights into the control of bone remodeling. *Journal of Bone and Mineral Research* **27**, 499–505 (2012). 10.1002/jbmr.1547

150. Bellido, T. Osteocyte-driven bone remodeling. *Calcified Tissue International* **94**, 25–34 (2014). 10.1007/s00223-013-9774-y

151. Pathak, J. L. *et al.* Mechanical loading reduces inflammation-induced human osteocyte-to-osteoclast communication. *Calcif Tissue Int* **97**, 169–178 (2015). 10.1007/s00223-015-9999-z

152. Sanchez, C., Gabay, O., Salvat, C., Henrotin, Y. E. & Berenbaum, F. Mechanical loading highly increases IL-6 production and decreases OPG expression by osteoblasts. *Osteoarthritis Cartilage* **17**, 473–481 (2009). 10.1016/j.joca.2008.09.007

153. Tan, S. D. *et al.* Osteocytes subjected to fluid flow inhibit osteoclast formation and bone resorption. *Bone* **41**, 745–751 (2007). 10.1016/j.bone.2007.07.019

154. Udagawa, N. *et al.* Osteoclast differentiation by RANKL and OPG signaling pathways. *J Bone Miner Metab* **39**, 19–26 (2021). 10.1007/s00774-020-01162-6

155. Nakashima, T. *et al.* Evidence for osteocyte regulation of bone homeostasis through RANKL expression. *Nat Med* **17**, 1231–1234 (2011). 10.1038/nm.2452

156. Kim, H. N. *et al.* Osteocyte RANKL is required for cortical bone loss with age and is induced by senescence. *JCI Insight* **5**, (2020). 10.1172/jci.insight.138815

157. Kim, B., Cho, Y. & Lim, W. Osteoporosis therapies and their mechanisms of action (Review). *Exp Ther Med* **22**, (2021). 10.3892/etm.2021.10815

158. Bonewald, L. F. & Wacker, M. J. FGF23 production by osteocytes. *Pediatric Nephrology* **28**, 563–568 (2013). 10.1007/s00467-012-2309-3

159. Martin, A., David, V. & Quarles, L. D. REGULATION AND FUNCTION OF THE FGF23/KLOTHO ENDOCRINE PATHWAYS. *Physiol Rev* **92**, 131–155 (2012). 10.1152/physrev.00002.2011.-Cal

160. Liu, S. *et al.* Pathogenic role of Fgf23 in Hyp mice. *Am J Physiol Endocrinol Metab* **291**, 38–49 (2006). 10.1152/ajpendo.00008.2006.-Inactivating

161. Choi, J. U. A., Kijas, A. W., Lauko, J. & Rowan, A. E. The Mechanosensory Role of Osteocytes and Implications for Bone Health and Disease States. *Frontiers in Cell and Developmental Biology* **9**, (2022). 10.3389/fcell.2021.770143

162. Mirza, M. A. I., Larsson, A., Lind, L. & Larsson, T. E. Circulating fibroblast growth factor-23 is associated with vascular dysfunction in the community. *Atherosclerosis* **205**, 385–390 (2009).

163. Ben-Dov, I. Z. *et al.* The parathyroid is a target organ for FGF23 in rats. *Journal of Clinical Investigation* **117**, 4003–4008 (2007). 10.1172/JCI32409

164. Krajisnik, T. *et al.* Fibroblast growth factor-23 regulates parathyroid hormone and 1α-hydroxylase expression in cultured bovine parathyroid cells. *Journal of Endocrinology* **195**, 125–131 (2007). 10.1677/JOE-07-0267

165. Rath Bonivtch, A., Bonewald, L. F. & Nicolella, D. P. Tissue strain amplification at the osteocyte lacuna: A microstructural finite element analysis. *J Biomech* **40**, 2199–2206 (2007). 10.1016/j.jbiomech.2006.10.040

166. Nicolella, D. P., Moravits, D. E., Gale, A. M., Bonewald, L. F. & Lankford, J. Osteocyte lacunae tissue strain in cortical bone. *J Biomech* **39**, 1735–1743 (2006). 10.1016/j.jbiomech.2005.04.032

167. Nicolella, D. P. *et al.* Effects of nanomechanical bone tissue properties on bone tissue strain: Implications for osteocyte mechanotransduction. *Journal of Musculoskeletal Neuronal Interactions* **8**, 330–331 (2008).

168. Tiwari, A. K. & Prasad, J. Computer modelling of bone's adaptation: the role of normal strain, shear strain and fluid flow. *Biomech Model Mechanobiol* **16**, 395–410 (2017). 10.1007/s10237-016-0824-z

169. Donahue, S. W., Jacobs, C. R. & Donahue, H. J. *Flow-induced calcium oscillations in rat osteoblasts are age, loading frequency, and shear stress dependent*.

170. Lewis, K. J. Osteocyte calcium signaling – A potential translator of mechanical load to mechanobiology. *Bone* **153**, (2021). 10.1016/j.bone.2021.116136

171. Burger, E. H. & Klein-Nulend, J. Mechanotransduction in bone—role of the lacunocanalicular network. *The FASEB Journal* **13**, 101–112 (1999). 10.1096/fasebj.13.9001.s101

172. Han, Y., Cowin, S. C., Schaffler, M. B. & Weinbaum, S. *Mechanotransduction and strain amplification in osteocyte cell processes*. *PNAS* **101**, (2004).

173. Pathak, J. L., Bravenboer, N. & Klein-Nulend, J. The Osteocyte as the New Discovery of Therapeutic Options in Rare Bone Diseases. *Front Endocrinol (Lausanne)* **11**, 1–14 (2020). 10.3389/fendo.2020.00405

174. Bacabac, R. G., Van Loon, J. J. W. A. & Klein-Nulend, J. Microgravity and Bone Cell Mechanosensitivity. *Biology in Space and Life on Earth: Effects of Spaceflight on Biological Systems* **22**, 157–177 (2007). 10.1002/9783527617005.ch6

175. Hemmatian, H., Bakker, A. D., Klein-Nulend, J. & van Lenthe, G. H. Aging, Osteocytes, and Mechanotransduction. *Curr Osteoporos Rep* **15**, 401–411 (2017).

176. Alemi, A. S. *et al.* Glucocorticoids cause mandibular bone fragility and suppress osteocyte perilacunar-canalicular remodeling. *Bone Rep* **9**, 145–153 (2018).

177. Yee, C. S., Schurman, C. A., White, C. R. & Alliston, T. Investigating Osteocytic Perilacunar/Canalicular Remodeling. *Current Osteoporosis Reports* **17**, 157–168 (2019). 10.1007/s11914-019-00514-0

178. Yee, C. S., Schurman, C. A., White, C. R. & Alliston, T. Investigating Osteocytic Perilacunar/Canalicular Remodeling. *Curr Osteoporos Rep* **17**, 157–168 (2019).

179. Kegelman, C. D. *et al.* YAP and TAZ Mediate Osteocyte Perilacunar/Canalicular Remodeling. *Journal of Bone and Mineral Research* **00**, 1–15 (2019). 10.1002/jbmr.3876

180. Dole, N. S., Yee, C. S., Mazur, C. M., Acevedo, C. & Alliston, T. TGFβ Regulation of Perilacunar/Canalicular Remodeling Is Sexually Dimorphic. *Journal of Bone and Mineral Research* **35**, 1549–1561 (2020). 10.1002/jbmr.4023

181. Dole, N. S., Yee, C. S., Mazur, C. M., Acevedo, C. & Alliston, T. TGFβ regulation of perilacunar/canalicular remodeling is sexually dimorphic. *Journal of Bone and Mineral Research* **35**, 1549–1561 (2020).

182. Qing, H. *et al.* Demonstration of osteocytic perilacunar/canalicular remodeling in mice during lactation. *Journal of Bone and Mineral Research* **27**, 1018–1029 (2012). 10.1002/jbmr.1567

183. Gardinier, J. D., Al-Omaishi, S., Morris, M. D. & Kohn, D. H. PTH signaling mediates perilacunar remodeling during exercise. *Matrix Biology* **52–54**, 162–175 (2016). PMC4875803

184. Qing, H. & Bonewald, L. F. Osteocyte remodeling of the perilacunar and pericanalicular matrix. *International journal of oral science* **1**, 59–65 (2009). 10.4248/ijos.09019

185. Wysolmerski, J. J. Osteocytes remove and replace perilacunar mineral during reproductive cycles. *Bone* **54**, 230–236 (2013). 10.1016/j.bone.2013.01.025

186. Dole, N. S. *et al.* Osteocyte-Intrinsic TGF-β Signaling Regulates Bone Quality through Perilacunar/Canalicular Remodeling. *Cell Rep* **21**, 2585–2596 (2017). 10.1016/j.celrep.2017.10.115

187. Tang, S., Herber, R.-P., Ho, S. & Alliston, T. Matrix Metalloproteinase-13 is Required for Osteocytic Perilacunar Remodeling and Maintains Bone Fracture Resistance SY. *J Bone Miner Res.* **27**, 1936–1950 (2012). 10.1002/jbmr.1646.Matrix

188. Farr, J. N. *et al.* Identification of Senescent Cells in the Bone Microenvironment. *Journal of Bone and Mineral Research* **31**, 1917–1919 (2016). 10.1002/jbmr.2994

189. Wang, Z. *et al.* Inflammation produced by senescent osteocytes mediates age-related bone loss. *Front Immunol* **14**, (2023). 10.3389/fimmu.2023.1114006

190. Sherk, V. D. & Rosen, J. Senescent and apoptotic osteocytes and aging : Exercise to the rescue ? **121**, 255–258 (2019). PMC6459182

191. Onal, M. *et al.* Suppression of autophagy in osteocytes mimics skeletal aging. *Journal of Biological Chemistry* **288**, 17432–17440 (2013). 10.1074/jbc.M112.444190

192. Chen, K., Yang, Y. H., Jiang, S. D. & Jiang, L. S. Decreased activity of osteocyte autophagy with aging may contribute to the bone loss in senile population. *Histochem Cell Biol* **142**, 285–295 (2014). 10.1007/s00418-014-1194-1

193. Jilka, R. L., Noble, B. & Weinstein, R. S. Osteocyte apoptosis. *Bone* **54**, 264–271 (2013). PMC3624050

194. Belanger, L. R. Osteocytic Osteolysis. *Calcif Tissue Int* **12**, 1–12 (1969).

195. Wergedal, J. E. & Baylink, D. J. *Distribution of acid and alkaline phosphatase activity ix un-demineralized sections of the rat tibial diaphysis*. (1969).

196. Baylink, D. J., Wergedal, J. E., Baylink, J. & J-, D. *Bone formation by osteocytes*. *AMERICAN JOURNAL OF PHYSIOLOGY* **221**, (1971).

197. Tazawa, K. *et al.* Osteocytic osteolysis observed in rats to which parathyroid hormone was continuously administered. *J Bone Miner Metab* **22**, 524–529 (2004). 10.1007/s00774-004-0519-x

198. Krempien, B. & Ritz, E. Effects of parathyroid hormone on osteocytes. Ultrastructural evidence for anisotropic osteolysis and involvement of the cytoskeleton. *Metab Bone Dis Relat Res* **1**, 55–65 (1978).

199. McKee, M. D. & Nanci, A. Osteopontin at mineralized tissue interfaces in bone, teeth, and osseointegrated implants: ultrastructural distribution and implications for mineralized tissue formation, turnover, and repair. *Microsc Res Tech* **33**, 141–164 (1996).

200. PARFITT, A. M. The cellular basis of bone turnover and bone loss: a rebuttal of the osteocytic resorption—bone flow theory. *Clin Orthop Relat Res* 236–247 (1977).

201. Lotinun, S. *et al.* Cathepsin K-deficient osteocytes prevent lactation-induced bone loss and parathyroid hormone suppression. *J Clin Invest* (2019).

202. Li, Y. *et al.* Maternal bone adaptation to mechanical loading during pregnancy, lactation, and post-weaning recovery. *Bone* **151**, (2021). 10.1016/j.bone.2021.116031

203. Kaya, S. *et al.* Lactation-induced changes in the volume of osteocyte lacunar-canalicular space alter mechanical properties in cortical bone tissue. *Journal of Bone and Mineral Research* **32**, 688–697 (2017). PMC5395324

204. Wysolmerski, J. J. Osteocytic osteolysis: time for a second look? *Bonekey Rep* **1**, (2012).

205. Jähn-Rickert, K. & Zimmermann, E. A. Potential Role of Perilacunar Remodeling in the Progression of Osteoporosis and Implications on Age-Related Decline in Fracture Resistance of Bone. *Current Osteoporosis Reports* **19**, 391–402 (2021). 10.1007/s11914-021-00686-8

206. Heveran, C. M., Rauff, A., King, K. B., Carpenter, R. D. & Ferguson, V. L. A new open-source tool for measuring 3D osteocyte lacunar geometries from confocal laser scanning microscopy reveals age-related changes to lacunar size and shape in cortical mouse bone. *Bone* **110**, (2018). PMC5878731

207. Schurman, C. A., Verbruggen, S. W. & Alliston, T. Disrupted osteocyte connectivity and pericellular fluid flow in bone with aging and defective TGF- β signaling. 1–11 (2021). doi:10.1073/pnas.2023999118/-/DCSupplemental.Published 10.1073/pnas.2023999118/-/DCSupplemental.Published

208. Tiede-Lewis, L. A. M. & Dallas, S. L. Changes in the osteocyte lacunocanalicular network with aging. *Bone* **122**, 101–113 (2019). 10.1016/j.bone.2019.01.025

209. Christopher, X. & Kovacs, S. Maternal Mineral and Bone Metabolism During Pregnancy, Lacta-tion, and Post-Weaning Recovery. *Physiol Rev* **96**, 449–547 (2016). 10.1152/physrev.00027.2015.-During

210. Liu, X. S., Wang, L., de Bakker, C. M. J. & Lai, X. Mechanical Regulation of the Maternal Skeleton during Reproduction and Lactation. *Current Osteoporosis Reports* **17**, 375–386 (2019). 10.1007/s11914-019-00555-5

211. Jähn, K. *et al.* Osteocytes Acidify Their Microenvironment in Response to PTHrP In Vitro and in Lactating Mice In Vivo. *Journal of Bone and Mineral Research* **32**, 1761–1772 (2017). 10.1002/jbmr.3167

212. Dole, N. S. *et al.* Osteocyte-intrinsic TGF-β signaling regulates bone quality through perilacunar/canalicular remodeling. *Cell Rep* **21**, 2585–2596 (2017).

213. Yajima, A. *et al.* Osteocytic perilacunar/canalicular turnover in hemodialysis patients with high and low serum PTH levels. *Bone* **113**, 68–76 (2018). 10.1016/j.bone.2018.05.002

214. Morrell, A. E., Robinson, S. T., Silva, M. J. & Guo, X. E. Mechanosensitive Ca2+ signaling and coordination is diminished in osteocytes of aged mice during ex vivo tibial loading. *Connect Tissue Res* **61**, 389–398 (2020). 10.1080/03008207.2020.1712377

215. Holguin, N., Brodt, M. D., Sanchez, M. E. & Silva, M. J. Aging diminishes lamellar and woven bone formation induced by tibial compression in adult C57BL/6. *Bone* **65**, 83–91 (2014). 10.1016/j.bone.2014.05.006

216. Mullender, M. G., Van Der Meer, D. D., Huiskes, R. & Lips, P. Osteocyte density changes in aging and osteoporosis. *Bone* **18**, 109–113 (1996). 10.1016/8756-3282(95)00444-0

217. LeAnn M. Tiede-Lewis, Y. X. M. A. H. R. C. M. R. D. V. D. L. F. B. S. L. D. Degeneration of the osteocyte network in the C57BL/6 mouse model of aging. *Aging* **9**, 2190–2208 (2017).

218. Schurman, C. A., Verbruggen, S. W. & Alliston, T. Disrupted osteocyte connectivity and pericellular fluid flow in bone with aging and defective TGF-β signaling. *Proceedings of the National Academy of Sciences* **118**, e2023999118 (2021). 10.1073/pnas.2023999118/-/DCSupplemental

219. Hemmatian, H. *et al.* Age-related changes in female mouse cortical bone microporosity. *Bone* **113**, 1–8 (2018).

220. Busse, B. *et al.* Decrease in the osteocyte lacunar density accompanied by hypermineralized lacunar occlusion reveals failure and delay of remodeling in aged human bone. *Aging Cell* **9**, 1065–1075 (2010).

221. Mullender, M. G., Van Der Meer, D. D., Huiskes, R. & Lips, P. Osteocyte density changes in aging and osteoporosis. *Bone* **18**, 109–113 (1996).

222. Bach-Gansmo, F. L. *et al.* Osteocyte lacunar properties and cortical microstructure in human iliac crest as a function of age and sex. *Bone* **91**, 11–19 (2016).

223. Carter, Y. *et al.* Variation in osteocyte lacunar morphology and density in the human femur—a synchrotron radiation micro-CT study. *Bone* **52**, 126–132 (2013).

224. Teti, A. & Zallone, A. Do osteocytes contribute to bone mineral homeostasis? Osteocytic osteolysis revisited. *Bone* **44**, 11–16 (2009).

225. AZ, Z. Z., Teti, A., Nico, B. & Primavera, M. V. Osteoplastic activity of mature osteocytes evaluated by H-proline incorporation. *Basic Appl Histochem* **26**, 65–67 (1982).

226. Kamel-ElSayed, S. A., Tiede-Lewis, L. M., Lu, Y., Veno, P. A. & Dallas, S. L. Novel approaches for two and three dimensional multiplexed imaging of osteocytes. *Bone* **76**, 129–140 (2015). PMC4591054

227. Youlten, S. E. *et al.* Osteocyte transcriptome mapping identifies a molecular landscape controlling skeletal homeostasis and susceptibility to skeletal disease. *Nat Commun* **12**, (2021). 10.1038/s41467-021-22517-1

228. Wee, N. K., Sims, N. A. & Morello, R. The Osteocyte Transcriptome: Discovering Messages Buried Within Bone. *Current Osteoporosis Reports* **19**, 604–615 (2021). 10.1007/s11914-021-00708-5

229. Nioi, P. *et al.* Transcriptional Profiling of Laser Capture Microdissected Subpopulations of the Osteoblast Lineage Provides Insight into the Early Response to Sclerostin Antibody in Rats. *Journal of Bone and Mineral Research* **30**, 1457–1467 (2015). 10.1002/jbmr.2482

230. Zimmerman, S. M., Dimori, M., Heard-Lipsmeyer, M. E. & Morello, R. The Osteocyte Transcriptome Is Extensively Dysregulated in Mouse Models of Osteogenesis Imperfecta. *JBMR Plus* **3**, (2019). 10.1002/jbm4.10171

231. Lane, N. E. *et al.* Glucocorticoid-Treated Mice Have Localized Changes in Trabecular Bone Material Properties and Osteocyte Lacunar Size That Are Not Observed in Placebo-Treated or Estrogen-Deficient Mice. *Journal of Bone and Mineral Research* **21**, 466–476 (2005).

232. Gardinier, J. D., Al-Omaishi, S., Morris, M. D. & Kohn, D. H. PTH signaling mediates perilacunar remodeling during exercise. *Matrix Biology* **52–54**, 162–175 (2016). PMC4875803

233. Sharma, D. *et al.* Alterations in the osteocyte lacunar–canalicular microenvironment due to estrogen deficiency. *Bone* **51**, 488–497 (2012).

234. Stern, A. R. *et al.* Effect of osteoporosis treatment agents on the cortical bone osteocyte microenvironment in adult estrogen-deficient, osteopenic rats. *Bone Rep* **8**, 115–124 (2018). 10.1016/j.bonr.2018.02.005

235. Milovanovic, P. *et al.* Osteocytic canalicular networks: Morphological implications for altered mechanosensitivity. *ACS Nano* **7**, 7542–7551 (2013). 10.1021/nn401360u

236. Bach-Gansmo, F. L. *et al.* Osteocyte lacunar properties in rat cortical bone: Differences between lamellar and central bone. *J Struct Biol* **191**, 59–67 (2015). PMID:26023043

237. Kaya, S. *et al.* Lactation-Induced Changes in the Volume of Osteocyte Lacunar-Canalicular Space Alter Mechanical Properties in Cortical Bone Tissue. *Journal of Bone and Mineral Research* **32**, 688–697 (2017). PMC5395324

238. Zhang, S., Bach-gansmo, F. L., Xia, D., Besenbacher, F. & Birkedal, H. Nanostructure and mechanical property of the osteocyte lacunar-canalicular network associated bone matrix revealed by quantitative nanomechanical mapping. (2015). doi:10.1007/s12274-015-0825-8 10.1007/s12274-015-0825-8

239. Vahidi, G., Rux, C., Sherk, V. D. & Heveran, C. M. Lacunar-canalicular bone remodeling: Impacts on bone quality and tools for assessment. *Bone* **143**, 115663 (2021). PMC7769905

240. Hesse, B. *et al.* Canalicular network morphology is the major determinant of the spatial distribution of mass density in human bone tissue: Evidence by means of synchrotron radiation phase-contrast nano-CT. *Journal of Bone and Mineral Research* **30**, 346–356 (2015). 10.1002/jbmr.2324

241. Nango, N. *et al.* Osteocyte-directed bone demineralization along canaliculi. *Bone* **84**, 279–288 (2016).

242. Killgore, J. P. & Delrio, F. W. Contact Resonance Force Microscopy for Viscoelastic Property Measurements: From Fundamentals to State-of-the-Art Applications. *Macromolecules* **51**, 6977–6996 (2018). 10.1021/acs.macromol.8b01178

243. Bushby, A., Ferguson, V. & Boyde, A. Nanoindentation of bone: Comparison of specimens tested in liquid and embedded in polymethylmethacrylate. *J Mater Res* **19**, 249–259 (2004).

244. Feng, L., Chittenden, M., Schirer, J., Dickinson, M. & Jasiuk, I. Mechanical properties of porcine femoral cortical bone measured by nanoindentation. *J Biomech* **45**, 1775–1782 (2012). 10.1016/j.jbiomech.2012.05.001

245. Granke, M., Does, M. D. & Nyman, J. S. The role of water compartments in the material properties of cortical bone. *Calcif Tissue Int* **97**, 292–307 (2015). 10.1007/s00223-015-9977-5

246. Parlak, Z., Tu, Q. & Zauscher, S. Liquid contact resonance AFM: Analytical models, experiments, and limitations. *Nanotechnology* **25**, (2014). 10.1088/0957-4484/25/44/445703

247. Tung, R. C., Killgore, J. P. & Hurley, D. C. Liquid contact resonance atomic force microscopy via experimental reconstruction of the hydrodynamic function. *J Appl Phys* **115**, (2014). 10.1063/1.4882755

248. Kocun, M., Labuda, A., Gannepalli, A. & Proksch, R. Contact resonance atomic force microscopy imaging in air and water using photothermal excitation. *Review of Scientific Instruments* **86**, (2015). 10.1063/1.4928105

249. Schaffler, M. B., Cheung, W. Y., Majeska, R. & Kennedy, O. Osteocytes: Master orchestrators of bone. *Calcif Tissue Int* **94**, 5–24 (2014). PMC3947191

250. Yee, C. S., Schurman, C. A., White, C. R. & Alliston, T. Investigating Osteocytic Perilacunar/Canalicular Remodeling. *Curr Osteoporos Rep* **17**, 157–168 (2019).

251. Bonewald, L. F. The amazing osteocyte. *Journal of Bone and Mineral Research* **26**, 229–238 (2011). PMC3179345

252. Buenzli, P. R. & Sims, N. A. Quantifying the osteocyte network in the human skeleton. *Bone* **75**, 144–150 (2015). PMID:25708054

253. Varga, P. *et al.* Synchrotron X-ray phase nano-tomography-based analysis of the lacunar–canalicular network morphology and its relation to the strains experienced by osteocytes in situ as predicted by case-specific finite element analysis. *Biomech Model Mechanobiol* **14**, 267–282 (2015). 10.1007/s10237-014-0601-9

254. Beno, T., Yoon, Y. J., Cowin, S. C. & Fritton, S. P. Estimation of bone permeability using accurate microstructural measurements. *J Biomech* **39**, 2378–2387 (2006). 10.1016/j.jbiomech.2005.08.005

255. Remaggi, F., Canè, V., Palumbo, C. & Ferretti, M. Histomorphometric study on the osteocyte lacuno-canalicular network in animals of different species. I. Woven-fibered and parallel-fibered bones. *Ital J Anat Embryol* **103**, 145–155 (1998).

256. Qing, H. & Bonewald, L. F. Osteocyte remodeling of the perilacunar and pericanalicular matrix. *Int J Oral Sci* **1**, 59–65 (2009). PMC3470108

257. Belanger, L. F. & Migicovsky, B. B. Histochemical evidence of proteolysis in bone: the influence of parathormone. *Journal of histochemistry & cytochemistry* **11**, 734–737 (1963).

258. Belanger, L. R. Osteocytic Osteolysis. *Calcif Tissue Int* **12**, 1–12 (1969).

259. Qing, H. *et al.* Demonstration of Osteocytic Perilacunar / Canalicular Remodeling During Lactation. *JBMR* **27**, 1018–1029 (2012). PMC3770147

260. Wysolmerski, J. J. Osteocytic osteolysis: time for a second look? *Bonekey Rep* **1**, 229 (2012). 10.1038/bonekey.2012.229

261. Tazawa, K. *et al.* Osteocytic osteolysis observed in rats to which parathyroid hormone was continuously administered. *JBMR* **22**, 524–529 (2004). 10.1007/s00774-004-0519-x

262. Heveran, C. M., Rauff, A., King, K. B., Carpenter, R. D. & Ferguson, V. L. A new open-source tool for measuring 3D osteocyte lacunar geometries from confocal laser scanning microscopy reveals age-related changes to lacunar size and shape in cortical mouse bone. *Bone* **110**, 115–127 (2018).

263. Tiede-Lewis, L. M. *et al.* Degeneration of the osteocyte network in the C57Bl/6 mouse model of aging. *Aging* **9**, 2190–2208 (2017). PMC5680562

264. Gerbaix, M. *et al.* One-month spaceflight compromises the bone mechanical properties, osteocyte survival and lacunae volume in mature mice skeletons. *Sci Rep* **7**, 2659 (2017). PMC5453937

265. Britz, H. M., Carter, Y., Jokihaara, J. & Leppanen, O. Prolonged unloading in growing rats reduces cortical osteocyte lacunar density and volume in the distal tibia. *Bone* **51**, 913–919 (2012).

266. Swift, J. M., Swift, S. N., Allen, M. R. & Bloomfield, S. A. Beta-1 Adrenergic Agonist Treatment Mitigates Negative Changes in Cancellous Bone Microarchitecture and Inhibits Osteocyte Apoptosis During Disuse. **9**, 1–8 (2014). PMC4161377

267. Jähn, K. *et al.* Osteocytes Acidify Their Microenvironment in Response to PTHrP In Vitro and in Lactating Mice In Vivo. *Journal of Bone and Mineral Research* **32**, 1761–1772 (2017).

268. Alemi, A. S. *et al.* Glucocorticoids cause mandibular bone fragility and suppress osteocyte perilacunar-canalicular remodeling. *Bone Rep* **9**, 145–153 (2018).

269. Fowler, T. W. *et al.* Glucocorticoid suppression of osteocyte perilacunar remodeling is associated with subchondral bone degeneration in osteonecrosis. *Sci Rep* **7**, 44618 (2017).

270. Dole, N. S. *et al.* Osteocyte-Intrinsic TGF-β Signaling Regulates Bone Quality through Perilacunar/Canalicular Remodeling. *Cell Rep* **21**, 2585–2596 (2017). PMC6014615

271. Lotinun, S. *et al.* Cathepsin K-deficient osteocytes prevent lactation-induced bone loss and parathyroid hormone suppression. *J Clin Invest* **130**, 3058–3071 (2019). PMC6668688

272. Sekita, A., Matsugaki, A., Ishimoto, T. & Nakano, T. Synchronous disruption of anisotropic arrangement of the osteocyte network and collagen/apatite in melanoma bone metastasis. *J Struct Biol* **197**, 260–270 (2017).

273. Yajima, A. *et al.* Osteocytic perilacunar/canalicular turnover in hemodialysis patients with high and low serum PTH levels. *Bone* **113**, 68–76 (2018). PMID:29738853

274. Nango, N. *et al.* Osteocyte-directed bone demineralization along canaliculi. *Bone* **84**, 279–288 (2016). PMID:26709236

275. Kaya, S. *et al.* Lactation-induced changes in the volume of osteocyte lacunar-canalicular space alter mechanical properties in cortical bone tissue. *Journal of Bone and Mineral Research* **32**, 688–697 (2017). PMC5395324

276. Ruffoni, D., Fratzl, P., Roschger, P., Klaushofer, K. & Weinkamer, R. The bone mineralization density distribution as a fingerprint of the mineralization process. *Bone* **40**, 1308–1319 (2007).

277. Martin, B. Mathematical model for the mineralization of bone. *Journal of Orthopaedic Research* **12**, 375–383 (1994).

278. Donnelly, E., Boskey, A. L., Baker, S. P. & Van Der Meulen, M. C. H. Effects of tissue age on bone tissue material composition and nanomechanical properties in the rat cortex. *J Biomed Mater Res A* **92**, 1048–1056 (2010). PMC4160143

279. Boskey, A. L. Mineralization of Bones and Teeth. *Elements* **3**, 385–391 (2007).

280. Nyman, J. S. *et al.* Age-related effect on the concentration of collagen crosslinks in human osteonal and interstitial bone tissue. *Bone* **39**, 1210–1217 (2006). PMC1847577

281. Lloyd, A. A. *et al.* Atypical fracture with long-term bisphosphonate therapy is associated with altered cortical composition and reduced fracture resistance. *PNAS* **114**, (2017). 10.1073/pnas.1704460114

282. Roschger, P., Paschalis, E. P., Fratzl, P. & Klaushofer, K. Bone mineralization density distribution in health and disease. *Bone* **42**, 456–466 (2008).

283. Schaffler, M. B., Choi, K. & Milgrom, C. Aging and matrix microdamage accumulation in human compact bone. *Bone* **17**, 521–525 (1995).

284. Hemmatian, H. *et al.* Age-related changes in female mouse cortical bone microporosity. *Bone* **113**, 1–8 (2018).

285. Hemmatian, H. *et al.* Mechanical Loading Differentially Affects Osteocytes in Fibulae from Lactating Mice Compared to Osteocytes in Virgin Mice: Possible Role for Lacuna Size. *Calcif Tissue Int* **103**, 675–685 (2018). PMC6208961

286. Tiede-Lewis, L. M. *et al.* Degeneration of the osteocyte network in the C57Bl/6 mouse model of aging. *Aging* **9**, 2190–2208 (2017). PMC5680562

287. Tang, S. Y., Herber, R. P., Ho, S. P. & Alliston, T. Matrix metalloproteinase-13 is required for osteocytic perilacunar remodeling and maintains bone fracture resistance. *Journal of Bone and Mineral Research* **27**, 1936–1950 (2012). PMC3415585

288. Kegelman, C. D. *et al.* YAP and TAZ Mediate Osteocyte Perilacunar/Canalicular Remodeling. *Journal of Bone and Mineral Research* **00**, 1–15 (2019). 10.1002/jbmr.3876

289. Mazur, C. M. *et al.* Osteocyte dysfunction promotes osteoarthritis through MMP13-dependent suppression of subchondral bone homeostasis. *Bone Res* 1–17 (2019). doi:10.1038/s41413-019-0070-y 10.1038/s41413-019-0070-y

290. Ritchie, R. O. *et al.* Measurement of the toughness of bone: A tutorial with special reference to small animal studies. *Bone* **43**, 798–812 (2008).

291. Wittig, N. K. *et al.* No Signature of Osteocytic Osteolysis in Cortical Bone from Lactating NMRI Mice. *Calcif Tissue Int* **105**, 308–315 (2019). 10.1007/s00223-019-00569-2

292. Boass, A., Garner, S. C., Schultz, V. L. & Toverud, S. U. Regulation of serum calcitriol by serum ionized calcium in rats during pregnancy and lactation. *Journal of Bone and Mineral Research* **12**, 909–914 (1997).

293. Knight, C. H., Maltz, E. & Docherty, A. H. Milk yield and composition in mice: Effects of litter size and lactation number. *Comp Biochem Physiol A Physiol* **84**, 127–133 (1986). 10.1016/0300-9629(86)90054-X

294. Speakman, J. R. The physiological costs of reproduction in small mammals. *Philosophical Transactions of the Royal Society B: Biological Sciences* **363**, 375–398 (2008). 10.1098/rstb.2007.2145

295. Gardinier, J. D., Al-Omaishi, S., Rostami, N., Morris, M. D. & Kohn, D. H. Examining the influence of PTH(1-34) on tissue strength and composition. *Bone* **117**, 130–137 (2018).

296. Tokarz, D. *et al.* Hormonal regulation of osteocyte perilacunar and canalicular remodeling in the hyp mouse model of x-linked hypophosphatemia. *Journal of Bone and Mineral Research* **33**, 499–509 (2018).

297. Misof, B. M. *et al.* Bone matrix mineralization and osteocyte lacunae characteristics in patients with chronic kidney disease - mineral bone disorder (CKD-MBD). *J Musculoskelet Neuronal Interact* **19**, 196–206 (2019).

298. Heveran, C. M. *et al.* Chronic kidney disease and aging differentially diminish bone material and microarchitecture in C57Bl/6 mice. *Bone* **127**, 91–103 (2019). PMC6760860

299. Busse, B. *et al.* Decrease in the osteocyte lacunar density accompanied by hypermineralized lacunar occlusion reveals failure and delay of remodeling in aged human bone. *Aging Cell* **9**, 1065–1075 (2010).

300. Vashishth, D., Verborgt, O., Divine, G., Schaffler, M. B. & Fyhrie, D. P. Decline in osteocyte lacunar density in human cortical bone is associated with accumulation of microcracks with age. *Bone* **26**, 375–380 (2000).

301. Mullender, M. G., Van Der Meer, D. D., Huiskes, R. & Lips, P. Osteocyte density changes in aging and osteoporosis. *Bone* **18**, 109–113 (1996).

302. Bach-Gansmo, F. L. *et al.* Osteocyte lacunar properties and cortical microstructure in human iliac crest as a function of age and sex. *Bone* **91**, 11–19 (2016). PMID:27397700

303. Carter, Y., Thomas, C. D. L., Clement, J. G. & Cooper, D. M. L. Femoral osteocyte lacunar density, volume and morphology in women across the lifespan. *J Struct Biol* **183**, 519–526 (2013).

304. Farr, J. *et al.* Identification of senescent cells in the bone microenvironment. *Journal of Bone and Mineral Research* **31**, 1920–1929 (2016).

305. Sherk, V. D. & Rosen, J. Senescent and apoptotic osteocytes and aging : Exercise to the rescue ? *Bone* **121**, 255–258 (2019). PMC6459182

306. Jilka, R. L., Noble, B. & Weinstein, R. S. Osteocyte apoptosis. *Bone* **54**, 264–271 (2013). PMC3624050

307. Bach-Gansmo, F. L., Wittig, N. K., Brüel, A., Thomsen, J. S. & Birkedal, H. Immobilization and long-term recovery results in large changes in bone structure and

strength but no corresponding alterations of osteocyte lacunar properties. *Bone* **91**, 139–147 (2016). 10.1016/j.bone.2016.07.005

308. Blaber, E. A. *et al.* Microgravity Induces Pelvic Bone Loss through Osteoclastic Activity, Osteocytic Osteolysis, and Osteoblastic Cell Cycle Inhibition by CDKN1a/p21. *PLoS One* **8**, (2013). 10.1371/journal.pone.0061372

309. Kohrt, W. M. *et al.* Maintenance of Serum Ionized Calcium During Exercise Attenuates Parathyroid Hormone and Bone Resorption Responses. *Journal of Bone and Mineral Research* **33**, 1326–1334 (2018). 10.1002/jbmr.3428

310. Kohrt, W. M. *et al.* Dermal calcium loss is not the primary determinant of parathyroid hormone secretion during exercise. *Med Sci Sports Exerc* **51**, 2117–2124 (2019).

311. Suniaga, S., Rolvien, T., Scheidt, A., Fiedler, I. A. K. & Hrishikesh, A. Increased mechanical loading through controlled swimming exercise induces bone formation and mineralization in adult zebrafish. *Sci Rep* 1–13 (2018). doi:10.1038/s41598-018-21776-1 10.1038/s41598-018-21776-1

312. Sharma-Ghimire, P., Chen, Z., Sherk, V., Bemben, M. & Bemben, D. Sclerostin and parathyroid hormone responses to acute whole-body vibration and resistance exercise in young women. *J Bone Miner Metab* **37**, 358–367 (2019). 10.1007/s00774-018-0933-0

313. Falk, B. *et al.* Differential sclerostin and parathyroid hormone response to exercise in boys and men. *Osteoporosis International* **27**, 1245–1249 (2016). 10.1007/s00198-015-3310-z

314. Tomkinson, A., Gevers, E. F., Wit, J. M., Reeve, J. & Noble, B. S. The Role of Estrogen in the Control of Rat Osteocyte Apoptosis. *JBMR* **13**, 1243–1250 (1998).

315. Follet, H. *et al.* Risedronate and alendronate suppress osteocyte apoptosis following cyclic fatigue loading. *Bone* **40**, 1172–1177 (2007). 10.1016/j.bone.2006.12.052

316. Bonivtch, A. R., Bonewald, L. F. & Nicolella, D. P. Tissue strain amplification at the osteocyte lacuna : A microstructural finite element analysis. *J Biomech* **40**, 2199–2206 (2007). 10.1016/j.jbiomech.2006.10.040

317. Ionova-Martin, S. S. *et al.* Reduced size-independent mechanical properties of cortical bone in high-fat diet-induced obesity. *Bone* **46**, 217–225 (2010). 10.1017/S0954579414000868.Child-evoked

318. Ionova-Martin, S. S. *et al.* Changes in cortical bone response to high-fat diet from adolescence to adulthood in mice. *Osteoporosis International* **22**, 2283–2293 (2011). 10.1007/s00198-010-1432-x

319. Hesse, B. *et al.* Canalicular network morphology is the major determinant of the spatial distribution of mass density in human bone tissue: Evidence by means of synchrotron radiation phase-contrast nano-CT. *Journal of Bone and Mineral Research* **30**, 346–356 (2015). PMID:25130720

320. Kerschnitzki, M. *et al.* Architecture of the osteocyte network correlates with bone material quality. *Journal of Bone and Mineral Research* **28**, 1837–1845 (2013). PMID:23494896

321. Nicolella, D. P. *et al.* Effects of nanomechanical bone tissue properties on bone tissue strain: Implications for osteocyte mechanotransduction. *Journal of Musculoskeletal Neuronal Interactions* **8**, 330–331 (2008).

322. Taylor, E. A. *et al.* Sequential Treatment of Estrogen Deficient, Osteopenic Rats with Alendronate, Parathyroid Hormone (1–34), or Raloxifene Alters Cortical Bone Mineral and Matrix Composition. *Calcif Tissue Int* **106**, 303–314 (2020). 10.1007/s00223-019-00634-w

323. Roschger, A. *et al.* The contribution of the pericanalicular matrix to mineral content in human osteonal bone. *Bone* **123**, 76–85 (2019). 10.1016/j.bone.2019.03.018

324. Wopenka, B. & Pasteris, J. D. A mineralogical perspective on the apatite in bone. *Materials Science and Engineering: C* **25**, 131–143 (2005).

325. Zhang, S. *et al.* Nanostructure and mechanical properties of the osteocyte lacunar-canalicular network-associated bone matrix revealed by quantitative nanomechanical mapping. *Nano Res* **8**, 3250–3260 (2015).

326. Lewis, G. & Nyman, J. S. The use of nanoindentation for characterizing the properties of mineralized hard tissues: State-of-the art review. *J Biomed Mater Res B Appl Biomater* **87**, 286–301 (2008). 10.1002/jbm.b.31092

327. Oyen, M. L., Ferguson, V. L., Bembey, A. K., Bushby, A. J. & Boyde, A. Composite bounds on the elastic modulus of bone. *J Biomech* **41**, 2585–2588 (2008). 10.1016/j.jbiomech.2008.05.018

328. Tai, K., Dao, M., Suresh, S., Palazoglu, A. & Ortiz, C. Nanoscale heterogeneity promotes energy dissipation in bone. *Nat Mater* **6**, 454–462 (2007).

329. McCreadie, B. R., Hollister, S. J., Schaffler, M. B. & Goldstein, S. A. Osteocyte lacuna size and shape in women with and without osteoporotic fracture. *J Biomech* **37**, 563–572 (2004). 10.1016/S0021-9290(03)00287-2

330. Nazer, R. Al, Lanovaz, J., Kawalilak, C., Johnston, J. D. & Kontulainen, S. Direct in vivo strain measurements in human bone — A systematic literature review. *J Biomech* **45**, 27–40 (2012). 10.1016/j.jbiomech.2011.08.004

331. Apostolopoulos, C. A. & Deligianni, D. D. Prediction of local cellular deformation in bone - Influence of microstructure dimensions. *Journal of Musculoskeletal Neuronal Interactions* **9**, 99–108 (2009).

332. Prendergast, P. J. & Huiskes, R. Microdamage and osteocyte-lacuna strain in bone: A microstructural finite element analysis. *J Biomech Eng* **118**, 240–246 (1996). 10.1115/1.2795966

333. Prideaux, M., Findlay, D. M. & Atkins, G. J. Osteocytes: The master cells in bone remodelling. *Curr Opin Pharmacol* **28**, 24–30 (2016).

334. Hemmatian, H., Bakker, A. D., Klein-Nulend, J. & van Lenthe, G. H. Aging, Osteocytes, and Mechanotransduction. *Curr Osteoporos Rep* **15**, 401–411 (2017).

335. Mader, K. S., Schneider, P., Müller, R. & Stampanoni, M. A quantitative framework for the 3D characterization of the osteocyte lacunar system. *Bone* **57**, 142–154 (2013). 10.1016/j.bone.2013.06.026

336. Obata, Y. *et al.* Quantitative and qualitative bone imaging: A review of synchrotron radiation microtomography analysis in bone research. *J Mech Behav Biomed Mater* **110**, 103887 (2020). 10.1016/j.jmbbm.2020.103887

337. Portier, H., Jaffré, C., Kewish, C. M., Chappard, C. & Pallu, S. New insights in osteocyte imaging by synchrotron radiation. *Journal of Spectral Imaging* **9**, 1–29 (2020). 10.1255/jsi.2020.a3

338. Akhter, M. P. & Recker, R. R. High resolution imaging in bone tissue research-review. *Bone* 115620 (2020). doi:10.1016/j.bone.2020.115620 10.1016/j.bone.2020.115620

339. Pfeiffer, F. X-ray ptychography. *Nat Photonics* **12**, 9–17 (2018). 10.1038/s41566-017-0072-5

340. Bazin, D. *et al.* Diffraction techniques and vibrational spectroscopy opportunities to characterise bones. *Osteoporosis International* **20**, 1065–1075 (2009). 10.1007/s00198-009-0868-3

341. Morris, M. D. & Mandair, G. S. Raman assessment of bone quality. *Clin Orthop Relat Res* **469**, 2160–2169 (2011). PMC3126952

342. Mandair, G. S. & Morris, M. D. Contributions of Raman spectroscopy to the understanding of bone strength. *Bonekey Rep* **4**, 1–8 (2015). PMC4296861

343. Paschalis, E. P., Gamsjaeger, S. & Klaushofer, K. Vibrational spectroscopic techniques to assess bone quality. *Osteoporosis International* 1–17 (2017). doi:10.1007/s00198-017-4019-y 10.1007/s00198-017-4019-y

344. Gamsjaeger, S. *et al.* Cortical bone composition and orientation as a function of animal and tissue age in mice by Raman spectroscopy. *Bone* **47**, 392–399 (2010).

345. Roschger, A. *et al.* Relationship between the v_2PO_4/amide III ratio assessed by Raman spectroscopy and the calcium content measured by quantitative backscattered electron microscopy in healthy human osteonal bone. *J Biomed Opt* **19**, 065002 (2014).

346. Yerramshetty, J. S., Lind, C. & Akkus, O. The compositional and physicochemical homogeneity of male femoral cortex increases after the sixth decade. *Bone* **39**, 1236–43 (2006).

347. Juang, C., Finzi, L. & Bustamante, C. J. Design and application of a computer-controlled confocal scanning differential polarization microscope. *Review of Scientific Instruments* **59**, 2399–2408 (1988). 10.1063/1.1139918

348. Taylor, N. W. & Sheard, C. Microscopic and x-ray investigations on the calcification of tissue. *Journal of Biological Chemistry* **81**, 479–493 (1928).

349. Ascenzi, A. & Fabry, C. Technique for Dissection and Measurement of Refractive Index. *J Biophys Biochem Cytol* **6**, 139–143 (1959).

350. Aparicio, S. *et al.* Optimal methods for processing mineralized tissues for Fourier transform infrared microspectroscopy. *Calcif Tissue Int* **70**, 422–429 (2002). 10.1007/s00223-001-1016-z

351. Boskey, A. & Pleshko Camacho, N. FT-IR imaging of native and tissue-engineered bone and cartilage. *Biomaterials* **28**, 2465–2478 (2007). 10.1016/j.biomaterials.2006.11.043

352. Boskey, A. & Mendelsohn, R. Infrared analysis of bone in health and disease. *J Biomed Opt* **10**, 031102 (2005). 10.1117/1.1922927

353. Goldstein, J. I. *et al. Scanning electron microscopy and X-ray microanalysis*. (Springer, 2017).

354. Arnal, F., Verdier, P. & Vincensini, P. Coefficient of backscattering in the case of monoelectric electrons arriving at the target with an oblique incidence. *Compt rend Acad Sci* **B 268**, 1526–1529 (1969).

355. Howell, P. G. T., Davy, K. M. W. & Boyde, A. Mean atomic number and backscattered electron coefficient calculations for some materials with low mean atomic number. *Scanning* **20**, 35–40 (1998). 10.1002/sca.1998.4950200105

356. Campbell, S. E., Geiss, R. H., Feller, S. A. & Ferguson, V. L. Tunable glass reference materials for quantitative backscattered electron imaging of mineralized tissues. *J Mater Res* **27**, 2568–2577 (2012). 10.1557/jmr.2012.266

357. Skedros, J. G., Bloebaum, R. D., Bachus, K. N., Boyce, T. M. & Constantz, B. Influence of mineral content and composition on graylevels in backscattered electron images of bone. *J Biomed Mater Res* (1993).

358. Roschger, P., Fratzl, P., Eschberger, J. & Klaushofer, K. Validation of quantitative backscattered electron imaging for the measurement of mineral density distribution in human bone biopsies. *Bone* **23**, 319–326 (1998).

359. Heveran, C. M. *et al.* Moderate chronic kidney disease impairs bone quality in C57Bl/6J mice. *Bone* **86**, 1–9 (2016). PMC4833654

360. Tamminen, I. S. *et al.* Increased heterogeneity of bone matrix mineralization in pediatric patients prone to fractures: A biopsy study. *Journal of Bone and Mineral Research* **29**, 1110–1117 (2014).

361. Roschger, P. *et al.* Alendronate increases degree and uniformity of mineralization in cancellous bone and decreases the porosity in cortical bone of osteoporotic women. *Bone* **29**, 185–191 (2001).

362. Ferguson, V. L., Bushby, A. J. & Boyde, A. Nanonmechanical properties and mineral concentration in articular calcified cartilage and subchondral bone. *J Anat* **203**, 191–202 (2003). 10.1046/j.1469-7580.2003.00193.x

363. Boyde, A., Travers, R., Glorieux, F. H. & Jones, S. J. The mineralization density of iliac crest bone from children with osteogenesis imperfecta. *Calcif Tissue Int* **64**, 185–190 (1999). 10.1007/s002239900600

364. Müllerová, I. & Frank, L. Contrast at Very Low Energies of the Gold/Carbon Specimen for Resolution Testing. *Scanning* **26**, 18–24 (2004). 10.1002/sca.4950260104

365. Lewis, P. *et al.* Exploring backscattered imaging in low voltage FE-SEM. *J Phys Conf Ser* **644**, (2015). 10.1088/1742-6596/644/1/012019

366. Howell, P. G. T. & Boyde, A. Monte Carlo simulations of electron scattering in bone. *Bone* **15**, 285–291 (1994). 10.1016/8756-3282(94)90290-9

367. Newbury, D. E. & Ritchie, N. W. M. Performing elemental microanalysis with high accuracy and high precision by scanning electron microscopy/silicon drift detector energy-dispersive X-ray spectrometry (SEM/SDD-EDS). *J Mater Sci* **50**, 493–518 (2014). 10.1007/s10853-014-8685-2

368. Newbury, D. E. & Ritchie, N. W. M. Electron-excited X-ray microanalysis at low beam energy: Almost always an adventure! *Microscopy and Microanalysis* **22**, 735–753 (2016). 10.1017/S1431927616011521

369. Kourkoumelis, N., Balatsoukas, I. & Tzaphlidou, M. Ca/P concentration ratio at different sites of normal and osteoporotic rabbit bones evaluated by Auger and energy dispersive X-ray spectroscopy. *J Biol Phys* **38**, 279–291 (2012).

370. Ritchie, N. W. M. M icroscopy M icroanalysis Spectrum Simulation in DTSA-II. 454–468 (2009).

371. Gunawardane, R. P. & Arumainayagam, C. R. AUGER ELECTRON SPECTROSCOPY\nHandbook of Applied Solid State Spectroscopy. *Handbook of Applied Solid State Spectroscopy* 451–483 (2006). doi:10.1007/0-387-37590-2_10 10.1007/0-387-37590-2_10

372. Ong, J. L. & Lucas, L. C. Auger electron spectroscopy and its use for the characterization of titanium and hydroxyapatite surfaces. *Biomaterials* **19**, 455–464 (1998). 10.1016/S0142-9612(97)00224-X

373. Miller, R. G., Bowles, C. Q., Gutshall, P. L. & Eick, J. D. The Effects of Ion Sputtering on Dentin and its Relation to Depth Profiling. *J Dent Res* **73**, 1457–1461 (1994). 10.1177/00220345940730081001

374. Tzaphlidou, M., Berillis, P. & Matthopoulos, D. Bone calcium, phosphorus detection by Auger electron spectroscopy. *Micron* **36**, 706–709 (2005).

375. Sundgren, J. E., Bodö, P. & Lundström, I. Auger electron spectroscopic studies of the interface between human tissue and implants of titanium and stainless steel. *J Colloid Interface Sci* **110**, 9–20 (1986). 10.1016/0021-9797(86)90348-6

376. Miller, R. G., Bowles, C. Q., Eick, J. D. & Gutshall, P. L. Auger electron spectroscopy of dentin: elemental quantification and the effects of electron and ion bombardment. *Dental Materials* **9**, 280–285 (1993). 10.1016/0109-5641(93)90075-2

377. Everts, V., Niehof, A., Tigchelaar-Gutter, W. & Beersten, W. Transmission Electron Microscopy of Bone. in *Methods in Molecular Biology* **816**, 351–363 (2012). 10.1007/978-1-61779-415-5_26

378. Schwarcz, H. P., McNally, E. A. & Botton, G. A. Dark-field transmission electron microscopy of cortical bone reveals details of extrafibrillar crystals. *J Struct Biol* **188**, 240–248 (2014). 10.1016/j.jsb.2014.10.005

379. Rubin, M. A. *et al.* TEM analysis of the nanostructure of normal and osteoporotic human trabecular bone. *Bone* **33**, 270–282 (2003). 10.1016/S8756-3282(03)00194-7

380. Suvorova, E. I., Petrenko, P. P. & Buffat, P. A. Scanning and transmission electron microscopy for evaluation of order/disorder in bone structure. *Scanning* **29**, 162–170 (2007). 10.1002/sca.20058

381. Suvorova, E. I., Buffat, P. A., Layrolle, P., Bouler, J. M. & Dacolsi, G. Electron diffraction and high resolution transmission electron microscopy in the characterization of calcium phosphate precipitation from aqueous solutions under biomineralization conditions. *Eur Cell Mater* **1**, 27–42 (2001). 10.22203/ecm.v001a04

382. Obata, Y. *et al.* Quantitative and qualitative bone imaging: A review of synchrotron radiation microtomography analysis in bone research. *J Mech Behav Biomed Mater* **110**, 103887 (2020). 10.1016/j.jmbbm.2020.103887

383. Akhter, M. P. & Recker, R. R. High resolution imaging in bone tissue research-review. *Bone* 115620 (2020). doi:10.1016/j.bone.2020.115620 10.1016/j.bone.2020.115620

384. Akhter, M. P., Kimmel, D. B., Lappe, J. M. & Recker, R. R. Effect of macroanatomic bone type and estrogen loss on osteocyte lacunar properties in healthy adult women. *Calcif Tissue Int* **100**, 619–630 (2017).

385. Hemmatian, H., Laurent, M. R., Claessens, F., Vanderschueren, D. & Lenthe, G. H. van. 3D assessment of mouse cortical bone microstructural architecture by desktop micro-CT. (2016).

386. Lau, S. H. *et al.* Multiscale 3D Bioimaging: from cell, tissue to whole organism. in *Scanning Microscopy 2009* **7378**, 73781V (International Society for Optics and Photonics, 2009).

387. Langer, M. *et al.* X-Ray Phase Nanotomography Resolves the 3D Human Bone Ultrastructure. *PLoS One* **7**, 1–7 (2012). 10.1371/journal.pone.0035691

388. Peyrin, F., Dong, P., Pacureanu, A. & Langer, M. Micro- and Nano-CT for the Study of Bone Ultrastructure. *Curr Osteoporos Rep* **12**, 465–474 (2014). 10.1007/s11914-014-0233-0

389. Langer, M. *et al.* X-Ray Phase Nanotomography Resolves the 3D Human Bone Ultrastructure. *PLoS One* **7**, 1–7 (2012). 10.1371/journal.pone.0035691

390. Larrue, A., Rattner, A., Laroche, N., Vico, L. & Peyrin, F. Feasibility of micro-crack detection in human trabecular bone images from 3D synchrotron microtomography. *Annual International Conference of the IEEE Engineering in Medicine and Biology - Proceedings* 3918–3921 (2007). doi:10.1109/IEMBS.2007.4353190 10.1109/IEMBS.2007.4353190

391. Brock, G. R. *et al.* Nanoscale Examination of Microdamage in Sheep Cortical Bone Using Synchrotron Radiation Transmission X-Ray Microscopy. *PLoS One* **8**, 4–12 (2013). 10.1371/journal.pone.0057942

392. Larrue, A. *et al.* Synchrotron radiation micro-CT at the Micrometer scale for the analysis of the three-dimensional morphology of microcracks in human trabecular bone. *PLoS One* **6**, (2011). 10.1371/journal.pone.0021297

393. Mürer, F. K. *et al.* 3D Maps of Mineral Composition and Hydroxyapatite Orientation in Fossil Bone Samples Obtained by X-ray Diffraction Computed Tomography. *Sci Rep* **8**, 10052 (2018). 10.1038/s41598-018-28269-1

394. Seidel, R. *et al.* Synchrotron 3D SAXS analysis of bone nanostructure. *Bioinspired, Biomimetic and Nanobiomaterials* **1**, 123–132 (2012). 10.1680/bbn.11.00014

395. Wagermaier, W. *et al.* Scanning texture analysis of lamellar bone using microbeam synchrotron radiation. *Acta Crystallogr A* **61**, c311–c311 (2005). 10.1107/s010876730508671x

396. Wagermaier, W. *et al.* Spiral twisting of fiber orientation inside bone lamellae. *Biointerphases* **1**, 1–5 (2006). 10.1116/1.2178386

397. Dierolf, M. *et al.* Ptychographic X-ray computed tomography at the nanoscale. *Nature* **467**, 436–439 (2010). 10.1038/nature09419

398. Hawkes, P. W. & Spence, J. C. H. *Handbook Microscopy*. (2019).

399. Pfeiffer, F. X-ray ptychography. *Nat Photonics* **12**, 9–17 (2018). 10.1038/s41566-017-0072-5

400. Holler, M. *et al.* X-ray ptychographic computed tomography at 16 nm isotropic 3D resolution. *Sci Rep* **4**, 1–5 (2014).

401. Ciani, A. *et al.* Ptychographic X-ray CT characterization of the osteocyte lacuno-canalicular network in a male rat's glucocorticoid induced osteoporosis model. *Bone Rep* **9**, 122–131 (2018).

402. Dierolf, M. *et al.* Ptychographic X-ray computed tomography at the nanoscale. *Nature* **467**, 436–439 (2010). 10.1038/nature09419

403. Oyen, M. L. & Cook, R. F. A practical guide for analysis of nanoindentation data. *J Mech Behav Biomed Mater* **2**, 396–407 (2009).

404. Campbell, S. E., Ferguson, V. L. & Hurley, D. C. Nanomechanical mapping of the osteochondral interface with contact resonance force microscopy and nanoindentation q. *Acta Biomater* **8**, 4389–4396 (2012). 10.1016/j.actbio.2012.07.042

405. Hurley, D. C. Contact Resonance Force Microscopy Techniques for Nanomechanical Measurements. *Applied Scanning Probe Methods* **XI**, 97–138 (2009).

406. Fischer-Cripps, A. C. *Nanoindentation*. (Springer, 2004).

407. Ebenstein, D. M. & Pruitt, L. A. Nanoindentation of biological tissues. *Nano Today* **1**, 26–33 (2006).

408. Labonte, D., Lenz, A.-K. & Oyen, M. L. On the relationship between indenation hardness and modulus, and the damage resistance of biological materials. *Acta Biomater* **57**, 373–383 (2017).

409. Rodriguez-Florez, N., Oyen, M. L. & Shefelbine, S. J. Insight into differences in nanoindentation properties of bone. *J Mech Behav Biomed Mater* **18**, 90–99 (2013). 10.1016/j.jmbbm.2012.11.005

410. Pathak, S. *et al.* Measuring the dynamic mechanical response of hydrated mouse bone by nanoindentation. *J Mech Behav Biomed Mater* **4**, 34–43 (2011). 10.1016/j.jmbbm.2010.09.002

411. Kopycinska-Müller, M., Geiss, R. H. & Hurley, D. C. Contact mechanics and tip shape in AFM-based nanomechanical measurements. *Ultramicroscopy* **106**, 466–474 (2006). 10.1016/j.ultramic.2005.12.006

412. Carden, A. & Morris, M. D. Application of vibrational spectroscopy to the study of mineralized tissues (review). *J Biomed Opt* **5**, 259 (2000). 10.1117/1.429994

413. Knapp, H. F., Reilly, G. C., Stemmer, A., Niederer, P. & Knothe Tate, M. L. Development of preparation methods for and insights obtained from atomic force microscopy of fluid spaces in cortical bone. *Scanning* **24**, 25–33 (2002). 10.1002/sca.4950240104

414. Feng, J. Q. *et al.* Loss of DMP1 causes rickets and osteomalacia and identifies a role for osteocytes in mineral metabolism. *Nat Genet* **38**, 1310–1315 (2006). 10.1099/mic.0.2008/022293-0.Quantitative

415. Mabilleau, G., Perrot, R., Flatt, P. R., Irwin, N. & Chappard, D. High fat-fed diabetic mice present with profound alterations of the osteocyte network. *Bone* **90**, 99–106 (2016). 10.1016/j.bone.2016.06.008

416. Newbury, D. E. & Ritchie, N. W. Is Scanning Electron Microscopy / Energy Dispersive X-ray Spectrometry (SEM / EDS) Quantitative ? *Scanning* **35**, 141–168 (2013).

417. Lai, X. *et al.* The dependences of osteocyte network on bone compartment, age, and disease. *Bone Res* **3**, 15009 (2015). 10.1038/boneres.2015.9

418. Akhter, M. P., Kimmel, D. B., Lappe, J. M. & Recker, R. R. Effect of macroanatomic bone type and estrogen loss on osteocyte lacunar properties in healthy adult women. *Calcif Tissue Int* **100**, 619–630 (2017).

419. Hemmatian, H., Laurent, M. R., Claessens, F., Vanderschueren, D. & Lenthe, G. H. van. 3D assessment of mouse cortical bone microstructural architecture by desktop micro-CT. (2016).

420. Lau, S. H. *et al.* Multiscale 3D Bioimaging: from cell, tissue to whole organism. in *Scanning Microscopy 2009* **7378**, 73781V (International Society for Optics and Photonics, 2009).

421. Weitkamp, T. *et al.* Parallel-beam imaging at the ESRF beamline ID19: current status and plans for the future. *AIP Conf Proc* **1234**, 83–86 (2010). 10.1063/1.3463345

422. Stampanoni, M. *et al.* Trends in synchrotron-based tomographic imaging: the SLS experience. in *Proc.SPIE* **6318**, (2006). 10.1117/12.679497

423. Chappard, C. *et al.* 3D characterization of pores in the cortical bone of human femur in the elderly at different locations as determined by synchrotron micro-computed tomography images. *Osteoporosis International* **24**, 1023–1033 (2013).

424. Schneider, P. *et al.* Ultrastructural properties in cortical bone vary greatly in two inbred strains of mice as assessed by synchrotron light based micro-and nano-CT. *Journal of Bone and Mineral Research* **22**, 1557–1570 (2007).

425. Yu, B., Pacureanu, A., Olivier, C., Cloetens, P. & Peyrin, F. Assessment of the human bone lacuno-canalicular network at the nanoscale and impact of spatial resolution. *Sci Rep* **10**, 1–12 (2020).

426. Peyrin, F., Dong, P., Pacureanu, A. & Langer, M. Micro- and Nano-CT for the Study of Bone Ultrastructure. *Curr Osteoporos Rep* **12**, 465–474 (2014). 10.1007/s11914-014-0233-0

427. Larrue, A., Rattner, A., Laroche, N., Vico, L. & Peyrin, F. Feasibility of micro-crack detection in human trabecular bone images from 3D synchrotron microtomography. *Annual International Conference of the IEEE Engineering in Medicine and Biology - Proceedings* 3918–3921 (2007). doi:10.1109/IEMBS.2007.4353190 10.1109/IEMBS.2007.4353190

428. Brock, G. R. *et al.* Nanoscale Examination of Microdamage in Sheep Cortical Bone Using Synchrotron Radiation Transmission X-Ray Microscopy. *PLoS One* **8**, 4–12 (2013). 10.1371/journal.pone.0057942

429. Larrue, A. *et al.* Synchrotron radiation micro-CT at the Micrometer scale for the analysis of the three-dimensional morphology of microcracks in human trabecular bone. *PLoS One* **6**, (2011). 10.1371/journal.pone.0021297

430. Djomehri, S. I. *et al.* Mineral density volume gradients in normal and diseased human tissues. *PLoS One* **10**, e0121611 (2015).

431. Kazakia, G. J., Burghardt, A. J., Cheung, S. & Majumdar, S. Assessment of bone tissue mineralization by conventional x-ray microcomputed tomography: Comparison with synchrotron radiation microcomputed tomography and ash measurements. *Med Phys* **35**, 3170–3179 (2008).

432. Nuzzo, S. *et al.* Synchrotron Radiation Microtomography Allows the Analysis of Three-Dimensional Microarchitecture and Degree of Mineralization of Human Iliac Crest Biopsy Specimens: Effects of Etidronate Treatment. *Journal of Bone and Mineral Research* **17**, 1372–1382 (2002). 10.1359/jbmr.2002.17.8.1372

433. Shahmoradian, S. H. *et al.* Three-dimensional imaging of biological tissue by cryo x-ray ptychography. *Sci Rep* **7**, 1–12 (2017).

434. Ciani, A. *et al.* Ptychographic X-ray CT characterization of the osteocyte lacuno-canalicular network in a male rat's glucocorticoid induced osteoporosis model. *Bone Rep* **9**, 122–131 (2018).

435. Holler, M. *et al.* X-ray ptychographic computed tomography at 16 nm isotropic 3D resolution. *Sci Rep* **4**, 1–5 (2014).

436. Langer, M. & Peyrin, F. 3D X-ray ultra-microscopy of bone tissue. *Osteoporosis International* **27**, 441–455 (2016).

437. Shahmoradian, S. H. *et al.* Three-dimensional imaging of biological tissue by cryo x-ray ptychography. *Sci Rep* **7**, 1–12 (2017).

438. Lin, Y. & Xu, S. AFM analysis of the lacunar-canalicular network in demineralized compact bone. *J Microsc* **241**, 291–302 (2011). 10.1111/j.1365-2818.2010.03431.x

439. Tiede-Lewis, L. M. *et al.* Degeneration of the osteocyte network in the C57Bl/6 mouse model of aging. *Aging* **9**, 2190–2208 (2017). PMC5680562

440. Lane, N. E. *et al.* Glucocorticoid-treated mice have localized changes in trabecular bone material properties and osteocyte lacunar size that are not observed in placebo-treated or estrogen-deficient mice. *Journal of Bone and Mineral Research* **21**, 466–476 (2006). 10.1359/JBMR.051103

441. Delmas, P. D. Biochemical markers of bone turnover for the clinical assessment of metabolic bone disease. *Endocrinol Metab Clin North Am* **19**, 1–18 (1990).

442. Shahnazari, M. *et al.* Bone turnover markers in peripheral blood and marrow plasma reflect trabecular bone loss but not endocortical expansion in aging mice. *Bone* **50**, 628–637 (2012). 10.1016/j.bone.2011.11.010

443. Wang, Y., Mcnamara, L. M., Schaffler, M. B. & Weinbaum, S. *Strain amplification and integrin based signaling in osteocytes*.

444. Lewis, K. J. *et al.* Estrogen depletion on In vivo osteocyte calcium signaling responses to mechanical loading. *Bone* **152**, (2021). 10.1016/j.bone.2021.116072

445. Nazer, R. Al, Lanovaz, J., Kawalilak, C., Johnston, J. D. & Kontulainen, S. Direct in vivo strain measurements in human bone — A systematic literature review. *J Biomech* **45**, 27–40 (2012). 10.1016/j.jbiomech.2011.08.004

446. Lai, X., Chung, R., Li, Y., Liu, X. S. & Wang, L. Lactation alters fluid flow and solute transport in maternal skeleton: A multiscale modeling study on the effects of microstructural changes and loading frequency. *Bone* **151**, (2021). 10.1016/j.bone.2021.116033

447. Sang, W. & Ural, A. Quantifying how altered lacunar morphology and perilacunar tissue properties influence local mechanical environment of osteocyte lacunae using finite element modeling. *J Mech Behav Biomed Mater* **135**, (2022). 10.1016/j.jmbbm.2022.105433

448. Rudman, K. E., Aspden, R. M. & Meakin, J. R. Compression or tension? The stress distribution in the proximal femur. *Biomed Eng Online* **5**, (2006). 10.1186/1475-925X-5-12

449. Ramasamy, J. G. & Akkus, O. Local variations in the micromechanical properties of mouse femur: The involvement of collagen fiber orientation and mineralization. *J Biomech* **40**, 910–918 (2007). 10.1016/j.jbiomech.2006.03.002

450. Bach-Gansmo, F. L. *et al.* Osteocyte lacunar properties in rat cortical bone: Differences between lamellar and central bone. *J Struct Biol* **191**, 59–67 (2015). https://doi.org/10.1016/j.jsb.2015.05.005

451. Palumbo, C. & Ferretti, M. *Histomorphometric study on the osteocyte lacuno-canalicular network in animals of different species. I. Woven-fibered and parallel-fibered bones*. *Article in Italian Journal of Anatomy and Embryology* (1998).

452. Schneider, C. A., Rasband, W. S. & Eliceiri, K. W. *NIH Image to ImageJ: 25 years of Image Analysis HHS Public Access*. *Nat Methods* **9**, (2012).

453. Ascenzi, M. G. *et al.* Hyperlipidemia affects multiscale structure and strength of murine femur. *J Biomech* **47**, 2436–2443 (2014). 10.1016/j.jbiomech.2014.04.006

454. Poundarik, A. A. & Vashishth, D. Multiscale imaging of bone microdamage. *Connect Tissue Res* **56**, 87–98 (2015). 10.3109/03008207.2015.1008133

455. Burr, D. B. & Hooser, M. *Alterations to the En Bloc Basic Fuchsin Staining Protocol for the Demonstration of Microdamage Produced In Vivo*. *Bone* **17**, (1995).

456. Hilton, M. J. *Skeletal Development and Repair*. (Springer, 2016).

457. Vahidi, G. *et al.* Germ-Free C57BL/6 Mice Have Increased Bone Mass and Altered Matrix Properties but Not Decreased Bone Fracture Resistance. *Journal of Bone and Mineral Research* **38**, 1154–1174 (2023). 10.1002/jbmr.4835

458. Milovanovic, P. & Busse, B. Inter-site variability of the human osteocyte lacunar network: implications for bone quality. *Curr Osteoporos Rep* **17**, 105–115 (2019).

459. Ashique, A. M. *et al.* Lacunar-canalicular network in femoral cortical bone is reduced in aged women and is predominantly due to a loss of canalicular porosity. *Bone Rep* **7**, 9–16 (2017). 10.1016/j.bonr.2017.06.002

460. Paschalis, E. P. *et al.* Aging Versus Postmenopausal Osteoporosis: Bone Composition and Maturation Kinetics at Actively-Forming Trabecular Surfaces of Female Subjects Aged 1 to 84 Years. *Journal of Bone and Mineral Research* **31**, 347–357 (2016). 10.1002/jbmr.2696

461. Creecy, A. *et al.* The age-related decrease in material properties of BALB/c mouse long bones involves alterations to the extracellular matrix. *Bone* **130**, 115126 (2020). 10.1016/j.bone.2019.115126

462. Cui, J., Shibata, Y., Zhu, T., Zhou, J. & Zhang, J. Osteocytes in bone aging: Advances, challenges, and future perspectives. *Ageing Research Reviews* **77**, (2022). 10.1016/j.arr.2022.101608

463. Ferretti, M., Muglia, M. A., Remaggi, F., Cane, V. & Palumbo, C. Histomorphometric study on the osteocyte lacuno-canalicular network in animals of different species. II. Parallel-fibered and lamellar bones. *Ital J Anat Embryol* **104**, 121–131 (1999).

464. Schemenz, V. *et al.* Heterogeneity of the osteocyte lacuno-canalicular network architecture and material characteristics across different tissue types in healing bone. *J Struct Biol* **212**, (2020). 10.1016/j.jsb.2020.107616

465. Hernandez, C. J., Majeska, R. J. & Schaffler, M. B. Osteocyte density in woven bone. *Bone* **35**, 1095–1099 (2004). 10.1016/j.bone.2004.07.002

466. Hasegawa, T. Ultrastructure and biological function of matrix vesicles in bone mineralization. *Histochemistry and Cell Biology* **149**, 289–304 (2018). 10.1007/s00418-018-1646-0

467. Golan, S., Elata, D. & Dinnar, U. Cortical Bone Periosteocytic Space Morphology Can Affect Osteocyte-Level Mass Flows and Shear Stresses. in *Engineering Systems Design and Analysis* **48364**, 77–84 (2008).

468. Rohrbach, D. *et al.* Spatial distribution of tissue level properties in a human femoral cortical bone. *J Biomech* **45**, 2264–2270 (2012). 10.1016/j.jbiomech.2012.06.003

469. Birkhold, A. I., Razi, H., Duda, G. N., Checa, S. & Willie, B. M. Tomography-Based Quantification of Regional Differences in Cortical Bone Surface Remodeling and Mechano-Response. *Calcif Tissue Int* **100**, 255–270 (2017). 10.1007/s00223-016-0217-4

470. Sun, Y. *et al.* Mechanical Stimulation on Mesenchymal Stem Cells and Surrounding Microenvironments in Bone Regeneration: Regulations and Applications. *Frontiers in Cell and Developmental Biology* **10**, (2022). 10.3389/fcell.2022.808303

471. McCreadie, B. R., Hollister, S. J., Schaffler, M. B. & Goldstein, S. A. Osteocyte lacuna size and shape in women with and without osteoporotic fracture. *J Biomech* **37**, 563–572 (2004). 10.1016/S0021-9290(03)00287-2

472. Carter, Y., Thomas, C. D. L., Clement, J. G. & Cooper, D. M. L. Femoral osteocyte lacunar density, volume and morphology in women across the lifespan. *J Struct Biol* **183**, 519–526 (2013). 10.1016/j.jsb.2013.07.004

473. Dong, P. *et al.* 3D osteocyte lacunar morphometric properties and distributions in human femoral cortical bone using synchrotron radiation micro-CT images. *Bone* **60**, 172–185 (2014). 10.1016/j.bone.2013.12.008

474. Varga, P. *et al.* Investigation of the three-dimensional orientation of mineralized collagen fibrils in human lamellar bone using synchrotron X-ray phase nano-tomography. *Acta Biomater* **9**, 8118–8127 (2013). 10.1016/j.actbio.2013.05.015

475. Matthews, M. M., Cook, E., Naguib, N., Wiesner, U. B. & Lewis, K. J. Intravital imaging of osteocyte integrin dynamics with locally injectable fluorescent nanoparticles. *Bone* **174**, (2023). 10.1016/j.bone.2023.116830

476. Okada, S., Yoshida, S., Ashrafi, S. H. & Schraufnagel, D. E. The canalicular structure of compact bone in the rat at different ages. *Microscopy and Microanalysis* **8**, 104–115 (2002). 10.1017/S1431927601020037

477. Weinkamer, R., Kollmannsberger, P. & Fratzl, P. Towards a Connectomic Description of the Osteocyte Lacunocanalicular Network in Bone. *Current Osteoporosis Reports* **17**, 186–194 (2019). 10.1007/s11914-019-00515-z

478. Dallas, S. L., Prideaux, M. & Bonewald, L. F. The osteocyte: An endocrine cell . . . and more. *Endocr Rev* **34**, 658–690 (2013). 10.1210/er.2012-1026

479. Robling, A. G. & Bonewald, L. F. The Osteocyte: New Insights. *Annu Rev Physiol* **82**, 485–506 (2020). 10.1146/annurev-physiol-021119-034332

480. Qing, H. *et al.* Demonstration of osteocytic perilacunar/canalicular remodeling in mice during lactation. *Journal of Bone and Mineral Research* **27**, 1018–1029 (2012). PMC3770147

481. Bélanger, L. F. Osteocytic osteolysis. *Calcif Tissue Res* **4**, 1–12 (1969). 10.1007/BF02279101

482. Heveran, C. M., Rauff, A., King, K. B., Carpenter, R. D. & Ferguson, V. L. A new open-source tool for measuring 3D osteocyte lacunar geometries from confocal laser scanning microscopy reveals age-related changes to lacunar size and shape in cortical mouse bone. *Bone* **110**, (2018). PMC5878731

483. Kovacs, C. S. The Skeleton Is a Storehouse of Mineral That Is Plundered During Lactation and (Fully?) Replenished Afterwards. *Journal of Bone and Mineral Research* **32**, 676–680 (2017). 10.1002/jbmr.3090

484. Schurman, C. A., Verbruggen, S. W. & Alliston, T. Disrupted osteocyte connectivity and pericellular fluid flow in bone with aging and defective TGF-β signaling. *Proc Natl Acad Sci U S A* **118**, 1–11 (2021). 10.1073/pnas.2023999118

485. Ashique, A. M. *et al.* Lacunar-canalicular network in femoral cortical bone is reduced in aged women and is predominantly due to a loss of canalicular porosity. (2017). doi:10.1016/j.bonr.2017.06.002 10.1016/j.bonr.2017.06.002

486. Tiede-Lewis, L. A. M. & Dallas, S. L. Changes in the osteocyte lacunocanalicular network with aging. *Bone* **122**, 101–113 (2019). PMC6638547

487. Carter, Y., David, C., Thomas, L., Clement, J. G. & Cooper, D. M. L. Femoral osteocyte lacunar density, volume and morphology in women across the lifespan. *J Struct Biol* (2013). doi:10.1016/j.jsb.2013.07.004 10.1016/j.jsb.2013.07.004

488. Jilka, R. L. & O'Brien, C. A. The Role of Osteocytes in Age-Related Bone Loss. *Curr Osteoporos Rep* **14**, 16–25 (2016).

489. Okada, S., Yoshida, S., Ashrafi, S. H. & Schraufnagel, D. E. The canalicular structure of compact bone in the rat at different ages. *Microscopy and Microanalysis* **8**, 104–115 (2002). 10.1017/S1431927601020037

490. Dole, N. S. *et al.* Osteocyte-Intrinsic TGF- b Signaling Regulates Bone Article Osteocyte-Intrinsic TGF- b Signaling Regulates Bone Quality through Perilacunar / Canalicular Remodeling. *CellReports* **21**, 2585–2596 (2017). 10.1016/j.celrep.2017.10.115

491. Zimmermann, E. A. & Ritchie, R. O. Bone as a Structural Material. *Adv Healthc Mater* **4**, 1287–1304 (2015). PMID:25865873

492. Wang, K. *et al.* Osteocytes but not osteoblasts directly build mineralized bone structures. *Int J Biol Sci* **17**, 2430–2448 (2021). 10.7150/ijbs.61012

493. van Gaalen, S. M. *et al.* Use of Fluorochrome Labels in In Vivo Bone Tissue Engineering Research. *Tissue Engineering: Part B* **16**, 209–217 (2010).

494. Pautke, C. *et al.* Polychrome labeling of bone with seven different fluorochromes: Enhancing fluorochrome discrimination by spectral image analysis. *Bone* **37**, 441–445 (2005). 10.1016/j.bone.2005.05.008

495. Calderón, T., Arnold, W., Stalder, G., Painer, J. & Köhler, M. Labelling experiments in red deer provide a general model for early bone growth dynamics in ruminants. *Sci Rep* **11**, 1–14 (2021). 10.1038/s41598-021-93547-4

496. Rahn, B. A. & Perren, S. M. Xylenol Orange, a fluorochrome useful in polychrome sequential labeling of calcifying tissues. *Biotechnic and Histochemistry* **46**, 125–129 (1971). 10.3109/10520297109067836

497. Carriero, A. *et al.* Spatial relationship between bone formation and mechanical stimulus within cortical bone: Combining 3D fluorochrome mapping and poroelastic finite element modelling. *Bone Rep* **8**, 72–80 (2018). 10.1016/j.bonr.2018.02.003

498. Kegelman, C. D. *et al.* YAP and TAZ Mediate Osteocyte Perilacunar/Canalicular Remodeling. *Journal of Bone and Mineral Research* **35**, 196–210 (2020). 10.1002/jbmr.3876

499. Baylink, D. J. & Wergedal, J. E. Bone formation by osteocytes. *Am J Physiol* **221**, 669–678 (1971). 10.1152/ajplegacy.1971.221.3.669

500. Hertz, V. H. H. Die lieber die Berührung fester elastischer Körper. 156–171 (1878).

501. Killgore, J. P., Geiss, R. H. & Hurley, D. C. Continuous measurement of atomic force microscope tip wear by contact resonance force microscopy. *Small* **7**, 1018–1022 (2011). 10.1002/smll.201002116

502. Chung, K. H., Lee, Y. H. & Kim, D. E. Characteristics of fracture during the approach process and wear mechanism of a silicon AFM tip. *Ultramicroscopy* **102**, 161–171 (2005). 10.1016/j.ultramic.2004.09.009

503. Kim, S. & Casper, R. Applications of Convolution in Image Processing with MATLAB. *University of Washington* 1–20 (2013).

504. Carter, Y., David, C., Thomas, L., Clement, J. G. & Cooper, D. M. L. Femoral osteocyte lacunar density, volume and morphology in women across the lifespan. *J Struct Biol* (2013). doi:10.1016/j.jsb.2013.07.004 10.1016/j.jsb.2013.07.004

505. Kegelman, C. D. *et al.* YAP and TAZ Mediate Osteocyte Perilacunar/Canalicular Remodeling. *Journal of Bone and Mineral Research* **35**, 196–210 (2020). 10.1002/jbmr.3876

506. Aido, M. *et al.* Relationship between nanoscale mineral properties and calcein labeling in mineralizing bone surfaces in mineralizing bone surfaces. *Connect Tissue Res* **55**, 15–17 (2014). 10.3109/03008207.2014.923869

507. Kola, S. K. *et al.* Osteocyte lacunar strain determination using multiscale finite element analysis. *Bone Rep* **12**, 100277 (2020). 10.1016/j.bonr.2020.100277

508. Bembey, A. K., Oyen, M., Bushby, A. & Boyde, A. Nanoindentation measurements of bone viscoelasticity as a function of hydration state. *MRS Online Proceedings Library (OPL)* **898**, 0898-L07 (2005).

509. Pathak, S. *et al.* Measuring the dynamic mechanical response of hydrated mouse bone by nanoindentation. *J Mech Behav Biomed Mater* **4**, 34–43 (2011). 10.1016/j.jmbbm.2010.09.002

510. Yamashita, J. *et al.* Collagen and bone viscoelasticity: A dynamic mechanical analysis. *J Biomed Mater Res* **63**, 31–36 (2002). 10.1002/jbm.10086

511. Ojanen, X. *et al.* Relationships between tissue composition and viscoelastic properties in human trabecular bone. *J Biomech* **48**, 269–275 (2015). 10.1016/j.jbiomech.2014.11.034

512. Yamashita, J., Furman, B. R., Rawls, H. R., Wang, X. & Agrawal, C. M. The use of dynamic mechanical analysis to assess the viscoelastic properties of human cortical bone. *J Biomed Mater Res* **58**, 47–53 (2001). 10.1002/1097-4636(2001)58:1<47::AID-JBM70>3.0.CO;2-U

513. Yeni, Y. N. *et al.* The effect of yield damage on the viscoelastic properties of cortical bone tissue as measured by dynamic mechanical analysis. *J Biomed Mater Res A* **82**, 530–537 (2007). 10.1002/jbm.a.31169

514. Buechner, P. M., Lakes, R. S., Swan, C. & Brand, R. A. A broadband viscoelastic spectroscopic study of bovine bone: Implications for fluid flow. *Ann Biomed Eng* **29**, 719–728 (2001). 10.1114/1.1385813

515. Abdel-Wahab, A. A., Alam, K. & Silberschmidt, V. V. Analysis of anisotropic viscoelastoplastic properties of cortical bone tissues. *J Mech Behav Biomed Mater* **4**, 807–820 (2011). 10.1016/j.jmbbm.2010.10.001

516. Isaksson, H. *et al.* Precision of nanoindentation protocols for measurement of viscoelasticity in cortical and trabecular bone. *J Biomech* **43**, 2410–2417 (2010). 10.1016/j.jbiomech.2010.04.017

517. Aldegaither, N. *et al.* Fracture toughness of bone at the microscale. *Acta Biomater* **121**, 475–483 (2021). 10.1016/j.actbio.2020.12.007

518. Ojanen, X. *et al.* Relationships between tissue composition and viscoelastic properties in human trabecular bone. *J Biomech* **48**, 269–275 (2015). 10.1016/j.jbiomech.2014.11.034

519. Yamashita, J. *et al.* Collagen and bone viscoelasticity: A dynamic mechanical analysis. *J Biomed Mater Res* **63**, 31–36 (2002). 10.1002/jbm.10086

520. Yeni, Y. N. *et al.* Do Sacrificial Bonds Affect the Viscoelastic and Fracture Properties of Bone? *Clinical Orthopaedics and Related Research (1976-2007)* **443**, (2006).

521. Buehler, M. J. Molecular nanomechanics of nascent bone: fibrillar toughening by mineralization. *Nanotechnology* **18**, 295102 (2007).

522. Gupta, H. S. *et al.* Fibrillar level fracture in bone beyond the yield point. *Int J Fract* **139**, 425–436 (2006).

523. Smith, B. L. *et al.* Molecular mechanistic origin of the toughness of natural adhesives, fibres and composites. *Nature* **399**, 761–763 (1999).

524. Nyman, J. S., Ni, Q., Nicolella, D. P. & Wang, X. Measurements of mobile and bound water by nuclear magnetic resonance correlate with mechanical properties of bone. *Bone* **42**, 193–199 (2008).

525. Wilson, E. E. *et al.* Highly ordered interstitial water observed in bone by nuclear magnetic resonance. *Journal of bone and mineral research* **20**, 625–634 (2005).

526. Tai, K., Dao, M., Suresh, S., Palazoglu, A. & Ortiz, C. Nanoscale heterogeneity promotes energy dissipation in bone. *Nat Mater* **6**, 454–462 (2007).

527. Zhang, S. *et al.* Nanostructure and mechanical properties of the osteocyte lacunar-canalicular network-associated bone matrix revealed by quantitative nanomechanical mapping. *Nano Res* **8**, 3250–3260 (2015). 10.1007/s12274-015-0825-8

528. Hengsberger, S., Kulik, A. & Zysset, P. A combined atomic force microscopy and nanoindentation technique to investigate the elastic properties of bone structural units. *Eur Cell Mater* **1**, 12–17 (2001).

529. Thurner, P. J. Atomic force microscopy and indentation force measurement of bone. *Wiley Interdiscip Rev Nanomed Nanobiotechnol* **1**, 624–649 (2009).

530. Yuya, P. A., Hurley, D. C. & Turner, J. A. Contact-resonance atomic force microscopy for viscoelasticity. *J Appl Phys* **104**, (2008). 10.1063/1.2996259

531. Killgore, J. P. *et al.* Viscoelastic property mapping with contact resonance force microscopy. *Langmuir* **27**, 13983–13987 (2011). 10.1021/la203434w

532. Hurley, D. C. Contact Resonance Force Microscopy Techniques for Nanomechanical Measurements *. **XI**, 97–138 (2009).

533. Campbell, S. E., Ferguson, V. L. & Hurley, D. C. Nanomechanical mapping of the osteochondral interface with contact resonance force microscopy and nanoindentation. *Acta Biomater* **8**, 4389–4396 (2012). 10.1016/j.actbio.2012.07.042

534. Tung, R. C., Killgore, J. P. & Hurley, D. C. Hydrodynamic corrections to contact resonance atomic force microscopy measurements of viscoelastic loss tangent. *Review of Scientific Instruments* **84**, (2013). 10.1063/1.4812633

535. Churnside, A. B., Tung, R. C. & Killgore, J. P. Quantitative Contact Resonance Force Microscopy for Viscoelastic Measurement of Soft Materials at the Solid-Liquid Interface. *Langmuir* **31**, 11143–11149 (2015). 10.1021/acs.langmuir.5b02860

536. Killgore, J. P. & Hurley, D. C. Low-force AFM nanomechanics with higher-eigenmode contact resonance spectroscopy. *Nanotechnology* **23**, (2012). 10.1088/0957-4484/23/5/055702

537. Hurley, D. C., Campbell, S. E., Killgore, J. P., Cox, L. M. & Ding, Y. Measurement of viscoelastic loss tangent with contact resonance modes of atomic force microscopy. *Macromolecules* **46**, 9396–9402 (2013). 10.1021/ma401988h

538. Churnside, A. B., Tung, R. C. & Killgore, J. P. Quantitative Contact Resonance Force Microscopy for Viscoelastic Measurement of Soft Materials at the Solid-Liquid Interface. *Langmuir* **31**, 11143–11149 (2015). 10.1021/acs.langmuir.5b02860

539. Yuya, P. A., Hurley, D. C. & Turner, J. A. Contact-resonance atomic force microscopy for viscoelasticity. *J Appl Phys* **104**, (2008). 10.1063/1.2996259

540. Sader, J. E., Larson, I., Mulvaney, P. & White, L. R. Method for the calibration of atomic force microscope cantilevers. *Review of Scientific Instruments* **66**, 3789–3798 (1995).

541. Rabe, U., Turner, J. & Arnold, W. *Analysis of the high-frequency response of atomic force microscope cantilevers*. *Appl. Phys. A* **66**, (1998).

542. Nise, N. S. *Control systems engineering*. (John Wiley & Sons, 2020).

543. Yuya, P. A., Hurley, D. C. & Turner, J. A. Relationship between Q-factor and sample damping for contact resonance atomic force microscope measurement of viscoelastic properties. *J Appl Phys* **109**, (2011). 10.1063/1.3592966

544. Ciesielski, P. N. *et al.* Engineering plant cell walls: Tuning lignin monomer composition for deconstructable biofuel feedstocks or resilient biomaterials. *Green Chemistry* **16**, 2627–2635 (2014). 10.1039/c3gc42422g

545. Bembey, A. K., Oyen, M. L., Bushby, A. J. & Boyde, A. Viscoelastic properties of bone as a function of hydration state determined by nanoindentation. *Philosophical Magazine* **86**, 5691–5703 (2006).

546. Sang, W. & Ural, A. Quantifying how altered lacunar morphology and perilacunar tissue properties influence local mechanical environment of osteocyte lacunae using finite element modeling. *J Mech Behav Biomed Mater* **135**, (2022). 10.1016/j.jmbbm.2022.105433

547. Xu, X. & Raman, A. Comparative dynamics of magnetically, acoustically, and Brownian motion driven microcantilevers in liquids. *J Appl Phys* **102**, (2007). 10.1063/1.2767202

548. Ratcliff, G. C., Erie, D. A. & Superfine, R. Photothermal modulation for oscillating mode atomic force microscopy in solution. *Appl Phys Lett* **72**, 1911–1913 (1998). 10.1063/1.121224

549. Umeda, N., Ishizaki, S. & Uwai, H. Scanning attractive force microscope using photothermal vibration. *Journal of Vacuum Science & Technology B: Microelectronics and Nanometer Structures Processing, Measurement, and Phenomena* **9**, 1318–1322 (1991). 10.1116/1.585187

550. Sader, J. E., Chon, J. W. M. & Mulvaney, P. Calibration of rectangular atomic force microscope cantilevers. *Review of scientific instruments* **70**, 3967–3969 (1999).

551. Donnelly, E. *et al.* Quasistatic and dynamic nanomechanical properties of cancellous bone tissue relate to collagen content and organization. *J Mater Res* **21**, 2106–2117 (2006). 10.1557/jmr.2006.0259

552. Weiner, S., Traub, W. & Wagner, H. D. Lamellar bone: structure–function relations. *J Struct Biol* **126**, 241–255 (1999).

553. Currey, J. D. The many adaptations of bone. *J Biomech* **36**, 1487–1495 (2003).

554. Fischer-Cripps, A. C. Multiple-frequency dynamic nanoindentation testing. *J Mater Res* **19**, 2981–2988 (2004).

555. Nyman, J. S., Granke, M., Singleton, R. C. & Pharr, G. M. Tissue-Level Mechanical Properties of Bone Contributing to Fracture Risk. *Current Osteoporosis Reports* **14**, 138–150 (2016). 10.1007/s11914-016-0314-3

556. Stern, A. R. *et al.* Effect of osteoporosis treatment agents on the cortical bone osteocyte microenvironment in adult estrogen-deficient, osteopenic rats. *Bone Rep* **8**, 115–124 (2018). 10.1016/j.bonr.2018.02.005

557. Kola, S. K. *et al.* Osteocyte lacunar strain determination using multiscale finite element analysis. *Bone Rep* **12**, 100277 (2020). 10.1016/j.bonr.2020.100277

558. Ciani, C., Doty, S. B. & Fritton, S. P. Mapping bone interstitial fluid movement: displacement of ferritin tracer during histological processing. *Bone* **37**, 379–387 (2005).

559. Klein-Nulend, J., Bacabac, R. G. & Bakker, A. D. Mechanical loading and how it affects bone cells: the role of the osteocyte cytoskeleton in maintaining our skeleton. *Eur Cell Mater* **24**, 279–291 (2012).

560. Bacabac, R. G. *et al.* Round versus flat: bone cell morphology, elasticity, and mechanosensing. *J Biomech* **41**, 1590–1598 (2008).

561. Wang, N., Butler, J. P. & Ingber, D. E. Mechanotransduction across the cell surface and through the cytoskeleton. *Science (1979)* **260**, 1124–1127 (1993).

562. Han, Y., Cowin, S. C., Schaffler, M. B. & Weinbaum, S. *Mechanotransduction and strain amplification in osteocyte cell processes*. *PNAS November* **23**, (2004).

563. Yokoyama, Y., Kameo, Y., Kamioka, H. & Adachi, T. High-resolution image-based simulation reveals membrane strain concentration on osteocyte processes caused by tethering elements. *Biomech Model Mechanobiol* **20**, 2353–2360 (2021). 10.1007/s10237-021-01511-y

564. Owan, I. *et al.* Mechanotransduction in bone: osteoblasts are more responsive to fluid forces than mechanical strain. *American Journal of Physiology-Cell Physiology* **273**, C810–C815 (1997).

565. Ling, J. *et al.* Microstructural compositional changes associated with osteocyte lacunae detected using Raman imaging. in *Journal of Bone and Mineral Research* **20**, S149–S150 (AMER SOC BONE & MINERAL RES 2025 M ST, NW, STE 800, WASHINGTON, DC 20036 …, 2005).

566. Hemmatian, H., Bakker, A. D., Klein-Nulend, J. & van Lenthe, G. H. Alterations in osteocyte lacunar morphology affect local bone tissue strains. *J Mech Behav Biomed Mater* **123**, (2021). 10.1016/j.jmbbm.2021.104730

567. Apostolopoulos, C. A. & Deligianni, D. D. Prediction of local cellular deformation in bone - Influence of microstructure dimensions. *Journal of Musculoskeletal Neuronal Interactions* **9**, 99–108 (2009).

568. Prendergast, p. J. & Huiskes, R. Microdamage and osteocyte-lacuna strain in bone: A microstructural finite element analysis. *J Biomech Eng* **118**, 240–246 (1996). 10.1115/1.2795966

569. Verbruggen, S. W., Vaughan, T. J. & McNamara, L. M. Strain amplification in bone mechanobiology: a computational investigation of the in vivo mechanics of osteocytes. *J R Soc Interface* **9**, 2735–2744 (2012).

570. Varga, P. *et al.* Synchrotron X-ray phase nano-tomography-based analysis of the lacunar–canalicular network morphology and its relation to the strains experienced by osteocytes in situ as predicted by case-specific finite element analysis. *Biomech Model Mechanobiol* **14**, 267–282 (2015). 10.1007/s10237-014-0601-9

571. Neer, R. M. *et al.* Effect of parathyroid hormone (1-34) on fractures and bone mineral density in postmenopausal women with osteoporosis. *New England journal of medicine* **344**, 1434–1441 (2001).

572. Watts, N. B. Treatment of osteoporosis with bisphosphonates. *Rheumatic Disease Clinics of North America* **27**, 197–214 (2001).

573. Russell, R. G. G., Watts, N. B., Ebetino, F. H. & Rogers, M. J. Mechanisms of action of bisphosphonates: similarities and differences and their potential influence on clinical efficacy. *Osteoporosis international* **19**, 733–759 (2008).

574. Donnelly, E. *et al.* Reduced cortical bone compositional heterogeneity with bisphosphonate treatment in postmenopausal women with intertrochanteric and subtrochanteric fractures. *Journal of Bone and Mineral Research* **27**, 672–678 (2012).

575. Lloyd, A. A. *et al.* Atypical fracture with long-term bisphosphonate therapy is associated with altered cortical composition and reduced fracture resistance. **114**, (2017). 10.1073/pnas.1704460114

576. Nealy, K. L. & Harris, K. B. Romosozumab: a novel injectable sclerostin inhibitor with anabolic and antiresorptive effects for osteoporosis. *Annals of Pharmacotherapy* **55**, 677–686 (2021).

577. Lovato, C. & Lewiecki, E. M. Emerging anabolic agents in the treatment of osteoporosis. *Expert Opin Emerg Drugs* **22**, 247–257 (2017).

578. Haas, A. V & LeBoff, M. S. Osteoanabolic agents for osteoporosis. *J Endocr Soc* **2**, 922–932 (2018).

579. Cosman, F. Anabolic therapy and optimal treatment sequences for patients with osteoporosis at high risk for fracture. *Endocrine Practice* **26**, 777–786 (2020).

580. Cosman, F. & Dempster, D. W. Anabolic Agents for Postmenopausal Osteoporosis: How Do You Choose? *Current Osteoporosis Reports* **19**, 189–205 (2021). 10.1007/s11914-021-00663-1

581. Bandeira, L. & Michael Lewiecki, E. Anabolic therapy for osteoporosis: update on efficacy and safety. *Archives of Endocrinology and Metabolism* **66**, 707–716 (2022). 10.20945/2359-3997000000566

582. Gobron, B. *et al.* Development of a First-in-Class Unimolecular Dual GIP/GLP-2 Analogue, GL-0001, for the Treatment of Bone Fragility. *Journal of Bone and Mineral Research* **38**, 733–748 (2023). 10.1002/jbmr.4792

583. Mieczkowska, A., Bouvard, B., Legrand, E. & Mabilleau, G. [Gly^2]-GLP-2, But Not Glucagon or [D-Ala^2]-GLP-1, Controls Collagen Crosslinking in Murine Osteoblast Cultures. *Front Endocrinol (Lausanne)* **12**, 721506 (2021).

584. Mieczkowska, A., Irwin, N., Flatt, P. R., Chappard, D. & Mabilleau, G. Glucose-dependent insulinotropic polypeptide (GIP) receptor deletion leads to reduced bone strength and quality. *Bone* **56**, 337–342 (2013).

585. Gobron, B. *et al.* Development of a First-in-Class Unimolecular Dual GIP/GLP-2 Analogue, GL-0001, for the Treatment of Bone Fragility. *Journal of Bone and Mineral Research* **38**, 733–748 (2023). 10.1002/jbmr.4792

APPENDICES

APPENDIX A

SUPPLEMENTARY INFORMATION FOR CHAPTER 3

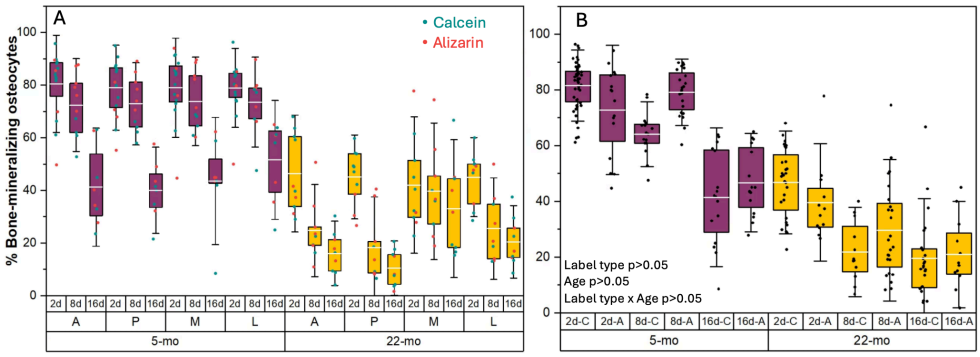

Figure A.1. The effect of calcein or alizarin label delivery order on the percentage of bone-mineralizing osteocytes (i.e., labeled lacunae). The order of calcein and alizarin labeling was alternated to assess the potential influence of label order on measurements of labeled lacunae. For every combination of time points, some mice received the calcein injection first followed by the alizarin injection, while others received the labels in the reverse order. A) The percentage of labeled lacunae for the cortical bone of 5 mo and 22 mo mice at different ROIs (A/P/M/L) and injection dates (2, 8, and 16d before euthanasia). The data points for calcein and alizarin are depicted in teal and red, respectively. B) Label order did not impact the percentage of bone mineralizing osteocytes for either age. Boxplots represent mean value (cross), interquartile range (box), minimum/maximum (whiskers), and symbols representing all data points. All p-values correspond with results of the omnibus mixed-model ANOVA.

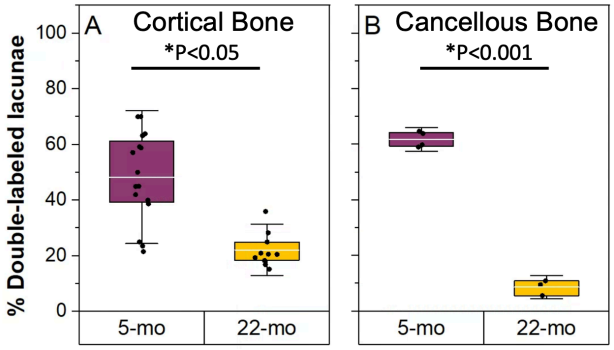

Figure A.2. The effect of aging on the percentage of double-labeled lacunae in cortical and cancellous bone. A & B) In cortical and cancellous bone, double-labeled lacunae (i.e., had both 2d and 16d labels) were abundant in 5 mo mice. The percentage of double-labeled lacunae declined with age (22 mo vs 5 mo: cortical bone, -45% and $p = 0.05$; cancellous bone, -85% and $p < 0.001$). Boxplots represent mean value (cross), interquartile range (box), minimum/maximum (whiskers), and symbols representing all data points. All p-values correspond with results of a two-sided t-test. * represents significant age effect.

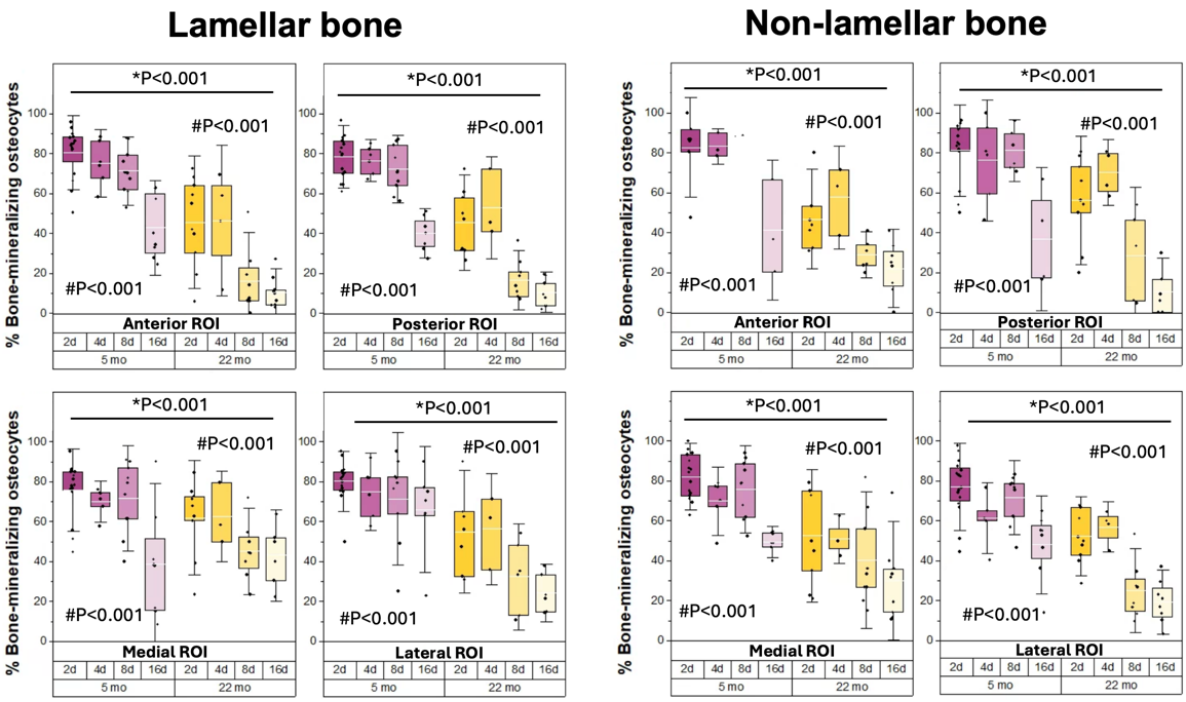

Figure A.3. The percentage of bone-mineralizing osteocytes in lamellar and non-lamellar compartments of cortical bone. In all cortical ROI regions, aging reduced the percentage of bone-mineralizing osteocytes for both lamellar and non-lamellar compartments. For both type of tissues, 16d labeled lacunae were significantly less abundant compared to 2d labeled lacunae, regardless of the age group. All data are reported as percentages (labeled lacunae/all lacunae). Boxplots represent mean value (cross), interquartile range (box), minimum/maximum (whiskers), and symbols representing all data points. All p-values correspond with results of the omnibus ANOVA test. *indicates a significant effect of age. # indicates a significant effect of injection date.

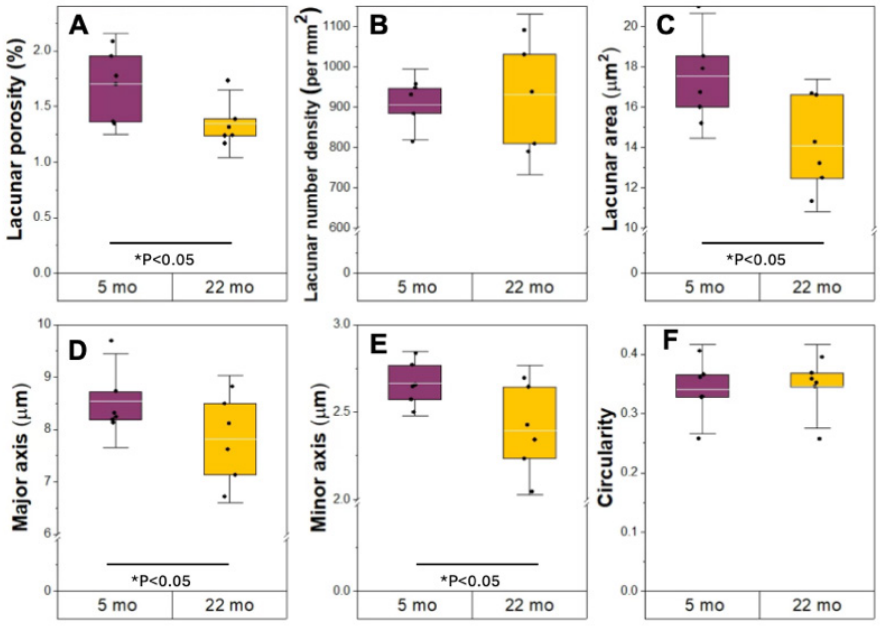

Figure A.4. Lacunar size decreases with age but increases with bone-mineralizing activity. Compared to 5 mo mice, 22 mo mice had A) decreased lacunar porosity (i.e., lacunar pore area / total area), B) unchanged lacunar number density, C-E) decreased lacunar area, major and minor axes, and F) unchanged circularity. Boxplots represent mean value (cross), interquartile range (box), minimum/maximum (whiskers), and symbols representing all data points. All p-values correspond with results of the omnibus ANOVA test. * represents significant age effect.

APPENDIX B

SUPPLEMENTARY INFORMATION FOR CHAPTER 4

Table B.1. Pearson correlations between lacunar size and shape measures vs. measures of modulus gradation.

	Lacuna area (μm)	Lacuna major Axis (μm)	Lacuna minor axis (μm)	Lacuna sphericity
Peak mean modulus (GPa)	0.128	0.202	-0.062	0.208
Area before peak mean modulus (μm^2)	0.020	0.059	-0.094	-0.131
Bulk modulus (GPa)	0.183	0.233	-0.041	-0.217
Δ Modulus (peak - bulk)	-0.178	-0.054	-0.105	-0.039
Normalized modulus, bulk:peak	0.203	0.18	0.004	-0.15
Modulus slope, peak to bulk (GPa/μm)	0.125	-0.006	0.094	0.074
Modulus slope edge to peak, (GPa/μm)	0.185	0.301	-0.026	-0.229
Normalized modulus, edge:peak	-0.304	-0.427	0.060	0.383
Peak standard deviation of modulus (GPa)	-0.007	0.044	-0.090	-0.117
Bulk standard deviation of modulus (GPa)	0.262	0.186	0.172	-0.003
Δ Standard deviation of modulus (peak - bulk)	-0.313	-0.144	-0.342	-0.184
Normalized standard deviation of modulus, bulk:peak	0.375	0.221	0.367	0.149
Standard deviation slope, peak to bulk (GPa/μm)	0.321	0.140	0.360	0.204

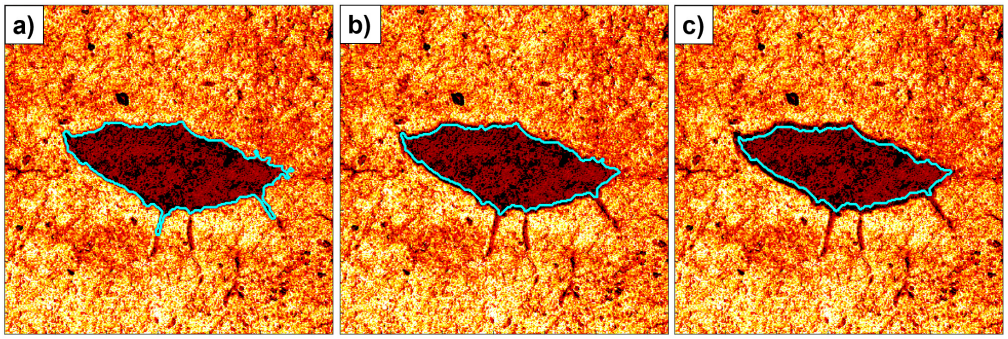

Figure B.1. a) Under-eroded lacuna. b) Properly eroded lacuna. c) Over-eroded lacuna.

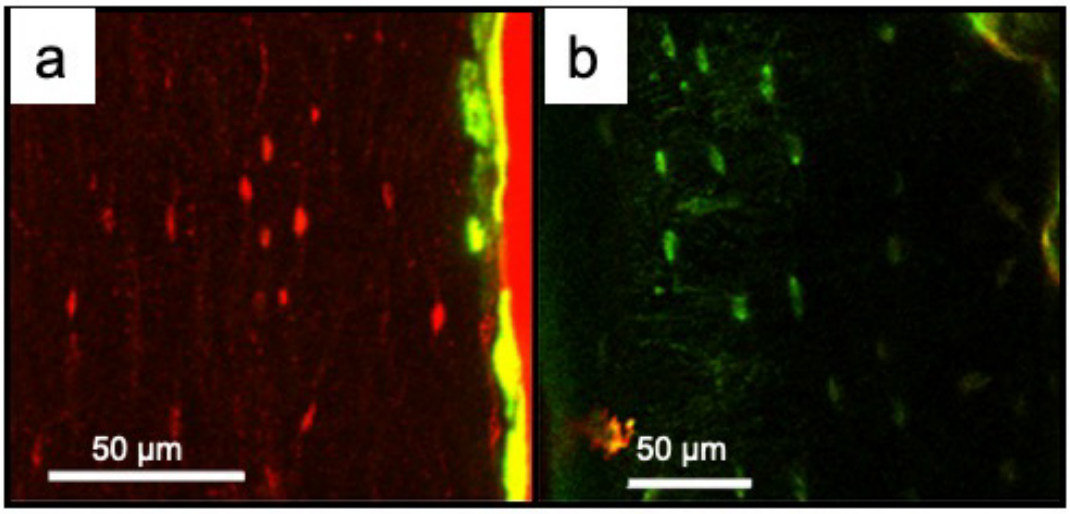

Figure B.2. Osteocyte remodeling abundantly occurs shortly before euthanasia (2 days) regardless of the fluorochrome labeling order. a) Alizarin was administrated 2 days prior to euthanasia (calcein injection 6 days prior). b) Calcein was administrated 2 days prior to euthanasia (alizarin injection 6 days prior). Images shown are composites of a complete z-stack.

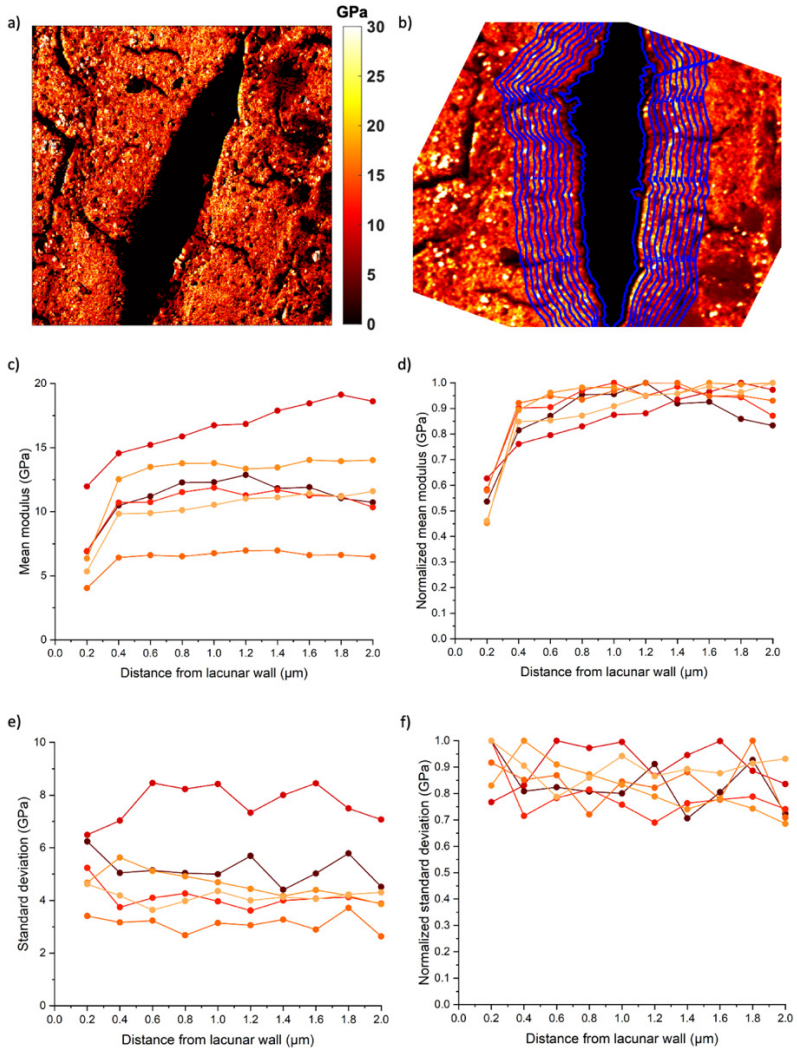

Figure B.3. a) A representative AFM modulus map for osteocyte perilacunar bone tissue from a semi-hydrated sample. b) The processed modulus map. c) Mean modulus for each concentric ring plotted against distance from the lacunar wall for all semi-hydrated maps. The distance from the lacunar wall indicates the outer distance of a bin (e.g., 0.4 μm indicates the 0.2 – 0.4 μm bin). Connected dots each represent individual osteocyte lacuna map. d) Normalized mean modulus for each concentric ring plotted against distance from the lacunar wall for all semi-hydrated lacuna maps. Mean modulus values were normalized against the peak mean modulus value for a given map. e) Mean standard deviation for each concentric ring plotted against distance from the lacunar wall for all semi-hydrated lacuna maps. f) Normalized standard deviations for each concentric ring plotted against distance from the lacunar wall for all semi-hydrated lacuna maps. Standard deviation values were normalized against the peak standard deviation value for a given map. Six AFM maps were obtained from lacunae from one 5 month old female C57Bl/6 mouse. The femur was embedded in epoxy, transversely sectioned, and rehydrated in tap water. The surface was wicked dry before testing.

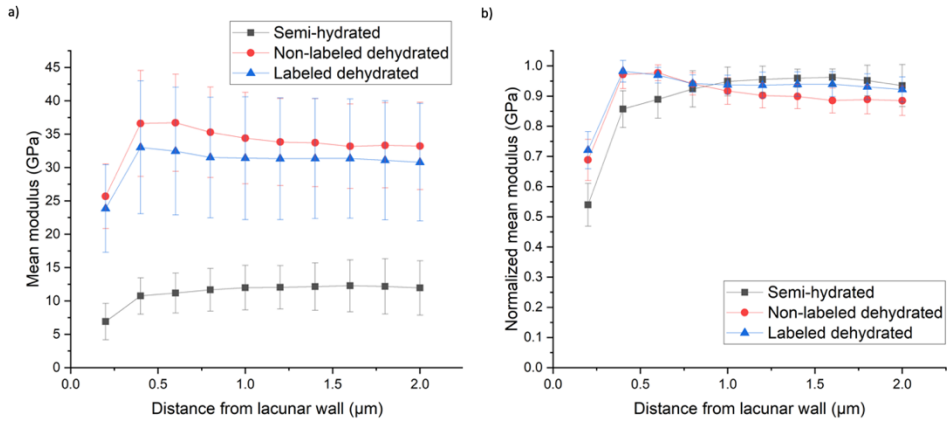

Figure B.4. a) Mean moduli for each concentric ring versus distance from the lacunar wall is plotted with averaged data from all semi-hydrated, non-labeled dehydrated, and labeled dehydrated lacunae. Error bars represent one standard deviation. The distance from the lacunar wall indicates the outer distance of a bin (e.g., 0.4 μm means 0.2 – 0.4 μm). b) Normalized mean moduli for each concentric ring versus distance from the lacunar wall is plotted with averaged data from semi-hydrated, non-labeled dehydrated, and labeled dehydrated lacunae. Error bars represent one standard deviation. Mean modulus values were normalized against the peak mean modulus value for a given map.

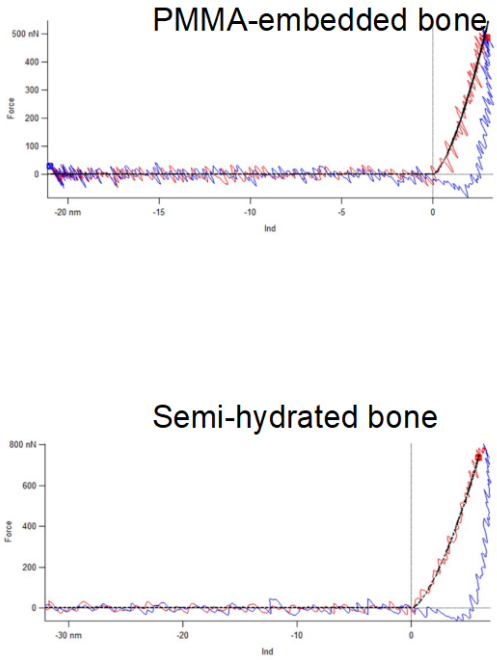

Figure B.5. Representative AFM curves from PMMA-embedded bone (top) and semi-hydrated bone (bottom). Both types of samples were analyzed using a Hertzian contact model fit to the extension curve (red).

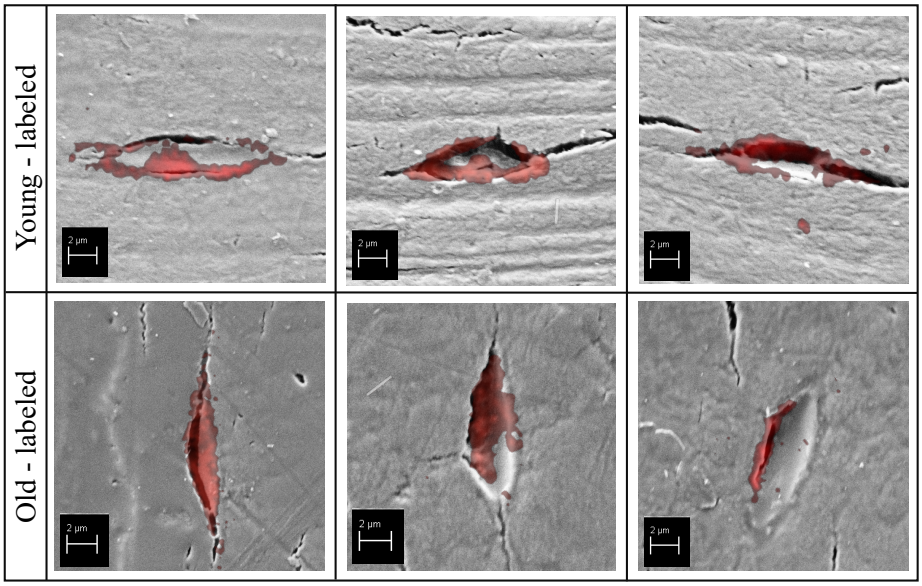

Figure B.6. Secondary mode SEM images (8-10kx) with superimposed alizarin fluorescent labels (2d before euthanasia) for young (5 month) and early old age (22 month) female C57Bl/6 mice. The label image is a composite of the ~30 µm stack of confocal laser scanning microscopy images.